9-4-2014

Charge Photogeneration Experiments and Theory in Aggregated Squaraine Donor Materials for Improved Organic Solar Cell Efficiencies

Susan Demetra Spencer

R·I·T

Charge Photogeneration Experiments and Theory in Aggregated Squaraine Donor Materials for Improved Organic Solar Cell Efficiencies

by

Susan Demetra Spencer

A dissertation submitted in partial fulfillment of the requirements for the degree of Doctorate of Philosophy in Microsystems Engineering

Microsystems Engineering Program

Kate Gleason College of Engineering

Rochester Institute of Technology

Rochester, New York

September 4, 2014

Charge Photogeneration Experiments and Theory in Aggregated Squaraine Donor Materials for Improved Organic Solar Cell Efficiencies

By

Susan D. Spencer

Committee Approval:

We, the undersigned committee members, certify that we have advised and/or supervised the candidate on the work described in this dissertation. We further certify that we have reviewed the dissertation manuscript and approve it in partial fulfillment of the requirements of the degree of Doctor of Philosophy in Microsystems Engineering.

Dr. Chris Collison Date

Associate Professor

Dr. John Andersen Date

Professor, Department of Physics and Astronomy

Dr. Jeremy Cody Date

Associate Professor, Department of Chemistry

Dr. Seth Hubbard Date

Associate Professor, Department of Physics

Certified by:

Dr. David Borkholder Date

Interim Director, Microsystems Engineering Program

Dr. Harvey Palmer Date

Dean, Kate Gleason College of Engineering

ABSTRACT

Kate Gleason College of
Engineering Rochester Institute of
Technology

Degree: Doctor of Philosophy **Program**: Microsystems Engineering

Authors Name: Susan D. Spencer

Advisors Name: Christopher Collison

Dissertation Title: *Charge Photogeneration Experiments and Theory in Aggregated Squaraine Donor Materials for Improved Organic Solar Cell Efficiencies*

Fossil fuel consumption has a deleterious effect on humans, the economy, and the environment. Renewable energy technologies must be identified and commercialized as quickly as possible so that the transition to renewables can happen at a minimum of financial and societal cost. Organic photovoltaic cells offer an inexpensive and disruptive energy technology, if the scientific challenges of understanding charge photogeneration in a bulk heterojunction material can be overcome. At RIT, there is a strong focus on creating new materials that can both offer fundamentally important scientific results relating to quantum photophysics, and simultaneously assist in the development of strong candidates for future commercialized technology. In this presentation, the results of intensive materials characterization of a series of squaraine small molecule donors will be presented, as well as a full study of the fabrication and optimization required to achieve >4% photovoltaic cell efficiency. A relationship between the molecular structure of the squaraine and its ability to form nanoscale aggregates will be explored. Squaraine aggregation will be described as a unique optoelectronic probe of the structure of the bulk heterojunction. This relationship will then be utilized to explain changes in crystallinity that impact the overall performance of the devices. Finally, a predictive summary will be given for the future of donor material research at RIT.

ACKNOWLEDGMENTS

First and foremost, to my daughter, Maya Patamon Spencer. You are my heart, my inspiration, my star, and your patience, love, goofiness, and brains have gotten us through this together. This is for you. My sister, Lisa Witt, has been an endless source of support, love, care, encouragement, and passion. I love you, Li. Couldn't have done it without you. I want to thank my grandpa and grandma, Bernie and Ginny Friday, for their constant belief that I could finish. Thanks to my aunts and uncles, Alan, Lynda, Janice, Jeff, Brian, Lynne, Larry, Ken, Janet, Bill and Shirley; you guys rock. Thanks to my cousins, Chris, Holly, Megan, Sarah, Aimee, Amanda, Rem, Eric, Erika, Sarah, David, and Stephen; just knowing you were around is a huge support. Thanks to my brothers-in-arms in the trenches everyday, Chris B., The Stephen, Morning Zac, Slopedog, YUSHUAI, Victor, Harry Hizzy, Li, Bi Zhu, AniRUDH, Heaphy, Guy the Third, Patrick C, James, and last but definitely not the least, the soon-to-be blonde, new and improved, Susan Spencer AKA Chenyu Zheng.

Enormous gratitude to all the professors that got me here: Kathy Lawton, James Anderson, Brian Edelbach and Lydia Tien, all of whom showed enormous support in my formative years as a chemist at MCC.

I owe a huge intellectual debt to my committee. John, thanks for always having an open door, talking quantum photophysics when no one else could, and giving me water at water stops. Seth, thanks for also always having an open door, putting up with questions from a chemist with zero double-E experience, and your support of my professional and personal advancement. Jeremy, thanks for also ALSO always having an open door, and taking a risk on a first year PhD student with an idea for these weird molecules that might do some really cool stuff.

Thanks to my department head, Bruce Smith, for unwavering support of all of my pursuits, and for a steadying influence during the loss of my mother. Lisa Zimmerman, you are a goddess among organizers of departmental things, and I literally would not be graduating without all of your attention.

Thanks to the friends who have seen me through: Mike, Nikars, Collin, Jason, Ken, James, Bill, Gruff, Juan, Bailey, Jason, Bianca, Liz, Mess, Jeff, John, Jill, Erik, Ian, Mitch, John, Jen, Luke, Michael, and every single person who has raised a glass, lent an ear, and supported me during the toughest years of my life.

Finally, an enormous debt of gratitude to my advisor, Chris Collison. Not only have you put up with my constant questioning, stubbornness, and growth process as a scientist, you have gone out of your way time and time again to be a pillar of support in my life through incredibly difficult times, as well as assisting me as I transition to the next stage of my career. Thank you.

DEDICATION

This work is dedicated to the memory of Gary W. Witt and Linda J. Witt, with all my love-SDS

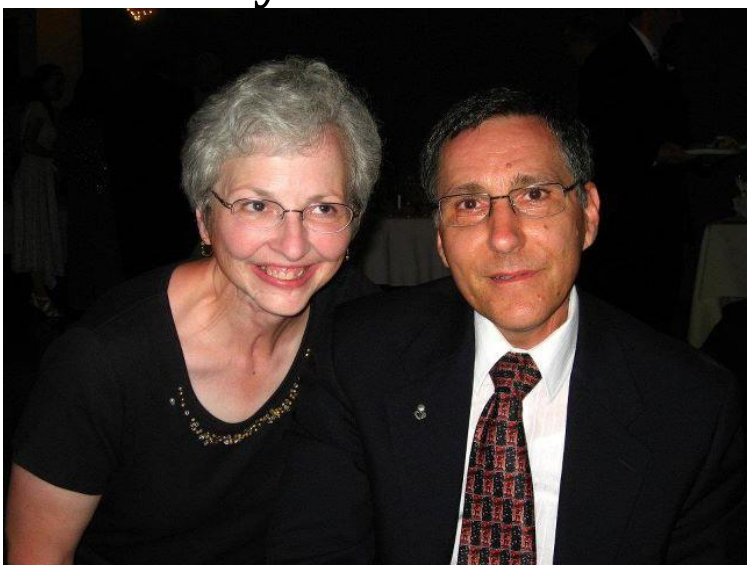

TABLE OF CONTENTS

LIST OF FIGURES

1. Introduction and Background

Chapter Abstract

In this chapter, a statement of purpose will be given for the entire dissertation. This will be followed by an exploration of the need for drastic changes in energy technologies, and how both organic photovoltaics and squaraine donor materials can serve a purpose in meeting those needs. A brief description of the operational photophysics of organic photovoltaics will be given to familiarize the reader.

1.1. Statement of Purpose

This dissertation will describe the complete doctoral work of my work since beginning the program in 2010. The Introduction (Chapter 1) provides a motivation for the usage of solar power, the push to commercialize organic solar cells through guided prescriptive fundamental research, and for the inclusion of squaraines as a donor material that offers both efficiency gains and unique research opportunities. In Experimental Methods (Chapter 2), a full description of the variety of techniques is given, along with a brief motivation for each technique. Chapter 3, Charge Photogeneration in Organic Photovoltaics, gives an overview of the process of converting light into electricity from both an experimental and theoretical point of view, with a concluding focus on how squaraine aggregates relate to charge photogeneration. Chapter 4, Squaraine Aggregates, details the important optoelectronic properties of the aggregates and how they are characterized both as a material system and as a device component. Chapter 5, Experimental Results, gives the comprehensive accumulated data analysis, beginning with a characterization study on a single squaraine, and then moving to characterization of a series of six squaraines. Device data is then presented, with a focus on both

squaraines and the polymer system used during the duration of the thesis. A statistically-focused summary of work performed is given at the end of the chapter, with metrics on number of devices fabricated. Chapter 6 (Discussion) explores the two fundamental questions that have been investigated and answered by this thesis work, and then the key findings are summarized for both squaraine and polymer devices. Chapter 7, Theoretical Analysis of Key Findings, turns to an examination of the theories described briefly in Chapter 3. A connection between Marcus-Hush theory and Onsager-Braun theory is given here through the lens of squaraine aggregate excitons at the bulk heterojunction (BHJ). Additionally, the thermodynamics that are responsible for the development of the BHJ are given a thorough discussion This treatment of thermodynamics leads into Chapter 8, Molecular Structure Predictions for Optimum BHJ Morphology. This capstone chapter ties together the theoretical work that has been done along with the characterization and device results to first describe the critical components for a squaraine molecule in order to maximize efficiency. Then, this molecular structure is related to the BHJ, followed by a brief review of the connection between the BHJ morphology and device performance detailed in Chapter 3. Finally, a detailed prescription for the ideal squaraine molecule and ideal device structure is presented, using all of the theoretical and experimental work explained previously. The Conclusion (Chapter 9) is divided into two sections; the first will detail the thesis contributions to the field of fundamental photophysical research, and the second summarizes the thesis contributions to the field of solar cell technologies as a whole. All References are given in Chapter 10. Chapter 11 contains the three Appendices; the first serves as a glossary of sorts that details and summarizes each of the relevant components of the thesis in short

paragraph form, the second gives additional figures referenced within the text as useful to the reader, and the third gives any additional pertinent raw data.

1.2. Energy and the Environment

Both globally and in the United States, consumers are facing an oncoming crisis of increasing oil, coal, and natural gas prices as the reserves of these nonrenewable energy sources begin to decline.[6] Figure 1 shows the historical, current, and projected world fuel consumption by fuel type from 1990 to 2035.

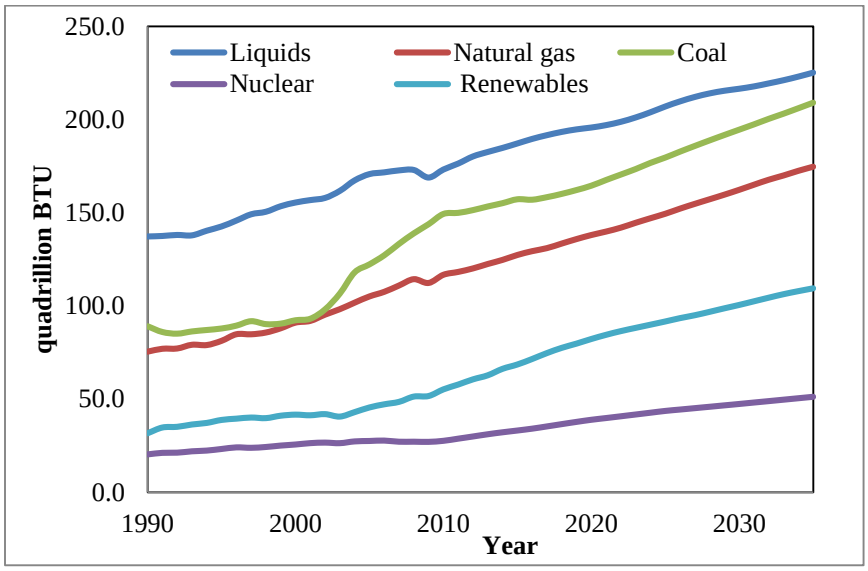

Figure 1 Measured and projected world fuel consumption by fuel type.[6]

The demand for energy is not going to decrease, because the world population is increasing, the standard of living is increasing, and industrialization of formerly third world countries is on the rise. As can be seen in Figure 1, the primary fuel consumed is liquid, and the primary liquid being consumed is oil. There are both severe economic and environmental implications to a continuing dependence on oil for our species, other species, and the planet as a whole.[7] The price of oil is expected to continue rising, while the ability to produce it

will begin to decline as the supplies are exhausted.[6] Figure 2 shows three potential price projections for a barrel of crude petroleum.

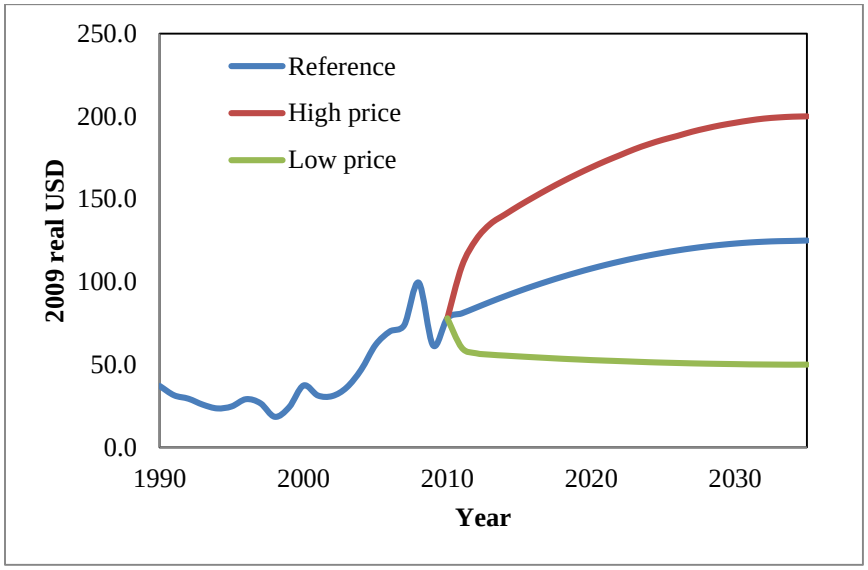

Figure 2 The price of a barrel of crude petroleum in 2009 US dollars.[6]

In addition to the economic costs, there are massive environmental implications of using fossil fuels. Because anthropogenic emissions of carbon dioxide result primarily from the combustion of fossil fuels, energy consumption is a major factor in understanding the pace and impact of climate change. Figure 3 shows the global energy consumption-related carbon dioxide emission projections by fuel type.

Atmospheric temperature changes caused by rising carbon dioxide concentrations are not expected to decrease significantly even if the carbon emissions were to cease immediately.[8] The irreversible changes to our environment include Artic Sea ice retreat, increases in heavy rainfall and flooding, permafrost melt, loss of glaciers and snow pack leading to reduced fresh water supply, and intensity increases of hurricanes.[9] Figure 4, prepared by Solomon et al, shows the impact of carbon dioxide emissions on surface warming of the earth and thermal expansion of the ocean.

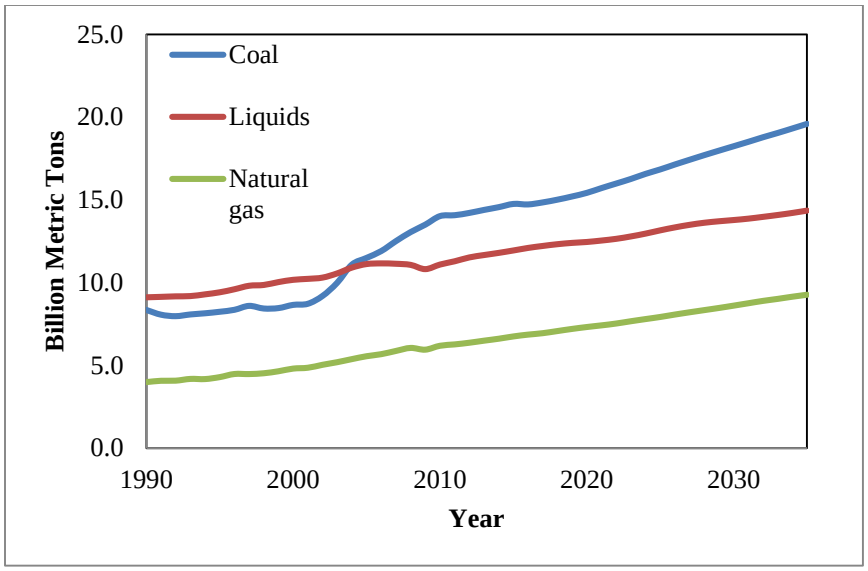

Figure 3 Historical and projected data showing a continuing increase of emitted carbon dioxide globally.[6]

In short, we face a catastrophic set of circumstances that cannot be rectified by one country, one institution, or one technology. The "bright spot" from these figures is the trendline predicted for Renewables, shown in Figure 1. Renewable energy sources, including wind, hydroelectric, solar, and nuclear power are all predicted to be the fastest growing source of energy for consumption over the next two decades.

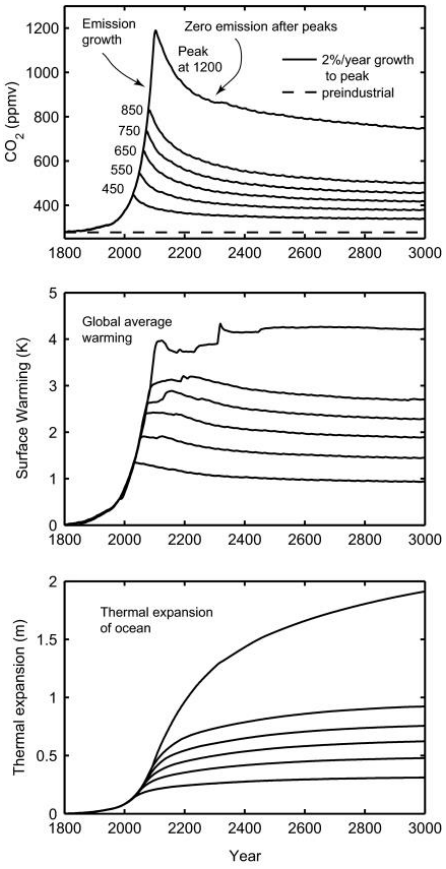

Figure 4 Top: Falloff of CO_2 concentrations following zero emissions after the peak. Middle: Globally averaged surface warming at the six peak values modeled in top figure. Warming over land is expected to be greater than these globally averaged values, with the greatest warming expected in the Artic. Bottom: Sea level rise in meters from thermal expansion only, not including loss of glaciers, ice caps, or ice sheets.[8]

1.3. Renewable Energy and OPV Potential

Two of these technologies, wind and solar, do not directly produce any carbon dioxide emissions. Utilization of solar power will act as a retardant upon inevitable and irreversible climate changes, potentially creating a window of opportunity for our species and the ecosystems we live in to adapt to the changes that industrialization has wrought.

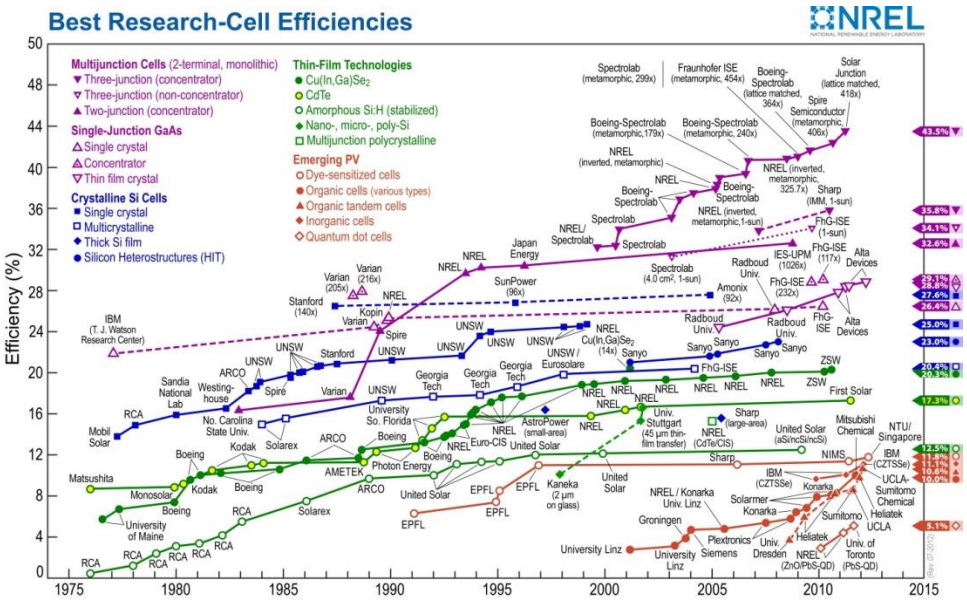

Figure 5 Pictorial representation of the growth of the solar cell industry as represented by the certified device efficiencies for a variety of prototypical solar cells over the last three decades. Both the chart and the certifications were done at the National Renewable Energy Laboratory.[10]

As shown in Figure 5, solar cell technology, converting photons into a measureable source of electricity, has been around since the late 1970s. All of the solar technologies shown have benefits and disadvantages; technologies that have been around the longest have reached higher efficiencies (e.g. crystalline Si cells, 27.6% efficiency) but are in turn at the end of their learning curve. There are only small modifications and improvements

that can be made to established technologies, and they will not therefore be able to become significantly more efficient. Additionally, III-V semiconductors and silicon are expensive to fabricate, both in terms of actual cost and energy use during fabrication.

Conversely, organic solar cells are a new and disruptive technology. Organic photovoltaic cells [OPVs] offer a low-cost, solution-processable alternative to conventional silicon based solar cells.[11] With increased potential for flexibility and reel-to-reel manufacturing combined with recently reported power conversion efficiencies regularly approaching 8%,[12] organic solar cell technology has become commercially interesting and the subject of intensive research[3,13,14] over the last decade. OPVs are able to compete with traditional silicon solar cells as well as the III-V semiconductor solar cells despite having lower efficiencies because of their cost and unique processing potential. OPVs are estimated to decrease in cost to a highly competitive 0.5-1 USD/WP by 2018.[15] By upscaling the typical in-house processing method of spin-coating to roll-to-roll processing, mass production of OPVs can be achieved[16,17]; there are numerous barriers to be overcome in order to reach this scale-up however, not the least of which being the need for materials that satisfy the "10-10 rule" (10% efficiency and 10 years of stability). Stability[18,19] is currently being addressed using inverted device structures[20] as well as encapsulation techniques.[21]

Beyond the barrier of the 10-10 rule, OPVs have some other significant roadblocks to becoming a prevalent technology. The true cost of any alternative energy technology, and any type of solar cell, can only be understood with an expanded perspective that encompasses the production of the ingredients used to make the device all the way to the eventual destruction and recycling of the device.[22] When examined

thus, the chemical processing of OPVs offers multiple difficulties. The solvents used to prepare them are often toxic and expensive to dispose of. Electrode materials can compose greater than 80% of the overall cost of the device.[23] The only ways to combat these potential costs of upscaling the technology are to use solvents that are less expensive (e.g. water), fabricate more efficient devices, and design cheaper electrodes. In order to use different solvents, the materials used to make the devices must be water soluble. For cheaper electrodes, new transparent conductors like carbon nanotubes must be utilized. But in order to fabricate more efficient devices, there must be a leap in fundamental understanding of the processes that govern the operation of organic photovoltaics; namely, the material's properties that impact the process of charge photogeneration at the interface between the light-absorbing material (electron donor) and the electron transport material (electron acceptor). It is this fundamental scientific understanding that I am going to contribute to with my body of work, as I examine the impact of a material's properties upon the process of charge photogeneration. Only by developing the model of charge photogeneration further can the efficiencies of organic devices ultimately be increased. Development of the model requires both sensible experimental design and incorporation of multiple theoretical treatments of charge photogeneration.

1.4. Squaraine Materials and Their Unique Capabilities

Prevailing experimental design for increasing the power conversion efficiency (PCE) is to increase the absorption of the materials within the solar cell; by increasing the

number of photons absorbed, the number of electrons generated will duly increase. Synthesizing ultraviolet-visible (UV-VIS) absorbing polymers with higher extinction coefficients has been one approach,[24] but another is to increase the range of wavelengths absorbed through incorporation of near-infrared (NIR) active materials in tandem devices.[25] Collection in the UV-VIS region of the solar spectrum garners only 40% of the available energy in the solar spectrum;[26] through design and synthesis of NIR absorbers with high extinction coefficients a greater amount of solar energy can be harvested with their addition, thereby increasing the PCE. Following successful production of a single junction NIR photovoltaic cell, tandem photovoltaic cells can be fabricated which incorporate absorbing layers to collect photons from the UV out to the NIR.

Squaraines are a family of molecular chromophores that have high extinction coefficients exceeding 10^5 L mol^{-1} cm^{-1} in the NIR,[27] low energy bandgaps less than 1.5 eV, and are solution processable.[28] Molecular chromophores offer advantages over polymers in that they are monodisperse and offer a greater amount of control and predictability of crystalline packing and aggregation. Additionally, squaraines offer the added benefit of enhanced solubility in water and alcohols making them much more promising candidates for roll-to-roll processing than other materials which require aromatic solvents.[29] Finally, the squaraines in this work are easily synthesizable, not commercially available, have a panchromatic absorption, and a unique donor-acceptor-donor structure leading to enhanced charge transfer state characteristics as well as aggregation. In terms of experimental design and theoretical complexity, the squaraines are fabricated as a molecular series, with differing lengths of hydrocarbon side chains or presence/absence of hydroxyl groups as shown in Figure 6. These molecular changes

generate changes in the packing of the molecules which in turn impact exciton and free charge carrier generation; these two intermediary states of exciton and free charge carriers comprise the crucial states involved in the process of charge photogeneration.

A comprehensive understanding of the impact of the molecular structure upon the morphology of the bulk heterojunction (BHJ) is critical for increasing the efficiency of these materials. The remainder of this thesis is devoted to a development of this understanding, as it moves from the relationship between molecular structure and aggregation, to the characterization of those aggregates, to the role of the aggregates at the BHJ, and finally how they impact overall efficiency of the devices.

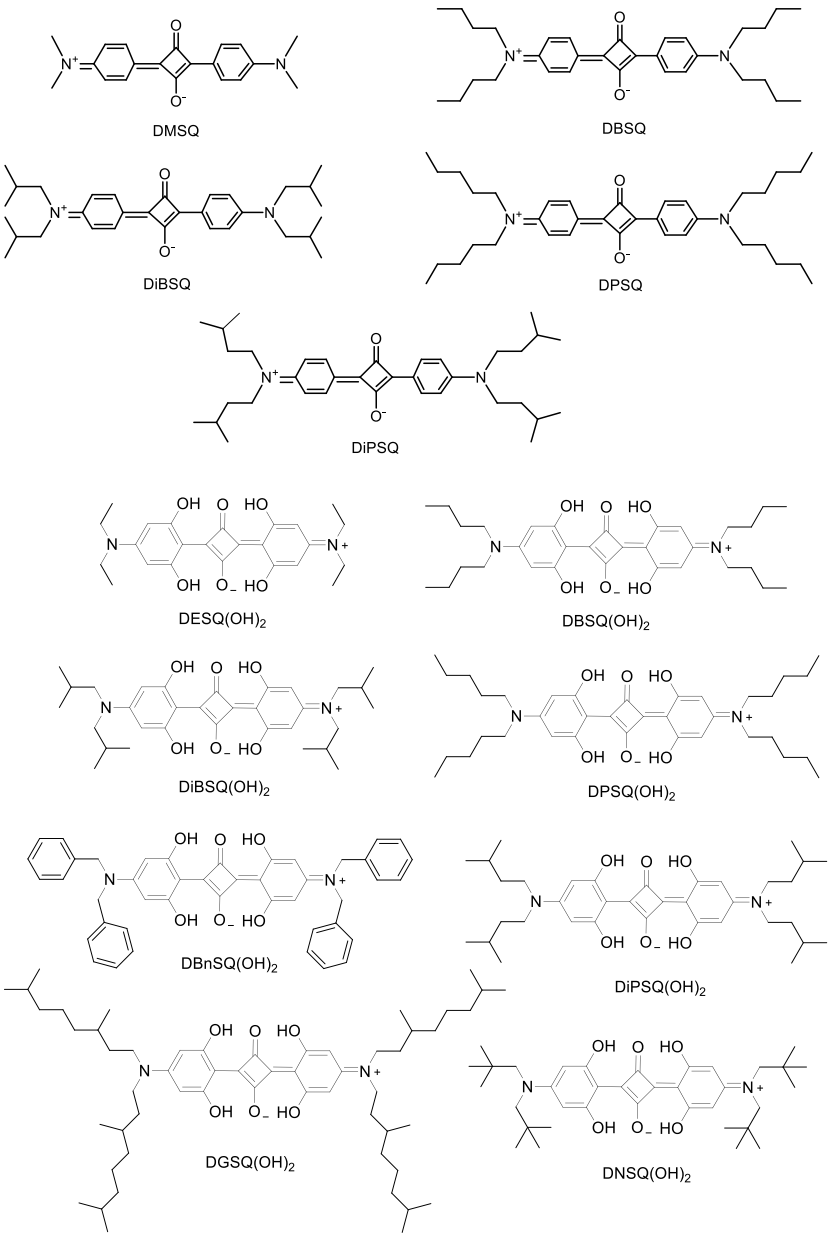

Figure 6 A list of some of the squaraines designed and synthesized by the Cody Group (Dr. Jeremy Cody, Cameron Gallivan, Patrick Heaphy, Michael Clark, and Amber Monfette). S. Spencer assisted in initial design.

1.5. Photophysics of OPVs and Their Relationship to Material Properties

There are three main metrics[30] that generate the photovoltaic power conversion efficiency (PCE), and they are the open circuit voltage (V_{OC}), short circuit current (J_{SC}), and fill factor (FF), as well as the spectral response of the device which can be used to calculate the external quantum efficiency (EQE). Each of these metrics is directly measured from the device, and each is a consequence of the material properties of the donor and acceptor[31–33]. The J_{SC} results from the number of electrons that are collected at the bulk heterojunction, which in turn depends on the localized mobility of each of the materials and associated charge recombination, the rates of exciton dissociation and charge transfer at the bulk heterojunction, the extent of exciton diffusion, and finally the number of photons that are initially absorbed by the materials. The V_{OC} is also dependent on the materials; specifically, the energy level gap between the highest occupied molecular orbital (HOMO) of the squaraine and the lowest unoccupied molecular orbital (LUMO) of the PCBM. In other words, the difference in energy levels between the ionization potential of the donor and the electron affinity of the acceptor control the maximum operating voltage that can be obtained within the device. The fill factor is determined by the extent of mixing between homogeneous domains of the donor and acceptor molecules, and as such is a metric for the goodness of the bulk morphology of the materials blended together under specific processing conditions like annealing temperature and blend concentration. Finally, the spectral response is determined by the absorbance properties of the materials, where the transitions occur that lead to the

generation of free charges. Since the spectral response is a measure of the electrons that are able to be collected for every photon, it also has to therefore take into account the properties that govern J_{SC}, V_{OC}, and FF. It is clear even from this brief discussion that there is a deep interrelationship between the squaraine materials that are chosen for the photovoltaic and the resultant values of each of these performance metrics[34]. Within this thesis, the balance between the crystallinity and amorphousness of the squaraines will be discussed in the context of the device performance metrics, as well as from a materials characterization perspective. When the squaraines' crystallinity and aggregation can be predicted from their molecular structure, and those morphology characteristics can be correlated to device performance, we will be able to prescribe the ideal squaraine molecule for a given photovoltaic application. This predictive ability will allow for a dramatic reduction in both the time cost and financial cost of device fabrication and upscaling, which will allow this disruptive technology to reach commercialization as quickly as possible.

2. Experimental Methods and Techniques

Chapter Abstract

In this chapter, the methods for all experiments reported in this dissertation are described in a linear fashion, progressing from the characterization of materials via optical, electronic, and spatial/morphological techniques, to the processing of the materials into both thin films and devices, finishing with descriptions of the testing set-up and protocols for device analysis.

2.1. Characterization

2.1.1. Optical

2.1.1.1. Absorbance

Motivation Absorbance directly impacts the efficiency of any photovoltaic device. Inclusion of materials that are effective absorbers of a wide range of photon energies generates the largest amount of free carriers, and is the best use of the light available from the solar spectrum. Understanding the properties of the excited states of these materials is critical. Because any extant charge transfer (CT) state cannot be directly probed or measured, detailed examination of the initial exciton, and the final free charges, will give vital information about the CT state. The absorbance studies performed in dilute solution are measuring the excitation of the monomer species of the squaraine donor materials, while absorbance measurements in thin films are measuring the excitation of the nanocrystalline aggregates and amorphous regions. The morphology of the region will create different absorbance spectra, because the extent of delocalization of the exciton will be highly dependent on the amount of crystallinity that is present. This in turn will affect what photon wavelengths are able to be absorbed Additionally, formation

of aggregates will cause Davydov splitting of the exciton which should be visible as peaks that are blue- and red-shifted from the monomer.[35] Therefore, absorbance measurements are an inexpensive, elucidative method for categorizing and assigning properties of each exciton formed on specific morphologies.

Technique For all absorbance measurements, films were prepared with identical processes, as described in Section 2.2.1. Multiple measurements were taken as randomly as possible over the surface of each film and the reported results are averaged over these measurements for that film. Small total process variation nevertheless exists which results in small but significant absolute absorption variance between otherwise identical films. Measurements were taken on a Shimadzu 2400 UV-VIS-NIR spectrophotometer, from wavelengths of 300 to 900 nm in increments of 0.5 nm. Before each measurement set, the instrument was blanked with the appropriate reference; typically, for device analogue films, the reference was a PEDOT:PSS/ITO/glass prepared film that was made in an identical fashion and at the same time as the films to be measured. In situations when the blank was not the PEDOT:PSS coated ITO film that will be clearly stated, and the actual blank used will be stated. This is an effort to take into account the known morphological variations of the PEDOT:PSS, but it is recognized that there will still be variations from film to film, as well as within each individual film set. The errors have been statistically accounted for by averaging the measured absorbance at three different places in the film. Because absorbance variations within an identical film set will be considered to be a function of variations in thickness of the film due to the spin-coating process, averaging the absorbance over the three measurements is considered to give an appropriate value, especially when the standard deviation is given. There will also be variations in thickness

of the ITO on the glass, and the spun-cast PEDOT:PSS on the ITO. However, the variations in ITO thickness are so small as to be considered negligible as given by the manufacturer (< 4 nm). Additionally, the variations in PEDOT:PSS, while larger because of the spin-coating process, are smaller relative to the overall thickness of the PEDOT:PSS layer (150 nm +/- 6 nm). Therefore, the blanking process is considered to take into account the subtle variations in the substrate. The varying thicknesses of the active layer (the layer whose absorbance is being measured and reported throughout this thesis) is therefore varying solely as a function of the process of spin-coating a heterogeneously mixed solution. All measurements reported for absorbance intensity in this work are therefore calculated across the three film measurements, and then across multiple films that have been prepared from identical solution. This gives a matrix of nine measurements per reported measurement in this thesis, with the standard deviation calculated from these nine measurements. By using the formula for unbiased standard deviation (given below), and having n=9, the bias of the sample is reduced to >0.1%, where the bias is defined as being the difference of the estimator's expected value and the true value of the parameter being estimated. In the measurement described here, the estimator is therefore the average absorbance value calculated as being representative of the absorbance of the film as a whole.

$$\hat{\sigma} = \sqrt{\frac{1}{N - 1.5}\sum_{i=1}^{n}(x_i - \bar{x})^2}$$

2.1.1.2. Fluorescence

Motivation Fluorescence is an ideal measurement for materials characterization, because it allows for examination of the relaxation mechanisms of the excited state for each material as a function of molecular structure, as well as giving an opportunity to extract energy level values of the excited state as a function of film properties like thickness or presence/absence of a quencher. Because fluorescence results from the radiative decay of the excited state, it gives information about that excited state and the extent of its coupling to the ground state. This then allows for inference of changes in deactivation pathways for the excited state as the morphology of the sample is changed. Unfortunately, despite all best efforts, fluorescence from squaraine thin films is all but impossible to measure because the quantum yield for fluorescence in these films tends to zero. Although the squaraines are extremely optically active in solution and give very nice fluorescence profiles, quantum yields, and lifetime measurements, there is little to no observable fluorescence when thin films are examined using standard techniques. The two workarounds for this are to use confocal microscopy to obtain fluorescence, or by preparing the squaraines as solid solutions using PMMA. The first technique, confocal microscopy, works because of increased sensitivity of an imaged microscopic region of the sample coupled with an intense laser excitation of the molecules; the detector is highly sensitive to even single photon fluorescence. The drawback is that this technique is very time consuming and expensive. The simplest solution to this would be to use a traditional optical bench setup with a tunable laser and PMT detector to measure fluorescence of thin films.

The second technique, using solid solutions of squaraine and PMMA, allows for measurement of fluorescence as a function of concentration of the squaraine in the solid solution. However, there is no way to prove that the morphologies of the squaraine in solid solution are the same as the morphologies present in the thin film. An extensive amount of work has been done on this topic by B. Zhu, G. Wolfe, and C. Zheng, and fluorescence will therefore not be utilized as a technique for materials characterization or evaluation of device-relatable properties within the contents of this thesis.

2.1.2. Electronic

2.1.2.1. X-ray Photoelectron Spectroscopy (XPS)

Motivation XPS is a very common technique used to measure the highest occupied molecular orbital (HOMO) energies of a material. The HOMO energy is a valuable material property to know, because it allows for a Jablonski diagram to be devised showing the possible paths for an electron and hole to travel when the overall electronics of the device are considered. Because electronic transitions can only occur between orbitals that are occupied by at least one electron to orbitals that are not already occupied by two electrons (the lowest unoccupied molecular orbitals, LUMO), many optical properties rely upon the HOMO-LUMO gap, and therefore the ability to accurately measure the HOMO values is critical to optimizing the electronic structure of an OPV. A sample Jablonski diagram showing all potential photophysical processes in charge photogeneration is shown in Figure 7, where the S_1 designation corresponds to the HOMO value that is measured with this technique.

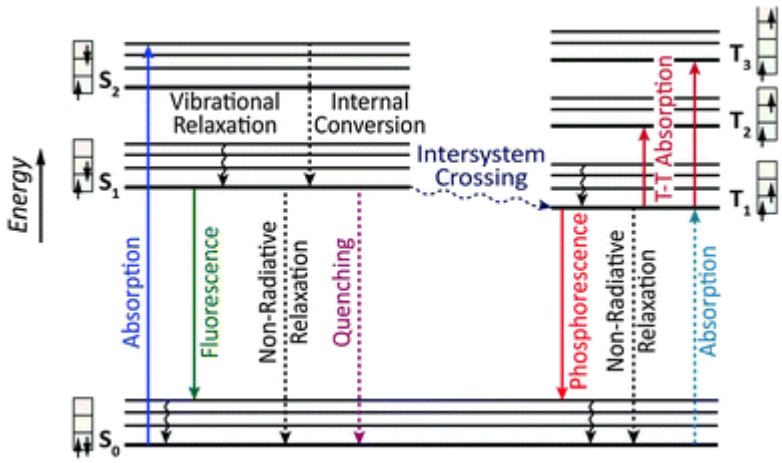

Figure 7 Jablonski energy level diagram showing principle electronic processes of organic molecules. Reprinted with permission from [1].

Additionally, the HOMO value of the donor material plays a role in determining the open-circuit voltage of a device, as will be described in Section 7.3. Finally, when an XPS-measured HOMO value is combined with the optical bandgap of the material that is measured by absorbance, an estimation of the lowest unoccupied molecular orbital (LUMO) value for the material can be made. The LUMO/HOMO energies of the material can then be compared within a particular series of donor material structures, and then be correlated with device efficiencies.

Technique All XPS measurements were performed at Xerox Corporation by Michael Mehan, and the following information has been quoted directly from his reports. The samples were analyzed with X-ray Photoelectron Spectroscopy (XPS), a surface analysis technique that provides elemental, chemical state and quantitative analyses for the top 2 – 5 nanometers of a sample's surface. A Physical Electronics Model 5800 XPS was employed for the characterization. A region about 1 millimeter in diameter was analyzed. The films were presented as prepared by the submitter. The substrates were

held in place on the stainless steel sample holder with screws and washers. The quantitative analyses are precise to within 5% relative for major constituents and 10% relative for minor constituents. The samples were irradiated with monochromatic Al kα radiation (1486 eV) and charge neutralized with a flood of low energy electrons from a BaO field emission charge neutralizer. This method of analysis minimized radiation damage to the samples. Spectra were acquired at an angle of 45 degrees.

2.1.3. Spatial/Morphological

2.1.3.1. AFM

Motivation AFM gives critical morphology information about how the materials under study are crystallizing, as well as data about the surface roughness of the film, and description of feature size. As such, it is a useful technique when considering how the surface structure of the film will impact the organic/electrode contact, but it cannot be used to make direct interpretations of the specific features of the bulk material or of the bulk heterojunction.

Technique The top surface of the BHJ thin-film was examined at Appalachian State University (Dr. Brad Conrad and Cortney Bougher) by tapping-mode AFM using a Bruker Dimension ICON SPM. Measurements were made in ambient conditions at room temperature in the dark with a scan rate of > 0.5 Hz. Commercially available Mikromasch cantilevers with a nominal force constant of 5 Nm^{-1} were used. Data were minimally image-processed and analyzed with Scan Probe Image Processor (SPIP), of Image Metrology A/S.

2.1.3.2. EFTEM

Motivation Energy-filtered transmission electron microscopy is a unique way of acquiring TEM data. It separates the electrons that are scattered by the material according to the energy with which they have been bounced off of the atom, which will be a specific energy for each element. This can then be used to create a map of the film at a nanoscale level that provides contrast for presence of carbon, nitrogen, or sulfur, respectively. By using this technique we can gain information about the composition and location of nanoscale domains within the bulk material.

Technique P3HT/PCBM thin films (70 ± 10 nm thickness) for transmission electron microscopy (TEM) were spun cast on PEDOT:PSS deposited on silicon substrates from 15 mg/mL solutions in a N_2 glovebox. Films were floated-off in deionized water and picked up with copper TEM grids followed by drying under vacuum for 24 hrs and thermal annealing in the N_2 glovebox. TEM experiments were performed at the Penn Regional Nanotechnology Facility, University of Pennsylvania on a JEOL 2010F FEG HRTEM/STEM. Bright field images, thickness maps and elemental maps were captured from the same sample areas. The intensity of sulfur maps is proportional to the sulfur concentration, thus directly related to the concentration of P3HT within domains. The domain composition was calculated by averaging the intensities in ten regions in carbon and sulfur maps as has been described extensively elsewhere[36].

2.1.3.3. XRD

Motivation X-ray diffraction is a non-destructive technique that measures the extent of crystallinity in a film or powder or single crystal. In a single crystal, very detailed

information about the spacing between atoms in a unit cell of that crystal can be obtained, which allows for high-level modeling of what that crystal looks like at the atomic level, and how each of the atoms and molecules relate together in a packing structure. XRD on a powder gives a similar level of detail as that for a single crystal, but because powders are often polycrystalline their diffraction patterns more closely resemble those of the thin films than the single crystal. Finally, XRD on a thin film gives detailed information about amount of crystallinity or amorphousness, the size of the crystalline domains, and the interplanar spacing between the molecules in the crystals. When in-situ temperature studies are done, the impact of annealing on crystallinity and all of the markers listed above can be ascertained.

Technique Thin-Film X-Ray diffraction (TFXRD) was performed on a Theta-Theta Siemens D500 with custom diffraction furnace and gas controllers. TFXRD data are shown for specific peaks corresponding to squaraine crystallinity. This was determined by scans on controls [substrate/Indium tin oxide (ITO), substrate/ITO/PEDOT:PSS, substrate/ITO/PCBM and substrate/ITO/PEDOT:PSS/PCBM] to ensure that the peaks examined were those of the squaraine. Values of τ, the coherent crystal domain size, were calculated using the Scherrer equation[37]. For all TFXRD measurements, films were prepared with identical processes as described in Section 2.2.1 unless specified. Multiple measurements for a given property were taken for each film, and the reported results are averaged over these films with error bars shown. In the case of TFXRD, the error bars are smaller than the symbol.

2.2. Processing

2.2.1. Thin Film and Device Fabrication

ITO substrate cleaning using acetone. All steps are completed while wearing dust-free laboratory gloves. 10 slides are placed into the acetone solution (purchased from Fischer Scientific Chemicals, ACS histological grade quality, used as purchased), and it is confirmed that the solvent is clean (almost no visual residues suspended in the bottom). The ITO slides must no longer be touched by fingers or gloves once they enter the acetone. A VWR Model 75D sonicator is set to 20 minutes without heating at a power level of 9. At this point, it is confirmed that the water is at the correct level in the sonication bath using indents in the corners toward the top of the bath. Once the sonicator is turned on, the position of the jar is adjusted until bubbles suspended in solution are seen coming off of the ITO slides. This means that the cavitation effect used to clean the slides is functioning properly.

Clean vials. 4 glass vials, from VWR with phenolic caps, are obtained for the PEDOT:PSS solution, active layer solution, deionized (DI) water and pure chloroform (ACS reagent grade, used as purchased from Sigma-Aldrich, >99.8% purity with amylene stabilizers), respectively. Each vial is rinsed by shaking with fresh chloroform and then decanting, which removes any residue left in the bottom of the vial from the manufacturing processes. One rinsed, each vial is dried using a clean-air gun, and is placed (without its cap) into the vacuum oven for 5 minutes at 150 °C to evaporate off any residual solvent, and is cooled for 3 minutes afterwards. The vials are labeled. The

squaraine materials for the study are selected from storage in the glove box, along with PCBM (Solenne BV 99.5%) to be ready for the subsequent steps.

Further cleaning of ITO substrates using IPA. When the sonication in acetone solution is finished, the slides are removed from the acetone one at a time, and are set onto a kimwipe. The kimwipe is folded over, and both sides of each slide are then scrubbed in a circular motion ensuring contact only with the kimwipes. The lint is blown off using a clean air gun. The slides are then placed into a bottle of isopropyl alcohol (IPA), (purchased from Macron Fine Chemicals, ACS reagent grade quality, used as purchased) again making sure the IPA solvent is clean. The substrates are sonicated with the same specifications as with the acetone sonication, above.

SQ:PCBM solution preparation. While the substrates are sonicating, the active layer solution is prepared. A VWR Model EP214C balance is calibrated. The appropriate masses of SQ and PCBM are weighed into the cleaned vials, and the necessary amount of chloroform is added. The bottle is sealed with Parafilm and sonicated for 5 min.

Tape the slides. By this point, the glass slides with the ITO substrate should be finished sonicating in the IPA. Take them out one by one and scrub each one with kimwipes. Blow off excess lint. Place them onto large kimwipes. Use a Fluke multimeter (set to "Ω") to determine which side is coated with ITO (the resistance of ITO side is about 15-20 Ω; the resistance of glass is unreadable). Affix a thin strip of Kapton tape onto the ITO side of the substrate, as the red rectangular shown in the figure below. This tape will be removed when testing the devices to expose the ITO contact.

Figure 8 Cartoon of film with tape on it.

Put SQ:PCBM solution into glovebox. Once finished the sonication of SQ:PCBM blend solution, move the bottle into glovebox for spin casting.

Bake the substrates. Blow off the lint after taped the substrates. Place the taped substrates on a larger thick glass plate, which has been cleaned and wiped down, and blown off until clean. Move the plate with the slides on it into a VWR 1400E vacuum oven and leave to bake for 10 minutes, to remove any residual solvent.

Make PEDOT:PSS solution. PEDOT:PSS bottle is kept in the small fridge to prevent its aggregation or crystal formation. Obtain a 5mL-syringe and a 0.45um-PTFE filter (if not PTFE, PSS will stick to it), and attach the two. Put 2.5mL of the PEDOT:PSS solution (purchased from Sigma Aldrich, high-conductivity grade) and 2.5mL of de-ionized H_2O into the syringe (use the mark on the syringe to scale). Force the solution through the filter into the clean vial prepared in step 2. Keep this in the fridge until you are ready for spin-coating.

Prepare enough film holders. Use kimwipes wetted by isopropanol to clean the inside of the holders. Do not use chloroform or acetone for this as they will degrade the plastic film holders. Dry them with clean air gun. Film holders should be labeled with squaraine

name, batch number, film number, date, name, and lab notebook number that corresponds to the written description of the specific device or film fabrication that is underway.

Prepare PEDOT:PSS spin coating area. Take out all the cleaned substrates and set them aside the spin-coater. When spin coating, place ITO substrates on a Chemat Technology spin coater, model KW-4A, set time to 30 seconds and speed to 5000 rpm. Use a test slide prior to depositing the PEDOT in order to adjust the RPM. Thereafter, take out PEDOT:PSS solution from the fridge.

Spin coat PEDOT:PSS. To start the PEDOT spin-coating process, turn on the spin-coater and the vacuum pump linked to the spin-coater. Gently place the slide at the center of the spin-coater. Turn on the vacuum. Suck up a full pipette of the PEDOT:PSS solution into a pipette, and QUICKLY spread it out over the slide. Suck most of the PEDOT:PSS solution back in the pipette before hit the start button, or PEDOT solution won't be coated evenly. Press start. Use new glass pipette every time spin coating PEDOT:PSS, because old PEDOT:PSS left in the pipette will aggregate. This must be done as expediently as possible to minimize the amount of interaction between the PEDOT:PSS and the water present in the air.

Bake substrates. Once the spin-coating process has been finished, dry the PEDOT slides in the vacuum oven for 60 minutes, under vacuum, to ensure complete removal of the water solvent.

Transfer substrates into glovebox. Open and line up the film holders. Open the vacuum oven, and slide the films into their holders. Once the all films have been placed in their cases, take all film holders to entry port of the glove box. The transfer of the PEDOT:PSS

from the vacuum oven to the glove box must be finished in a minimum of time. This prevents any water or other contaminants from sticking on the films.

Spin coating the active layer; prepare the spin coater. When working in the glove box, keep in mind rubber gloves must be protected by plastic gloves. Turn on the vacuum pump located under the glovebox. Open the vacuum pump valve inside the glovebox. Turn on the spin coater inside the glove box.

Set up spin coater. Take out the film holders from the entry port, and line them up. Use test substrates to set the spin coater at 800 rpm for 18 seconds.

Spin coat SQ:PCBM solution. Use the Pipette in the glove box to acquire the SQ:PCBM solution. Set the volume of the pipette for 90 μL. Hold a pipette in one hand and the vial of SQ:PCBM on the other and quickly suck some of the solution into the pipette. Spread the solution over the entirety of the film and immediately press the start button. Cap the bottle immediately after pressed start button to prevent solvent evaporation in the glove box.

Transfer devices/films into second glove box. When finished, put each slide into film holders. Open the latch of the antechamber, and pull the tray out. Set the films on the tray. Close the latch, and screw down to only hand-tight. Pump-down for 30 minutes, then refill. Clean the first glove box.

Deposition of aluminum top contact; Install devices. When devices arrived in the second glove box, find the device holders which are two pieces of steel pads. Place devices one by one into the rectangular gap of one steel pad. Anchor the two using screw spikes with hand. Pay attention on front and back, right and left. Twist tight using back

end of the tweezers. The holder can install 8 devices at one time. Once finished one side, tape the edge of this side of the device holder to prevent devices falling off.

Put the device holder into evaporation chamber. Before open the aluminum chamber, make sure it is pressure over. Open the chamber cap and carefully anchor the device holder onto the inside of chamber cap. Stop rotating when you feel the strength against your hands. The evaporator is an Angstrom vacuum deposition system, Model number S6458, powered by an Inficon SQC-310 Deposition Controller, and vacuum controlled with a Varian Turbo-V 81-AG turbomolecular pump. The rotation of the device holder is mediated by an Oriental Motor Company Gearhead, model 2GN36KA, whose functionality is controlled by the deposition controller.

Check the aluminum. Find a tungsten evaporation boat in the chamber (used as purchased from R.D. Mathis). Remove the remaining aluminum residue in the "boat" if there is any and place three aluminum pellets on it (used as purchased from Alfa Aesar Puratronic, alumina shot, 4-8mm, 99.999% purity). Close the chamber cap, and clean all the rubbish in the second glove box.

Evacuate chamber. Press "start" button on the right operational pad. Then the pressure inside the chamber is going down. The pressure decreases along with the increasing whine of the turbo. The power value will steadily increase to ~98W, and then go back and stay as 8W. The frequency will stay at 1350Hz. Wait for 12 hours.

Inspect the aluminum chamber. For deposition to begin, the pressure in the aluminum chamber should be 10^{-6}~10^{-7} torr. Record starting temperature, pressure, current and

voltage (should be unchanged 0.2A and 36V) from the right operational pad. Record crystal life from the left operational pad (Next Menu→Sensor Info→Life).

Deposit aluminum. Make sure the instrument is on "manual" mode. When the recording is done, press "start layer" button on the left operational pad. Increase the power level "0→1→2→3…→30" by rotating the knob in every 5 seconds. Record "pressure" and "deposition rate" in each power level. Stay 30 seconds in power level of 30, then return back to 5 second in each power level of "31→32…→47". "47" is enough for aluminum evaporation. The maximum power level is "55". When it reached 47, stay at 47 until the end of the deposition process. The system will automatically shut down and pressure inside the chamber will return back to ambient level.

Take out devices. Wait around 10 minutes and the right operational pad displays "pressure over". Prepare the film holders, line them up. Open the chamber and take off the device holder. Carefully take off the tape and use tweezers transport device into its corresponding film holder one by one. When the transportation is finished, put everything where it originally belongs and take out the rubbish (tapes and gloves).

2.3. Testing

2.3.1. Solar Simulator

Current density-Voltage (J-V) characteristics of the devices were obtained in the dark and under simulated 1 sun, 100 mW cm^{-2} power density, provided by a Newport 91159 Full Spectrum solar simulator with xenon lamp that had been calibrated with a round-robin InGaAs photovoltaic cell fabricated at NASA. The calibration is performed weekly. The

NASA calibration photovoltaic was independently calibrated at NASA before shipment. This standard will last for approximately 15 years, because it is an encapsulated InGaAs solar cell, and will not begin degrading until after that point in time. The devices are tested between 0-6 hours after evaporation of the aluminum contacts. The devices retain approximately 20% of their original efficiency after two weeks in ambient conditions, but their potential for high stability has not been completely evaluated. Values (and errors) for efficiency, short-circuit current, open-circuit voltage, and fill factor reported here are averages obtained by testing a minimum group size of 4 devices per film, with 8 films per set, and averaging the resulting values.

The devices are measured in 2014 using a Keithley 2400 Sourcemeter, but were previously measured (before April 2014) using a NI 3671 SMU. In both occurrences, the data were tabulated and collected using an internally-developed LabView program. After calibration of the lamp, a film containing 11 devices is removed from the glove box and brought to the testing station. 4-point probes are used to make the measurement, and they are brought into light contact with the two electrodes. A dark current measurement is made, and then the shutter is opened and the active device is measured. The film is placed in the same location on the testing surface every time in an effort to minimize errors.

2.3.2. Spectral Response

Spectral response was measured on an Optronic Laboratories (OL) 750 spectroradiometric measurement system with a high intensity source attachment that generates the light required for the measurement using a quartz halogen bulb. The system was calibrated against a Si standard supplied by OL. The system uses a chopped source and lock-in phase sensitive detection. Our measurements are made using an external

preamplifier and lock-in-amplifier, both from Stanford Research Systems. The external preamplifier is an SRS Model SR750 low-noise current preamplifier, and the lock-in amplifier is an SRS Model SR830 DSP lock-in amplifier. Optical filters were modified slightly from the supplied system to eliminate small but non-negligible second order diffraction that would otherwise leak through the system at undesired wavelengths. A zoomed out view of the testing setup is shown in Figure 9, with a schematic of the set-up shown in Figure 10.

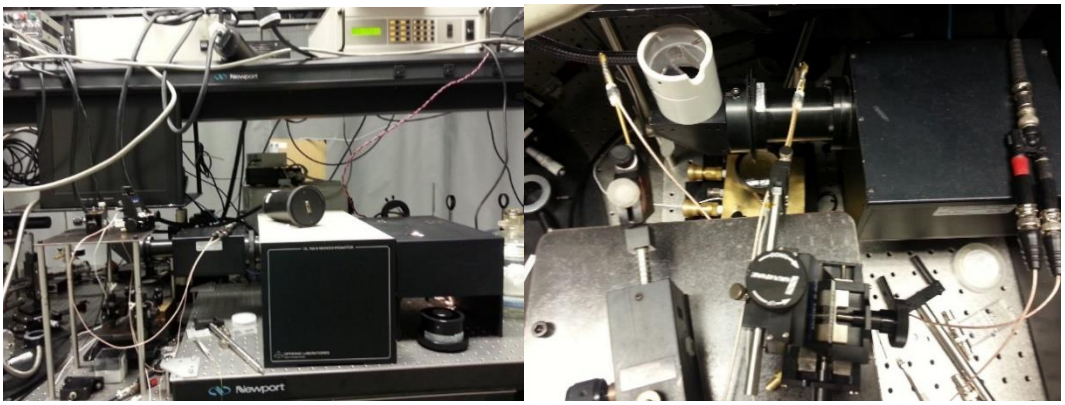

Figure 9a, left Testing set-up for spectral response, showing the monochromator (lower right), testing stand (lower left), lamp control (upper right), OL750 lock-in amplifier (upper left, old method), and the detector and preamplifier combination (cylinder in middle of screen, old method). A zoomed-in top down view of the testing is shown in Figure 9b, right.

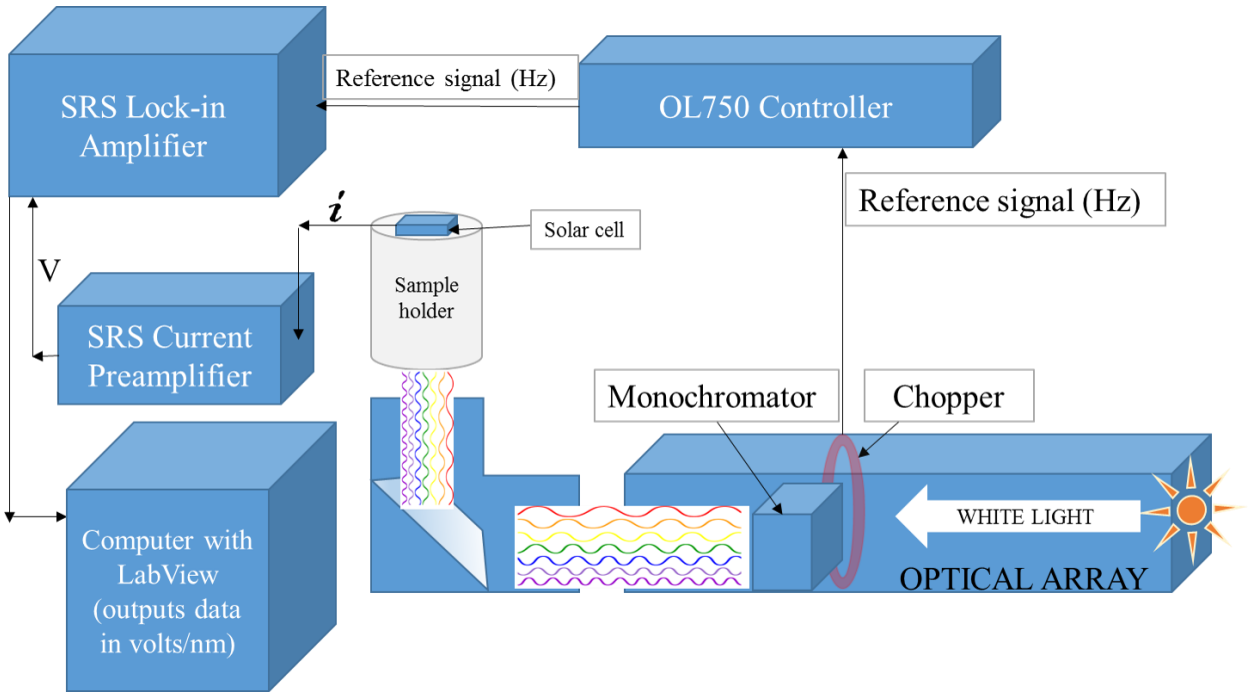

Figure 10 A cartoon schematic of the testing set-up for spectral response. The rainbow of light represents the monochromated light, but each wavelength of light excites the sample at discreet times in order to extract the fraction of electrons collected per photon in at a specific wavelength. The current is measured by probes.

By relying on a testing method using external amplifiers and detectors, we are able to achieve much higher sensitivities for detecting very small amounts of current. The preamplifier is able to detect nanoamperes of current, and then upconverts them to much higher voltages detectable by the lock-in amplifier. This is critical when working with new materials and unoptimized devices. The film is placed on the PVC sample holder that sits in the monochromator mirror beam. The sample holder has a cut out region that the device is placed over so that nothing interferes with the monochromated light intensity. Each probe is brought into contact with their respective electrodes, and monochromatic light is

shown on the device while the current is measured in order to extrapolate out the efficiency with which the materials are able to convert photons into electrons.

2.3.3. Time-resolved Photoconductivity

Motivation This technique is a contactless measure of localized spatially averaged charge carrier quantum yields and mobilities as summarized by the yield-mobility product value that is directly extrapolated from the transient decay data obtained from the measurement. It allows for a measurement of the mobility of free carriers within thin films. Because of the constraints of the disorder of the films, as well as their architecture, this technique is one of the only ones available that can measure mobility of a device analogue film. All other measurements, such as time-of-flight, require a much thicker film that is not an accurate representation of the true morphology of a device. As such, this technique is a useful way to directly probe the photophysics of neat squaraine films.

Technique Measurements were performed on the flash-photolysis time-resolved microwave conductivity experimental setup at the National Renewable Energy Laboratories, as described elsewhere[38–40]. All transient data reported were fit with a tri-exponential function convoluted with the instrument response function (IRF). The IRF was modeled with a Gaussian laser pulse convoluted with the known single exponential decay time of the microwave cavity. All fitting was done in Igor Pro 6 with a global analysis technique to simultaneously fit all transients at varying light intensities for a given sample. The reported figure of merit, the yield-mobility product ($\varphi\Delta\mu$) is calculated from the change in photoconductance at t=0 extracted from the global analysis fit. It is

the product of the quantum yield of free charge carriers multiplied by the localized spatially averaged charge carrier mobility[41].

3. Charge Photogeneration in Organic Photovoltaics

Chapter Abstract

The process of converting light into electricity through the interaction of a photon with matter is described in detail in this chapter, as it pertains to the specific issues and challenges of organic photovoltaic devices. First, a step-by-step simplified pictorial description of the process is given, and the currently debated points in the OPV community are highlighted. Then, a brief overview of the theories behind the process is offered, and again, the components still under examination by the community are identified and the differing viewpoints briefly explored. Next, the viability of squaraine aggregates as candidates to resolve some of the debate is discussed. Finally, connections are made between the experimental and theoretical descriptions of charge photogeneration using squaraine aggregates as the vehicle to relate the two disciplines.

3.1. Experimental Description of Charge Photogeneration

3.1.1. Pictorial Overview

Charge photogeneration describes the entire process of a photon generating an exciton that can then form free carriers, which are transported to electrodes to generate the photocurrent. The actual process of charge photogeneration is composed of four or five distinct steps: i) absorption of a photon in the donor material to generate an exciton, ii) diffusion of the exciton to an interface between the donor and acceptor, iii) dissociation of the exciton to form the charge transfer state, iv) dissociation of the charge transfer state to form free charge carriers, and v) free charge carrier transport through the materials to the electrodes for current collection. Through performing the work that will be discussed, and in ongoing discussions with the OPV community, it is an agreed statement that the processes of exciton dissociation and charge transfer state dissociation are still not well understood. This is why it is described as having four or five steps, where the uncertainty

is whether or not a charge transfer is actually formed as opposed to the exciton dissociating directly into free charge carriers. The next section will give greater detail regarding the debate, but the following serves as a brief overview of the process using cartoon representations of the device.

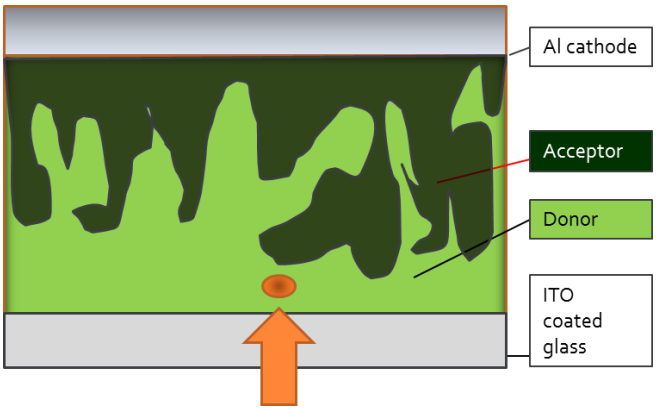

Figure 11, Absorbance. Light (orange arrow) enters through the transparent ITO coated glass and generates an excitation in the donor material.

Figure 11 shows the process of absorbance, as well as the structure of the OPV. The structure is a single layer bulk heterojunction unencapsulated standard architecture, where it is lit from the back of the substrate, and current is collected from the top contact. The substrate is indium tin oxide (ITO) coated glass that is coated with a polymer buffer layer designed to both smooth any surface roughness of the ITO, as well as block electrons. In the cartoon, the actual active layer is shown as a blend of two green materials. This layer is created by spin-coating microliters of solution containing both the donor and acceptor molecule. It is a heterogeneous blend of the two materials, and can contain a variety of domain sizes, phases, concentration gradients, and micro- and nanostructures, depending on the initial solution components and mixing, the spin speed, the environment in which it was coated, and any treatment given to the film after the layer has been added, like thermal

or solvent annealing. Finally, multiple aluminum contacts are deposited on top of the film, which is what defines the device active area. Absorbance occurs when light is shone up through the bottom of the cell through the transparent ITO. The light will be absorbed by both the donor and acceptor materials. If the materials have different optical bandgaps, and if there are a variety of absorbance transitions that could occur ($0\rightarrow1$, $0\rightarrow2$, etc.), then a range of photon energies can be absorbed by the material. The photon absorption process creates an exciton, which is a neutral excited state consisting of an excited electron and a hole bound together. The exciton can be considered to be either diffuse, delocalized and not tightly bound (Wannier-Mott) or highly localized and tightly bound (Frenkel). The type of exciton that is formed is material dependent, and in organic semiconducting materials it is typically a Frenkel exciton. This will be discussed in the context of Figure 12. Before moving on from absorbance it is important to point out the loss mechanisms that can occur during this step. First, the excited electron can simply recombine with the hole, emitting a photon through fluorescence. Second, the excited electron can participate in a non-radiative decay process. Both intersystem crossing and internal conversion can occur, and in each case the energy of the excited electron is lost through vibrational relaxation and eventual decay to the ground state.

Figure 12 shows the process of exciton diffusion to the BHJ, which can occur during the lifetime of the excited state. This lifetime has been measured as being between 1 and 4 ns for the squaraine excited state in solution by a prior student (B. Zhu), which means that the exciton can travel between 1 to 4 nm during this diffusive process[42–45]. The diffusion is random, because the exciton is a neutral species and is therefore unaffected by electric fields created by dipole-dipole interactions within the materials. This is one of the

key limiting factors in creating ideal BHJ morphologies, because the materials must be able to interdigitate at the nanoscale in order to collect 100% of the excitons generated in the materials which aren't lost immediately after absorbance.

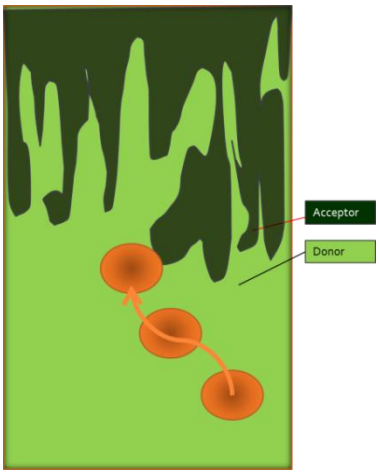

Figure 12, Exciton Diffusion. Zooming in on the BHJ interface, the exciton (orange oval) diffuses through the donor material through hopping or coherent motion until it reaches an interface.

Again, there are loss mechanisms that are present during this step as well. The exciton can still recombine to the ground state, but it can also now interact with traps and defects that are present which will prevent the excitation from movement through phonon-polaron interactions. This leads to recombination as well, because there is a very limited amount of time for the exciton to be able to reach the BHJ as stated above. Additionally, the exciton can recombine with free charge carriers, as well as with other excitons through exciton-exciton annihilation.

Figure 13 illustrates what occurs once the exciton has successfully reached the BHJ. The materials for OPV are chosen such that the acceptor molecule has lower energy levels for the excited electron to drop into from the exciton, leaving the hole behind on the donor. Ideally, these materials will also have a preferential step-up when going from the acceptor

to the donor, so that the acceptor is able to transfer a hole thereby dissociating an exciton that has been formed within the acceptor material through photon absorption. Figure 14 is a simplified energy level diagram illustrating the dissociation of the exciton.

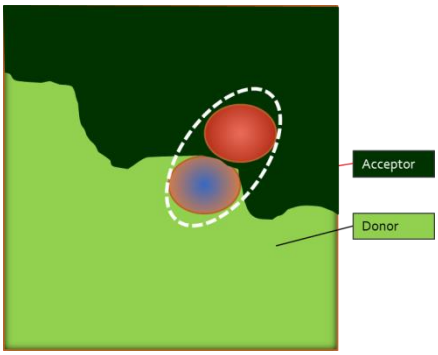

Figure 13, Exciton Dissociation. The exciton dissociates through LUMO to LUMO electron transfer from donor to acceptor; the red oval represents the electron and the blue oval represents the hole. The white dashed line indicates the Coulombic binding present between the two charge carriers as the charge transfer state is formed.

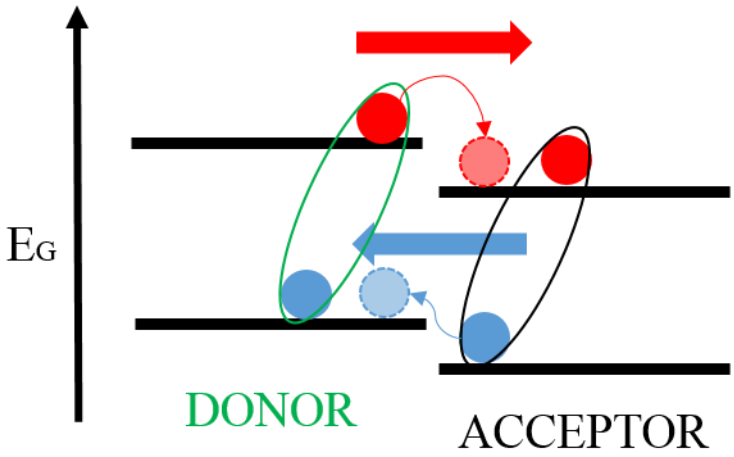

Figure 14 A simplified energy level diagram for the BHJ. Energy is shown as the y-axis, and the left set of double black lines represent energy levels of the donor material, while the right set of double black lines represent energy levels of the acceptor material. The red straight arrow indicates the direction of electron flow, and the blue straight arrow indicates

the direction of hole flow. The red circles represent electrons, and the blue circles represent holes. The green oval indicates an exciton formed on the donor, whereas the black oval indicates an exciton formed on the acceptor. The curved colored arrows represent respectively, electron and hole transfer for the red and blue arrows.

The exciton has either dissociated into a charge transfer state (Figure 15) or free charges (Figure 16).

Figure 15 shows the step of charge transfer state dissociation, which is still up for debate in the OPV community. At this step, the bound electron-hole pair dissociate from the charge transfer state formed upon the dissociation of the exciton. This means that the electron and hole have overcome the Coulombic binding, and they are no longer an associated pair.

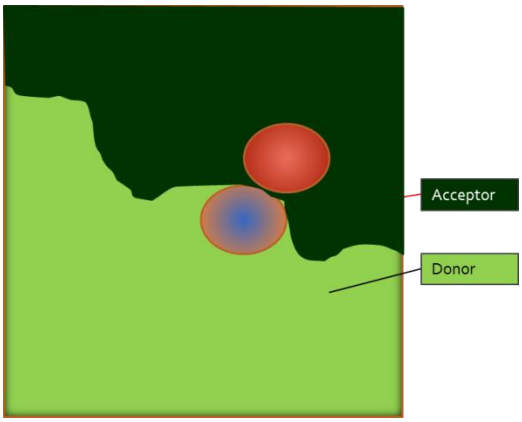

Figure 15, Charge Transfer State Dissociation. In an ultrafast process represented here by the disappearance of the white dashed line, the electron and hole dissociate into free charges, overcoming the Coulombic binding interaction between them.

Finally, Figure 16 concludes the pictorial description of the process of charge photogeneration, and it shows the hole and electron each moving to their associated electrodes to be collected as current.

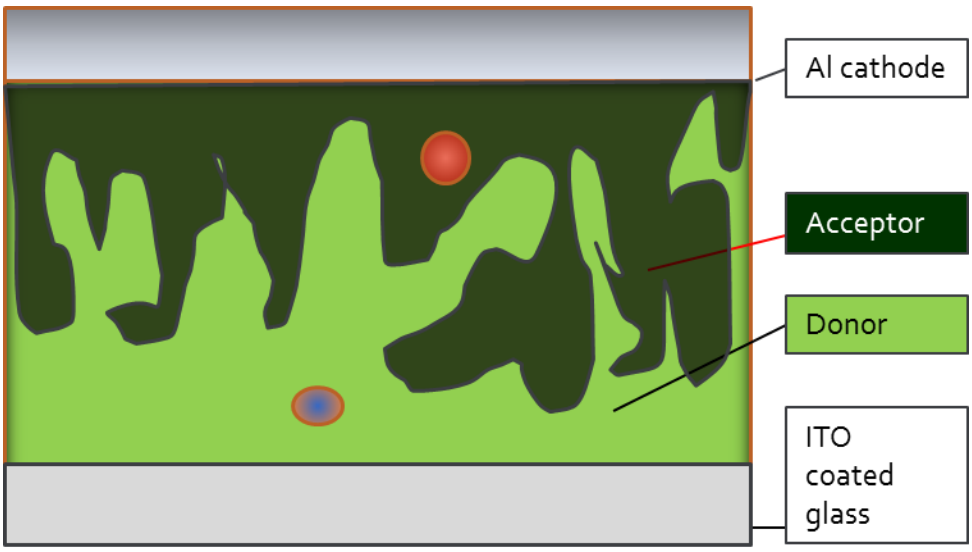

Figure 16, Charge Carrier Transport and Collection. Once the free charge carriers have been formed, they must move through drift and diffusion to their respective electrodes; the electron moves through the acceptor to the aluminum cathode and the hole moves through the donor to the ITO anode thereby generating current.

3.1.2. Issues

As stated in the previous section, there is still debate about the third and fourth steps of the charge photogeneration process, in that the separation of the exciton into free charge carriers may proceed either directly, or through an intermediary step of charge transfer state dissociation. There is currently no experimental method that is able to examine this process[41,46,47], because the dissociation itself is occurring at ultrafast time scales and at nanoscopic regions of the thin film. It is currently accepted[48] that the reality of the process likely lies somewhere between the two extremes presented as separate steps in the proceeding section. In other words, it is currently thought that once the exciton migrates to the bulk heterojunction, it can dissociate into free charges, but the most common path is for it to begin dissociating into a charge transfer state first and then

have the final dissociation occur; all of this is occurring at an ultrafast time scale. The question becomes then, how can this be quantified and evaluated, and more importantly tied to specific morphologies of the BHJ and then even further to the molecules that are forming the BHJ and their optoelectronic structure. The next section therefore details the salient theories that are currently utilized to describe exciton and charge transfer state dissociation, and is then followed by a description of the specific molecules under study in this thesis work, and the theory behind their nanostructural aggregation patterns.

3.2. Theoretical Description of Charge Photogeneration

Once the exciton has been generated and diffuses to an interface, it can dissociate into the charge transfer state, which must then further dissociate into free charges, or it can immediately dissociate into free charges, or something between those two extremes, as described in the proceeding sections. Two separate theories have been proposed to describe these steps. Marcus Theory is named for Rudolph Marcus who used it to explain the rates of electron transfer reactions. The chemical reaction is described as the crossing of an electron from a reactant well to a product well[49], as shown in Figure 17. First, a description of the general Marcus model, as summarized from Libby's 1952 work on the theory of electron exchange reactions in aqueous solutions[50].

When considering the Marcus model of electron transfer, the primary result of the transfer process is the rearrangement of charges. The environment within which the electron is transferred has an enormous impact on the rate of transfer, because the ability of the environment to engage in orientation polarization will determine the free energy of activation, which controls the reaction rate. This is a unique process, because the reaction

of electron transfer is considered to take place in a concerted and continuous way. In the Marcus model, donor-acceptor is fairly weak, and both the donor and acceptor state retain separate and unique quantum mechanical identities throughout the process. The electron being an elementary particle, must transfer as a whole. This is much faster than any movement of the surrounding environment, which means the nuclear position of the reaction partners and the surrounding environment are identical before and after the transfer; this is the Franck-Condon principle[51]. Electron transfer is governed by quantum mechanical rules, it is only possible if also the energy of the system does not change during the jump. The arrangement of the environment depends on the charge distribution on the reactants. If the environmental configuration must be the same before and after the jump and the energy may not change, then the environment cannot be in the state of the precursor nor in that of the successor; it has to be somewhere in between. An arrangement of the environment exactly in the middle of those of precursor and successor complex would meet the conditions of symmetry for the self-exchange reaction. This means that the environmental arrangement with half of the electron on the donor state and half on the acceptor state would be the correct environment for jumping. As previously stated however, the electron as an elementary particle cannot be divided, residing either on the donor or the acceptor and arranging the surrounding electronic environment accordingly in an equilibrium. The transition state, on the other hand, requires an environmental configuration which would result from the transfer of half an electron, which is impossible. This means that real charge distribution and required environmental polarization are not in an equilibrium. Yet it is possible that the environment takes a configuration corresponding to the transition state, even if the electron sits on the donor

or acceptor. This, however, requires energy which may be provided by the thermal energy of environment while random thermal fluctuations can produce the correct polarization state. Once this has been reached the electron can jump. The creation of the correct solvent arrangement and the electron jump are decoupled and do not happen in a synchronous process. Thus the energy of the transition state is mostly polarization energy of the environment; this means that the environment at the BHJ of the donor and acceptor states has a high degree of influence on the transition rate of the electron from the donor to the acceptor. As will be discussed in detail later, the Marcus-Hush approach to electron transport in BHJ OPVs considers the donor state as the reactant in the electron transfer, and the acceptor state to be the product. For clarity, the reactant/donor state is actually defined as both a donor and acceptor molecule in close proximity, where the exciton is localized on the donor molecule. The product/acceptor state is where the exciton has delocalized across the BHJ and transferred the electron to the acceptor molecule, leaving the hole behind on the donor. The extent of Coulombic binding between the two charge carriers is not specifically addressed by Marcus-Hush theory.

In Figure 17, the nuclear coordinate of the reactant (R) and product (P) is related to the geometry of the molecules and the state of polarization of the surrounding medium. The ordinate is the energy, with ΔG°' the difference between the bottoms of the wells being the reaction free energy. The middle parabola corresponds to the transition state between the reactant and product.

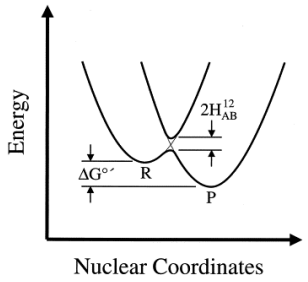

Figure 17 The model of an electron transfer reaction as the intersection of two parabolic potential energy wells[2].

The activation energy of the reaction is the difference in energy between the intersection point of the two main parabolas and the bottom of the reactant well. $2H_{AB}^{12}$ is the electronic coupling matrix element. If the simplest assumption is made of harmonic energy wells, then the energy difference between the bottom of the reactant well and product well at the intersection point is the reorganization energy, λ. A more specific case is shown in Figure 18, which illustrates Marcus Theory applied to a donor/acceptor system.

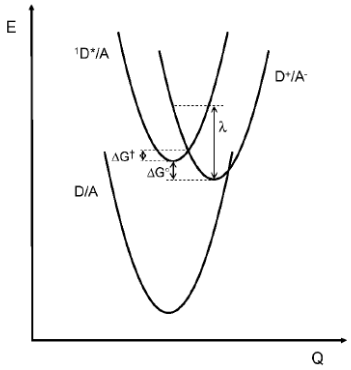

Figure 18. Potential energy surfaces for a D/A system where photoexcitation generates the exciton $^1D^*/A$ and subsequent electron transfer generates the charge transfer state, D^+/A^{-3}.

We now move to a consideration of the charge transfer state; as stated above, the extent of Coulombic binding between the electron and hole after electron transfer is not

specifically addressed in Marcus-Hush theory, and therefore Onsager-Braun theory will now be considered.

The charge transfer state (CT) potentially generated by the process of exciton dissociation is a Coulombically bound electron-hole pair, with the electron now in the lowest unoccupied molecular orbital of the acceptor molecule. In order for free charge carriers to be created, this CT state must also dissociate; the probability of this dissociation is given by Onsager-Braun theory. Lars Onsager first developed the theory of ion separation and recombination in weak electrolytic solutions[52,53]. His work described the probability of separation/recombination of an ion pair based upon the relative effect of an applied electric field; it is a solution to a steady state diffusion equation with infinitely long lived ions. While this work was experimentally verifiable for a variety of molecules[54–57] the theory broke down when applied to solid state mixed donor acceptor materials. Charles Braun introduced a modification to the theory to correct the problem; Onsager's work predicted very large electron transfer distances that did not match those measured spectroscopically[58]. Braun's modification mathematically incorporated the kinetics of CT state dissociation in the case where partial dissociation to free charge carriers and regeneration of the CT state can occur as is seen in solid donor-acceptor blends. The importance of the morphology and energetics of the donor-acceptor interface on CT state dissociation and the overall charge photogeneration efficiency cannot be overstated, but it is still an open question as to whether the CT state needs to actually be considered when discussing the process of charge photogeneration. The following section will address the theoretical description of aggregates; because the theory required for the understanding of exciton dissociation is entirely based on the coupling of wavefunctions through vibrational

overlaps it is critical to understand how the squaraine molecules interact with each other, specifically when they have been photoexcited. This establishes a basis from which understanding of the behavior of a squaraine molecule can be described both experimentally and theoretically in the remainder of the thesis.

3.3. Squaraine Aggregates and Charge Photogeneration

In 1965, M. Kasha, H.R. Rawls, and M. Ashraf El-Bayoumi published a seminal paper entitled "The Exciton Model In Molecular Spectroscopy" [59]. The paper discusses the presence of exciton effects in molecular aggregates as measured by the appearance of spectral shifts or splitting of the absorbance band for the molecules comprising the aggregates. Dye aggregate excitations were first researched by Kautsky and Merkel [60] who showed that an enhancement of "metastable state excitation" improved the dyes' ability as photophysical sensitizers in reactions. In 1946, Förster examined dye molecule dimers' phosphorescence and suggested that phosphorescence was caused by the presence of parallel transition dipoles in the dimers using the quasi-classical vector model. McRae and Kasha further refined the model [61] to explain both singlet and triplet state behavior.

In order for the exciton splitting to occur, there must be strong coupling between the associated molecules of the aggregate. Perturbation theory can be applied if the molecular units are able to preserve their "individuality" when they have aggregated. The application of the wave-function formalism is similar to molecular orbital theory but with very different physical basis and interpretations. Equation 1 describes the ground state function of the aggregate dimer.

$$\Psi_G = \psi_u \psi_v \tag{1}$$

The subscripts indicate the two molecules, u and v, and ψ represent their wavefunctions. The Hamiltonian operator for the dimer is

$$H = H_u + H_v + V_{uv} \tag{2}$$

where H_u and H_v are the Hamiltonian operators for the two molecules, and V_{uv} is the perturbation; it is a coulombic potential generated using the point-dipole point-dipole approximation and point-multipole expansion.

The exciton wave functions are

$$\Psi_E = r\psi_u^1 \psi_v + s\psi_u \psi_v^1 \tag{3}$$

where r and s are coefficients to be determined. The Schrödinger equation for the excited state is

$$H(r\psi_u^1 \psi_v + s\psi_u \psi_v^1) = E_E(r\psi_u^1 \psi_v + s\psi_u \psi_v^1) \tag{4}$$

and the resultant determinant answer including the intrinsic orthonormality conditions for the wavefunctions give the exciton splitting term.

$$\xi = \iint \psi_u^1 \psi_v (V_{uv}) \psi_u \psi_v^1 d\tau_u d\tau_v \tag{5}$$

Using the point-dipole approximation this becomes

$$\xi = \frac{\boldsymbol{M_u M_v}}{r^3} - \frac{3(\boldsymbol{M_u r})(\boldsymbol{M_v r})}{r^5} \tag{6}$$

giving an interaction energy based on the exchange of excitation energy between the two molecules. M_u is the transition moment in molecule u and r is the position vector of the v

dipole referenced to the u dipole as the origin. The transition energy of the composite molecule becomes

$$\Delta E_{composite} = \Delta E_{unit} + \Delta D \pm \xi \quad (7)$$

where ΔD is the difference of the van der Waals terms in the ground state interactions of the two molecules and the excited state interactions of the two molecules. This equation is the fundamental equation of exciton theory, as it shows the resonance splitting of the excited state dimer energy levels that were formerly non-degenerate in the monomer units. The van der Waals interactions in effect displace the ground state of the dimer relative to the initial monomer molecule ground state.

The following three figures show different composite systems that can occur when two monomer units are brought together; ΔD is shown relative to a fixed ground state and ξ, the exciton splitting, is symbolically shown as a function of vector components for the composite molecule. In each of the figures, the ovals correspond to the molecular profile and the double arrow is indicative of the polarization axis for the molecular electronic transition. The vector diagrams give the qualitative description of the energy of ξ as well as the transition moments M. The oscillator strength is f.

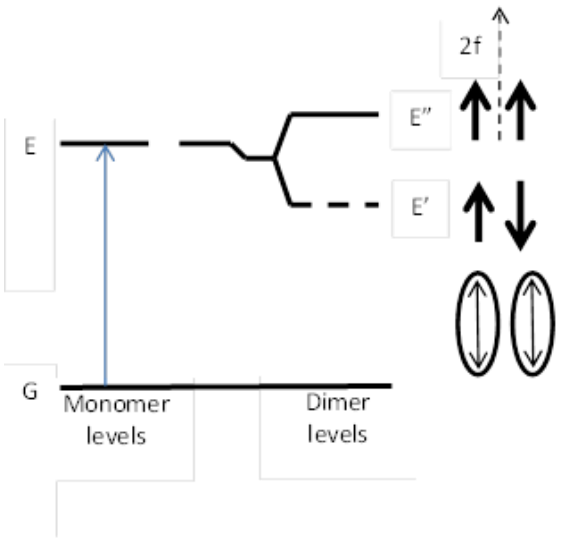

Figure 19 Exciton band energy diagram for a molecular dimer with parallel transition dipoles.

The out of phase dipole arrangement (thick black arrows, lower) corresponds to a lowering of energy (ξ is negative) so E' is lower than the van der Waals displaced state of the dimer; the in phase dipole arrangement (thick black arrows, upper) gives a repulsion which increases the energy (ξ is positive) so E" is higher. The vector sum of each of these dipole arrangements gives the transition moment probability; E' is a forbidden transition (f/dimer=0) and E" is an allowed transition (f/dimer=2). This means that only the higher energy transition will be seen, which corresponds to the H-aggregate being blue-shifted from the monomer. This is one of the most frequently occurring dimers, the London-force dimer between planar conjugated molecules. As the conjugate molecule number (unit aggregate size) increases, the band splitting will also increase as predicted by this model and shown experimentally[62,63].

Using the quasi-classical vector model again, the energy of the exciton states generated in the dimer can be analyzed as well as the transition moment from ground state

to exciton states. The in-phase arrangement of the dipoles (Figure 20) gives an attraction, producing E', while the out-of-phase arrangements gives a repulsion producing E".

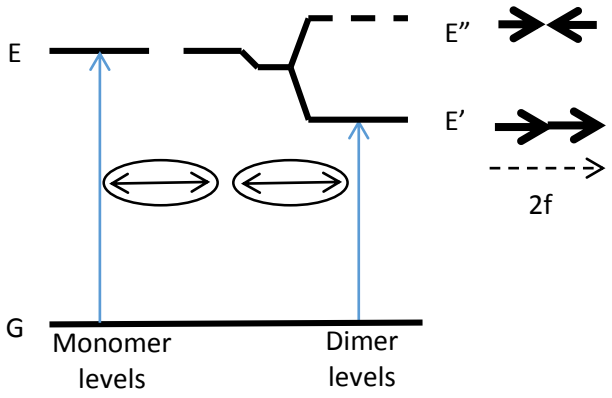

Figure 20 Exciton band energy diagram for a molecular dimer with in-line transition dipoles.

In this case however the sum of the transition dipole moments is zero for the E" case, and nonzero for the E' case; this means that the observed excitation will be red-shifted from the monomer and corresponds with the J-aggregate.

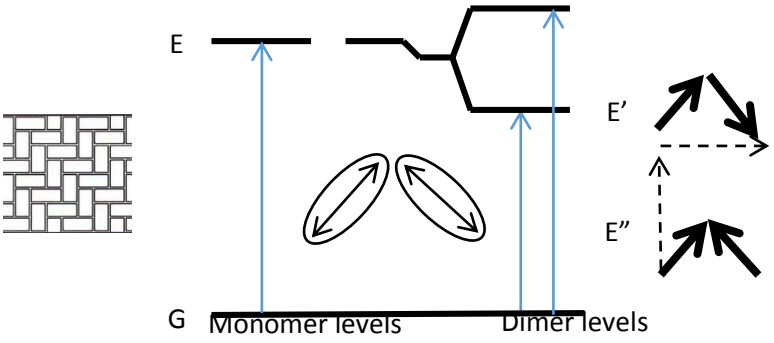

Figure 21 Exciton band energy diagram for a molecular dimer with oblique transition dipoles.

Figure 21 gives one of the more interesting cases. In a herringbone crystal packing structure often found in squaraines[64] and shown in Figure 10, the molecules orient in such a way that

oblique transition dipoles form. The difference here is that the transition dipole moments from the ground state to excited state are both non-vanishing, meaning that both the H-and J-aggregate transitions will be seen in absorbance spectra.

The three energy diagrams illustrate the impact of dimerization of squaraine molecules upon the energy levels of the exciton; the exciton's energy level impacts what portion of the solar spectrum it is able to collect photons from. The exciton itself has distinct properties as well, and these are critical for understanding the transport properties of the exciton which impacts the overall efficiency of exciton dissociation at a bulk heterojunction interface in an organic photovoltaic. In molecular crystals the type of exciton that is typically formed is a Frenkel exciton, defined as a migrating quantum of electronic energy[65] that is formed tightly bound and highly localized but then travels through the crystal as an excitation wave[66].

3.4. Relationships Between Theory and Experiment

To briefly summarize Chapter Three, the primary challenge this thesis attempts to address is the current inability to accurately prescribe molecular structures which allow for maximum efficiencies. The lack of ability is due to the dearth of information about the exact nature of the charge separation process at the BHJ. In order to understand the interplay of morphology, optoelectronic structure of the molecules, and bulk properties of the devices, both experimental data on each of the steps must be collected, as well as correlating this data to theories of electron transfer and charge separation that offer a coherent and logical explanation of the results. Materials must also be selected which

offer unique nanoscale properties to take data on, and therefore we turn to a description of the squaraine aggregates in Chapter 4.

4. Squaraine Aggregates

Chapter Abstract

This chapter gives a brief discussion of the relationships between aggregates and the ways they are measured, before an in-depth analysis of the aggregate data is presented in Chapter Five. The goal of this chapter is to summarize the salient points of each of the measurement metrics, and how they relate to the aggregate, the material prescription, charge photogeneration, and the bulk heterojunction formation.

4.1. Metrics of Characterization

Absorbance and XRD are utilized as two techniques to describe the extent of aggregation and crystallinity respectively. Aggregation is tied to crystallinity, because the regularity of crystals allows for the maximum amount of interaction between two or more molecules to achieve "long-range" order and electronic interaction. The metrics for absorbance are peak intensities, peak positions, and the full-width half maximum of the peaks. The metrics for XRD are count number (extent of crystallinity), interplanar spacing in the crystals, and τ, the coherent crystal domain size.

4.1.1. Absorbance

There is a wealth of information to be gleaned from absorbance data. The position of the absorbance peaks are of course an indication of the energy of the excited state that is formed on the squaraine upon interaction with light, and as stated in Chapter 3 can give valuable information about the type of aggregate (J or H) that is present. The FWHM values act as an indicator of the amount of localized order for a specific excitation. A broader peak indicates a wider ensemble range of the aggregates or monomers, while a narrower peak

indicates that only a small subset of molecular interactions are responsible for the excitation. Finally, the peak intensity gives information about the strength of the optical transition, as well as the amount of aggregate that is present in the thin film.

4.1.1.1. Relationship to material prescription

OPV materials are currently unable to be created at the highest potential for efficiency (>20%) because the interplay of molecular structure and BHJ morphology is still unknown. We are not able to predict how a given molecule's structure will impact the formation of the BHJ, or how that BHJ must be morphologically to achieve maximum power conversion efficiencies. State of the art devices rely on optimization of materials to achieve maximum absorption of the solar spectrum, high charge carrier mobilities, a large open circuit voltage, or ease of deposition/reproducibility. There is no way currently to directly tie a specific component of molecular structure to enhanced performance resulting from some preferential BHJ nanomorphology. To that end, we have characterized a series of squaraines, with and without hydroxyl groups, with varying side chain lengths. The characterization entails steady state absorbance, modeling of the absorbance spectra, powder and thin-film XRD (both neat and in-situ thermal characterizations), and device characterization. We hypothesize that there are two competing mechanisms for how these squaraine interact with each other. The extent of squaraine-squaraine interaction is characterized as a function of their aggregation. The squaraines are known to aggregate as n-mers, where an excitation is formed over multiple molecules. As such, there are characteristic shifts in absorbance wavelengths. These can be correlated to the extent of crystallinity. Because of this propensity for aggregation, the

squaraines offer a unique probe of the relationship between structure and function within the BHJ. Not only do they offer a probe of the finished, static, structure of a working device, but we can also use their molecular structure differences to examine how the BHJ forms, through the aforementioned competing thermodynamic mechanisms. The first mechanism can be thought of in terms of two squaraine molecules with no hydroxyl groups interacting with each other; as the two molecules approach each other, the dominant forces of interaction are van der Waals forces and the steric hindrance imposed by the chain lengths. As the chain length increases, the molecules are less able to pack tightly, resulting in crystals with more deformations and packing faults, as well as more amorphous domains. Conversely, when OH groups are present there is a second competing force of interaction, hydrogen bonding. At short chain lengths, hydrogen bonding will dominate. This will impact not only the crystal packing, but there will be significant electronic differences in the energetics of the excitons formed on the aggregates. Again as the chain length increases the dominant mechanisms for aggregate formation will shift from hydrogen-bond-mediated to chain-sterics-mediated, but the excitons formed on these aggregates will still contain some electronic characteristics of the H-bonding that will be extant. Thus, we have a series of squaraines that will vary in molecular structure but twill also give differences in their absorbance, crystallinity, and electronic performance that can be tied to both BHJ morphological electronic structure and the molecular thermodynamic characteristics of each specific squaraine's chemical composition.

4.1.1.2. Relationship to charge photogeneration

Absorbance is of course the first step in the process of charge photogeneration, and as such is rate-limiting in that the materials that are chosen must be strong absorbers of light. Fortunately the squaraine aggregates are incredibly strong absorbers, with extinction coefficients greater than 10^5. This is a very good indicator that they will be strong absorbers; additionally they can be synthesized as to broaden their absorption for panchromaticity. Both of these factors mean that the squaraine aggregates are strong candidates for high efficiency in the first step of charge photogeneration.

4.1.2. Crystallinity

The powder XRD serves to give an indication of the "innate crystallinity" of the raw squaraine, before it has been dissolved into chloroform and cast in a thin film. We consider interplanar spacing (calculated from peak position) and amount of crystallinity (represented by peak height) as the two metrics for evaluating "innate crystallinity". In the thin film XRD, the amount of crystallinity (peak height), interplanar spacing, and τ are presented, where τ is calculated from the Scherrer equation using the FWHM of the peak of interest. τ is considered to be the coherent scattering domain size, which is defined by the number of aligned unit cells of the crystal in a row. This is useful for us in terms of characterizing the extent of long range order that is present in the homogeneous squaraine regions. The relationship between aggregation and crystallinity will be described further in Section 5.1.1.

4.1.2.1. Relationship to material prescription

The ability to predict a molecule's packing structure would be highly advantageous for both modeling of the absorbance spectra of the molecule, as well as gaining insight into exactly where the excitons of specific aggregates are forming upon the crystal itself. The difficulty arises if molecular design is focused solely on optimizing a particular material to be highly crystalline. The reason for this is that while crystallinity is a hallmark for high mobilities of the free charge carriers, which is only the case for the homogeneous material. In an OPV, there is a heterogeneous mix of materials, and the composition of the BHJ is impossible to pinpoint solely from the predicted crystallinity of the molecule that is being used as a donor. However, if a correlational or causational relationship can be developed between the molecular structure, the aggregation, and the crystallinity, this would be highly valuable. Additionally, knowing how a particular molecule will crystallize can allow for a better understanding of the thermodynamics of mixing and annealing, which will in turn allow for prediction of molecular structure impact on the formation and growth of the BHJ.

4.1.2.2. Relationship to charge photogeneration

Crystallinity is innately tied to the device performance of the OPV, and impacts at multiple critical steps. Examining the impacts in the order at which they occur during charge photogeneration, the first point is during the exciton diffusion process. There is a large body of work extant detailing the diffusion of excitons in crystalline and amorphous materials[67–72], but the following summary will be based primarily on the work of Madigan and Bulovic[67]. The exciton transfer rate, W, between two molecules is given by

$$W = X(R)P(\epsilon_D, \epsilon_A)$$

where the second term accounts for energetic disorder through a Boltzmann distribution,

$$P(\epsilon_i, \epsilon_j) = \begin{cases} \exp\left[-\frac{\epsilon_A - \epsilon_D}{k_B T}\right] when\ \epsilon_A > \epsilon_D; \\ 1, otherwise \end{cases}$$

and the first term accounts for the dependence on lifetime and spectral overlap,

$$X(R) = (\frac{1}{\tau})(\frac{R_F}{R})^6$$

In these equations, τ is the radiative lifetime, k_B is Boltzmann's constant, R is the separation distance between the two molecules, T is the temperature, ϵ_D and ϵ_A are the energies of the exciton donating and exciton accepting molecules respectively, and R_F is the Forster radius. The Forster radius is dependent upon the overlap of the donor and acceptor wavefunctions, as well as their mutual molecular orientation. Additionally, the excitonic density of states (DOS) is considered to be Gaussian in distribution, reflecting the energetic disorder of the system, and all excitons will relax to a thermodynamic equilibrium over time. In crystalline solids, the behavior can be modeled using an ordered cubic lattice of molecular sites, but for amorphous thin films, the model must be composed of a spatially random lattice of sites. Through the modeling work done by Madigan and Bulovic and recreated by Dastoor et al[69], it can be concluded that the exciton diffusion distance decreases as energetic disorder increases, with small organic molecules generally having a greater exciton diffusion distance than polymers because of their relatively smaller energetic disorder. The extent of energetic order in small molecules, including squaraines, is completely dependent upon both the amount of crystalline material that is present, as well as the coherent crystal domain size of the crystals. Therefore, crystallinity has a large impact on the distance that an exciton can

diffuse, which will directly impact the amount of current that can be generated in a device. This can be controlled through management of the crystal domain sizes via annealing techniques and appropriate materials selection.

Next, we consider the impact of crystallinity upon the next step in charge photogeneration, exciton dissociation at the BHJ. While I have recently published on this[73], there is a large body of work detailing the ways in which crystallinity at the BHJ impacts dissociation[74–79] that portrays accurately the state of the discussion regarding the process of exciton dissociation, as there are conflicting interpretations of the impact of crystallinity at the BHJ. First examining the work of Darling et al[74], they examined crystallinity in a polymer:fullerene system, under the assumption that a charge transfer state is always formed. They state that crystallinity at the BHJ will reduce the charge transfer energy and lead to a larger polaron distance in the charge transfer state, facilitating exciton dissociation. However, they add that it is not solely the presence of the crystals, but rather the presence of highly specific hierarchal nanomorphologies that are formed between the donor:acceptor system that they investigated which are primarily responsible for their increased rates of exciton dissociation. Ostroverkhova et al[76] show that it is nearly impossible to separate the influence of crystals at the BHJ on direct exciton dissociation from the influence of the homogeneous crystal domains in actually transporting the free charge carriers that have been created. As will be discussed in greater detail in Section 5.2.1.2, squaraine crystallinity was found to have a potentially deleterious effect on exciton dissociation, because the exciton was able to delocalize to the point where it became energetically unfavorable for it to dissociate. This can all be summarized, in terms of the impact of crystallinity upon exciton dissociation, as

demonstrating that a) it is incredibly important, and b) neither well understood nor generally applicable to all systems used in OPV. The discussion of crystallinity and charge transfer state dissociation is also under debate, but offers identical conclusions to those given above[80,81]. Therefore, the final step of charge collection will be considered.

Charge collection entails both the movement of the free charge carriers from the BHJ, as well as their collection at the organic/electrode interface. High crystallinity will have a favorable impact upon the ability of the charges to move from the BHJ, because they are moving within the homogeneous domains of the donor and acceptor materials. As the crystallinity increases, so too will the mobility of the free charge carriers[82]. For the actual collection of charges at the organic/electrode interface, the presence of crystallinity is more nuanced[83]. First, ion or metal diffusion into the organic layer during post-deposition annealing (a common technique to increase the crystallinity) creating crystalline nanoclusters of electrode interspersed in the crystalline organic layer[84]. These act as filled trap states which change the electronic field distribution inside of the device, as well as screening the electronic field at the interface. Next, the formation of non-preferential dipoles at the organic-electrode interface can create an energy barrier that free charge carriers must overcome. The presence of crystallinity can modify the extant dipoles either positively or negatively, depending on the molecular orbital energy levels of the crystalline region[85]. Another way that crystalline domains can impact the organic/electrode interface is through band-bending; this band-bending is caused by temperature-dependent charge diffusion from the metal contact into the organic layer[86,87]. This creates a non-zero field in the bulk, which can lead to buildup of charge. Again, the presence of crystallinity can impact this positively or negatively, depending on the

LUMO/HOMO energies of the crystal structures. Finally, there can be an actual chemical reaction during thermal annealing that causes bond formation between the electrode and the organics present. In systems involving aluminum and organics with carbon-carbon double bonds, a variety of new bonds can be created, including oxygen bridging structures and the breaking of C=C bonds to form C-Al[88,89]. These all lead to recombination of charges which will reduce the current[90]. The importance of crystallinity in this case is the temperature at which the most amount of bonding will occur is above T_G (the glass transition temperature of the organic layer) and the relative amount of crystallinity versus amorphousness before the annealing step will impact the T_G of the overall film. Besides these four highly specified areas within which crystallinity can impact the collection of charges at the organic/electrode interface, there is the macroscopic perspective of enhanced surface area. The more crystals that are present, the greater the roughness of the organic layer before deposition of the electrode occurs. Higher amounts of roughness result in a larger interfacial area from which charge can be extracted by the deposited electrode. Therefore, if the four specific parameter effects detailed above are either accounted for or negligible, the net effect of crystallinity at the organic/electrode interface will be positive.

To summarize, the presence of aggregates and crystallinity create numerous, and sometimes competing, ways that charge photogeneration is changed. Absorbance is positively impacted by aggregates, and negligibly influenced by crystallinity. Exciton diffusion is not affected by aggregates, but increases can be strongly correlated positively with increasing crystallinity of the donor. Exciton dissociation and charge transfer state separation are still hotly debated, but both aggregates and crystallinity will have dramatic

consequences on the actual formation of free charges from the bound exciton. Finally, charge collection is not swayed by aggregates, whereas crystallinity has potential to generate significant differences when compared to amorphous regions. Chapter Four continues with a discussion of the role of aggregates in forming the BHJ, as well as the performance of the static BHJ product within a device; this will now be considered from the perspective of device performance as opposed to characterization.

4.2. Metrics of Device Performance

There are four basic metrics for evaluating the performance of an OPV: the open-circuit voltage, short-circuit current, power conversion efficiency, and external quantum efficiency. Additional metrics include but are not limited to the fill factor, shunt resistance, series resistance, dark current, and ideality factor. As has been discussed throughout the thesis so far, the role of the BHJ in charge photogeneration is absolutely crucial. Therefore, this section will attempt to tie together a) the impact of molecular structure on the formation of the BHJ, b) the relationship between how the BHJ is formed and charge photogeneration, c) molecular structure and performance of the BHJ, and d) charge photogeneration and performance of the BHJ, all from the perspective of the four basic device metrics. Where Section 4.1 described fundamental materials science and characterization, this section will focus on device engineering and testing. Figure 22 shows the current-voltage characteristics of an OPV, from which the first three device metrics are extracted.

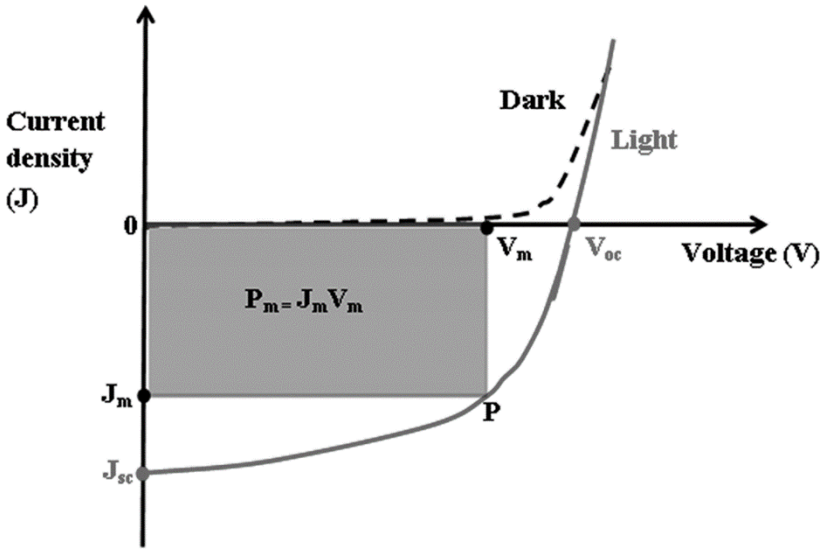

Figure 22 Typical characteristics of an OPV, reprinted with permission from Manthrim et al[4]; both dark (dashed curve) and illuminated (solid curve).

The illuminated curve is the superposition of the IV curve of the solar cell in the dark, plus the photogenerated current. This is easily described by modifying the Shockley ideal diode equation[75]to include a term for the photocurrent.

$$I = I_0 \left[exp\left(\frac{qV}{nkT}\right) - 1 \right] - I_L$$

The net current flowing, I, is therefore the dark saturation current I_0 (or leakage current) as a function of applied voltage V, the electron charge q, the Boltzmann constant k, temperature T, ideality factor n, with the photocurrent I_L acting to shift "down" I. The metrics directly extracted from the graph are J_{SC}, the short-circuit current, and V_{OC}, the open-circuit voltage. J_{SC} is the current that is flowing through the cell when the cell is short-circuited (V=0), and it is due solely to the generation and collection of photogenerated carriers. The open-circuit voltage is the maximum voltage that can be achieved (I=0), and is equal to the amount of forward bias on the solar cell from the bias

of the heterojunction created by the photocurrent. Modeling the V_{OC}, even simplistically, allows for a better understanding of its origin. When I=0,

$$V_{OC} = \frac{nkT}{q} \ln(\frac{I_L}{I_0} + 1)$$

meaning that the V_{OC} can be considered to be dependent on both the dark current and the photocurrent. Since the dark current depends on the extent of recombination in the device, a high open circuit voltage can therefore indicate minimal amounts of recombination. Additionally, the Voc can be considered as arising from material properties; specifically the LUMO-HOMO energy difference (or bandgap) of the materials present at the heterojunction.

The power conversion efficiency (PCE) of the OPV is the fraction of the incident power that is converted to electricity.

$$PCE = \frac{V_{OC} J_{SC} FF}{P_{inc}}$$

P_{inc} is the incident power, and FF is the fill factor. FF is essentially the area of the largest rectangle that will fit inside the IV curve and is shown in Figure 22. It is the maximum power achievable (P_m) restrained by the shape of the curve divided by the greatest power possible if only the open circuit voltage and short circuit current were examined.

$$FF = \frac{I_{MP} V_{MP}}{I_{SC} V_{OC}}$$

Thus, the "squareness" of the IV curve plays a role in the fill factor. By examining how the curve slopes, a relationship can found between the FF and resistances present in the

cell, which makes it an important albeit slightly metric for evaluating the goodness of the device morphology.

The series resistance can be calculate directly from the slope of the line as it crosses through the x-axis at the Voc; ideally the resistance will be zero. Series resistance has been determined to be caused by three main factors: i)innate resistance arising through the movement 2.1.of charges through the homogeneous domains of donor and acceptor, ii) contact resistance between the metal and the organic interface, and iii) the built in resistances of the top and bottom contact. The shunt resistance can be calculated from the slope of the curve as it passes through the Jsc. Conversely, this resistance is desired to be as large possible, because a low shunt resistance means there are a multitude of pathways (shunts) for the charges to travel down that will cause a loss of current, and a concurrent loss of voltage. To summarize, the ideal bulk heterojunction will promote a low series resistance and a high shunt resistance, as will the contact between the organic and the electrode, and the innate resistance of the electrodes. This will contribute to improving the squareness of the IV curve, which will then increase P_M. The goal would be to have $P_M=I_{SC}*V_{OC}$, thereby generating a FF of 1, which will in turn maximize the PCE.

The final characterization metric to be discussed is the external quantum efficiency (EQE), which is measured using the spectral response. The spectral response is the ratio of the current generated to the power incident on the cell; this is easily converted into the number of electrons generated at a particular wavelength compared to the number of photons incident on the cell at that same particular wavelength. At any given wavelength, the desired EQE is unity, because that indicates that every photon incident

upon the cell at that wavelength is able to undergo charge photogeneration completely from total absorbance to free charge carrier generation. However, multiple loss mechanisms inherent in the solar cell architecture will mean that EQE can never be unity, even if the material systems had been perfectly optimized for charge photogeneration. Green light will be absorbed in the bulk of the solar cell, where short diffusion lengths will have the greatest impact thereby reducing the EQE of the wavelengths representing green light. Additionally, EQE does not correct for losses from parasitic absorption by other materials, transmitted light that is not absorbed and is therefore lost, and reflection of light by either the ITO glass or the backside of the aluminum. These can be taken into account through measurement of the devices' transmission and reflectivity, giving the internal quantum efficiency (IQE) of the solar cell so that the internal process of charge photogeneration can be best probed. An alternative method that generates a quasi-IQE will be presented in Section 5.2.1.2.2. Following this definition of the different metrics for analyzing the quality of an OPV, we will now turn to a brief discussion of their correlation to formation and performance of the BHJ from both a materials prescription perspective and the fundamental photophysics of charge photogeneration.

4.2.1. Formation of the Bulk Heterojunction

4.2.1.1. Material prescription and charge photogeneration

Short circuit current and open circuit voltage both result from how the BHJ is formed. The current will be tied to the extent of crystalline homogeneous domain formation adjacent to the BHJ that can efficiently transport charge. In the case of squaraine OPVs, the voltage will be tied to the specific energetics of the aggregates that

are formed directly at the interface between donor and acceptor. When considered purely from an electronic perspective, the amount of leakage (dark) current that is present, which reduces the V_{OC}, is directly attributable to which species are present at the BHJ. If there are a variety of energetic species present as there are in squaraine OPVs, then the likelihood of exciton recombination and exciplex regeneration will be increased, resulting in larger amounts of electron-hole pair geminate recombination at the BHJ[91,92]. Fill factor will also be tied to the formation of the BHJ, because it is an indicator of the "goodness" of domain size for effect photocurrent generation and collection. Materials must be selected for inclusion which are able to balance the need for homogenous crystalline domains, preferential energy levels between donor and acceptor to discourage recombination, and small enough domain sizes that charge photogeneration is efficient. In order to select these materials the mechanism for BHJ formation must be explained thermodynamically in relation to domain size and crystalline domain formation. Experimental work on this will be discussed in detail in Section 5.1.2. Control over the amount and type of aggregates that are formed is much more challenging to tie to the molecular structure, and work on this with the Spano group is ongoing for the foreseeable future.

4.2.2. Performance of the Bulk Heterojunction

4.2.2.1. Material prescription and charge photogeneration

The device metrics given above are truly the only way to examine the performance of the BHJ from an electronic perspective. The presence or absence of aggregates will have an impact at each step of the process of charge photogeneration, and

this can be optimized through appropriate material design. Exciton dissociation will be mediated very strongly by the energy levels of the materials that are at the BHJ. The greatest number of excitons will be dissociated into free charges, and therefore the greatest amount of current will be generated, when there is sufficient driving force for the excited electron to transfer from the donor to the acceptor. There must also be strong coupling between the initial and final states of the system during the exciton dissociation process. While short-circuit current is a useful marker for the number of charges that are generated, the EQE can also give valuable information about which aggregate types are able to most efficiently transfer an excited electron from the squaraines to the PCBM. Combining these two techniques can give a clear picture of which aggregate types are preferential. Using the characterization data to tie together the molecular structure to aggregate formation, and then relate this to the device metrics, allows for the best possible predictive technique. While the shunt and series resistance are not directly related to the BHJ, the fill factor can be used to understand how much mixing is occurring within the blend, and the ideal domain size as a function of that mixing of the two components can be used to guide the choice of materials.

To summarize Chapter Four, the characterization and device metrics have been briefly examined within the context of the squaraine aggregates. Hypotheses about relationships between the characterization and molecular structure, and the characterization and device analysis have been very briefly presented. This then allows us to move to Chapter Five, which will give a complete and thorough description and analysis of all experimental work performed during the duration of the thesis.

5. Experimental Results

Chapter Abstract

Within this chapter, a complete description of the experimental work performed will be presented. First, characterization data for a specific squaraine will be presented, as an illustrative example of the information that can be obtained from simple characterization method. Then, a fairly exhaustive study of six different squaraines' absorbance and XRD data will be presented, the highlight of which is the discussion of trends present or absent when examining the squaraine series from multiple perspectives, including chain length and aggregate composition. Next, device work will be presented for a specific squaraine. This full matrix study examines device performance metrics as a function of blend ratio and annealing temperature, with a brief foray into device degradation, device size impacts, and the effect of light biasing on one of the device metrics. A detailed study of the same squaraine is given, where devices that had been optimized were characterized with a variety of techniques in order to understand changing performance. Finally, all other devices made during the thesis will be discussed, including polymer:PCBM devices and ternary blends.

5.1. Aggregation and Crystallinity

5.1.1. DiPSQ(OH)$_2$

5.1.1.1. Characterization Study

5.1.1.1.1. Purpose and Utility

The characterization of a squaraine, 1,3-bis[4-(N,N-diisopentylamino)-2,6-dihydroxyphenyl]squaraine [DiPSQ(OH)$_2$] is presented in this section. This squaraine shows significant promise for incorporation into industrial-scale organic solar cells, based upon encouraging unoptimized device performance, and the generalized attributes associated with most molecules in this class of compounds. The stack motif of these molecules gives rise to H-aggregates and J-aggregates, respectively evidenced by blue-

shifted and red-shifted signatures in an absorbance spectrum. These H- and J- aggregates have their own intrinsic optical and electronic properties, determined by the interaction of transition dipole moments and Davydov splitting. [59] J-aggregates tend to result from a head-to-tail or brickwork stacking arrangement and H-aggregates tend to result from a vertical stack of molecules. [93] Based on a large body of work with squaraines, Law states that aggregation and extent of crystallinity should be viewed and described separately when considering structure and function of squaraines in optoelectronic applications[94]. Significantly, I demonstrate a relation between aggregation and extent of crystallinity. This is important since the crystallinity will directly impact the mobility and hence the photovoltaic efficiency of devices made from a new squaraine[75,95–101].

Steady-state UV-VIS-NIR absorbance and thin-film X-ray diffraction (TFXRD) of device analogue thin films can be used to characterize the extent of component crystallinity and the impact of differing molecular orientations on optical and electrical properties. Atomic Force Microscopy (AFM) data acts to complement and strengthen this characterization. Measurements of neat squaraine films and blended films, with phenyl-C_{61}-butyric acid methyl ester (PCBM) as the acceptor, allow comparison of pure squaraine crystallization and aggregation patterns versus the device analogue film where a bulk heterojunction is present. Absorbance measurements provide access to the relative energy levels of different aggregate species in the thin-films based upon the peak position as well as changes in concentration of the aggregates that are present. Active control of amount and type of aggregate formed is demonstrated, and also the impact of a particular conditioning treatment (thermal annealing, cosolvent) on the formation of different types of aggregates. The TFXRD measurements provide a correlating measurement of

aggregate amount and total film crystallinity when performed on identical films as absorbance. Using concurrent measurements of aggregate absorption and extent of crystallinity can elucidate the actual structure of the aggregate, and specifically address the true relationship with crystallinity/amorphousness.

In this section, significant changes in absorbance intensity and peak location, as well as crystallinity, are found upon thermal annealing of $DiPSQ(OH)_2$ neat and blended thin films. Morphology control of the squaraine domains is discussed, along with its propensity to crystallize despite a large molecular weight and the presence of four large, flexible isopentyl sidechains, which would be expected to present a barrier to effective intermolecular interaction. The ability to selectively control the morphology of the squaraine domains indicates both the molecule and the family of squaraines can offer high potential in mechanistic studies of device performance. Because the characterization of the squaraine domains is demonstrated using relatively simple techniques, I believe this material can offer a highly selective probe into the bulk heterojunction.

5.1.1.1.2. Data and Discussion

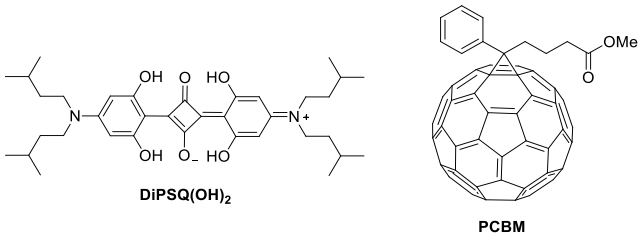

Figure 23 Chemical structure of $DiPSQ(OH)_2$ and PCBM.

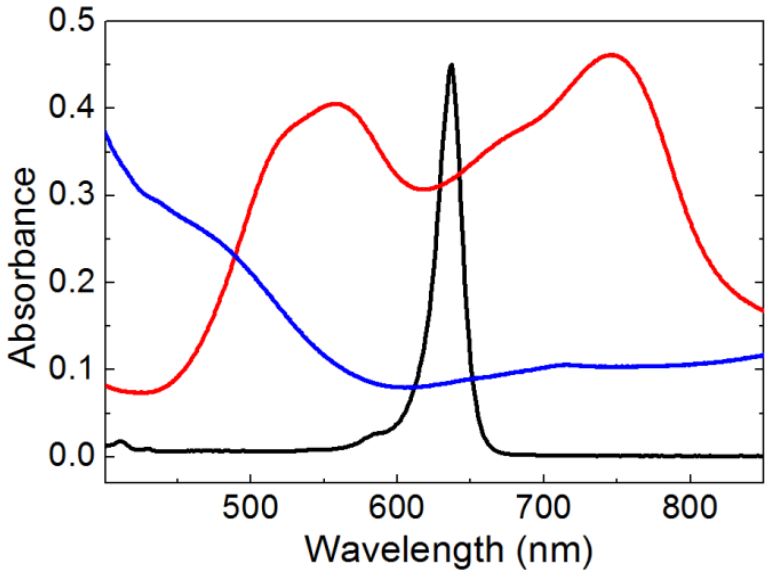

Figure 24 Spectra of DiPSQ(OH)$_2$ film (red), PCBM film (blue), and DiPSQ(OH)$_2$ in solution (black). Black squares are PCBM intensity at 476 nm, red circles are DiPSQ(OH)$_2$ intensity at 762 nm.

The absorbance spectra of DiPSQ(OH)$_2$ in solution and thin film are shown in Figure 24 along with a thin film absorbance spectrum of PCBM, alone. The DiPSQ(OH)$_2$ solution absorbance profile, for which only monomers are present, is characteristically narrow with a distinct monomer peak at 660 nm. The interaction of two or more monomers in solid solution or thin-film broadens the spectrum and creates new peaks. Thus, there are three peaks or shoulders in the neat DiPSQ(OH)$_2$ thin film spectrum at 557 nm (2.23 eV, 17953 cm-1), 678 nm (1.83 eV, 14749 cm-1) and 748 nm (1.66 eV, 13369 cm-1) seen in Figure 24. I assign these peaks respectively to H-aggregates, amorphous monomers, and J-aggregates. The splitting between peaks 1 and 2 is 3200 cm-1, and between peaks 1 and 3 is 4580 cm-1. Aggregation and crystallization of the molecules allows for interaction of transition dipole moments of the two monomers, which is associated with exciton/Davydov splitting.[59,102,103] The presence of both H- and

J-aggregate peaks is consistent with the presence of oblique transition dipole moments as shown in analogous molecules synthesized by the authors, which pack in a herringbone structure as demonstrated using single crystal x-ray diffraction.[64] Oblique transition dipoles generate both in-plane and out-of-plane dipole arrangements corresponding to a respective raising and lowering of the energy level relative to the monomer. Therefore, the spin-coating process and subsequent crystallization creates these new peaks in the absorbance spectra as shown.

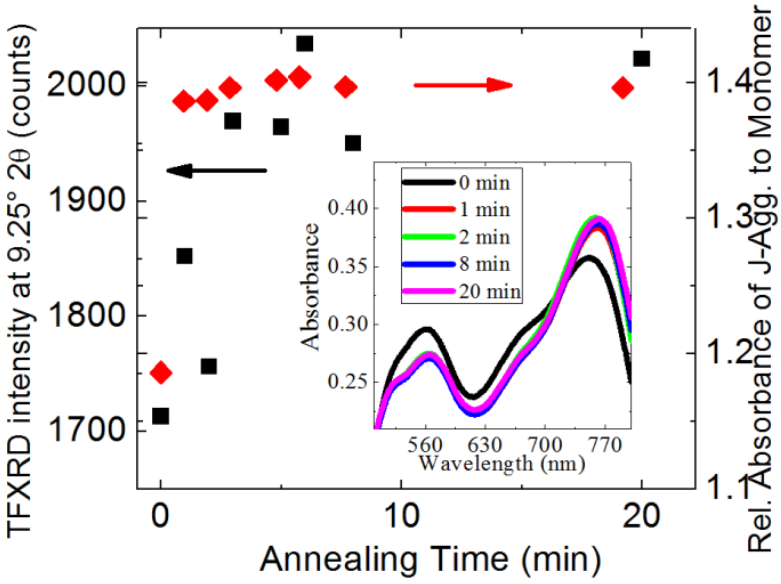

Figure 25 A correlation of the pure DiPSQ(OH)$_2$ TFXRD peak intensity (black squares) and relative absorbance intensity of J-aggregate at 762nm to monomer feature at 680nm (red diamonds) as a function of annealing time at 150°C. The inset shows the absorbance spectra for the pure DiPSQ(OH)$_2$ film as a function of incremental annealing time.

The impact of annealing upon absorbance and extent of crystallinity is explored in Figure 25. Examination of the TFXRD data and absorbance spectra throughout the annealing process shows concurrent increases in intensity of the squaraine XRD peak and

relative absorbance intensity of the J-aggregate peak. The TFXRD signal intensity (left axis), corresponding with the TFXRD counts at the $DiPSQ(OH)_2$ peak at 9.25° 2θ, increases by 19% in the first few minutes of annealing. At the same time, the relative absorbance (right axis) of J-aggregate (762 nm) to monomer (680 nm) for the $DiPSQ(OH)_2$ demonstrates an 18% increase. Both sets of measurements show a sudden initial increase upon annealing, with change slowing upon further annealing. These data indicate that, upon annealing, the amount of crystallinity in the $DiPSQ(OH)_2$ increases. In addition, the growth in relative J-aggregate absorbance at 762 nm results from an increase in population of J-aggregates and, therefore, a lowering of the sample's transition energy, as averaged over all observable transitions. For clarity, the inset shows the absorbance spectra, exhibiting features at 560 nm, 680 nm and 762 nm associated with H-aggregate, monomer and J-aggregate, respectively. The relative changes can be seen qualitatively to the entire spectrum as annealing time is incrementally changed.

It is important to note that, for all TFXRD measurements, there is only one TFXRD peak associated with the $DiPSQ(OH)_2$, which supports there being only one crystal structure. This implies that H- and J-aggregation are sourced from the same single crystalline structure in the $DiPSQ(OH)_2$ material.[59]

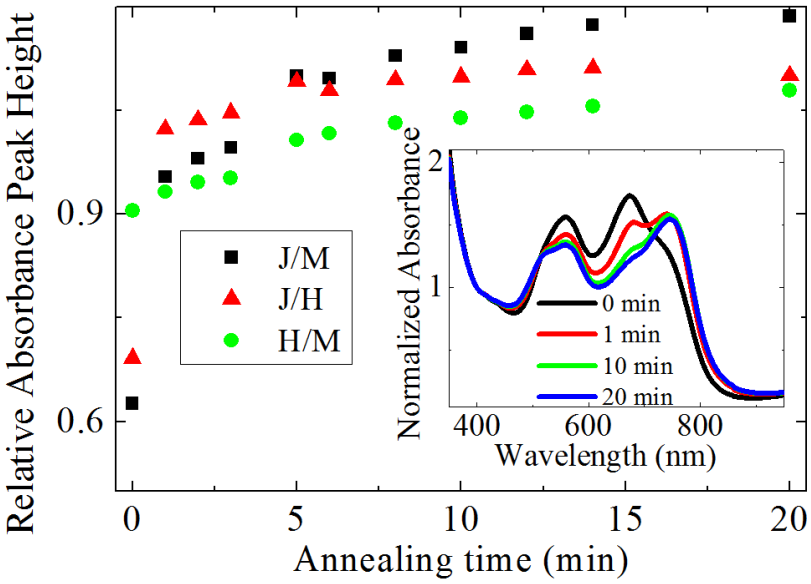

Figure 26 The relative absorbance peak heights of J-aggregate peak to monomer peak (black square), J-aggregate peak to H-aggregate peak (red triangle) and H-aggregate peak to monomer peak (green circle) for 1:2 DiPSQ(OH)$_2$:PCBM blend thin film device analogues. Inset shows absorbance spectra normalized to 400 nm for different annealing times.

These same DiPSQ(OH)$_2$ measurements were repeated with the incorporation of PCBM in the spin-cast films, with samples now analogous to the bulk heterojunctions (BHJ) of photovoltaic devices. The relative peak heights, J-aggregate peak (762 nm) to monomer peak (680 nm), J-aggregate peak (762 nm) to H-aggregate feature (554 nm) and H-aggregate feature (554 nm) to monomer peak (680 nm) are shown in Figure 26 as a function of incremental annealing time. The absorbance spectra of films made with a 1:2 DiPSQ(OH)$_2$:PCBM blend ratio, sequentially annealed at 150°C for a total of 20 minutes is shown in the inset.

There is a very sharp increase in the relative absorbance of J-aggregate to monomer over incremental annealing time. This suggests substantial ordering in the

sample. At the same time the relative absorbance of the J-aggregate to the H-aggregate also increases sharply. Both data sets show a continued small but steady increase in relative J-aggregate absorbance at 762nm as incremental changes are made in annealing time. Furthermore, the ratio of H-aggregate absorbance to monomer absorbance is significant yet much smaller, without the sharp change at early times representative of the J-aggregate. With only one $DiPSQ(OH)_2$ crystal peak for all TFXRD data suggesting a dominant crystal structure with no evidence in differential scanning calorimetry to suggest the existence of a second crystal phase, the relative dominance of the J-aggregate peak with annealing draws significant interest.

With respect to this inset, and by comparison with the absorbance spectra of the neat $DiPSQ(OH)_2$ in Figure 24 and 25, the absorbance spectrum of the unannealed pristine $DiPSQ(OH)_2$:PCBM blend has similar features. However the J-aggregate feature is now a shoulder at 745nm greatly smaller in size than the now more significant monomeric peak. The PCBM has greatly disrupted the formation of J-aggregates in the pristine spin-cast films with the relative J-aggregate to monomer absorbance ratio dropping from 1.19 to 0.63.

Significantly, upon annealing, the relative sizes of the monomeric and J-aggregate absorbance peaks change drastically – the 30% decrease (0.09 raw optical density decrease) in peak intensity at 680 nm corresponds with a 20% increase in absorbance at 745 nm. In summary, absorbance data shows there is an even bigger impact of annealing on films containing PCBM, analogous to those of functioning devices.

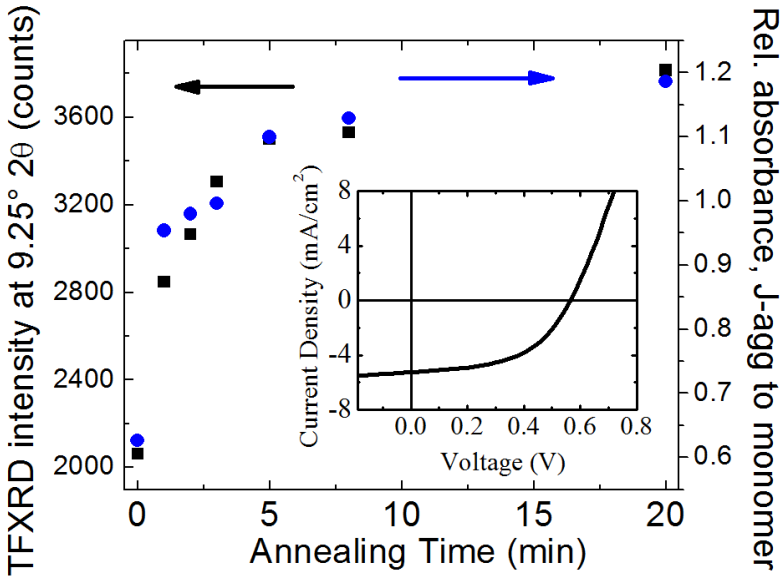

Figure 27 A direct comparison of TFXRD intensity at 9.25° 2θ (black squares) with the relative absorbance intensity of the assigned J-aggregate peak, J-aggregate to monomer, (blue circles) in a 1:2 DiPSQ(OH)$_2$:PCBM blend film.

A relative increase in both crystallinity, as measured by TFXRD, and relative absorption of the J-aggregate peak to the monomer feature for the 1:2 DiPSQ(OH)$_2$:PCBM blend BHJ film is shown in Figure 27. A concurrent increase in crystallinity upon annealing appears to be directly related to these changes in absorbance. Hence, the drop in absorbance intensity at 680 nm from Figure 25 is attributed to a reduction in population of amorphous, and therefore monomeric DiPSQ(OH)$_2$, upon annealing. The corresponding increase at 762 nm is assigned to an increase in crystallinity. The correlation between extent of crystallinity and relative J-aggregate absorption intensity is striking, indicating a substantial benefit in that absorbance measurements can be used to characterize the bulk morphology of these blend films.

The potential of this squaraine to be used in future high efficiency devices is marked in the inset to Figure 27. The J-V curve for unoptimized devices is shown. The fill factor of 51.9% with standard deviation of 4.5% is low, typical for unoptimized devices, suggesting optimization will be fruitful. A promising average PCE of 1.54%, (standard deviation of 0.16%) will be improved, targeted for a future parallel study.

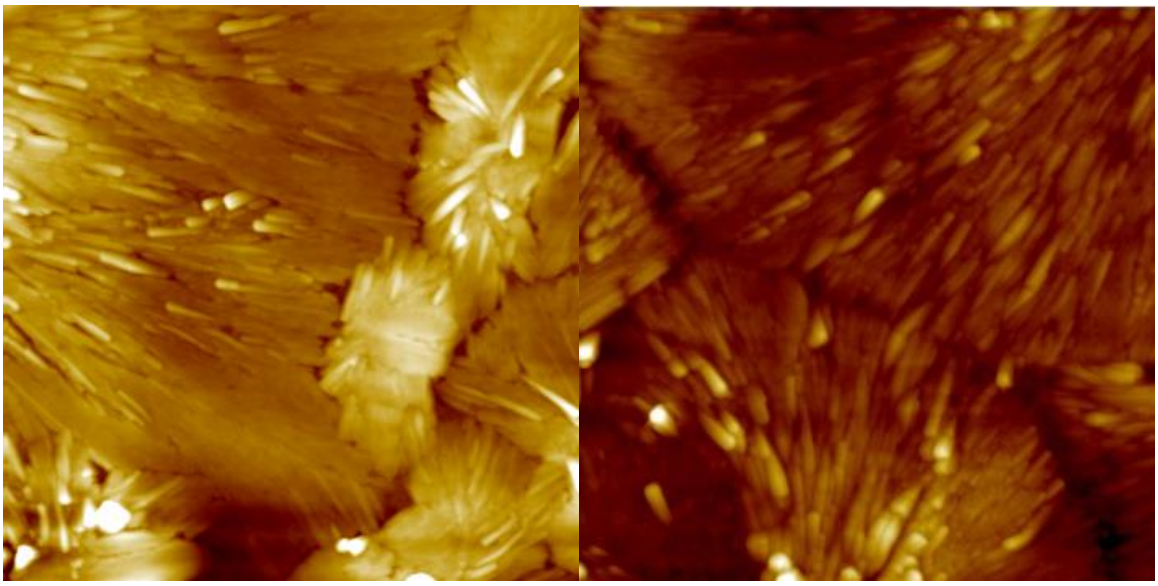

Figure 28 (5 μm)^2 AFM images of neat DiPSQ(OH)$_2$ films that are (a) pristine and (b) annealed for 20 minutes at 150°C in ambient atmosphere. Height ranges are 205 nm and 137 nm for (a) and (b), respectively. Pixel size is 9.8 nm.

The bulk film crystallization observations for absorbance and TFXRD are supported by AFM measurements of the pure DiPSQ(OH)$_2$ and BHJ films through the annealing process. Figure 28 displays (5 μm)^2 AFM images of DiPSQ(OH)$_2$ films both unannealed and annealed for 20 minutes at 150 °C, respectively. High aspect ratio, needle-like crystals ~100 nm wide and in excess of 0.5 μm in length are aligned in ordered structures, consistent with crystal grains. These needle-like growths dominate the

large, ordered regions. The crystal structures display circular and bow-tie growth patterns and, upon annealing, the crystals become more well-defined, larger in size, and the needle-like features are longer. Significantly, in the annealed films there is an increase and development of more well defined regions between crystal nucleation sites, as is displayed in the dark boundaries of Figure 28b. Observations are consistent with pristine film images containing crystals within a quasi-homogeneous background, which is likely dominated by amorphous squaraine, the monomeric DiPSQ$(OH)_2$. The general observation after annealing is an increase in structures consistent with well-ordered crystals.

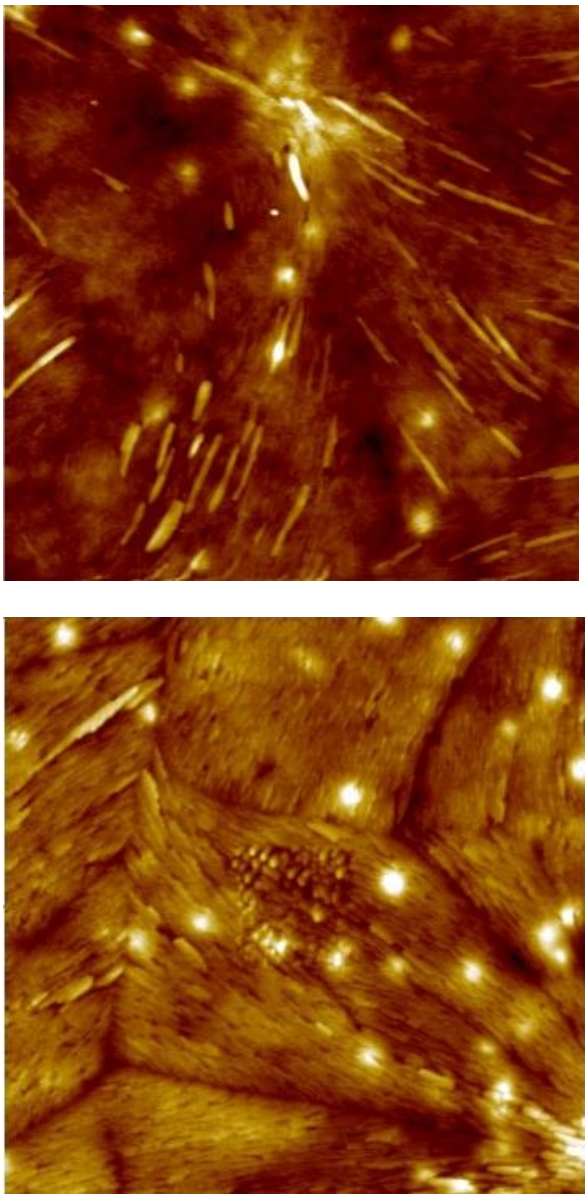

Figure 29 (5 μm)2 AFM images of a DiPSQ$(OH)_2$:PCBM blends that are (a) pristine and (b) annealed for 20 minutes at 150 °C. Height ranges are 29 nm and 38 nm respectively for (a) and (b). Pixel size is 9.8 nm.

Similar trends are observed in the $(5\ \mu m)^2$ AFM images of the blended DiPSQ$(OH)_2$:PCBM BHJ films of Figure 29. Figure 29a and 29b are the BHJ both unannealed and annealed for 20 minutes at 150°C, respectively. Similar needle like

crystals are observed in the unannealed film, as seen in Figure 28a, with typical sizes of ~100 nm in width and ~400 nm in length. Compared to the neat DiPSQ(OH)$_2$ film, fewer crystals stand out from the relatively smooth film surface in this unannealed film. Additionally, spherical growths are observed on the film surface, consistent with the spherical PCBM crystals seen in other BHJs[104,105]. Upon annealing, both crystal structures become much more well-defined, with boundaries between crystal grains becoming clearly visible and demarcated by film separation as is expected for film crystallization. More importantly the average well-defined crystal size for the blended films increases by approximately a factor of two for the 20 minute annealed BHJ. In addition, the relative size and height of PCBM-like crystals increases, suggesting increased phase separation during the annealing process. This could indicate that PCBM disrupts the formation of crystals in the as-cast blend.

These data demonstrate a strong correlation between annealing of a blended film and an increase in extent of crystallinity of both components. This also gives us insight as to the cause of the J-aggregate peak intensity. The crystals primarily grow in a rod-like structure that suggests that one crystal axis may dominate the other. Given that the H-aggregates and J-aggregates are oriented at some fixed angle from each other, it seems likely that the growth in absorption due to the J-aggregate is associated with a relative increase in crystal growth along the dominant crystal axis. This I expect to be more pronounced as aggregate size increases.

The ultimate proposal in this section is that, with an appropriate control of crystallinity or film morphology, which may include some optimization of blend ratio because of the disruptive effect of PCBM on crystals of DiPSQ(OH)$_2$, the overall bulk

mobility and spatially averaged localized charge carrier mobility of this small molecule can be improved. This work demonstrates that a selective increase in J-aggregation may be afforded in the event that the molecule of interest grows in a favored crystal axis.

5.1.1.1.3 Conclusion

DiPSQ(OH)$_2$ is an interesting target molecule for organic photovoltaics because of its unusually broad panchromaticity, presumably caused by a tighter molecular packing than one would expect to see, given such bulky alkyl groups attached to the anilinic nitrogen. A comprehensive explanation of how DiPSQ(OH)$_2$ aggregates are affected by annealing and crystal growth is provided. I demonstrate a direct relationship between the absorbance of the aggregates and their enhanced crystallinity using both bulk and surface measurements. I show a morphology of quasi-crystalline squaraine in an amorphous background that can be tightly controlled using thermal annealing. This control of crystalline structure at the bulk heterojunction and its relationship to the energy level of the aggregate creates a unique system to examine charge photogeneration. Hence this work demonstrates that with some control of blend ratio, and more importantly, an appropriate annealing strategy, crystalline regions of higher mobility can be developed so as to correlate conclusively in future work the need for high ordering and crystallinity in small molecules with the efficiency required to achieve long term goals for commercially viable NIR-active OPV devices.

5.1.2. Deshydroxy and Dihydroxy Squaraine Series

5.1.2.1. Goal of the Study

As has been discussed at length already, there is no keystone technique or method of analysis that can be universally applied to determine what impact molecular structure will have on the final device efficiency[41]. The missing component is a description of how molecular structure impacts the formation mechanism of the homogeneous regions as well as the BHJ interface, and how the thin film's optical and electronic properties of exciton generation, transport, and dissociation are governed by the molecular structure. To address this question, we work with six squaraine materials. We can control the amount of crystallinity, and subsequent formation of aggregates, using thermal annealing[106].

In this section, we examine an entire series of squaraine dyes using complementary techniques of absorbance and powder and in-situ thin-film x-ray diffraction (TFXRD). Comparisons are made of both neat squaraine films and squaraine:PCBM blended films where the materials are characterized both pristine (as-cast) and annealed. The as-cast thin films provide valuable information for understanding what the dominant thermodynamic interaction of BHJ formation is, and how molecular structure of the squaraine impacts the thermodynamics. By annealing the thin films and devices, the formation of crystalline domains can be monitored and their impact on both exciton dissociation at the BHJ as well as exciton/charge carrier transport in the homogeneous regions of the devices. This series of squaraines is varied in both length of the carbon side chains, and the presence or absence of the hydroxyl groups on the central

squaric acid moiety. By varying the length of the side chains, we are impacting the ability of the squaraine to pack into crystals. As the chain length increases, the squaraine-squaraine interaction will be more disordered, and there will be more amorphous regions than crystalline in the pristine materials. Shorter side chains conversely should behave with much greater planarity. Hydroxyl groups control the thermodynamic interaction strengths that allow for the molecules to come together during the spin-coating process forming the BHJ. These two "knobs" allow for an in-depth examination of the dominant mechanism of BHJ formation.

As described in Section 4.1, absorbance gives valuable information about the energetics and quantity of optical excitations present in the neat and blend films. TFXRD illuminates the amount of crystals present in the thin film, their structure, and their size. By examining identical films with both the TFXRD and the absorbance as the films are annealed at increasing temperatures, correlations can be made between changes in the optical excitations that are allowed (visible in absorbance spectra) and the crystallinity and type of crystals that are present in the thin film. We then explain how the molecular structure of the squaraine controls the thermodynamics of mixing/BHJ formation. The molecular structure therefore leads to the morphology of the BHJ which can be described and investigated with EQE results for its efficacy; this gives a direct prescriptive method to move from a molecular structure to EQE and short circuit current results.

5.1.2.2. Discussion of Trends

5.1.2.2.1. Chain Length

The chain length of the squaraines was varied from three to five carbons. It was expected that this variation would have an impact primarily on the packing structure of the squaraine crystals, and not on the optoelectronic properties of the excitation. This is because the side chains are not strongly electron-withdrawing or electron-donating groups, and as such will do little to impact the electron density of the molecule and exciton.

In the neat squaraine films, as the number of carbons in the side chains increased, so did the absorbance intensity of all of the absorbing species: H-aggregate, J-aggregate, and monomer. This indicates that while more aggregate excitations were present, there was also a greater amount of disorder from side chain interactions, thereby enhancing the monomer absorbance as well. For the neat squaraine films, as the number of carbons increased, the ensemble size of the H- and J-aggregate changed relative to one another. The relationship was mediated by the presence or absence of the hydroxyl groups; in the deshydroxy series, increasing chain length led to an increase in the ensemble size of the H-aggregate while the J-aggregate band remained narrow. In the dihydroxy series, increasing chain length led to an increase in the ensemble size of the J-aggregate while the H-aggregate band remained narrow.

Examining the powder XRD of the raw squaraine material, all chain lengths demonstrated significant crystallinity with large variation in crystal structure. The neat thin film XRD for the the deshydroxy series showed strong amorphous characteristics for

all chain lengths except the five carbon material, while the dihydroxy series was crystalline for all chain lengths, but with no clear trends for interplanar spacing, coherent crystal domain size, or intensity with increasing chain lengths.

In the blend squaraine films, as the side chain length increased, the H-aggregates red-shifted in the deshydroxy films, but blue-shifted in the dihydroxy films. Increasing chain length in the deshydroxy series correlated with a reduction in the formation of the monomer, but in the dihydroxy series it correlated with an increase in the formation of the monomer. As was found for the neat films, the size of the H-aggregate ensemble increased for the deshydroxy squaraines, but decreased for the J-aggregate ensemble in the dihydroxy squaraines. For the thin film blend XRD, there was no trend found correlating crystallinity with chain length.

In summary, the chain length alone of the squaraine does not serve as a predictive method for understanding the types and amount of aggregates that will form, nor the amount of crystallinity that will be present in the thin films of either neat or blended squaraine. This is not unexpected, but serves to indicate that the process of spin-coating the films has the potential to generate radically different environments for the formation of domains that cannot be correlated directly to the chain length of the material that is being spun cast.

5.1.2.2.2. Hydroxy Groups

Each of the 3 chain lengths was prepared as both a deshydroxy and dihydroxy squaraine. The dihydroxy squaraines have a total of 4 OH groups surrounding the central squaric acid moiety, and the deshydroxy squaraines have no OH groups present. The

hydroxy groups are believed to impact the optoelectronic properties of the material by changing the HOMO and LUMO of the squaraine, as well as having an impact on the formation of crystals and aggregates through hydrogen bond-mediated interactions.

In neat squaraine films, the presence of the hydroxyl groups gave much stronger TFXRD crystallinity intensity than the corresponding deshydroxy squaraine for every pair considered. Additionally, in every pair comparison, the dihydroxy squaraine gave a greater panchromatic absorbance. This increased optical bandgap for a given dihydroxy squaraine as compared to its deshydroxy counterpart lends credence to the hypothesis that the hydroxy groups are indeed shifting the HOMO and LUMO of the material.

In the blend films, when there are no hydroxy groups present to interact with the PCBM, there is a preferential broadening of the H-aggregate ensemble as the chain length increases. With hydroxyl groups present to interact with the PCBM, there is a preferential narrowing of the J-aggregate ensemble as the chain length increases. If the ensemble size is considered to be a representation of the number of types of allowable molecular configurations that can generate an exciton upon interaction with photons, then PCBM forces additional H-aggregate molecular configurations as chain length increases when there are no hydroxy groups present. Conversely, PCBM reduces the number of allowable J-aggregate molecular configurations as chain length increases when there are hydroxy groups available. This points to PCBM's inclusion having an effect above and beyond the simplistic picture of mechanical disruption of squaraine molecular order. Relative to the neat film, H-aggregates in the blend film were all blue-shifted except for the DiPSQ. This means that the red shift of the blend film deshydroxy aggregates as a function of chain length shows an increasing tendency for the squaraines to behave as

though no PCBM were present as the side chains get longer. This is a strong indication that the dominant packing mechanism when no hydroxyl groups are present is indeed the side chain interaction of one squaraine to another. The blend film dihydroxy H-aggregates blue-shifting as chain length increases, along with the blue shift of the blend film relative to the neat film, seems to indicate that the hydroxyl group presence is acting to localize the exciton upon a specific region of the aggregate. Finally, the presence of the hydroxyl groups gave much stronger TFXRD crystallinity intensity than the corresponding deshydroxy squaraine for every pair considered except for the DBSQ series.

To summarize, the presence of the hydroxyl groups has a favorable impact on both absorbance and crystallinity. This indicates that their presence will be a necessity in choosing future squaraines for OPV inclusion, as both panchromaticity and the presence of some crystal sturcutre is required to achieve high-performance devices.

5.1.2.2.3. Aggregates, Crystallinity, and Annealing

Both H- and J-aggregates truly exist only as optical excitations, and as such, do not by themselves necessarily offer information about the morphology of the neat squaraine domains or the BHJ of the film. But by classifying their behavior as a function of annealing, they can be correlated to crystal structure in a way that allows for a description of both the optoelectronics and the morphology simultaneously.

The DPrSQ neat and blend films both demonstrated a loss of crystallinity and aggregate intensity upon annealing with a concurrent increase in monomer intensity. Without the stabilizing influence of the hydroxy groups, such short chain lengths were

unable to interact to create crystal packing structures, leaving instead a solid solution of randomly orientated molecules. The $DPrSQ(OH)_2$ neat and blend films conversely demonstrated a very high degree of crystalline order, which can be attributed to the presence of the hydroxy groups controlling the formation of crystals through hydrogen bond-mediated crystal packing. There are two crystal phases present in the $DPrSQ(OH)_2$ neat and blend films, and there is a clear transition between them at 150°C. There is not a significant change in the type or amount of aggregate that is being formed however, but this is explained as the aggregate being highly localized onto dimers as opposed to extended over crystals, thus not being impacted by the change between crystal phases.

The DBSQ series was shown to be quite remarkable, and actually demonstrates the intermediate state between the highly localized aggregates and highly crystalline structure of the $DPrSQ(OH)_2$ and the more delocalized aggregates, and somewhat crystalline structure of the $DiPSQ(OH)_2$. . In this scenario, the DPrSQ is kinetically and thermodynamically favored to create amorphous domains of randomly interspersed monomers, because the chains are not long enough to interact with each other without steric hindrance or repulsion from one central squaraine moiety to another. There are no mitigating OH groups present on the DPrSQ, so it disperses during the spin coating process into something resembling a homogeneously mixed, randomly oriented, solid solution. When the DiPSQ is considered, there is both crystalline order and aggregation formation because the chains are long enough to interact in a kinetically favorable way during the spin coating process, that then becomes thermodynamically favorable during annealing. Because the DBSQ is truly in between those two extremes in terms of self-assembly, then the spectra that has been acquired is expected. It is a mix of randomly

orientated solid solution, as well as regions that are composed of kinetically favorable dimers as well as thermodynamically favorable dimers, where the dimer is not large enough to create the long-range order required to achieve measurable crystallinity.

Finally, the DiPSQ series shows the current "best" squaraine to be the $DiPSQ(OH)_2$, because of its ability to form all three donor species, and give a blend of both crystalline and amorphous domains. The next section gives an in-depth full matrix study that was composed of over 1000 devices to determine exactly what the optimum device preparation conditions would be for this squaraine.

5.2. Device Performance

5.2.1. $DiPSQ(OH)_2$

5.2.1.1. Full Matrix Study

5.2.1.1.1. Goals of the Study

Preliminary data (Qimeng Li) on a 1:2 wt% blend ratio of DiPSQ[OH]2:PCBM provided interesting results that were to be reproduced, with additional annealing temperatures and complementary current voltage data missing from the previous work. This blend ratio and annealing study fits into the larger blend ratio/annealing study for DiPSQ[OH]2:PCBM that will attempt to give a comprehensive picture of (i) the impact of the PCBM amount on device performance, and (ii) the impact of different annealing temperatures on device performance. It is hypothesized that the PCBM concentration will have an impact on the morphology/crystallinity of both the homogenous regions of the device as well as the bulk heterojunction interface, which will impact the device

performance. Different annealing temperatures could change the amount and type of crystallization that is able to occur with additional significance to device efficiency.

5.2.1.1.2. Results

One of the main results of this study was a realization that the device area size impact on performance is a non-trivial problem. For the purposes of the summary results, only medium area (0.0962 cm2) devices will be considered, because it is important to be able to compare across a large section of films due to the extent of the full matrix study. Description and results of the device area size impact will be offered later in the section.

5.2.1.1.2.1. Blend Ratio Study

The concentration of PCBM was varied from 33 weight % to 75 weight %. It was expected that increasing the [PCBM] would have a positive impact on the short circuit current, because of the PCBM's relatively high electron mobility. However, the positive impact will have a limit because the presence of too much PCBM will create shunts in the device. Additionally, the PCBM will have an impact on the squaraine's ability to form aggregates and larger crystal domains, but the extent of that was unpredictable.

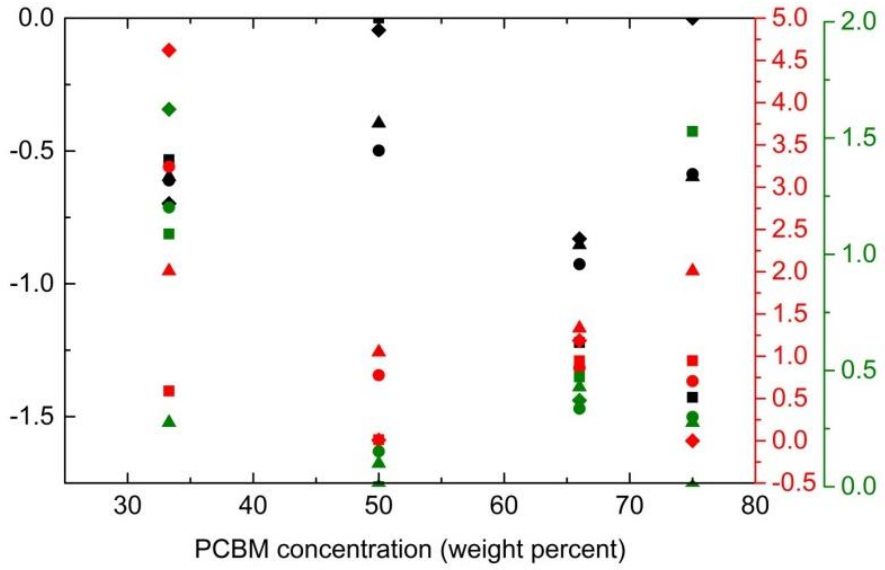

Figure 30 shows a full set of medium area devices prepared at a variety of PCBM concentrations.

The left black y-axis shows the measured short circuit current in $mA*cm^{-2}$, and all black data points correspond to that axis. The right red y-axis corresponds to the measured open circuit voltage in V, and all red data points correspond to that axis. Finally, the right green y-axis corresponds to the measured power conversion efficiency as a percentage, and all green data points correspond to that axis. The square data points are unannealed devices, the circle data points are devices annealed at 150°C, the triangle data points are devices annealed at 165°C, and the diamond data points are devices annealed at 180°C. This graph is only useful to see the true extent of the different results that can be obtained by varying a small parameter set; it doesn't allow for a clear picture of any trends that may be present. In order to examine those trends, we will examine the impact of PCBM concentration on the three selected figures of merit: short-circuit current (Jsc), open-circuit voltage (Voc), and power conversion efficiency (PCE). These figures of merit were chosen because they are easily comparable across a wide sample of

devices, and should have self-consistent results when comparing identically prepared devices.

As expected, and shown in Figure 31, high amounts of PCBM result in an enhanced short circuit current.

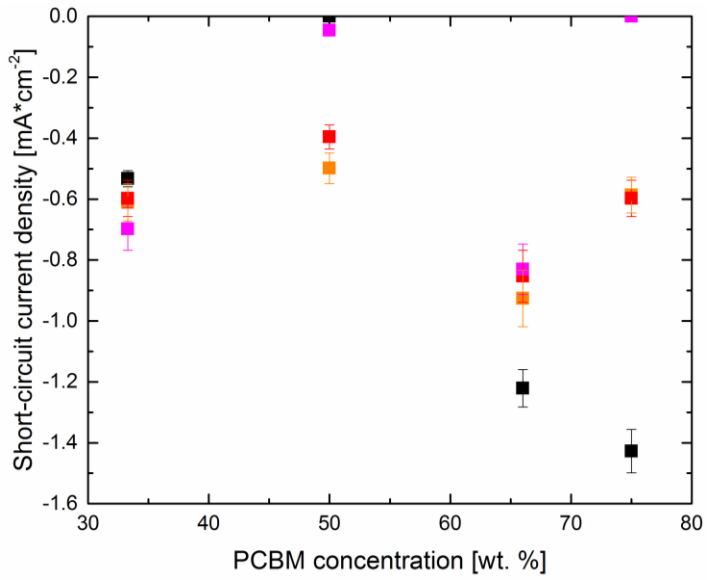

Figure 31 Each symbol is averaged and shown with error bars; black is unannealed, orange is 150°C, red is 165°C, and magenta is 180° C annealing temperature.

The increase in short circuit current with increasing PCBM concentration is only apparent for unannealed devices. This is likely because before annealing the PCBM and squaraine domains are of a size that allows for the greatest amount of charge extraction. Based on the data, it would appear that when greater amounts of PCBM are present, the process of charge photogeneration is more efficacious. If there are more domains that are of the ideal size for charge extraction then it makes sense that the increasing amount of PCBM will increase the short circuit current. The remaining annealed devices do not

appear to have a statistically significant trend of increasing or decreasing short circuit current density, with the current.

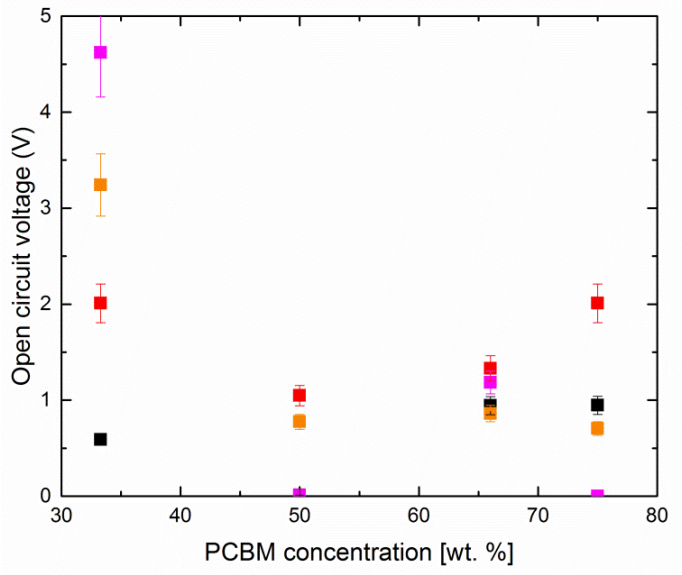

Figure 32 Each symbol is averaged and shown with error bars; black is unannealed, red is 150°C, orange is 165°C, and magenta is 180°C annealed devices.

Figure 32 shows a very interesting result: devices with low PCBM concentration (33%) have dramatically different Voc dependent upon their annealing temperature. At PCBM concentrations above 50%, the Voc is no longer as different. This indicates that the dramatic differences in Voc are likely a result of the squaraine forming large crystalline domains; as the PCBM concentration increases the domain size of the squaraine will decrease. If the Voc is considered as strictly a materials property, then the larger crystals that form with higher annealing temperatures must have much deeper HOMO levels than the smaller crystalline domains, indicating a high amount of long range order that serves to stabilize the squaraine. If the Voc is considered to be the result of a multijunction (discussed further in a later section), then this indicates that as the device is annealed

when small amounts of PCBM are present, more multijunctions are able to form in such a way that their voltages become additive. As the amount of PCBM is increased, a multijunction array in series becomes less likely and so the voltages drop. They are slightly increased at very high concentrations of PCBM because the probability of a series multijunction interacting with a PCBM molecule or cluster is very high.

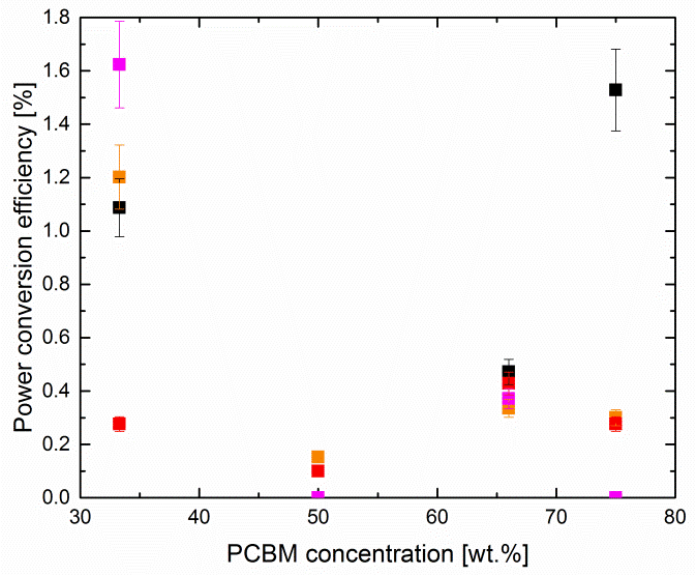

Figure 33 Each symbol is averaged and shown with error bars; black is unannealed, red is 150°C, orange is 165°C, and magenta is 180°C annealed devices.

Figure 33 shows the changes in power conversion efficiency for these devices. We see that at low concentrations of PCBM, the performance is generally improved with annealing. The only time that is not true for low concentrations of PCBM is when the device is annealed at 150° C. At high concentrations of PCBM, only the unannealed devices have good PCE values (>1%). It is also important to point out that at the 1:2 blend ratio (which has been the "standard" blend ratio used) we do not see a significant change in PCE no matter the annealing temperature, beyond a slight drop in performance

when comparing annealed to unannealed devices. Frankly, this graph doesn't show what would be desired, which are clear trends that indicate the best PCBM concentration to use when making DiPSQ(OH)$_2$ devices. This could mean that the factors that are influencing the PCE (preferential BHJ morphology, ideal ohmic contact between active layer and electrodes) are not in a one-to-one relationship with the PCBM concentration, which would not be a complete surprise. It should be noted however that other groups have not found "neat and tidy" relationships either, and we often rely on complicated explanations in order to justify this lack of relationship. Figure 83 shows a graph taken from Forrest et al [75] where they rationalize changes in device performance upon changing blend ratios by examining the RMS roughness of the films.

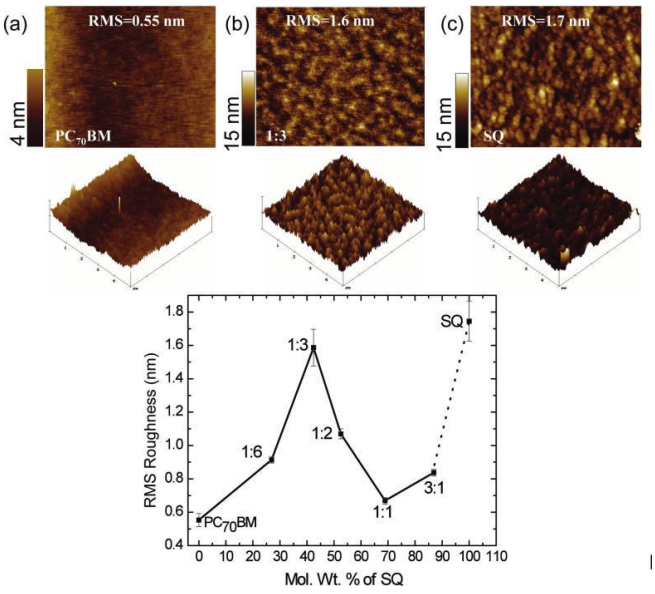

Figure 34 Atomic force microscope topographic and 3D images of (a) pure $PC_{70}BM$, (b) 1:3 SQ:$PC_{70}BM$, and (c) pure SQ films deposited on indium tin oxide coated glass. (d) the RMS roughness versus the molecular weight ratio of squaraine blended into $PC_{70}BM$ taken from the AFM data.

At this time we do not have the RMS values for the blend ratios we have studied to compare with those found in literature, but it is worth nothing that the trend is still not a "neat and tidy" trend. Our lack of neat trends could also result from insufficient data collection, or from one of the solutions and subsequent film series being contaminated or poorly prepared. While every effort is made to not have that happen, it must still be stated as a possibility. Until a way is found to make these films that the devices are prepared on much more homogeneous, this will be a continuing issue.

5.2.1.1.2.2. Annealing Temperature

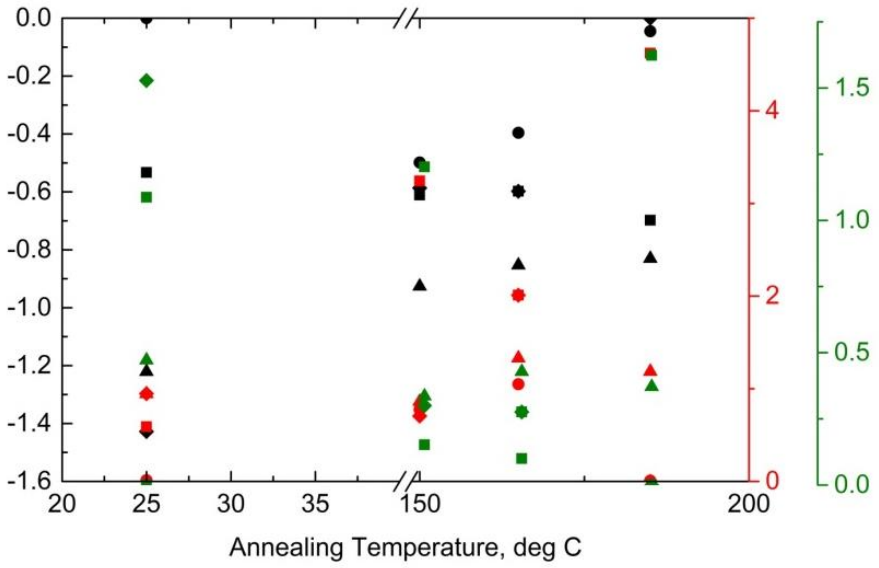

Figure 35 shows a full set of medium area devices prepared at a variety of annealing temperatures.

The left black y-axis shows the measured short circuit current in mA*cm-2, and all black data points correspond to that axis. The right red y-axis corresponds to the measured open circuit voltage in V, and all red data points correspond to that axis. Finally, the right

green y-axis corresponds to the measured power conversion efficiency as a percentage, and all green data points correspond to that axis. The square data points are 1:0.5 SQ:PCBM devices, the circle data points are 1:1 SQ:PCBM devices, the triangle data points are 1:2 SQ:PCBM devices, and the diamond data points are 1:3 SQ:PCBM devices. Again, because it is impossible to pull actual trends from this graph, we will look at a series of graphs for each different variable of interest as done in the Blend Ratio section.

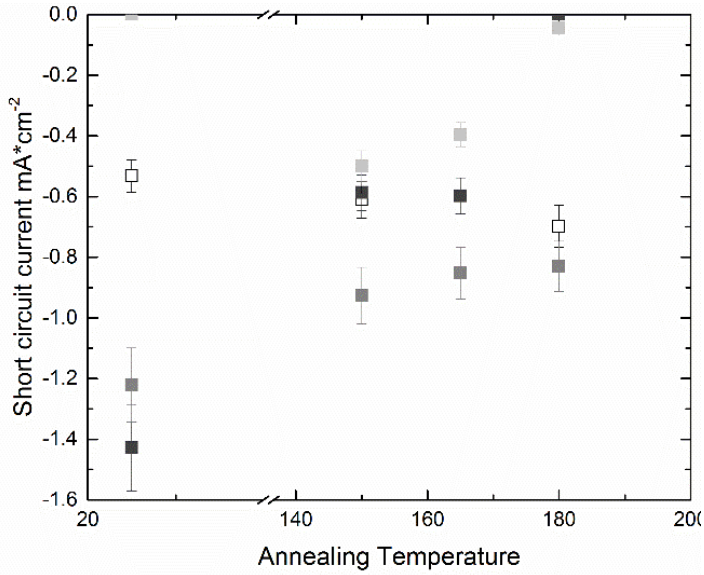

Figure 36 Averages are shown with error bars; open squares are 1:0.5 SQ:PCBM, light grey squares are 1:1 SQ:PCBM, dark grey squares are 1:2 SQ:PCBM, and black squares 1:3 SQ:PCBM.

While there was not a distinctive trend in Figure 33 (showing the relationship between short-circuit current and PCBM concentration), Figure 36 shows a statistically significant correlation between the short circuit current and the annealing temperature, at a variety of PCBM concentrations. For concentrations of >50% PCBM, any annealing causes a loss of short circuit current. At concentrations of <50% PCBM, annealing causes

a slight increase in short circuit current. The change in short-circuit current is most obvious going from unannealed to 150°C; increasing the temperature from there continues to have an impact but the trend begins to level off. Two key conclusions can be drawn from this. First, the fact that there is only a trend present when we are examining the annealing temperature indicates that the PCBM concentration is not the driving force for changes in short circuit current, but rather the annealing process itself. Second, the unannealed devices are the best performing. This is consistent with the spectral response work and with our recent publication. The annealing process therefore is responsible for changing the morphology in a way that is "non-preferential" for higher J_{sc} values. There are two regions within which this could happen: in the homogeneous domains of donor and acceptor materials, and at the bulk heterojunction itself. High short-circuit currents require efficient exciton dissociation as well as homogeneous domains of material with low trap density and reasonable charge mobility. Annealing can impact both of those things; if the increasing annealing temperature is changing the domain sizes, then excitons formed may not be able to reach the bulk heterojunction as the domain size is increasing. Figure 86 shows results incorporating device data and AFM data that tentatively supports this first explanation. The second thing which annealing can impact are the homogeneous regions of donor and acceptor.

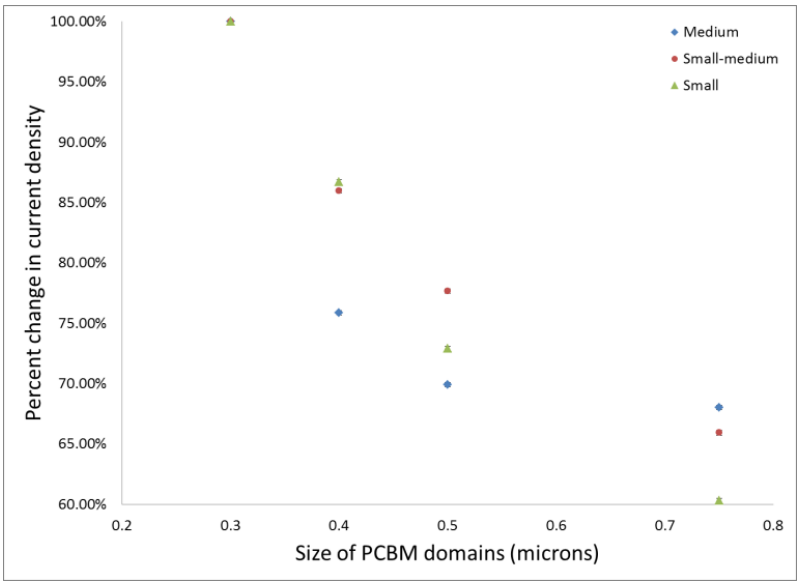

Figure 37 The y-axis shows the percent current relative to the initial current. As an example, the medium device with PCBM domains of 0.4 microns has approximately 75% of the original current density for an unannealed device (0.3 micron PCBM domains).

We know from neat thin film squaraine work that annealing at increasing temperatures will create large crystalline squaraine regions. This could be what is occurring in the 33% PCBM solar cells that show increasing short circuit with annealing temperature; as the crystallinity increases, the trap density decreases thereby increasing the charge carrier mobility in the squaraine region. Since the amount of PCBM is smaller than the amount of squaraine, ideal domain sizes for efficient exciton dissociation can still be formed. In higher PCBM concentrations, detrimental morphologies could result from annealing if the PCBM domains are aggregating together in an amorphous way that doesn't promote efficacious free carrier transport.

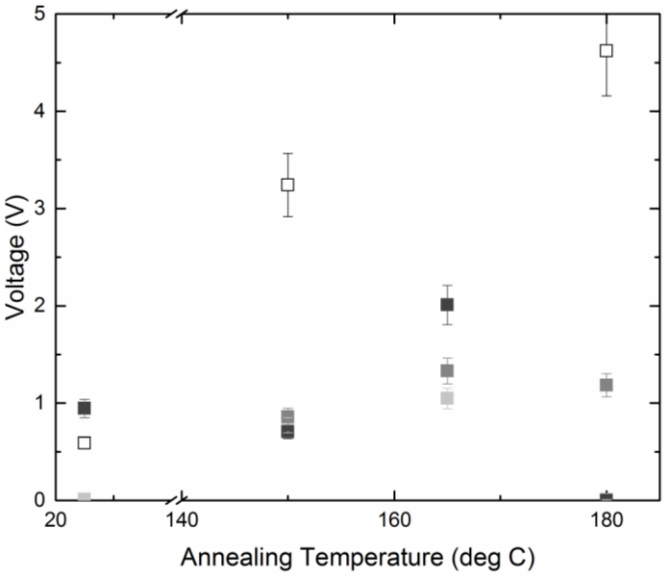

Figure 38 Averaged values are shown with error bars; open squares are 1:0.5 SQ:PCBM, light grey squares are 1:1 SQ:PCBM, dark grey squares are 1:2 SQ:PCBM, and black squares 1:3 SQ:PCBM.

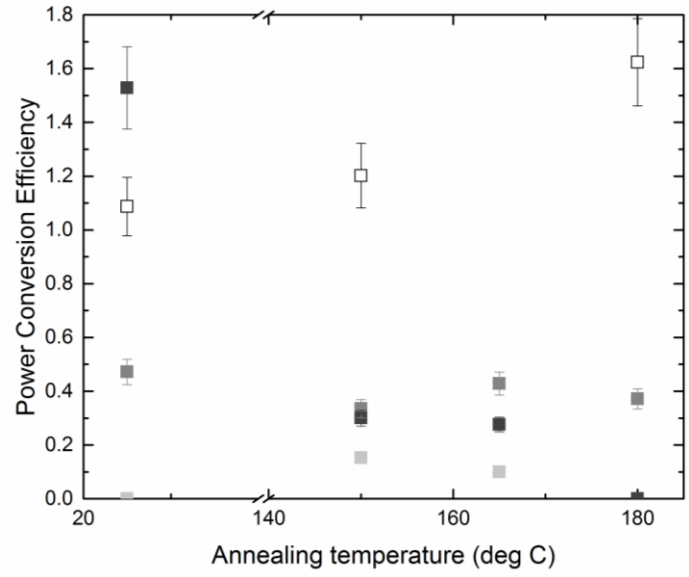

Figure 39 All data is averaged and shown with error bars; open squares are 1:0.5 SQ:PCBM, light grey squares are 1:1 SQ:PCBM, dark grey squares are 1:2 SQ:PCBM, and black squares 1:3 SQ:PCBM.

There is another distinctive trend in Figure 38 that was also reflected in Figure 32; the devices with low PCBM content showed very dramatic increases in the Voc upon annealing.

The power conversion results shown in Figure 39 are slightly more conclusive for annealing temperature trends than they were for PCBM concentrations (Figure 33). The low PCBM concentration devices demonstrate a steady increase in PCE with annealing temperature that is almost solely driven by their Voc. The high PCBM concentration devices conversely perform very poorly when annealed. We can tentatively conclude from this that the annealing process is driving the changes in device performance; whether those changes are positive or negative is mediated by the amount of PCBM that is present. Because this is only apparent when comparing the two extremes, it doesn't necessarily mean that this a trend that will hold up over a variety of materials, but it is worth keeping an eye out for as we move forward in device fabrication.

5.2.1.1.2.3. Degradation

A set of unannealed 1:2 SQ:PCBM devices were left out in the lab to test what happened when they were exposed to air. They were kept in plastic thin film holders on the floating laser table in the Photovoltaics Characterization Lab where they were also exposed to natural light at a regular light cycle for the month of December. Over 6 days they received approximately 50 hours of natural light.

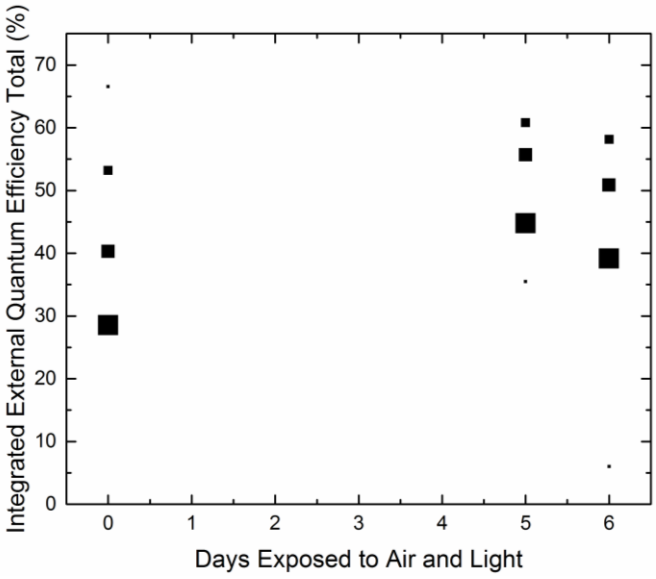

Figure 40 Summary of degradation. The relative size of the data points indicates the device area for each data point. This work was performed on 1:2 SQ:PCBM devices.

Interestingly, the devices appear to actually increase their spectral response after air and light exposure. Only the small area devices lost EQE. The remaining devices did not.

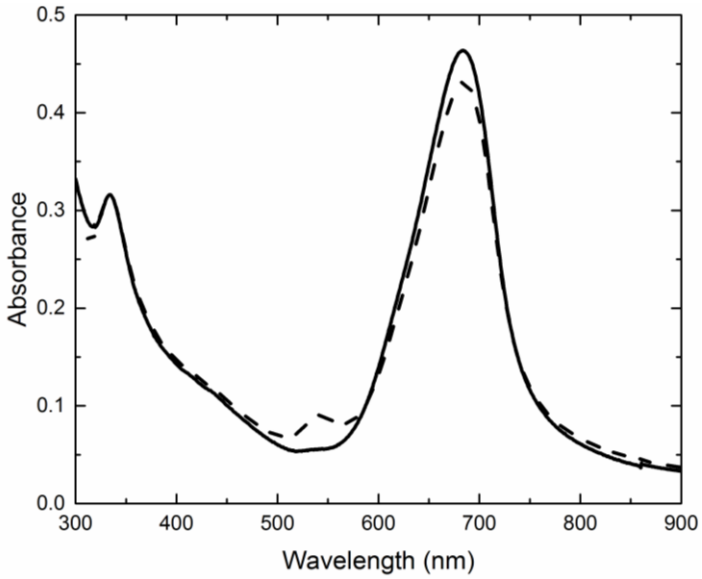

Figure 41 Solid line shows the initial DiPSQ(OH):PCBM film, and the dashed line shows the same film after 45 days of air and light exposure.

We expect that the squaraines will not be photoreactive, and we also expect that they will have a greater stability in air than the P3HT:PCBM blends, based upon previous work done showing no absorbance changes in thin films as shown in Figure 41. Figure 42 shows actual EQE data for small and large devices over time.

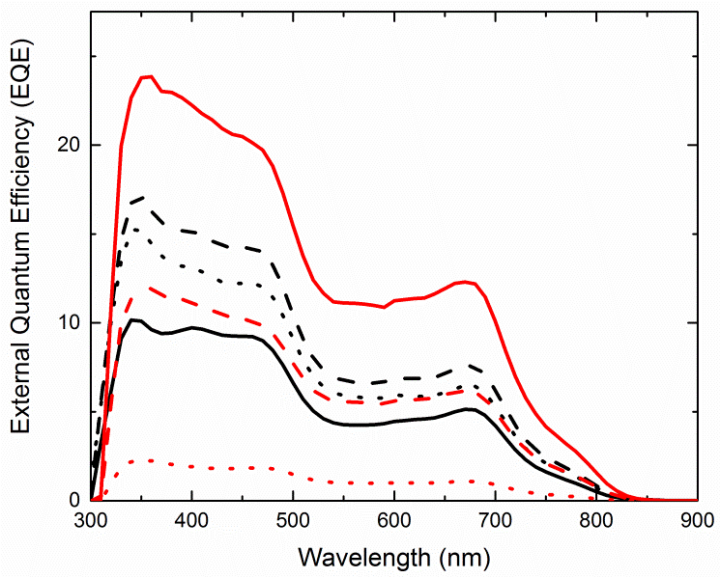

Figure 42 Raw data for degradation. Black indicates large devices, red indicates small devices; solid line is 0 days of exposure, dashed line is 5 days of exposure, and dotted line is 6 days of exposure.

In order for more reproducible conclusions to be drawn from this data, there needs to be a more comprehensive degradation study performed. The devices were only remeasured because they had been left out over a weekend unintentionally. Unfortunately I was not able to continue the testing because there was a backlog of devices to be tested, and the spectral response equipment was required by other users. Despite the paucity of data, the degradation of these devices is certainly "study-worthy", because device lifetime has become a major focus for increasing the commercializability of OPV.[18,19] If we can show

that our materials degrade at a much slower rate than other materials with comparable efficiencies that would be advantageous.

5.2.1.1.2.4. Device Size Area Impact

Each film has 11 devices made on it by thermally evaporating aluminum contacts. These contacts are each circular, and are distributed quasi-randomly upon each film. The phrase quasi-random is used as a descriptor because the contacts are evaporated using a premade mask, but this mask allows for evaporation of different sized devices over the entire area of the film, without any sense of prejudice or choice on the part of the experimenter as to where a specific device will be made. This allows for a more realistic sampling of the film's morphology over a very large scale relative to the device thickness.

It was expected that as devices were made smaller, they would become more efficient. The reason for this expectation was not apparent to me, and I have had a very difficult time explaining why it would be the case. My initial hypothesis was that the film is made up of preferential and non-preferential morphologies. If, hypothetically, the ratio of "good" to "bad" is greater than 1 :1, (like 2:1 or 3:1) then a smaller device is going to encounter more good than bad, and would therefore be more efficient. This doesn't really make a lot of sense, and was therefore discounted as a valid hypothesis. Next, I thought about the aspect ratio of the devices. Even for the smallest device, there is going to be an aspect ratio of 375:1 (area:thickness) which would indicate that the area of the device isn't going to be meaningfully impacting the current until it gets very very small. However, this neglected an important parameter in the generation of current, by assuming

that all of the current that is generated is flowing unidirectionally through the device from top to bottom. After extensive literature searching, I found that this is not going to be the case when PEDOT:PSS is used as a buffer layer. [116] The reason for this as described by Lee et al is that the PEDOT:PSS has a very strong lateral conductivity, which leads to the collection of unexpected currents from the perimeter of the device. This finding has led to the discovery that the trends for the squaraine devices when compared to P3HT:PCBM devices are not the same, with the squaraine devices showing a much greater change as a function of device size than the PCBM. This is being discussed in more detail with a proposed paper outline titled "Mixed interfacial layers and their impact on short-circuit current in OPVs". Figure 43 shows the trend in the squaraine devices.

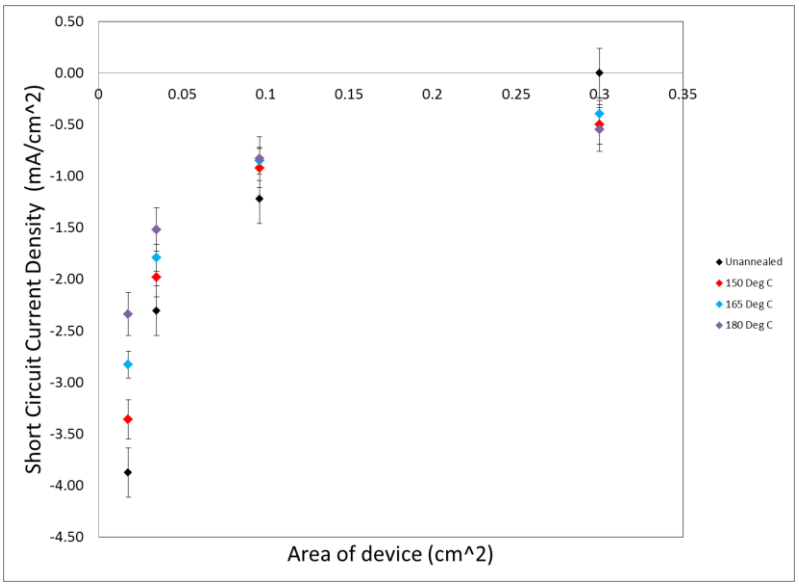

Figure 43 A plot of short-circuit current density as a function of device area for a variety of annealing temperatures.

The current operating hypothesis for the difference in the short circuit in the squaraine devices is that there is a strong perimeter effect created by the PEDOT:PSS, and

the PEDOT:PSS and squaraine are forming a mixed interfacial layer that is different from the PEDOT:PSS and P3HT mixed interfacial layer. This mixed interfacial layer would also be impacting the open-circuit voltage. We would expect the impact on Voc to be uniform, no matter the device area, because the effect is to change the built-in potential and this should not be size dependent. However, as shown in Figure 44, this does not appear to be the case.

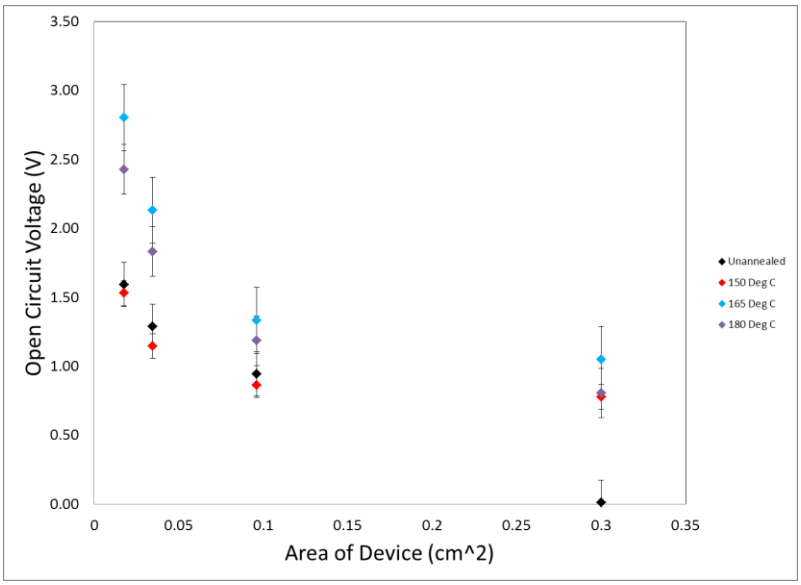

Figure 44 Open-circuit voltage trends with different areas and annealing temperatures.

As the device area decreases, the Voc increases. The highest Voc is achieved in all cases with annealing at 165 deg C. This could indicate a temperature at which the mixed interfacial layer is either most crystalline or is at the most preferential mixture for rectification of charge carriers. If Voc is considered as a material property, then the 165 deg C indicates the highest built-in potential for the mixed interfacial layer, or in other words, the most optimal ionization potential. Figure 94 shows the resultant impacts on efficiency from these gains in Voc and Jsc.

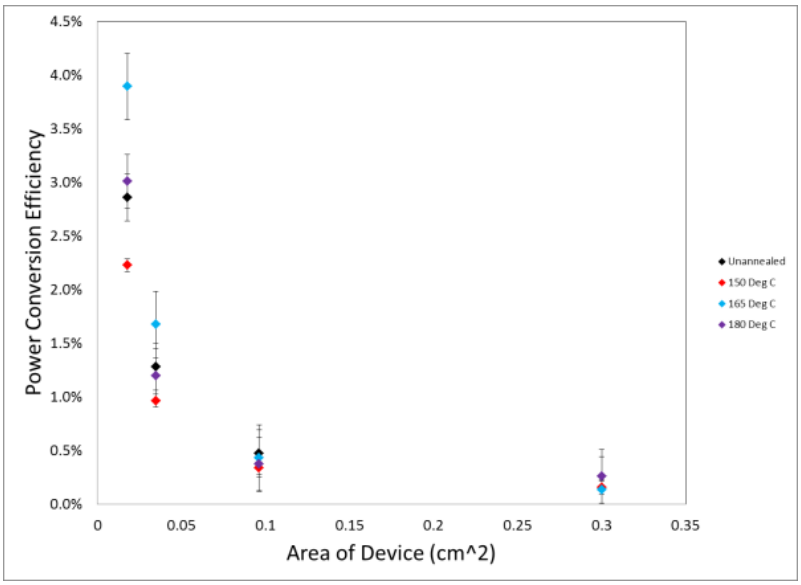

Figure 45 Efficiency as a function of area.

5.2.1.1.2.5. Light Biasing

In traditional diodes the ideality factor is a measure of how well the diode actually follows the ideal diode equation. Information about the different types of recombination can then be gained based on the value of the ideality factor, with 1 as the best[117]. In a solar cell, the ideality factor is typically seen as a measure of junction quality as well as types of recombination which may be occurring[34]. Additionally, "a high n-value not only degrades the FF, but since it will also usually signal high recombination, it gives low-open circuit voltages." In the devices measured in this report, we had the opposite occur with high fill factors and very high open circuit voltages. In order to explain the Voc, the relationship between Voc and ideality factor can be examined.

If Voc is considered not as a material property, but rather as a reflection of the relationship between the saturation current, light-generated current, and the Voc then a different possibility can be examined.

$$V_{OC} = \frac{nkT}{q} ln\left(\frac{I_L}{I_0} + 1\right)$$

In this equation, I_L is the light generated current, k is the Boltzmann factor, T is the temperature, q is the charge, n is the diode ideality factor, and I_0 is the saturation current. The saturation current can be modeled as (intrinsic carrier concentration)^2 *(carrier diffusivity/lifetime)$^{-1/2}$, where carrier diffusivity is[118]

$$D_n = \frac{L^2}{\tau_d}$$

where L is the thickness of the diffusion layer (in our case ~50 nm) and τ_d is the transit time[119]. For our devices, D_n is approximately 2.5E-09 m^2/s. If the lifetime for our materials is assumed to be 2 ns, and the carrier density is assumed to be in the range of 10^{-6} to 1 cm^{-3}, then the saturation current is in the range of 8E-11 A to 8E-3 A. Returning to equation 1 and using that range of saturation current the modeling results are shown in Figure 46.

In order for this model to work, the ideality factor actually has to increase (move away from 1, which is ideal) as the device area decreases. It has been shown in inorganic semiconductors that high ideality factors (n>2) are possible when a system of heterojunctions is present[120]. If we were to consider our bulk heterojunction of J- and H-aggregates and monomers each interacting with the PCBM, then we would effectively have three diodes, which is very similar to how the authors of ref. 4 look at their system. This is shown in Figure 47, which is taken directly from the paper.

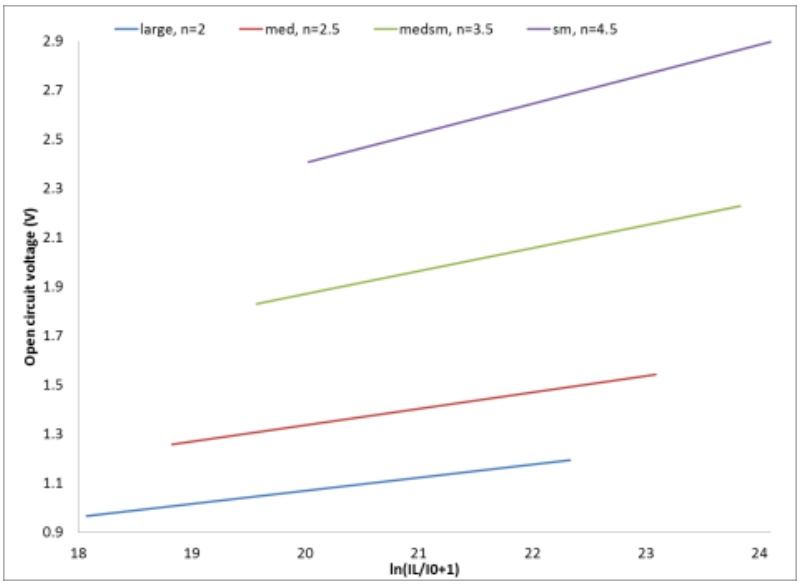

Figure 46 Ideality factor modeling.

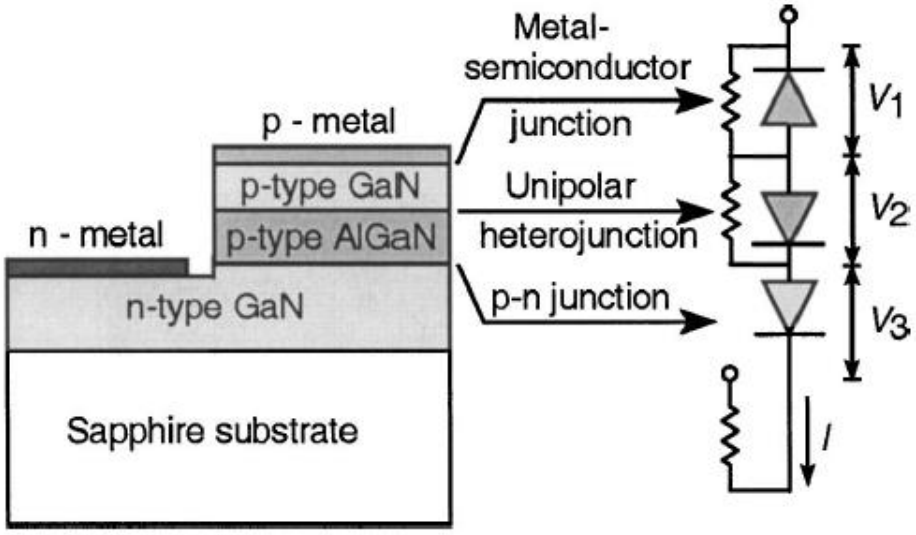

Figure 47 Schematic structure of p-n junction diode and equivalent circuit consisting of three diodes.

5.2.1.2. External Quantum Efficiency and Marcus-Hush Theory

5.2.1.2.1. Goal of the Study

In this section, I show that increasing the annealing temperature in our $DiPSQ(OH)_2$ films results in enhanced absorption and crystallinity, quantified using solid-state absorbance, thin-film x-ray diffraction (TFXRD). Annealing should thus have a positive impact on exciton generation and diffusion efficiencies[121–123] as well as free charge carrier generation and charge collection efficiencies[124,125]. Localized charge carrier generation is measured using transient microwave photoconductivity. Despite the expected positive impact, when the spectral response of devices made with and without annealing is examined, the results indicate that annealing has a deleterious effect on the external quantum efficiency (EQE) of the squaraine region.

After examining each potential cause for the drop in efficiency, we hypothesize that poor EQE results, measured after annealing, result from a drop in the overall rate of electron transfer during the exciton dissociation. This could occur from either a decrease in the driving energy for electron transfer or a change in the electronic coupling matrix element between the reactant state and the product state as described by Marcus-Hush theory[49,126,127]. Both changes could also occur simultaneously and work in concert or opposition to each other; in this work we consider the origins of these changes.

We find annealing causes no phase separation of the small molecules, but instead a subtle change in the interplanar spacing and size of the donor crystals, and propose a resulting displacement of the normal phonon mode oscillation and a change in the dipole-

dipole interaction environment. This will change the energy level of the charge transfer state, resulting in a change in driving energy for electron transfer, as well as a change in the electronic coupling. Therefore, despite the positive effects of enhanced NIR absorption and crystallization, the limiting factor in our EQE measurement is electron transfer during exciton dissociation. This determination could help refocus research efforts onto materials which have high potential for larger electron transfer rates, given that it can play such a significant role as a bottleneck in bulk heterojunction organic photovoltaic cells.

5.2.1.2.2. Results and Discussion

The absorbance spectrum of a DiPSQ[OH]$_2$:PCBM film is presented in Figure 48 along with a corresponding absorbance spectrum of the squaraine in dilute chloroform solution. Three distinct features are observed for the film and are assigned to respectively, a J-mer peak centered at 748 nm, an H-mer peak centered at 564 nm, and a monomer peak centered at 679 nm, which is shifted from the corresponding monomer peak in solution at 648 nm. These assignments are described in more detail elsewhere[93,108]. The colored background highlights the distinctness of the states contributing to absorbance for each of these three regions.

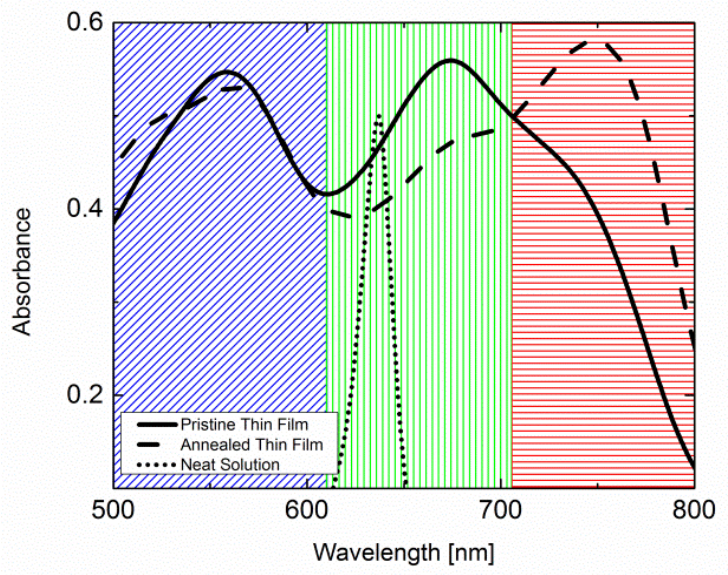

Figure 48 Absorbance spectra of the DiPSQ[OH]2:PCBM blend, both pristine (solid line) and annealed (dashed line) as well as solution (dotted line). The regions illustrated within the plot correspond to the assigned H-mer region (blue diagonal lines), monomer region (green vertical lines), and J-mer region (red horizontal lines).

The spectral properties of this and similar squaraine films have been shown to change as a function of heat treatments for blended films, as illustrated by the dashed line in Figure 48. Corresponding absorbance peak height data from a series of DiPSQ[OH]$_2$:PCBM thin films are shown in Figure 49, illustrating an increase in peak height for the J-mer upon annealing and the concurrent decrease in peak height for the monomer regions. The increasing J-mer/decreasing monomer trend has been shown to correlate with an increase in film crystallinity measured with thin film X-ray diffraction[106,107]. The increase in J-aggregate population was expected to improve device efficiency, given recent observations that suggest J-aggregation empirically leads to increased power conversion efficiencies[108,128]. In addition, increasing the NIR absorbance of the films is a known method for improving efficiency, given that larger currents can

theoretically be obtained in spectral regions of high photon flux in the solar spectrum. Thus, both the increased absorbance and the enhanced crystallinity after annealing were expected to benefit the device efficiency.

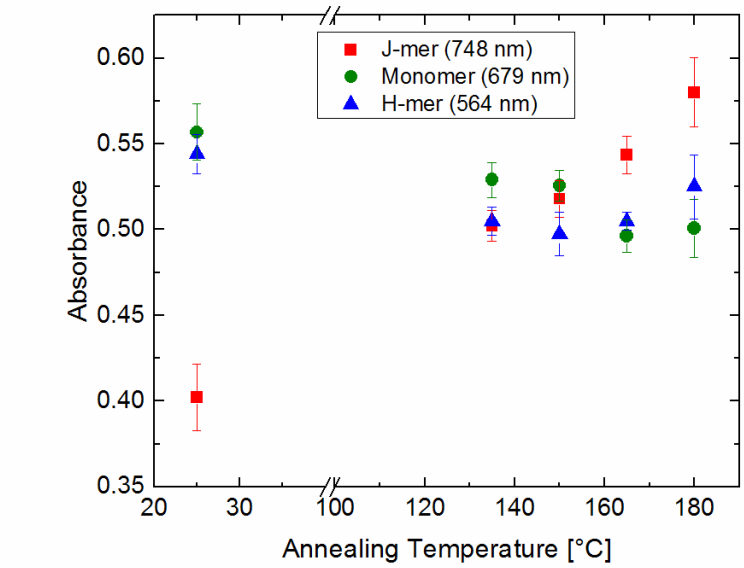

Figure 49 Absorbance peak height values for the three spectral features of interest (J-mer, Monomer and H-mer) are shown as a function of increasing annealing temperature.

A rigorous in-situ XRD measurement was made to study the changes taking place during the annealing process in a blended film, analogous to a device. The results are shown in Figure 50. All data were collected from the 7.5° 2θ peak generated specifically in the squaraine crystalline regions. Thus, only the changes in squaraine crystallinity are considered when the peak height, interplanar spacing, and coherent crystal domain size are calculated. The impact of annealing on the squaraine is illustrated through collective analysis of Figures 49 and 50. An increase in the J-mer absorbance and a decrease in the monomer absorbance are observed in figure 49, for an overall increase in absorbance of ~6% from pristine film to a film annealed at 180 °C. There is also a significant increase

(~67%) in extent of crystallinity of the squaraine with increasing temperature, as seen in Figure 50, associated with the peak height increase. In addition, increasing annealing temperature leads to an increase in size for the crystalline regions in the squaraine blend as evidenced by the increase in τ, while the interplanar spacing of the squaraines decreased[106]. After cooling the annealed film the increased crystallinity, domain size and reduced interplanar spacing remains as demonstrated in the second set (open symbols) of data recorded at 30°C.

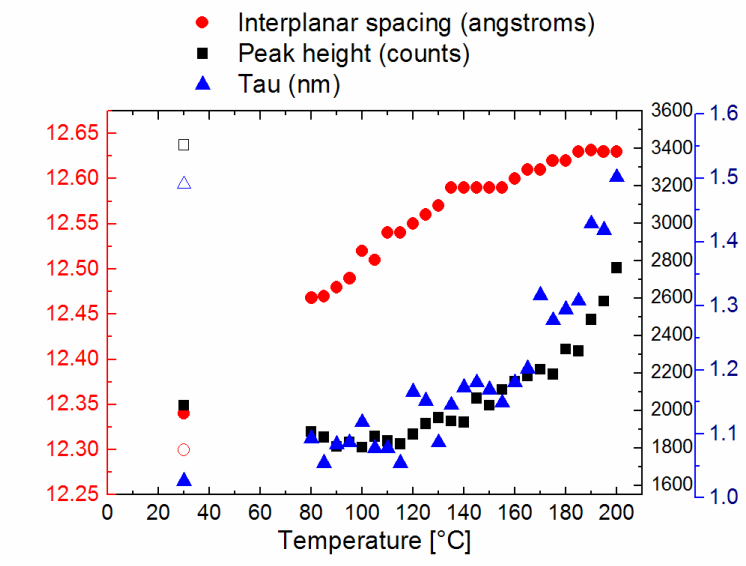

Figure 50 TFXRD data taken on a device analogue film of DiPSQ[OH]2:PCBM. The LHS red y-axis corresponds to the interplanar spacing (red circles), the inner RHS black y-axis corresponds to the peak height (black squares), and the outer RHS blue y-axis corresponds to the coherent crystal domain size, τ (blue triangles). The open symbols for each data set represent the measurement taken after the annealing, once the films had been cooled back to 30°C.

As introduced above, this enhancement of crystallinity is expected to result in better exciton diffusion efficiency and increased free charge carrier mobility in the squaraine region. Both exciton diffusion efficiency and free charge carrier mobility will be enhanced because there will be fewer defect sites for recombination[129]. AFM results on similar films, published elsewhere[106], demonstrate a decreasing RMS roughness of the organic active layer surface with increasing annealing. Since AFM is measuring the surface upon which the aluminum electrode will be deposited, a decreasing RMS roughness will correlate with a smoother deposition of the contact. A smoother interface between organic and electrode would reduce the amount of shunting thereby enhancing the charge collection efficiency[130] and also contributing to an expected increase in power conversion efficiency. In summary, exciton generation and diffusion, charge transfer state dissociation, and charge collection should all be improved with enhanced crystallinity and aggregation and efficiency is expected to increase.

External quantum efficiency (EQE) data for pristine and annealed devices were measured to test for the expected increase in efficiency with annealing, and are shown in Figure 51. A significant drop in EQE for the squaraine region (510-800 nm) is shown for the annealed film. It is also important to note that there is very little change in the PCBM region (300-450 nm). The simplest explanation for a loss of EQE with annealing and consequent crystallization would be phase separation, associated with a reduction of total surface area of heterojunction. However, since the PCBM EQE does not change significantly upon annealing, this explanation is inconsistent; if phase separation tended towards a bilayer geometry then charge generation resulting from photoexcited PCBM excitons would similarly be reduced because of the smaller heterojunction surface area.

Instead, there is only a dramatic decrease in charge generation resulting from squaraine absorption but no change associated with PCBM absorption.

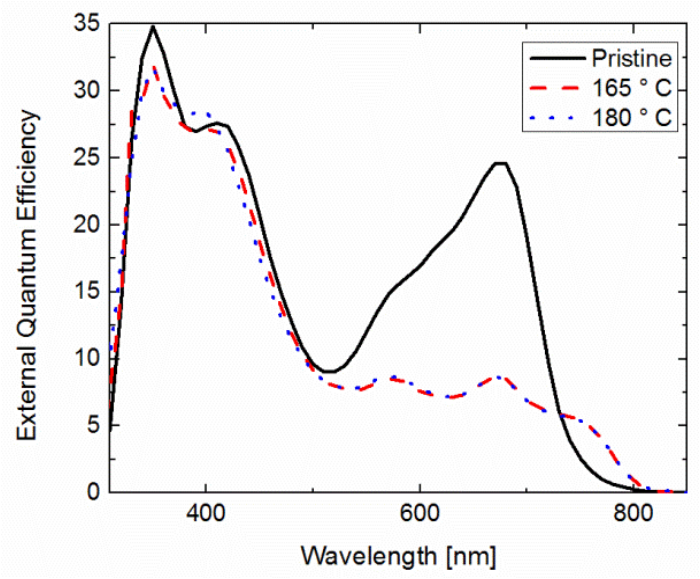

Figure 51 The black line shows the as-cast DiPSQ[OH]2 device EQE. The red dashed line is an annealed device at 165°C, and the blue dotted line is an annealed device at 185°C.

Given that the absorption of the film changes with the annealing process, it is instructive to look at an EQE plot that is corrected and normalized to the absorption and this data is shown in Figure 52. Despite correcting the EQE for the absorbance changes (a drop in the monomer region and an increase in the J-mer region), there is still a significant difference between the pristine films and the annealed films. This further indicates that the loss in efficiency in the squaraine region is not due to changes in absorbance and, again, enhancing crystallinity would be expected to produce favorable results for the other steps, as described above.

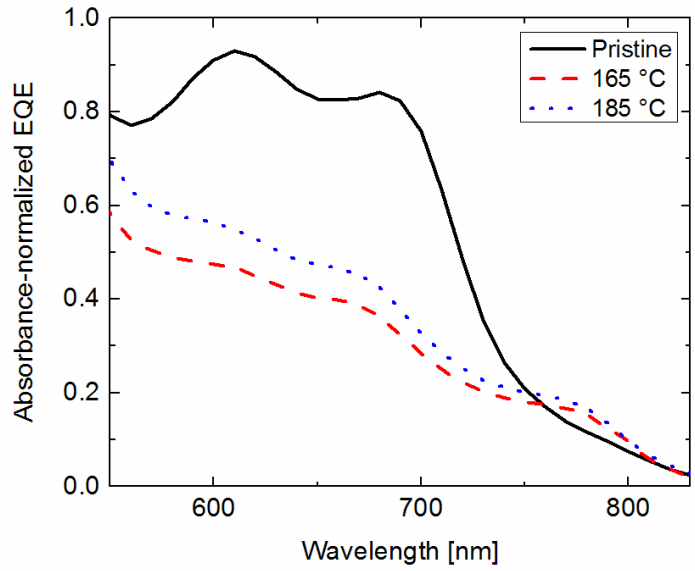

Figure 52 EQE data, normalized using the calculated absorbance efficiency of the squaraine.

We conclude, therefore, that the decrease in performance is not due to changing populations of excited states and that it does not result from changes in charge collection efficiency or exciton diffusion efficiency since improved crystallinity would undoubtedly *enhance* the associated efficiency – not reduce it. The two remaining efficiency contributors to examine are exciton dissociation efficiency and the resultant charge carrier generation efficiency.

Charge carrier generation efficiency was measured for a blended film with very low levels of PCBM (<1 wt. %) by examining the transient microwave conductivity of pristine and annealed films of DiPSQ[OH]$_2$. This measurement technique is described in detail elsewhere[38–40] and offers a contactless method of measuring photoconductance transients to extrapolate information about the mobility of the charge carriers that are present . In the devices, there is more than twice as much PCBM as squaraine but for these low-PCBM

samples the goal was to "freeze" any electrons generated through exciton dissociation so that only the generated holes would be able to move and thereby generate a transient response in the TRMC measurement. The figure of merit from the measurement is the yield-mobility product, $\phi\Sigma\mu$. This is the density-weighted average local mobility of both electrons and holes multiplied by the yield. This quantity is calculated from the initial amplitude of the microwave photoconductance transients at the lowest measureable excitation fluence. Exciting the sample at 540 nm will generate excitons predominately in H-mers, while exciting the sample at 600 nm will generate excitons predominately in monomers. Exciting the sample at 450 nm will generate excitons solely in the PCBM regions, assumed to be isolated islands unable to transfer charge (very low electron mobility) because of the low levels of PCBM present in the sample.

The differences in yield-mobility products with increasing pump fluence for 450, 540, and 600 nm excitation of both pristine and annealed SQ:PCBM films are shown in Figure 53. The data sets are all within a narrow range of yield-mobility product ($9.0\text{x}10^{-6}$ - $4.0\text{x}10^{-5}$), which indicates there is no statistically significant change when comparing pristine and annealed films. This unchanging yield-mobility product could arise from two circumstances; either (i) there is no change in *both* localized spatially averaged charge carrier mobility and the quantum yield of free charges or, (ii) one is increasing while the other is decreasing.

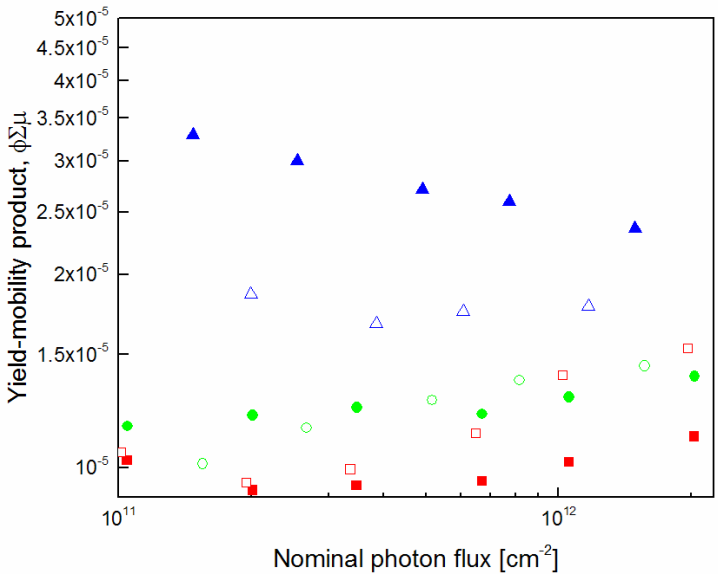

Figure 53 Time-resolved microwave conductivity data for as-cast (closed symbols) and annealed (open symbols) DiPSQ(OH)2:PCBM at excitation wavelengths of 600 nm (red squares), 540 nm (green circles) and 450 nm (blue triangles).

If neither the quantum yield of free charges nor the mobility is changing upon annealing, case (i), we would expect that the charge carrier generation efficiency is not changing markedly upon annealing and therefore we can rule this out as the reason for the drop in power conversion efficiency with annealing. With case (ii), in order for the quantum yield of free charges to change, the ionization potential of the squaraine upon annealing would need to be different. However, the EQE data indicates that the driving force for hole transfer from the PCBM remains the same because the EQE data in the PCBM region have not changed. Therefore the ionization potential of the squaraine donor cannot have changed and so case (ii) is not valid in this regard. Indeed, preliminary XPS data of neat squaraine films shows very little change in the extrapolated HOMO energy level (6.3+/-0.1 eV) of the squaraine upon annealing[131]. The conclusion from data shown in Figure 53 is that there is not a statistically significant change in either of the markers

(yield-mobility product) for charge carrier generation efficiency. This means the only step in the charge photogeneration process to which the EQE decreases can be attributed is during exciton dissociation and we explain this using a Marcus-Hush approach.

Exciton dissociation can be described as an electron transfer process. The driving energy for electron transfer, ΔG, is given by[132,133]

$$\Delta G = (IP_D - E_{EXC}) - EA_A \quad (1)$$

where IP_D is the ionization potential of the donor, E_{EXC} is the excited state energy of the exciton, and EA_A is the electron affinity of the acceptor. In the DiPSQ[OH]$_2$:PCBM device set, the electron affinity of the acceptor is a constant, because the same PCBM acceptor is used in every device. There are three "donor species" that can participate in electron transfer from an exciton; the H-mer, monomer, and J-mer. Each of these materials has a different E_{EXC}, as inferred from the absorbance spectrum of the blend film with the underlying assumption that the ground state energy does not change significantly for each squaraine species. Considering energy levels driving hole transfer from PCBM to squaraine, this assumption is strengthened because there is relatively little change in the PCBM EQE upon annealing. In addition, based on the surface structure, AFM results published elsewhere[134] suggest that the PCBM is distributed throughout the blend and therefore interacting with all three of the donor species. The PCBM hole transfer process is not impacted by changing the amount and type of donor species present in the blend and therefore the ionization potential of each of the donor species is identical. Thus, the energetics driving exciton dissociation must be dominated by the initial energy levels of the excited states on the donor species.

During exciton dissociation, the bulk heterojunction can be considered as a system with at least two distinct "initial" states, A, and one "final" state, B. The initial state, A, represented in Figure 8 as a blue-dotted(red-dashed) Gibbs energy parabola comprises the H (J) donor species interacting with an acceptor molecule, where the excitation is localized exclusively on the donor. The final state, B, represented in Figure 103 as a solid black line, comprises the same donor-acceptor molecule pair, but the excited electron has now been transferred to the acceptor species leaving the hole on the donor species. The true system is much more complex because in a bulk heterojunction there will be many of these state pairs, all interacting with each other. Additionally, the exciton's initial delocalization/localization size in the donor material will vary depending on the surrounding environment and morphology that the exciton experiences.

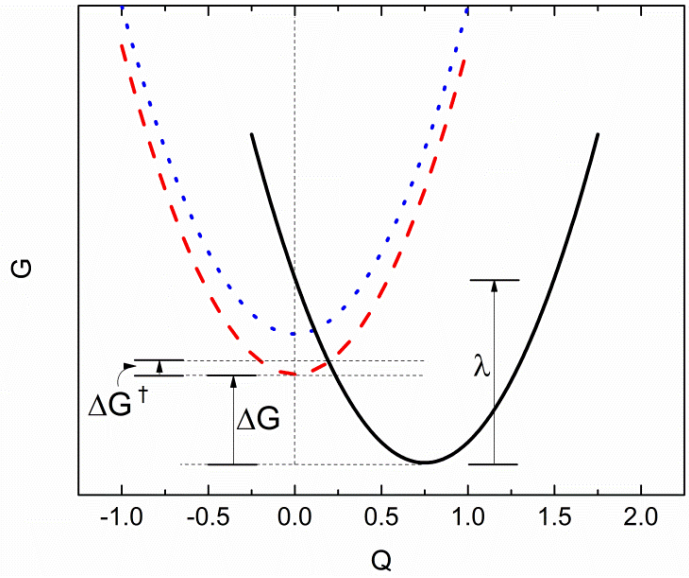

Figure 54 Marcus-Hush theory parabolas showing the Gibbs energy surfaces for the H-mer (blue dotted line) and J-mer(red dashed line) excited states, and the charge transfer state (black solid line) as a function of the reaction coordinate *Q*. The position of the H- and J-mer parabolas relative to each other was determined by the energy of their excited

state from absorbance peaks. The energy of the charge-separated species was chosen to reflect working device parameters.

A simplified equation for the rate constant for electron transfer using the Marcus model is[3,135]

$$k_{ET} = \frac{2\pi}{\hbar\sqrt{4\pi\lambda kT}} V^2 exp\left(-\frac{(\Delta G^{\dagger})}{kT}\right) \quad (2)$$

V^2 is the electronic coupling matrix between the many-electron states, ΔG† is the activation energy to transfer the electron from state A of the system to state B of the system, and λ is the reorganization energy required to go from state A to state B. Each of these variables is dependent upon the position of the Gibbs energy minimum of the initial state relative to that of the final state, (the relative ordinate position)as well as any accompanying changes in the normal oscillatory modes of the system when going from state A to state B (relative change in the abscissa position of parabola).

As seen in Equation 2, the electron transfer rate is strongly impacted by the activation energy term. When comparing the H- and J-mers, the H-mer has higher excitation energy than the J-mer, which would result in a lower activation energy for charge transfer from the H-mer. It is therefore expected that the H-mer will consistently have a higher electron transfer rate, no matter the energy level of the charge transfer state B, as long as the normal oscillatory mode of the states is the same for H- or J-mers. This is reflected in the absorbance normalized EQE results shown in Figure 101, where the EQE decreases consistently as wavelength increases and the energy level of the initial excited state decreases (H-mer to monomer to J-mer). These results are consistent with the Marcus theory approach; states that have a higher initial energy (E_{EX}) will have a

higher driving energy for electron transfer (ΔG) and a lower activation energy (ΔG†). With a higher ΔG and a lower ΔG†, the rate constant for electron transfer should be increasing, which in turn should increase the EQE. This means that the EQE for the H-mer species will be higher than the EQE for the monomer and J-mer species. However, this simple H-mer to J-mer comparison cannot explain the total change in EQE upon annealing, as there is no change seen in the EEX term when comparing the H(J)-mers before and after annealing. In other words, when we normalize the data for absorbance changes it is seen that the photocurrent decreases substantially for the H-mer and monomer states and increases for the J-mer and ultimately there is a significant loss in overall efficiency of the device when all species are taken into account.

In order to explain the decrease in performance upon annealing, we need to examine the electronic coupling matrix term, V^2, in Equation 2 using the generalized Mulliken-Hush method[136–141]. The electronic coupling matrix term describes the extent of coupling between state A and state B in the Marcus-Hush model. As the extent of coupling increases, the barrier height for the transition from state A to state B decreases. Therefore, as the extent of coupling increases, so does the rate of exciton dissociation. Equation 3 describes the electronic coupling matrix element in terms of fundamental properties of the molecules involved in the transfer of the electron from state A to state B.

$$V = \frac{|\boldsymbol{\mu}_{12}|\boldsymbol{\Delta}E_{ab}}{|\boldsymbol{\Delta\mu}_{ab}|} \tag{3}$$

In Equation 3, $|\boldsymbol{\mu}_{12}|$ is the adiabatic transition dipole moment between states A and B. $\boldsymbol{\Delta}E_{ab}$ is the diabatic state energy gap, approximated by the observed (adiabatic) energy difference between the two states (ΔG). $|\boldsymbol{\Delta\mu}_{ab}|$ is the change in diabatic transition dipole

moment when moving from state A to state B. Considering each term and how annealing impacts its magnitude allows us to understand which material property has caused the drop in EQE in the squaraine regions. In the numerator of (3), the observed energy difference between state A and state B, $\mathbf{\Delta}E_{ab}$, would increase as we go from pristine devices to annealed devices. This is because the enhanced crystallinity of the donor material after annealing will increase the exciton delocalization and thus stabilize the charge transfer state, thereby reducing its overall energy. The adiabatic transition dipole moment term will also be greater upon annealing[142] because of this enhanced delocalization. Therefore, the numerator of (3) will increase in magnitude as the devices are annealed and the observed reduction in squaraine EQE resulting from a decreased rate of electron transfer, must originate from an increase in magnitude of the denominator of (3). Assuming that all local dipole vectors are collinear, $|\mathbf{\Delta\mu}_{ab}|$ can be approximated by er^0_{DA}, where r^0_{DA} is the effective separation between donor and acceptor[49,143,144] and *e* is the fundamental charge. An increase in the effective separation between donor and acceptor that has not been caused by phase segregation can only result from a change in the location of the exciton. The experimentally observed increase in crystalline domain size upon annealing, shown in Figure 99, predicts an increase in r^0_{DA} through enhanced delocalization of the electron upon the donor species.

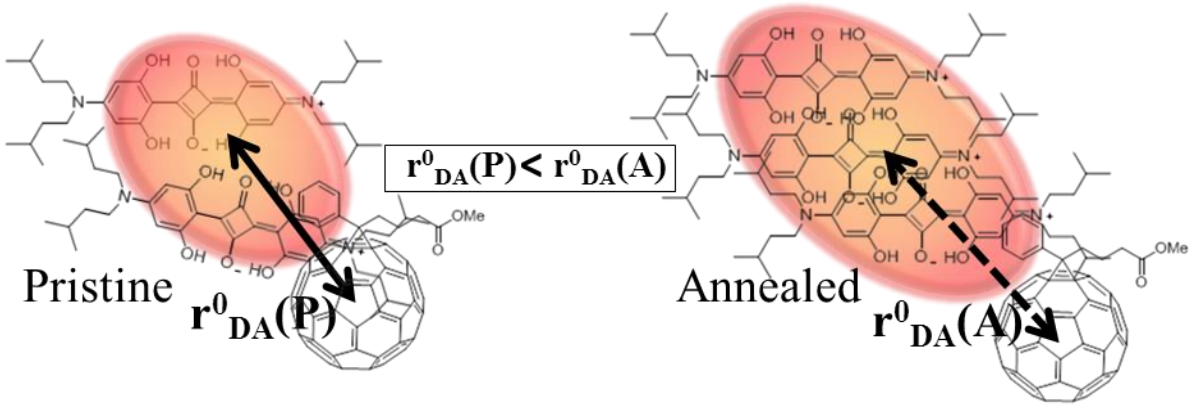

Figure 55 Cartoon scheme showing the change in r^0_{DA} upon annealing as represented by solid and dashed double headed arrows. The oval represents the exciton delocalization in the donor material, which is affected by the extent of crystallinity of the squaraine.

A simple cartoon representation of the enhanced delocalization is offered in Figure 104. On the left, a snapshot of the bulk heterojunction is depicted before annealing. The exciton is less delocalized for a more amorphous squaraine packing structure and is a fixed distance r^0_{DA} (solid line) from the nearest PCBM molecule. On the right, the same snapshot is shown after annealing. Here, as observed with TFXRD, squaraines are now part of a crystalline region with a larger coherent crystal domain size, and the resulting exciton delocalization is occurring over a larger area. This increases the r^0_{DA} (dashed line) representing the distance between the exciton center and the nearest PCBM molecule. The difference in r^0_{DA} before and after annealing is highlighted in the center of the image. The increase in r^0_{DA} therefore decreases the size of the coupling matrix element, V^2, for all of the donor species, which results in a decrease of the electron transfer rate and concurrent decrease in EQE for all of the donor species, despite the favorability of H-mers when only the activation energy is considered.

5.2.1.2.3. Conclusion

In this work, an improved efficiency of charge generation was expected for solution processed squaraine-based bulk heterojunction devices upon annealing. However, the performance suffered despite an increased extent of crystallinity in the donor material. We identified how the Marcus-Hush theory can be used to explain why the increased crystallinity has a detrimental effect upon electron transfer rate. A new approach to understanding the potential exciton dissociation efficiency of a variety of donor species has thus been proposed. Future work can be focused on a quantitative description of the impact of the changing r^0_{DA} on the rate of electron transfer and the overall efficiency of these devices through computational modeling of the exciton dissociation on the aggregate, as well as transient absorption spectroscopy measurements of the charge transfer states. These techniques combined will allow for extraction and analysis of numerical values for the calculation of the rate of electron transfer at the bulk heterojunction.

The work demonstrates that exciton dissociation at the bulk heterojunction is a critical rate-limiting step in small molecule devices, and that squaraines are highly selective energetic and spatial probes of this crucial charge-generating process. Marcus-Hush theory offers a predictive method for understanding which aggregates and materials could present preferential electron transfer rate constants. In a complex system with multiple donor species, the intermolecular coupling between the donor and acceptor will vary depending on the electronic and spatial properties of those donor species. This variation will impact the exciton dissociation efficiency and could make a species that is energetically less favorable actually be more efficient, as seen for the J-aggregates

presented in this work. Thus, the aggregation observed in squaraines allows for a more granular appreciation of this theory since H- and J-aggregates exist within a single crystal structure[106] and the relative importance of the simple thermodynamic activation energy barrier for charge transfer can be compared with the seemingly larger impact of the coupling matrix element. This contributes to a mapping of the complete interaction of the donor and acceptor at the bulk heterojunction for a fuller understanding of this rate-limiting step in charge photogeneration.

5.2.2. Other Devices

5.2.2.1. Squaraine Devices

5.2.2.1.1. DiPSQ(OH)

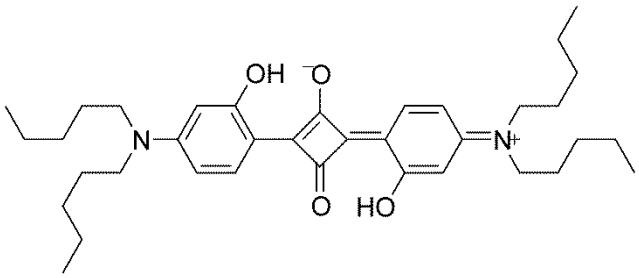

Figure 56 Structural formula of *2,4-Bis[4-(N,N-dipentylamino)-2-hydroxyphenyl]squaraine (DPSQ(OH))*.

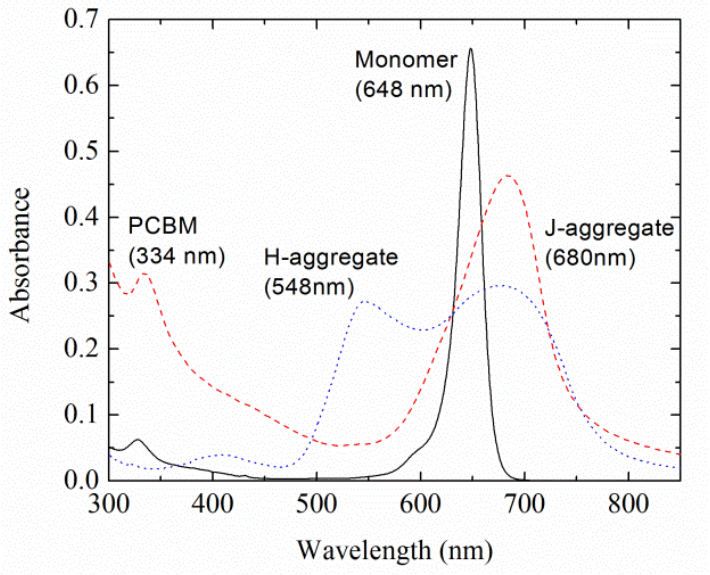

Figure 57 Absorbance spectra of DPSQ(OH) in chloroform solution (black solid line), DPSQ(OH) thin film (blue dotted line), and DPSQ(OH):PCBM thin film (red dashed line). (Film thickness 120 +/-15 nm.)

The absorbance spectra for DPSQ(OH) (shown in Figure 56) in chloroform solution and thin films spin-cast from chloroform are shown in Figure 57. The characteristically narrow (FWHM = 26 nm, 0.087 eV) monomer absorbance peak occurs at 648nm. Upon spin-casting a pure DPSQ(OH) film a substantial broadening or panchromaticity is evident, consistent with new transitions to H- and J-aggregates at 548nm and 680nm respectively. Spin-casting a film from a DPSQ(OH):PCBM solution mixture (3:7 mg/mL in chloroform) causes a relative enhancement of the J-aggregate peak to be observed.

Solvent	**MW (g/mol)**	**Boiling Point (°C)**	**Viscocity (mPa*s)**	**Dielectric Constant**
Chloroform	119.38	61.2	0.54	4.81
THF	72.11	66	0.461	7.52
DMA	87.12	166	2.14	38.85

Table 2 Solvent properties of solvents and co-solvents thought to influence the time of approach to equilibrium in spin-casting of DPSQ(OH):PCBM active layers.

The extinction coefficient for DPSQ(OH) was measured as 1.9 x 10^5 +/- 0.2 cm^{-1} in the pure film at λ_{max}=721 nm, and from the absorbance onset the optical bandgap in film was determined to be 1.481 +/-0.008 eV. The absorbance spectrum of the DPSQ(OH) in solution shows a distinct monomer peak at 648 nm. Solid-state absorbance spectra reveal the presence of aggregates as expected for this molecular chromophore. The aggregates can be characterized by the relative red or blue shift of the peak position; we assign the J-

aggregate peak by the bathochromic shift to 680 nm, and the H-aggregate peak by the hypsochromic shift to 548 nm. Upon addition of PCBM, there is a dramatic reduction of the H-aggregate peak concurrent with a grow-in of the J-aggregate peak.

When co-solvents are added to the blend of DPSQ(OH):PCBM:Chloroform, additional changes in J- and H-aggregate peak positions and their intensities occur, as shown in Figure 107, after the incorporation of dimethylacetamide (DMA) and tetrohydrofuran (THF).

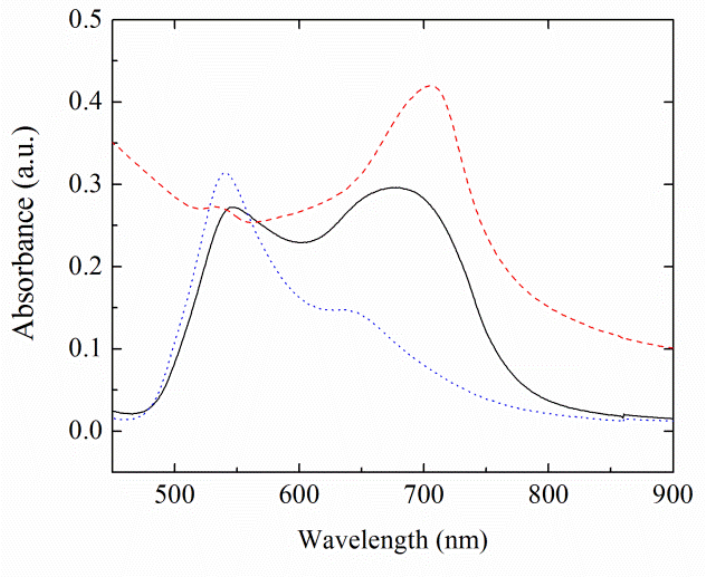

Figure 58 Absorbance spectra of DPSQ(OH):PCBM in chloroform (black solid line), DPSQ(OH):PCBM with tetrohydrofuran cosolvent (red dashed line), and DPSQ(OH):PCBM with dimethylacetamide cosolvent (blue dotted line).

The THF appears to further promote J-aggregation, shifting the λ_{max} to 715 nm while the DMA appears to promote H-aggregation, increasing the intensity of the peak at the λ_{max} of 548 nm by about 18%. One interpretation is that incorporation of different solvents allows for macroscopic control of these nanoscale aggregation patterns. The role

of co-solvents [16],[17],[18] to modify the bulk heterojunction morphology has been invoked previously and, while not completely understood, has led to improved efficiencies. Peet et al.[16] describe strong dependence of the morphology and device performance on the alkyl chain length of a series of dithiol co-solvents, which influence the physical interactions between polymer chains and/or between the polymer and fullerene phases. When considering the thermodynamics of the solution as it is evaporating, there are both solvent-donor and solvent-acceptor interactions that must be considered. It makes some sense to consider molecular weight, boiling point, viscosity and dielectric constant, especially since the rate of evaporation will also influence the fluidity of the deposited solution during the spin-casting process. The aggregate size will also depend on the time allowed for equilibrium to be approached during this spin-casting process. For this reason the solvent properties are presented in Table 6 and we point out that DMA and THF have similar molecular weights, but differing boiling points and dielectric constants.

An increase in the aggregation of these DPSQ(OH) films as a result of the changing solvent environment during spin-casting is likely to have a significant impact on the device properties. Also the relative mixing of DPSQ(OH) and PCBM will contribute to the efficiency, with the importance of proximity between squaraine donors and charge acceptors being explored by many groups[19]. In order for efficacious exciton dissociation to occur, the blend of the donor and acceptor must be well-mixed so that as many excitons as possible formed in the donor are able to diffuse to the bulk heterojunction, while the mixing simultaneously creates enough homogeneous and contiguous domains of the donor and acceptor materials for the free charge carriers

generated by exciton dissociation to actually reach their respective electrodes. A DPSQ(OH):PCBM photovoltaic was first prepared without any buffer layer deposition or co-solvent optimization giving a J_{SC} of 2.53 mA/cm^2 , V_{OC} of 0.503 V, fill factor of 32.81%, and power conversion efficiency (PCE) of 0.4+/-0.2%. As demonstrated in Figure 107, our chosen optimization conditions had dramatic effects on the short circuit current and on the efficiency, with lesser but still important effects on the open circuit voltage. These changes are also presented in Table 7.

Our best devices to date have a 10 nm thick Alq3 cathode buffer layer and THF as co-solvent to give a J_{SC} of 13.18 mA, V_{OC} of 0.601 V, fill factor of 31.3%, and a power conversion efficiency of 2.4+/-0.3%.

Device name	**J_{sc} (mA/cm^2)**	**V_{oc} (V)**	**Fill Factor**	**Efficiency**
Unoptimized DPSQ(OH):PCBM	2.53	0.503	32.8%	**0.4+/-0.2%**
DPSQ(OH):PCBM:Alq3	8.95	0.562	32.1%	**1.6+/-0.3%**
DPSQ(OH):PCBM:THF cosolvent:Alq3	13.18	0.601	31.3%	**2.4+/-0.3%**

Table 3 Current and Voltage characteristics for the devices shown in Figure 107.

The short-circuit current has increased from 2.53 mA/cm^2 to 8.95 mA/cm^2 with incorporation of the Alq3 buffer layer and from 8.95 mA/cm^2 to 13.18 mA/cm^2 upon using the THF co-solvent. The fill factor remained low at around 30%, which offers promise of opportunity for further optimization of the device. The dramatic increase in the short circuit current can be explained by considering each optimization separately.

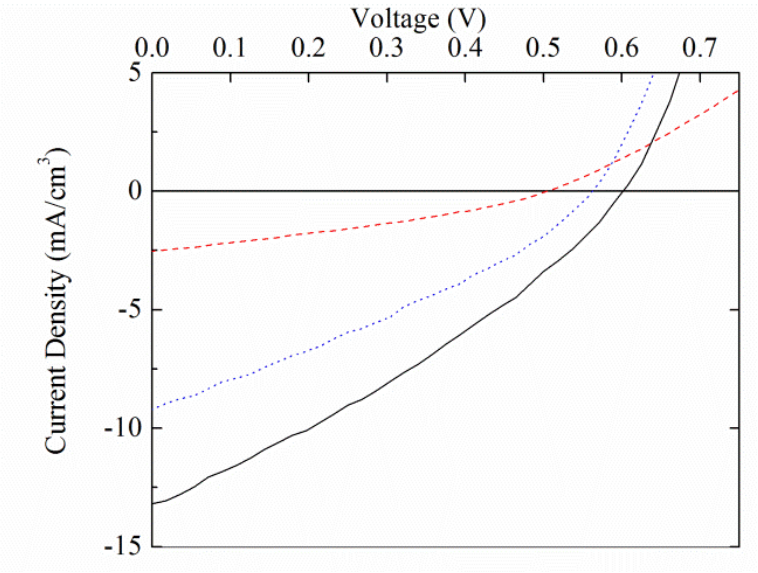

Figure 58 Unoptimized device (red dashed line) was prepared with no cathode buffer layer **[PCE=0.4%]**. Optimized device (blue dotted line) **[PCE=1.6%].** J-aggregate device (black solid line) **[PCE=2.4%].**

The largest contributor to the optimization was the inclusion of a cathode buffer layer; Alq3 (shown in Figure 59) is a widely used material in OLEDs and organic PV because it acts as a generic buffer layer preventing oxygenation of the active layer as well as oxidation of the metal cathode in contact with the active layer.[20] This metal cathode oxidation would otherwise create an uneven layer of aluminum oxide, which decreases the required interfacial surface area between organic active layer and aluminum, in turn reducing a device's efficiency through reduction in charge collection efficiency at the electrode.

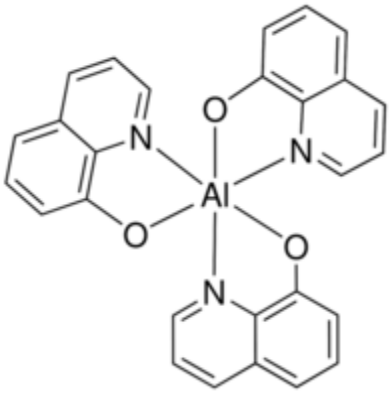

Figure 60 Molecular structure of Alq3

Addition of the Alq3 buffer layers provides a contiguous interfacial contact between the active layer and the aluminum electrode. Critical to this optimization is Alq3's selective electron conducting property, which facilitates electron transport from the organic active layer to the electrode while simultaneously increasing the rectification effect on the current. Finally, Alq3 acts to increase the measured shunt resistance through reduction of diffusion of the cathode layer into the active organic layer. Each of these factors contributes to the increase of 6.42mA/cm^2 in the current density demonstrated in Figure 58 and summarized in Table 3.

The interpretation of the increase in short circuit current upon addition of the co-solvent and increased amount of J-aggregate is more complex. As discussed above, the choice of co-solvent has a direct impact on the propensity of the DPSQ(OH) to form aggregates. The extent of aggregation, delocalization of the excited state and mobility of generated carriers had not been quantified in squaraine donors before this thesis work. However, it has been demonstrated elsewhere that increasing crystallinity and aggregation has a direct impact upon photocurrent generation and mobility of the charge carriers. Further chapters address the impact of aggregates on the bulk heterojunction; it

must be stated that this work which was initially published in 2012 was groundbreaking for the field because of the connection made between the presence of squaraine aggregates and the improvements seen in the device metrics.

Increase in efficiency may be correlated with extended exciton delocalization or exciton diffusion, although it is likely that an associated decrease in excited state lifetime may offset this gain. We also suggest that this increase in current density is consistent with an increase in hole mobility through the aggregated squaraine. Mobility is related to the short circuit current through $J_{SC} = ne\mu E$, where n is the density of charge carriers, e is the elementary charge, μ is the mobility, and E is the electric field. Since current density is typically dominated however by LUMO to LUMO electron transfer in the PCBM domains, there might be additional effects of changing the mobility. The Onsager-Braun model of charge dissociation has been used to describe charge separation by Peumans and Forrest as well as Durrant et al, and offers further explanation for the results shown in this work. Since the probability of charge separation is proportional to the mobility of the charge carriers, it seems likely that the increased J-aggregation has increased the probability of charge separation which would then increase the short circuit current in a more dramatic fashion than just increasing the hole mobility as it directly relates to the J_{SC}.

5.2.2.2. Polymer:PCBM Devices

5.2.2.2.1. Gelation Study

The devices appeared almost black. They looked a lot thicker (much less transparent) then the standard P3HT:PCBM devices, which are typically a deep rose

color. Spin coating the solution was a bit challenging because it was so sludgy to get out of the vial, but it appeared to give uniform coverage of the glass slide.

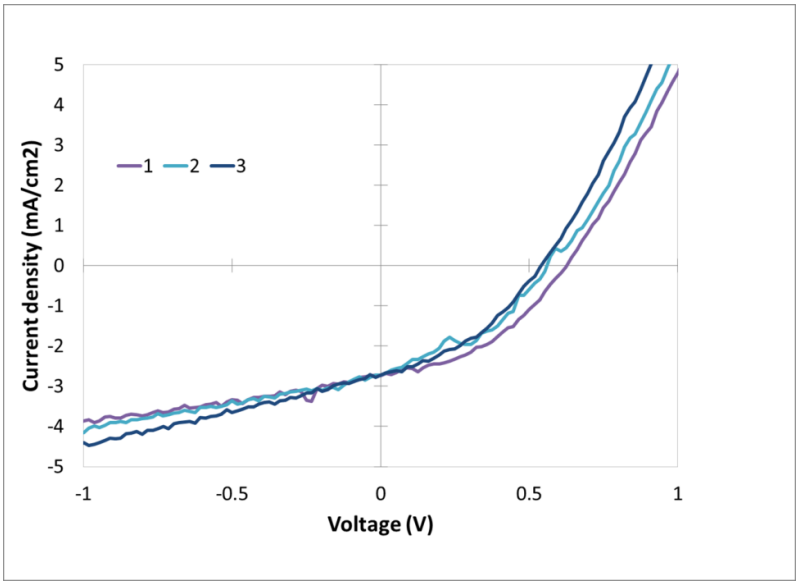

Worksheet #	Area	Jsc	Voc	FF	Efficiency
1	0.123	-2.73	0.627	41.26%	0.71%
2	0.123	-2.73	0.560	39.35%	0.60%
3	0.123	-2.73	0.540	38.70%	0.57%

Figure 61 Standard P3HT:PCBM devices made with degraded P3HT. This resulted in reduced performance.

It has been shown by Brabec et al in the literature that allowing P3HT to gelate by letting it sit in solution will create crosslinking of the polymers [1]. The implications of this in devices are twofold. First, the crosslinking is a random process, and there has not been any work done really to attempt to control it, beyond limiting the amount of time that the system is allowed to gelate. This is problematic if we are trying to make reproducible devices, and if we are trying to spin-coat films that have some level of homogeneity throughout. Second, the crosslinking can produce highly favorable device morphologies allowing for maximum short circuit current because of the increase in pathways for hole transport. It could also increase the Voc because the crosslinking is changing the

ionization potential of the donor species. There is no reason to expect or predict the fill factor to change, but these devices could have higher efficiencies than those that are prepared fresh from solution.

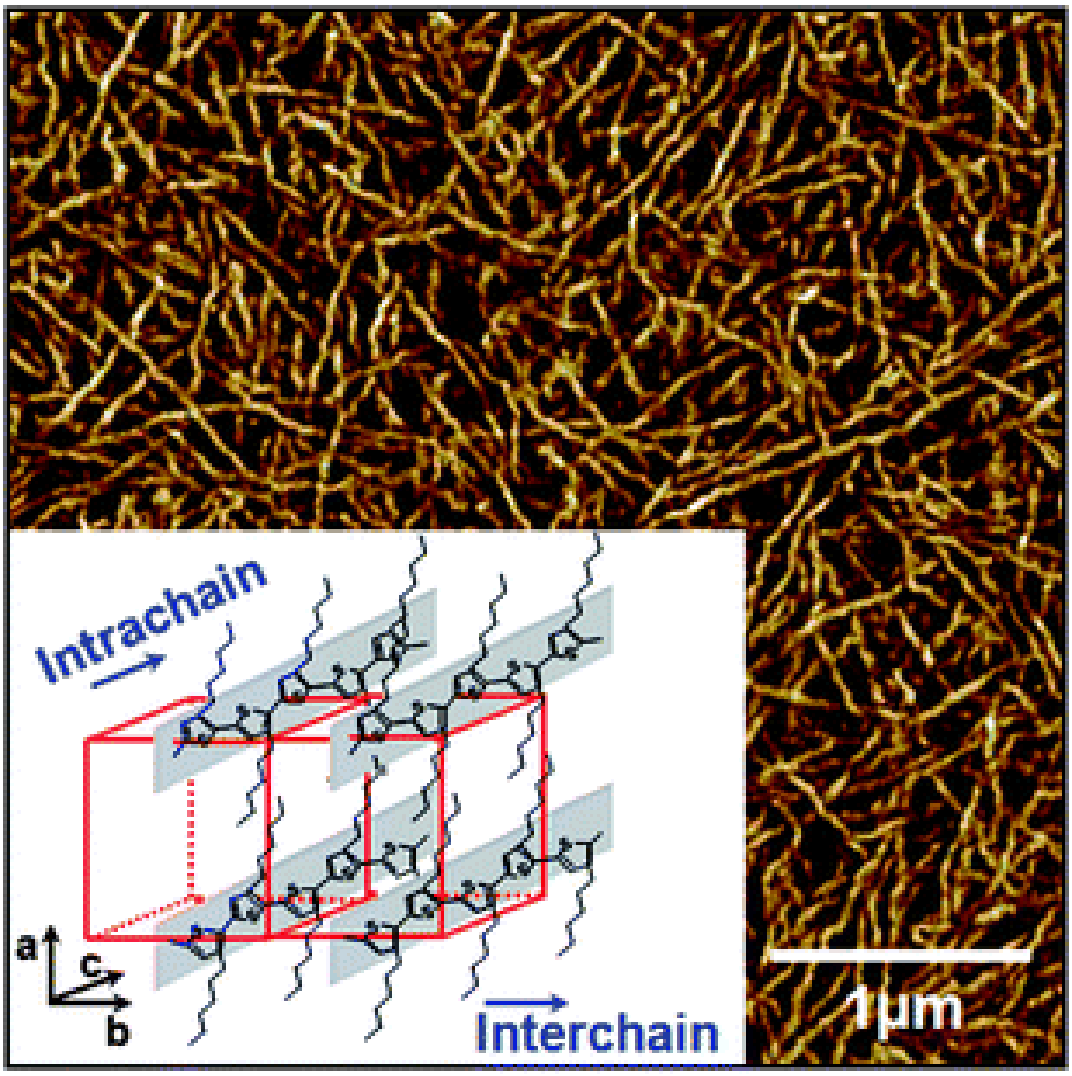

Figure 62 AFM image of crosslinked P3HT[5].

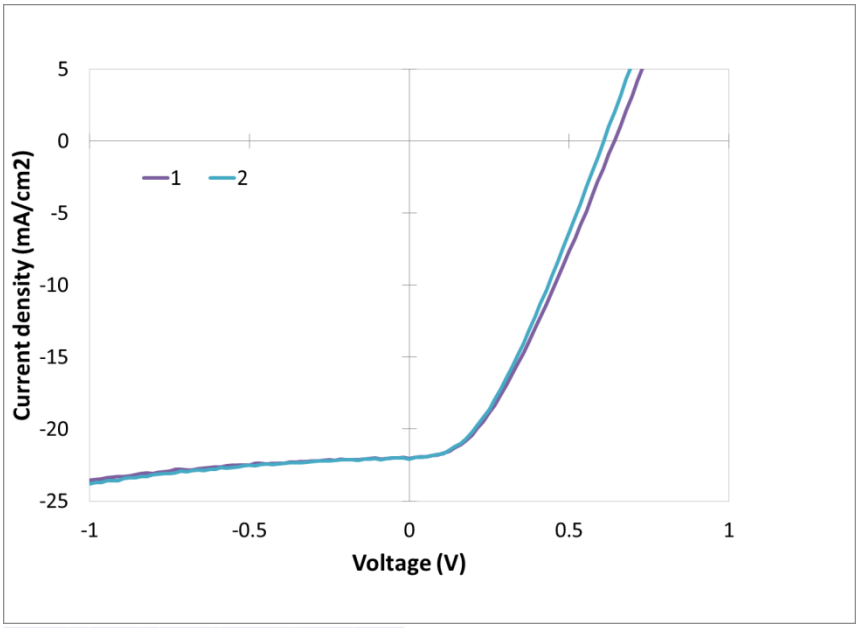

Worksheet	Device area	Jsc	Voc	FF	PCE
10	0.123	-22.04	0.642	37.09%	5.25%
11	0.123	-22.07	0.608	37.62%	5.05%

Figure 63 Gelated P3HT:PCBM devices.

The gelated devices have an slightly higher average open circuit voltage of 0.625 V when compared to the regular device results of 0.575 V. This could indicate a difference in the material properties. The increase in Voc could be resulting from longer chain length polymer donor species, which will have a larger ionization potential than their shorter chain counterparts. There is a marked increase in the short circuit current, which we would expect from the crosslinking of the polymers. The fill factor is worse in the gelated solar cells than the standard ones. This is also not surprising because we are expecting that the crosslinking will be random, and not very ordered. This means that there will be areas of non-preferential morphology which will bring down the fill factor. Overall however it can be seen that the efficiency increases dramatically, from an average of 0.63+/-0.6% to 5.2+/-0.3%. This is almost exclusively due to the increase in short-circuit

current, which appears to be derived from the charge carrier transport enhancement of the crosslinked polymers.

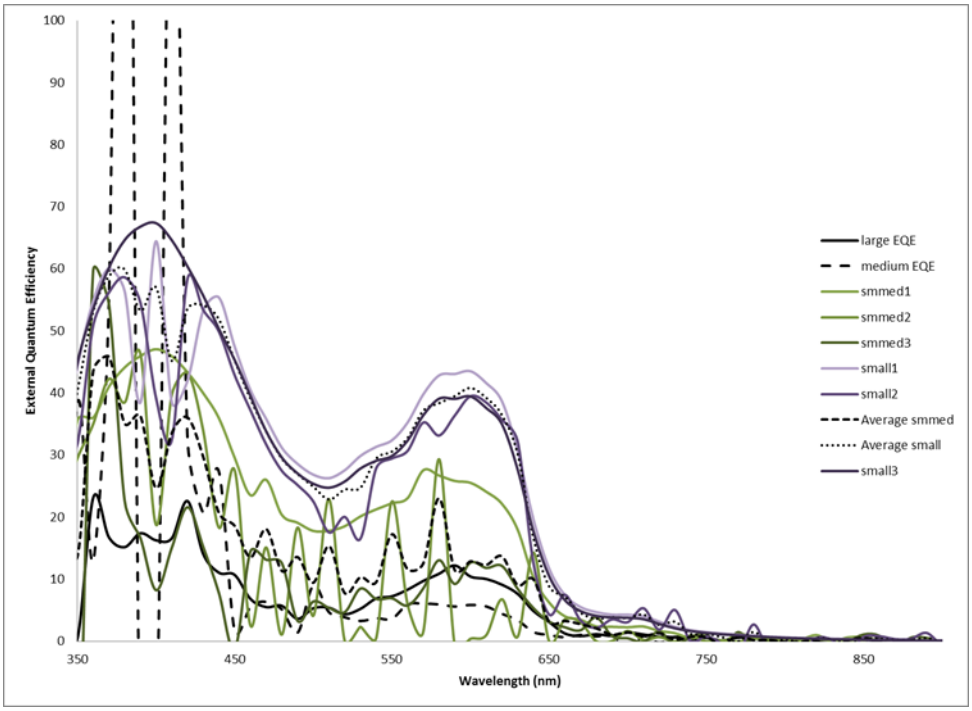

Figure 64 External Quantum Efficiency for gelated P3HT:PCBM devices.

As shown in Figure 64, some of the devices measured have high EQE of over 60% in the PCBM region and over 40% in the P3HT region. This corresponds to the enhanced short circuit current. However, it can also be seen that some of the devices had very poor performance, or that their performance was not uniformly consistent across the wavelengths of interest.

Conclusions: This work opens the door to an interesting series of questions. Can this gelation be controlled through process optimization in a way that results in consistently favorable morphologies? Is gelation a potential way to increase short-circuit currents above what would be predicted with theory, because material properties are actually

changing? Could gelation be used in a SQ:PCBM device to create “quasi-polymers” or oligomers of squaraine that would be more easy to control during the post-fabrication processing phase? While all of these are interesting questions, the primary issue is that while I was able to demonstrate reproducibility, I was unable to demonstrate consistent performance across a film (11 devices). Until film consistency can be controlled, this is not a viable technique for device fabrication.

5.2.2.2.2. Ternary Blend Study

: The finished devices were atypical of a P3HT:PCBM device. They were greyish-green in color, and had a “sheen” on them when tilted back and forth under light that I have always considered typical of a SQ film.

Device Name	Jsc	Voc	FF	PCE
6	-22.00	0.584	49.31%	6.33%
7	-22.41	0.562	47.81%	6.02%
9	-21.91	0.749	46.10%	7.57%

Table 4 Ternary blend device results.

These devices had amazingly good results. The short circuit current was very high, approaching what would be the maximum for a squaraine:PCBM device. The V_{oc}

was as expected for two of the devices (around 550-600 mV), but was very high for the third device, at 0.75 V. This is very unexpected, as the V_{oc} is typically considered to be a materials property. It must, however, be taken with a grain of salt, as this was a limited project with no further work done on reproducibility. All of the devices demonstrate excellent fill factors of almost 50%, which are the highest our lab has reported as of yet. Additionally we have high PCEs, with one at greater than 7.5%.

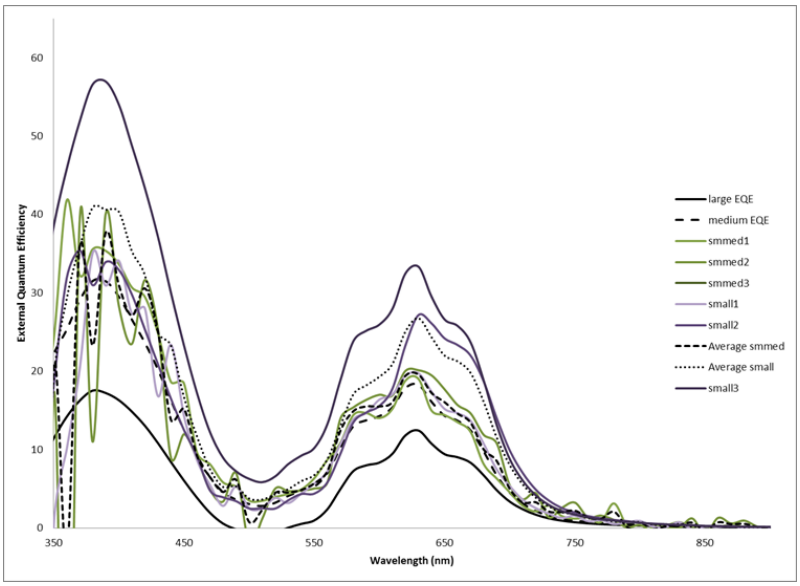

Figure 65 External quantum efficiency results for ternary blends, with annealing performed before the evaporation process.

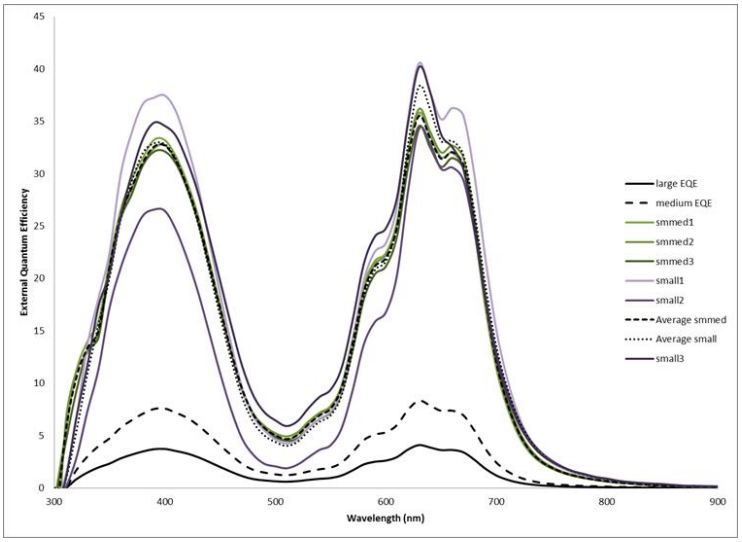

Figure 66 EQE results for ternary blends, with the annealing step performed after the evaporation process.

Figure 65 and 66 are very interesting, but again, all discussion about these results is fairly speculative until they are reproduced. The first thing to point out is that there is are significant differences between the two graphs. The only processing difference between them is that the second graph (Figure 113) is results from devices that were annealed after having the top contact evaporated. Recent work by Moule et al (2013) has shown that highly preferential segregation occurs when annealing is done with the Al contact present. The second graph also has less disparity of EQE as a function of device size. This could indicate that annealing when the Al contact is present somehow impacts the change in short circuit current density with device size, but that is highly speculative. The second thing to point out is that there is a stunning difference between the amount of squaraine present (<2%) and the EQE of the squaraine. It was expected that there would be an identical EQE to that of a binary solar cell, with perhaps a small sub-bandgap bump indicating the squaraine functionality. Instead, the EQE appears to be dominated by the

squaraines, to the point that the P3HT region is nonexistent. The three peaks in the region between 550 and 700 nm are highly typical of squaraine EQE. Figure 67 allows for a direct comparison of the binary and ternary blends. The results presented in Figure 67 are the ternary and binary blend EQE averaged over all device sizes, which is the values are significantly lower than those presented in Figure 65 and 66.

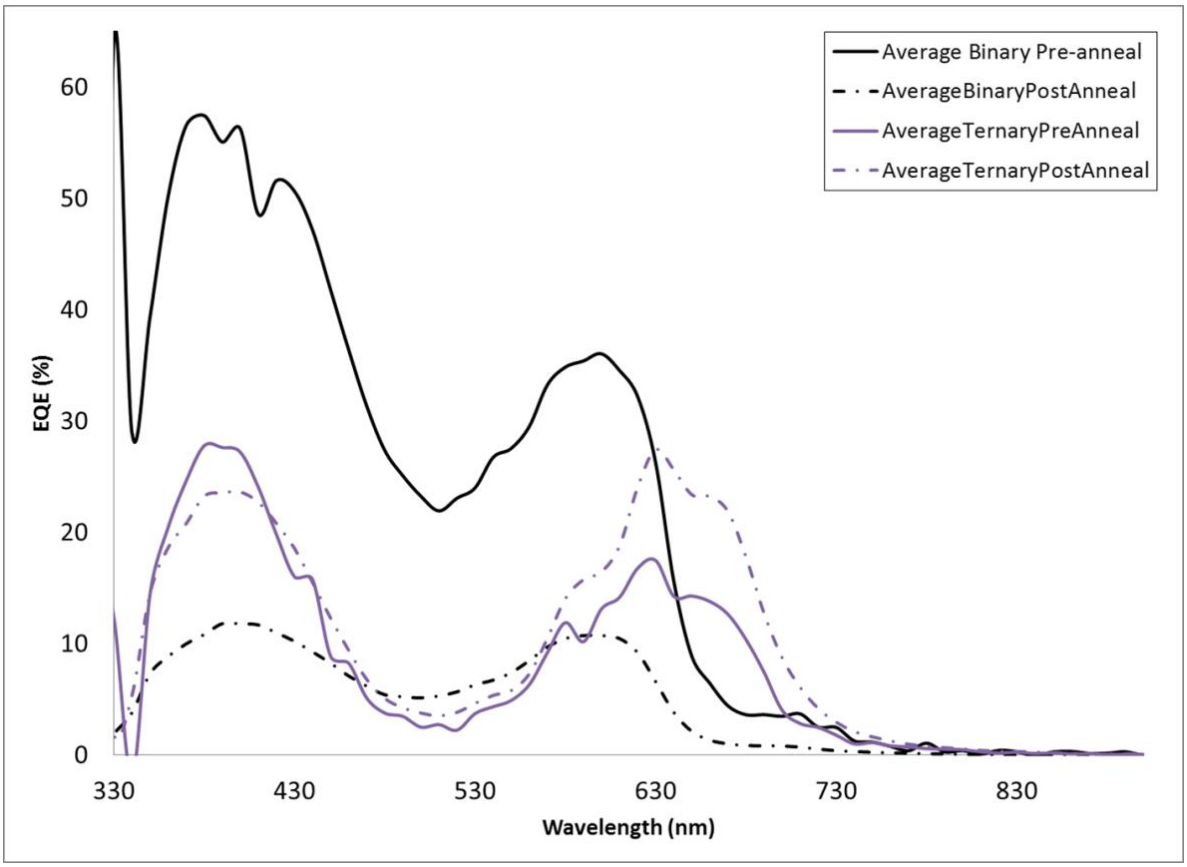

Figure 67 EQE results for binary and ternary blends, with annealing done before and after evaporation.

Figure 67 gives a very clear picture of how remarkably different the EQEs are. There is no way to explain this completely with the data that is available right now, but there are a couple possibilities. The first is that I somehow made the solutions wrong, and there was

actually a lot more squaraine in there than stated. I don't find this very likely however, as by now I am meticulous about solution prep. The second possibility is that somehow, the P3HT is absorbing a photon, and transferring that photon to the squaraine, where it then forms a lower energy exciton which dissociates and creates charge. In order for this to happen, the squaraine and the P3HT would need to be in very close proximity to each other, and it would need to be an energetically favorable transition that could happen in an ultrafast pathway so that it could be measurable and have some quantum yield for the energetic process.

Conclusion: This is really cool, but is a single result. It is a moderate risk-high reward experiment, and I consider it worth looking into further.

6. Discussion

Chapter Abstract

This discussion will be used as an opportunity to summarize key results as they relate to the fundamental questions being asked within the dissertation. Extensive discussion of individual results has been undertaken within Chapter Five, and therefore this will be a highly targeted summary of the results before the Theory presented in Chapter Seven.

6.1. Why is Aggregation Critical to Device Performance?

OPV materials are currently unable to be created at the highest potential for efficiency (>20%) because the interplay of molecular structure and BHJ morphology is still unknown. We are not able to predict how a given molecule's structure will impact the formation of the BHJ, or how that BHJ must be morphologically to achieve maximum power conversion efficiencies. State of the art devices rely on optimization of materials to achieve maximum absorption of the solar spectrum, high charge carrier mobilities, a large open circuit voltage, or ease of deposition/reproducibility. There is no way currently to directly tie a specific component of molecular structure to enhanced performance resulting from some preferential BHJ nanomorphology.

The extent of squaraine-squaraine interaction is characterized as a function of their aggregation. The squaraines are known to aggregate as n-mers, where an excitation is formed over multiple molecules. As such, there are characteristic shifts in absorbance wavelengths. Because of this propensity for aggregation, the squaraines offer a unique

probe of the relationship between structure and function within the BHJ. Not only do they offer a probe of the finished, static, structure of a working device, but we can also use their molecular structure differences to examine how the BHJ forms, through the aforementioned competing thermodynamic mechanisms. The first mechanism can be thought of in terms of two squaraine molecules with no hydroxyl groups interacting with each other; as the two molecules approach each other, the dominant forces of interaction are van der Waals forces and the steric hindrance imposed by the chain lengths. As the chain length increases, the molecules are less able to pack tightly, resulting in crystals with more deformations and packing faults, as well as more amorphous domains. Conversely, when OH groups are present there is a second competing force of interaction, hydrogen bonding. At short chain lengths, hydrogen bonding will dominate. This will impact not only the crystal packing, but there will be significant electronic differences in the energetics of the excitons formed on the aggregates. Again as the chain length increases the dominant mechanisms for aggregate formation will shift from hydrogen-bond-mediated to chain-sterics-mediated, but the excitons formed on these aggregates will still contain some electronic characteristics of the H-bonding that will be extant. The existence of aggregates is not unique to squaraines; they are present in many types of photoactive polymers as well.[41,145,146] Excluding Dr. Spano's work, most of the state-of-the-art work in literature detailing the influence of squaraine aggregates in OPV[128,147,148] references papers from the 1920s[60,149], Kasha's work[59], or a simplified discussion of the photophysics of neat squaraines or squaraines in solution[35,102,150–152]. While none of this work is incorrect, it fails to address the fundamental importance of the squaraine aggregate. First, the presence of aggregates causes a broadening of the

absorbance spectra that can then be utilized to collect a greater portion of the solar spectrum, increasing the efficiency of the solar cell simply by acquiring more photons to be converted into current. This thesis has demonstrated that the aggregates behave in ensembles, where there is no single molecular structure that can be claimed as an H- or J-aggregate, but rather there exists a collection of molecular orientations that when taken together form a collective absorbance profile. The presence of aggregates at the BHJ also influences the charge separation process. When the aggregates are part of a larger crystal structure, the exciton formed on the aggregate becomes more delocalized and therefore more difficult to dissociate. Finally, there is still fundamental work ongoing to understand the "true nature" of the aggregate. If it is considered as purely an optoelectronic phenom+enon that only exists when light interacts with dimers, then the vibronic coupling and signatures extant for both types of aggregates will behave differently from each other as they are considered to be part of a coupled system with PCBM at the BHJ. In order for efficiency of squaraine OPVs to be maximized, the dynamics of the aggregate-PCBM system must be clearly understood. This thesis has led to the point where the fundamental understanding of the aggregate has progressed through peer-reviewed publication, and highlighted the importance of the computational collaboration with Dr. Spano's group.

6.2. Why are Squaraines a Unique Probe of the Bulk Heterojunction?

One of the most frustrating parts of OPV fabrication, testing, and publication is that two groups, using the same material, can achieve radically different results which they then attribute to specific morphologies that are actually too small to be visible with

current experimental techniques[153,154]. Dean Delongchamp and others consider this to be one of the fundamental questions that must be addressed in order for upscaling and efficiency enhancement to move forward. Based on the current state of the art OPVs, there is no one BHJ morphology that will consistently give high efficiency solar cells across a range of materials; similarly, there is no one set of donor-acceptor materials that will give consistently high efficiency solar cells across a range of morphologies. This leaves the community optimizing every morphology or donor/acceptor set through a unique process, which will hamper the ability of the technology to be upscaled; if every material system and morphology requires a different set of conditions in order to be at maximum efficiency, and different systems and morphologies are required for different applications (flexibility, transparency, aesthetics, size, etc.) then it will be virtually impossible to design a single process that can work well, at an industrial scale, to prepare the devices. Manufacturing technology relies upon reproducible results that can be implemented from one factory to the next with ease. I believe that the reason for the lack of a unifying theory is the lack of basic understanding about the charge photogeneration process at the BHJ. This thesis has demonstrated that the rate-limiting step is going to be the dissociation of the exciton, regardless of what the exciton dissociates into first (free charges v. charge transfer state). Therefore, the squaraine materials that have been characterized for both absorbance and crystallinity properties and then made into devices ($DiPSQ(OH)_2$ and $DBSQ(OH)_2$) have acted as probes of the BHJ in a way that other materials have not. Because this thesis has tied together both their fundamental structure and optical transitions, to their ability to generate charge, a new approach to considering materials as viable candidates for selection can be proposed. Since the squaraines can be

both crystalline and amorphous, and absorb a wide range of the solar spectrum, their ability to perform as a function of those characteristics at the rate limiting step of exciton dissociation is offered as a unique method for investigating charge photogeneration that cannot be replicated easily with polymers or other small molecules like cyanine dyes which do not form such a wide array of molecular configurations at the BHJ.

6.3. Key Findings for Squaraine OPVS

Results from over 2000 squaraine devices are presented within this thesis. The highest efficiency single squaraine device prepared was 5.2%, for a 3:7 blend of the DiPSQ($OH)_2$:PCBM; the average highest efficiency devices were for the same squaraine, with 4.1 +/- 0.3% achieved in 1:2 blend of DiPSQ($OH)_2$:PCBM. It was found that the short-circuit current could be manipulated by changing the type of aggregate that was present, which is a direct result of positive impacts upon the rate of exciton dissociation at the BHJ. Direct correlations were established between the presence of aggregates and the formation of crystals, and variations from trends were explained using the kinetics of spin coating and the thermodynamics of annealing. Intense materials characterization was performed for 8 different squaraines, as well as for a variety of cyanine dyes, porphyrins, and oxides that were all considered as viable candidates for inclusion into the device architectures.

6.4. Key Findings for Other Devices

Two key results must be highlighted for the P3HT:PCBM devices that were prepared during this thesis work. The first is for gelated P3HT:PCBM devices, which

were prepared from a degraded vial of P3HT that was made into a gelated solution through crosslinking of the polymers. Devices prepared immediately without gelation gave efficiencies of 0.63 +/-0.3%. After the gelation process, the efficiencies were 5.2 +/-0.3%, which is one of the higher efficiencies for that material system when compared to literature[83,155,156]. This is a greater than 8-fold increase in performance. The second key result is for ternary blend devices, prepared with the top performing squaraine to date, $DiPSQ(OH)_2$ and P3HT:PCBM. The ternary blend resulted in efficiencies of 6.6 +/-0.8%. These results are highlighted here to draw attention to the potential for these two projects (gelation and ternary blends) that were unable to be explored by S. Spencer during the duration of her thesis.

7. Theoretical Analysis of Key Findings

Chapter Abstract

Key portions of Marcus-Hush theory and Onsager-Braun theory are revisited, with a unifying connection between the two proposed in the OB section. The thermodynamic analysis (with some portions Appended) describes the current understanding of the thermodynamics of mixing for the spin coating and annealing process.

7.1. Marcus-Hush Theory

Returning to the theoretical discussion of charge photogeneration, once the exciton has been generated and diffuses to an interface, it can dissociate into the charge transfer state, which must then further dissociate into free charges, or it can immediately dissociate into free charges, or something between those two extremes. As was demonstrated in Section 5.2.1.2, MH offers a valuable path to understand the kinetics of the electron transfer rate in a variety of materials by relating together their energetics and quantum mechanical behavior.

In Figure 68, the nuclear coordinate of the reactant (R) and product (P) is related to the geometry of the molecules and the state of polarization of the surrounding medium. The ordinate is the energy with ΔG°' the difference between the bottoms of the wells being the reaction free energy. The middle parabola corresponds to the transition state between the reactant and product.

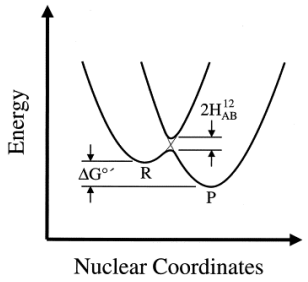

Figure 68. The model of an electron transfer reaction as the intersection of two parabolic potential energy wells[2].

The activation energy of the reaction is the difference in energy between the intersection point of the two main parabolas and the bottom of the reactant well. $2H_{AB}^{12}$ is the electronic coupling matrix element. If the simplest assumption is made of harmonic energy wells, then the energy difference between the bottom of the reactant well and product well at the intersection point is the reorganization energy, λ. A more specific case is shown in Figure 69, which illustrates Marcus Theory applied to a donor/acceptor system.

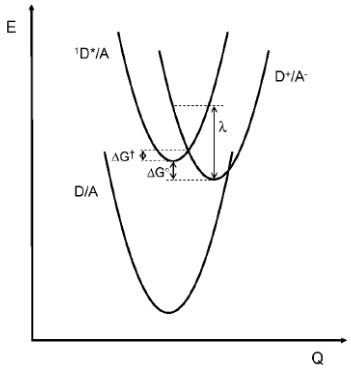

Figure 69. Potential energy surfaces for a D/A system where photoexcitation generates the exciton $^1D^*/A$ and subsequent electron transfer generates the charge transfer state, D^+/A^{-3}.

7.2. Onsager-Braun Theory

The charge transfer state (CT) potentially generated by the process of exciton dissociation is a Coulombically bound electron-hole pair, with the electron now in the lowest unoccupied molecular orbital of the acceptor molecule. In order for free charge carriers to be created, this CT state must also dissociate; the probability of this dissociation is given by Onsager-Braun theory. Lars Onsager first developed the theory of ion separation and recombination in weak electrolytic solutions[52,53]. His work described the probability of separation/recombination of an ion pair based upon the relative effect of an applied electric field; it is a solution to a steady state diffusion equation with infinitely long lived ions. While this work was experimentally verifiable for a variety of molecules[54–57] the theory broke down when applied to solid state mixed donor acceptor materials.

Onsager's 1938 geminate recombination theory, developed for ions in solution, when applied to solids composed of donor and acceptor materials, gives inconsistent electron transfer distance results. It predicts electron-transfer distances between 2-3 nm, but spectroscopic evaluation shows that a CT exciton involves nearest-neighbor (0.5 nm) electron transfer. Onsager's theory is the result of solving a diffusion equation for the relative motion of two opposite charges in the net potential provided by their Coulombic attraction and any applied field; this can then be used to predict the probability that the pair will be able to separate to infinity. One of the important boundary conditions on the solution is that if the pair separation reaches zero (recombination) the pair irrevocably disappears.

Charles Braun's 1984 paper[58] postulates that this cannot be the case for free charge generation from charge transfer states, because the charge transfer state is a metastable state, and recombination and "re-dissociation" phenomena can happen repeatedly over the state's lifetime, as shown in Figure 125.

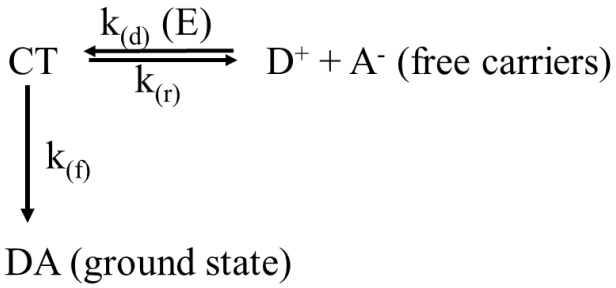

Figure 70 The kinetics of charge transfer state dissociation.

In Figure 70, CT is the charge transfer state, DA is the ground state that has recombined through fluorescence with rate constant $k_{(f)}$, D^+ and A^- represent the free carriers that have been formed through dissociation, with an energy dependent rate constant $k_{(d)}(E)$, which can also recombine to the charge transfer state with associated rate constant $k_{(r)}$. The charge transfer state (CT) can either disappear through dissociation into free carriers (that have an electric-field dependent rate constant) or decay to the ground state. The major breakthrough of Braun's modification is to examine the possibility of partial dissociation of the charge transfer state during the lifetime of the CT. These partial dissociations recombine to form the CT, which may then fully dissociate at a later point in time. From Figure 70, the probability that the charges will dissociate is given by

$$P(E) = k_d(E)\tau(E), where\ \tau(E) = lifetime\ of\ CT = [k_f + k_d(E)]^{-1}$$

In order for this to be applicable and for Figure 125 to be representative of the actual situation, the rate constants must allow for zero-field charge carrier generation quantum yields to match those measured experimentally.

Braun uses the Wannier-Mott exciton as a representative exciton for the CT state exciton. The equilibrium constant K(0) for the dissociation of a Wannier-Mott exciton in an applied field as a function of the energy difference between the exciton and the first singlet excited state (conduction band) is shown in Figure 126, and was calculated using the following equation[157–159].

$$K(0) = (\frac{\mu kT}{3\pi\hbar^2})^{3/2}\exp(\frac{-\Delta E}{kT})$$

In this equation, μ is the reduced mass of the exciton (estimated at $1.82*10^{-30}$ kg) and ΔE is the difference in energy between the exciton and the LUMO of the acceptor. K(0) is equal to the ratio of $k_d(0)$ to k_r as demonstrated by Langevin[160,161], where the bimolecular rate constant for hole-electron recombination, k_r, is given by the following equation.

$$k_r = \frac{\langle u \rangle e}{\langle \epsilon \rangle \epsilon_0}$$

In the Langevin equation for bimolecular recombination, <u> is the spatially averaged sum of electron and hole mobilities, e is the elementary charge, <ϵ> is the spatially averaged dielectric constant, and ϵ_0 is the permittivity of the vacuum.

Because $k_d(0)=k_rK(0)$, the entire equation for the rate of CT state dissociation can be rewritten as follows[3].

$$k_d(E) = \frac{3\langle u \rangle e}{4\pi\langle \epsilon \rangle\, \epsilon_0 a^3} \exp\left(\frac{-\Delta E}{k_B T}\right)\left[1 + b + \frac{b^2}{3} + \frac{b^3}{18} + \cdots\right]$$

In this, the complete Onsager-Braun equation for the rate of dissocation, a is the thermalization length of the two separated charges, and the summation is a modified first order Bessel function where $b=e^3E/8\pi(\epsilon)\epsilon_0 k_B{}^2T^2$. The primary variable to consider here is a, the thermalization length of the electron. A potential energy diagram of the charge transfer state separation process is shown in Figure 72.

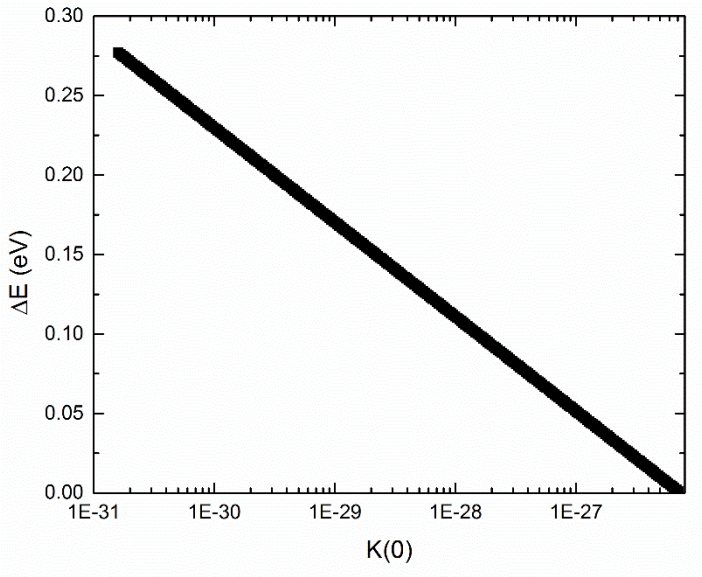

Figure 71 Relationship between energy difference of the excited state and the acceptor LUMO to the equilibrium constant for dissociation of a Wannier-Mott exciton in an applied field.

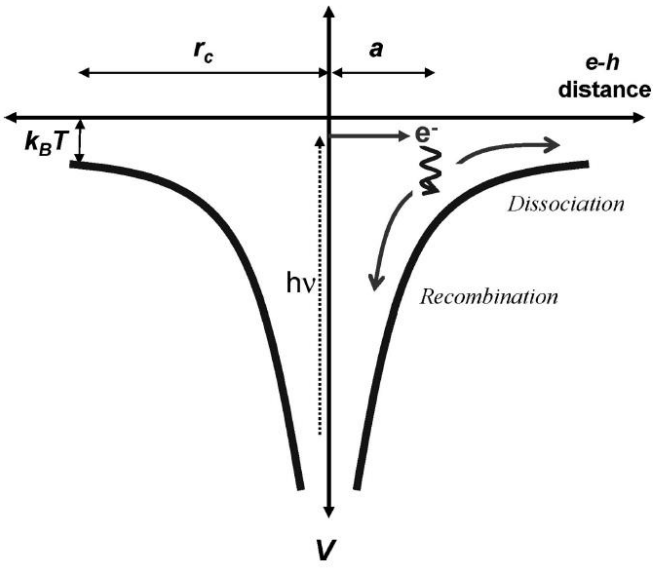

Figure 72 Potential energy diagram summarizing OB theory. Photoexcitation results in generation of a hot, mobile, electron. This electron then thermalizes at a particular distance from the hole, a. If a is less than the Coulomb capture radius, $r_{c,}$ then the CT state can either recombine or dissociate into free charges.

The problem with OB theory is that it currently shows that there is no chance (P(E)< 10^8) for an exciton to dissociate into free charges when parameters are chosen for the equation which accurately reflect the disordered reality of the BHJ. In order for the model to work, an external field must be assumed, such that interfacial partial dipoles are formed upon dissociation of the exciton into the charge transfer state. Nevertheless, it is important to relate the thermalization length a, and the Coulomb capture radius r_c, to the variables within Marcus-Hush theory to form a complete picture of charge photogeneration if indeed these CT states are formed.

Remembering the MH main equation for rate of exciton dissociation, it can be seen that the electron-hole separation is actually defined by the thermodynamic driving force for charge separation.

$$\Delta G° = IP_D - \Delta E_G - EA_A - \frac{e^2}{4\pi\epsilon r_{DA}}$$

In this equation, IP_D is the ionization potential (HOMO) of the donor, ΔE_G is the optical band gap of the excited state species formed on the donor, EA_A is the electron affinity (LUMO) of the acceptor, e is the elementary charge, ϵ is the dielectric constant, and r_{DA} is the effective separation radius between the donor and acceptor. I posit that this effective distance can be equally representative of the size of the excited state after dissociation across the BHJ, and have demonstrated this in published literature[73]. If we substitute this value into the Marcus-Hush full equation, we obtain the following results for the rate of exciton dissociation at the BHJ.

$$k = \frac{2\pi}{\hbar}|H_{DA}|^2 \frac{1}{\sqrt{4\pi\lambda k_B T}}\ exp\left(\frac{-\left((IP_D - \Delta E_G - EA_A - \frac{e^2}{4\pi\epsilon r_{DA}}) + \lambda\right)^2}{4\lambda k_B T}\right)$$

Letting the pre-exponential factor be temporarily equal to A, and solving for r_{DA}, we obtain a term to substitute into the OB theory for a, the thermalization length. I claim that the thermalization length is the same thing as twice the effective donor-acceptor radius, because it is defined as the dissociated length of the exciton at the BHJ, which must by definition be bounded by the DA radius. It is possible that a will be smaller than r_{DA}, and therefore the following two equations will be used to define the upper limit of a.

$$r_{DA} = \frac{-e^2}{8\pi\epsilon\sqrt{-k_B T log \frac{k_r}{\frac{2\pi}{\hbar}|H_{DA}|^2 \frac{1}{\sqrt{4\pi\lambda k_B T}}}} - \lambda + IP_D + \Delta E_G + EA_A}$$

$$P(E) = k_r \frac{3}{4\pi r_{DA}^3} exp \frac{-\Delta E}{k_B T}$$

The second equation of the two presented above directly ties together Marcus-Hush and Onsager-Braun theory. The solution of the equation is non-trivial, but many of the variables are actually able to measured experimentally, thereby reducing the complexity of the equation. Most importantly, my most recent publication has shown that r_{DA}can be measured using the TFXRD technique and taking the coherent crystal domain size, τ, as a relative measurement for r_{DA}. This means then that the probability of free charge generation, P€, can be directly calculated from experimental measurements of τ and ΔE, as well as k_r. This then gives a potential way to directly prescribe molecular design from both theoretical and experimental components.

7.3 Thermodynamics of Aggregation, Crystallization, and BHJ Morphology

7.2.1. Thermodynamics and Organic Photovoltaic Devices

We use a mechanistic approach to design, by synthesizing a sequential variety of squaraine donor molecules with slightly different molecular structures that will impact how

the materials pack in the solid state as well as their transition energetics. Understanding the complex relationship between the molecular structure of the donor, the morphology of the homogeneous domain, the morphology of the bulk heterojunction, and the optoelectronic properties of the finished solar cell is a core research goal of the group.

There are two specific steps of device fabrication and optimization during which the thermodynamics of the system can potentially dominate the resultant morphology being formed: spin-coating the initial device from a heterogeneous solution of donor/acceptor/solvent, and annealing the solid film. In both of these cases it is the Gibbs energy of mixing that is sought because the sign of the energy will tell if the spin-coating/annealing processes are spontaneous or activated. If we are able to generate phase diagrams for a variety of temperatures and compositions, we will be able to predict what phase transitions will occur during a given set of conditions, and understand what annealing temperature is required to move from one phase transition to another. The importance of phase transitions are that they describe how and when a material moves from amorphous to crystalline; the type of morphology present in a solar cell is a dominating factor in its performance and it would be advantageous to have a set of parameters describing the optimum conditions for a specific morphology. Currently, we have no prescriptive approach for explaining the interactions between donor/acceptor/solvent at a nanoscale level. We don't know what happens DURING spin-coating and annealing, because we can only see the final form. Thermodynamics could be the missing link between our different pieces of data.

7.3.2 Our Systems and Phase Segregation

A phase is defined as being a uniform state of a single or multi-component system with reproducible, stable properties dependent only upon thermodynamic phases. The system that we work with in our devices is a three component system initially because it contains a donor, acceptor, and solvent, and upon spin-coating it becomes a two-component system comprised of the donor and acceptor. While still in solution, it is useful to consider the system as being a single phase, with all the molecules dissolved, and no aggregation occurring. This has been verified by absorbance measurements in our group on a variety of squaraines, showing that there is no aggregation of the components in solution unless "special conditions" like co-solvents or PMMA is present. Once the solution has been spun cast, the system is at a minimum bimodal, or composed of two phases. Those two phases would be considered crystalline and amorphous. The composition of those two phases will vary, depending on the composition of the system and the concentration of the two components (donor and acceptor). The amount of the two phases will vary depending on system composition as well as the annealing temperature and time. An example of this is shown in Figure 73.

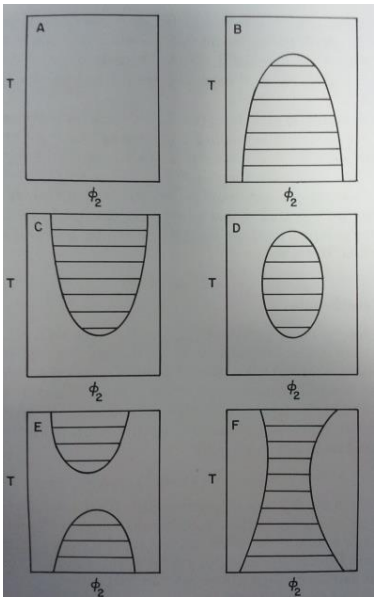

Figure 73 Temperature-composition diagrams showing different variations on complete miscibility and partial miscibility of a two component mixture.

Figure 73 gives a specific example of the miscibility of two components, where complete miscibility and partial miscibility are the two possible phases. In our OPV systems, miscibility becomes very important when we consider how the bulk heterojunction is formed and what it would look like. A thorough explanation of the figure will be provided, because it is informative for any two phase system, whether that system is describing two phases of miscibility or two phases of matter. Interpretations are given of the figure both as it was published, and as it could be interpreted for a SQ/PCBM system. The latter interpretations may or may not be applicable or accurate for our systems, which indicates that the figure/model may or may not give a complete picture. The reason for this is that in order to be examined as a bimodal system, the SQ/PCBM film will be described as two **phases**: **crystalline** *SQ* and **amorphous** *SQ/PCBM*, with the second phase obviously composed of two *components*. Another approach would be to describe the

system as trimodal (not shown) where the crystalline and amorphous phases of the squaraine are considered as separate phases, and each of the three phases therefore will have only one component. A third approach would be to consider the components' miscibility without considering their phases of matter; i.e. exactly as the diagram is drawn, but interpreted for our system. The first approach could be the most simple, and as discussed below appears to give at least some similarities to our actual system, but very quickly breaks down as an interpretative method. The second (trimodal) approach will not be considered as the diagram is only for a bimodal system. The third approach (SQ:PCBM miscibility) is the most logical, but it will result in limited information about the phase change of the individual components (whether they are crystalline or amorphous) and can only be used as a broad brush approach towards describing our system.

(A) shows a two component system with very high miscibility; regardless of the composition or temperature, the system is completely miscible throughout. (B) shows a two component system that has defined parameters; at a fairly wide range of compositions and temperatures, phase segregation (defined as partial miscibility in this figure) can be achieved. If phase segregation were defined instead as crystalline squaraine and amorphous SQ/PCBM, this figure would be interpreted as follows: when no amorphous SQ/PCBM is present the system is fully composed of crystalline squaraine at any temperature. At very high compositions of amorphous SQ/PCBM, the system is entirely crystalline again. This is an obvious example of how an overly simplistic description of a system can break down very quickly, despite initially seeming accurate. At a 50:50 concentration of the two, at high enough temperatures, the system is also purely crystalline. If we return to the original purpose of the picture and consider our system, then we are looking at the change between

partial and complete miscibility of the SQ:PCBM film with increasing PCBM concentration and changing temperature. The diagram then indicates that at most PCBM concentrations and concentrations, the SQ and PCBM would be partially miscible. At high temperatures, no matter the PCBM concentration, there would be complete miscibility of the two components.

(C) shows a system that is essentially identical to (B) in terms of concentration effects, but the opposite of (B) in terms of temperature effects. As demonstrated above in the interpretation for diagram B, our first approach (crystalline SQ/amorphous SQ-PCBM) cannot be effectively utilized to interpret the bimodal diagram in a meaningful way. We will therefore only use the third interpretation approach for (C) and the remaining diagrams. In this case, at low temperatures, as PCBM concentration increases, there is no deviation from complete miscibility. Partial miscibility can only occur at higher temperature. If we think about "partial miscibility" as phase segregation, where the two materials are moving from heterogenous thin films to a quasi-bilayer, this diagram is the one that makes the most sense in terms of our materials. With high enough temperatures, we will get very large domains, that may be composed of exclusively one material. Again, without the ability (theoretical or experimental) to determine the composition of the domains, it is difficult to know the true amount of phase separation that is occurring, as well as whether those phases are crystalline or amorphous.

(D) illustrates a system that requires very specific parameters of temperature and composition to achieve partial miscibility. At low and high temperatures, as well as low and high concentrations of PCBM, the SQ:PCBM film would have complete miscibility of the two materials. This does not seem like a likely situation for our films, as we know from

AFM that with annealing, large squaraine crystals form that do not appear to contain any PCBM. Again, until we better understand the composition of the crystal domains (hopefully through EFTEM!) we cannot completely rule this diagram out.

(E) and (F) are both diagrams of similar phenomena. In (E) there is a temperature at which the system is completely miscible, no matter the concentration of the second compenent. In (F) there is a concentration at which the system is partially miscible, no matter the temperature. We know that in our system of SQ:PCBM, (E) cannot be accurate, because at high concentrations of PCBM phase segregation does occur. (F) is trickier, because there may be a temperature range, for a specific concentration of PCBM, that will always cause partial miscibilitity.

This lengthy discussion of what is a very simple figure serves to illustrate the point that modeling our system is very complicated. The end goal of this thermodynamic consideration was to develop an accurate and predictive temperature-composition phase diagram for a donor/acceptor solid film. Figure 73 and the resultant discussion shows that the first step in establishing a temperature-composition phase diagram is understanding what the species are that will be under investigation, and what phase transitions and phase segregations these species are able to go through. A bimodal description is the simplest, and is the framework for the rest of the paper. Individual components, like SQ aggregates or monomers, will have to be considered separately from each other and their interaction with PCBM described as separate phase-composition diagrams. In the next section, emphasis is placed on understanding the two processes for phase segregation, and the models that can be used to describe them.

7.3.3. Models for Describing Phase Segregation Processes

7.3.3.1. Mixing of Materials

The miscibility of two materials is defined and determined by the Gibbs energy of mixing, which has both entropic and enthalpic terms.

$$\Delta G_{mixing} = \Delta H_{mixing} - T\Delta S_{mixing} \quad (1)$$

Equation 1, the equation of state for mixing, applies to ideal solutions. An ideal solution is a solution whose thermodynamic properties are analogous to the thermodynamic properties of a mixture of ideal gases. While we obviously cannot define a solid film as an ideal solution, Equation 1 is the basis for the models that will be considered. Qualitatively, mixing can be considered as occurring because of interaction/attraction of components, or because of incompatibility/segregation of components. Liquid-liquid phase transitions can occur through either set of processes, whereas liquid-solid phase transitions can only occur through interaction/attraction. In order to know what phase transitions are occurring, it is therefore important to understand the two competing processes of interaction/attraction and incompatibility/segregation, and why one would occur at the expense of the other in the same solid film.

Interaction/attraction can be more accurately called nucleation, while incompatibility/segregation can be called decomposition. In both cases, whether a solid film undergoes one or the other during temperature changes (annealing) is determined by

the initial stability, or free energy, of the film. The initial film stability can be first explained by using a metaphorical mechanical example, as shown in Figure 74.

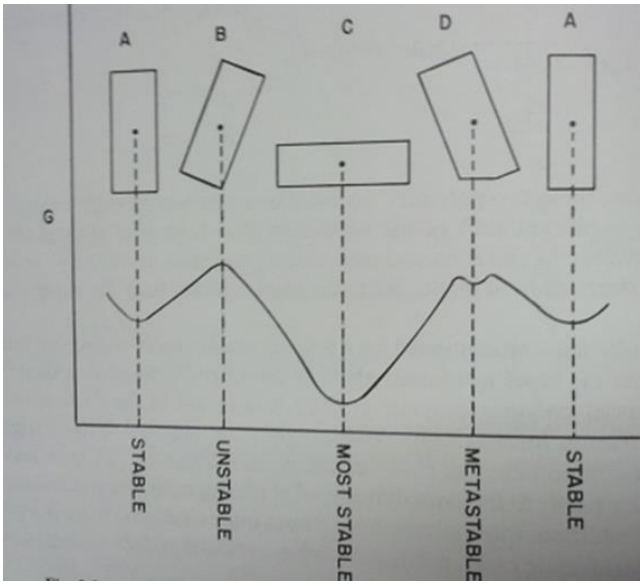

Figure 74 Stability of a block in five positions.

In Figure 74, the abscissa is the position of the block and the ordinate is the Gibbs energy of the block in that state. It is easily seen and understood that the most stable energetic position (C) is when the block is lying on its long axis; it would take a large amount of energy to move it from that position to any of the other positions shown on the diagram. The two stable points (A) are when the block is lying on its short axis, and the unstable point is when the block is balanced precariously on a corner (B). Any small perturbation of the block while it is balanced on that corner would cause it to topple over to either the stable position or the most stable position. The metastable condition (C) is an interesting case because it involves a deformation to the block itself. Cutting off the corner of the block allows it to have a slightly more stable position than the unstable position. If we then extrapolate this metaphor to thin films, we can gain insight into initial film stability

as understood by that film's free energy. To do this, we will look first at the two extremes shown in Figure 74, most stable and unstable. A "most stable" film would have a low Gibbs energy; the film would have been made by a method that allows for both thermodynamic and kinetic energy minima to be reached during film formation, such as drop-casting. An "unstable" film would have a high Gibbs energy; it would be prepared through spin-coating from a very low boiling point solvent, where the film phase morphology is essentially "frozen" after a very short period of time, resulting in a system that has not reached a thermodynamic minima, and whose kinetic minima may be very localized, creating small domains of stability in an otherwise unstable film. The "stable" film could consist of a variety of things, but we can consider it to be a highly kinetically stable film, but whose components may not be at their most thermodynamically stable. In other words, the film may be amorphous, but could become crystalline, which would result in a lower Gibbs energy for the film. The "metastable" film is one that is only slightly more stable than the spun-cast example, and should be considered to be a point on the continuum of film stability in a spun-cast film. Figure 117 shows a possible representation of this continuum, where the continuum is the result of the mechanical metaphor extrapolation just discussed.

SQ:PCBM film to ever be at one or the other extremes, but it is useful to understand what those extremes are.

Once the initial stability has been established, we can then move on to understanding what happens when we subject our film to a variety of temperature changes through annealing, at a variety of different concentrations, by generating a bimodal phase

diagram. A variety of these diagrams were shown in Figure 1, but we will now examine nucleation and decomposition bimodal phase diagrams to understand what can be extracted from them to give us information about our system, based on input parameters like material properties and interaction strengths.

7.3.3.2 Nucleation and Growth

The process of nucleation and growth is the process that forms highly stable crystals and crystalline domains from a metastable initial phase through a liquid to solid transition. As shown in Figure 115, the process of moving from a metastable phase to a more stable phase will require energy and is therefore an activated process. Figure 118 shows a cartoon representation of how this occurs. Starting with a homogeneous solution of composition C_0 (ordinate of upper diagram) the thermodynamics of a two-phase system state that if a nucleus of composition $C`_a$ is formed, the composition of the mother phase in the immediate vicinity of the nucleus would be C_a. As you move away from the nucleus, the composition of the mother phase returns to C_0. The individual molecules that compose the nucleus region are strongly interacting with each other, and cannot diffuse away. Downhill diffusion from the mother phase would occur, setting up a chemical potential gradient shown with arrows in Figure 75, which would continue to feed the nucleus. This will result in a finely dispersed two phase system, with droplet/nucleus sizes dependent upon the time scale of the experiment and the rate of diffusion.

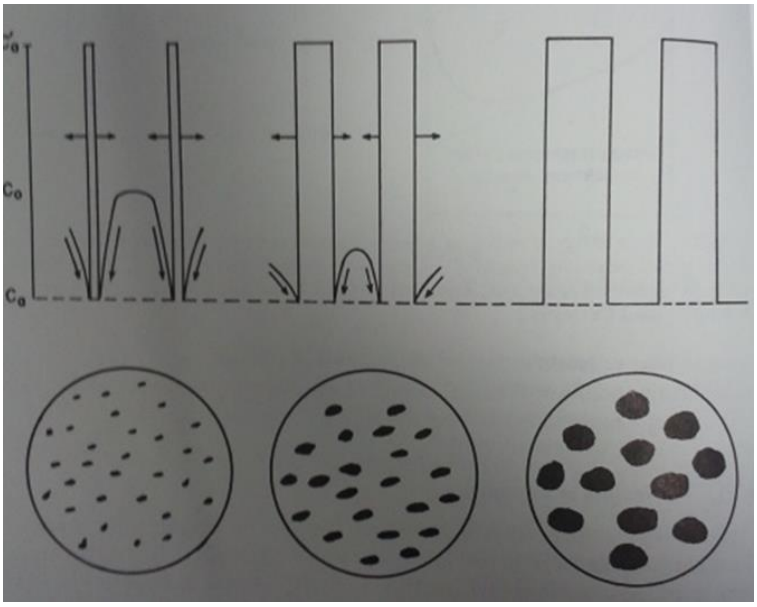

Figure 75 Schematic of the nucleation and growth process. The upper figure shows the time evolution of the process (x-axis) as a function of the concentrations of the initial film phase (mother or metastable phase) and the more stable phase that is being grown, as discussed. The lower figure is simply a cartoon representation of the process, showing the nucleus growing as the phase transition occurs.

As stated above, the reason that a nucleus even exists is because of intermolecular interactions, and it is these interactions that govern the size of the initial nucleus and therefore the extent of the influence the nucleus has on the metastable region around it transforming into the more stable phase. These intermolecular interactions will now be listed and briefly discussed, and we will then move on to the creation of a bimodal diagram for the nucleation process.

i. **Random dipole-induced dipole (London dispersive force)** The only requirement for this force is a ground state oscillation of charge. This oscillation results in an instantaneous temporary dipole

moment (TDM) which can then induce other dipoles in all neighboring molecules. These dipoles can then all interact with each other. The strength of this force is inherently tied to the polarizability of the molecules involved. This can be estimated using the Lorentz equation, Equation 2, where n is the refractive index, V is molar volume, N is Avogadro's number, and α is the polarizability of the molecules.

$$\alpha = \left[\frac{n^2 - 1}{n^2 + 2}\right]\left(\frac{3V}{4\pi N}\right) \quad (2)$$

After α has been calculated it can be used to estimate the magnitude of the interaction energy using the London relationship where U is the London Energy, I is the ionization potential, α is the polarizability, and r is the distance between molecules 1 and 2.

$$U = -\frac{3I_1 I_2 \alpha_1 \alpha_2}{2(I_1 + I_2)r^6} \quad (3)$$

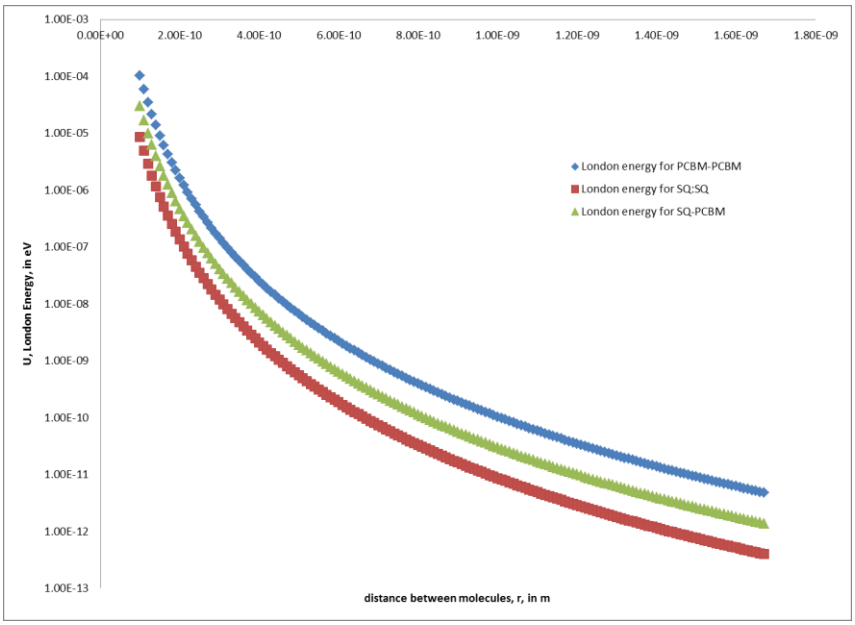

Figure 76 A semi-log plot showing the relationship between the London dispersive force (London energy) and the distance between molecules.

Figure 76 is a "quick and dirty" plot that was made to guide the reader's understanding of the relative size of the interaction, as well as the trend with intermolecular distance. The polarizability value (calculated from Equation 2) was generated with refractive indices that "made sense", and with calculated molar volumes based on the molecular structure of the two components. The ionization potential was taken from XPS measurements of the two molecules, and the distance range was chosen based upon crystallography work. The dispersive force magnitude is dominated by the polarizability terms, which are in turn dominated by the size of the molecule, and the amount of it that is present. Figure 76 was chosen to reflect a 3:7 wt. ratio blend of $DiPSQ(OH)_2$:PCBM.

ii. **Dipole-induced dipole (Debye induction force)** If one molecule has a

permanent dipole moment it will induce dipoles in symmetrical neighboring molecules. This force is weaker than the dispersive force and the electronic force by an order of magnitude, and is calculated using the Debye Induction equation, where α is polarizability, μ is the dipole moment, and U is the Debye induction force

$$U = -\frac{(\alpha_1\mu_2^2 + \alpha_2\mu_1^2)}{r^6} \quad (4)$$

iii. **Dipole-Dipole** If there is a field of dipoles, then the polarizability will no longer be an issue.

$$U = -\frac{2\mu_1^2 2\mu_2^2}{3kTr^6} \quad (5)$$

If the temperature is reasonably small, μ is large, and there are no geometric constraints, the dipoles will align, reducing the r^6 dependence to an r^3 dependence.

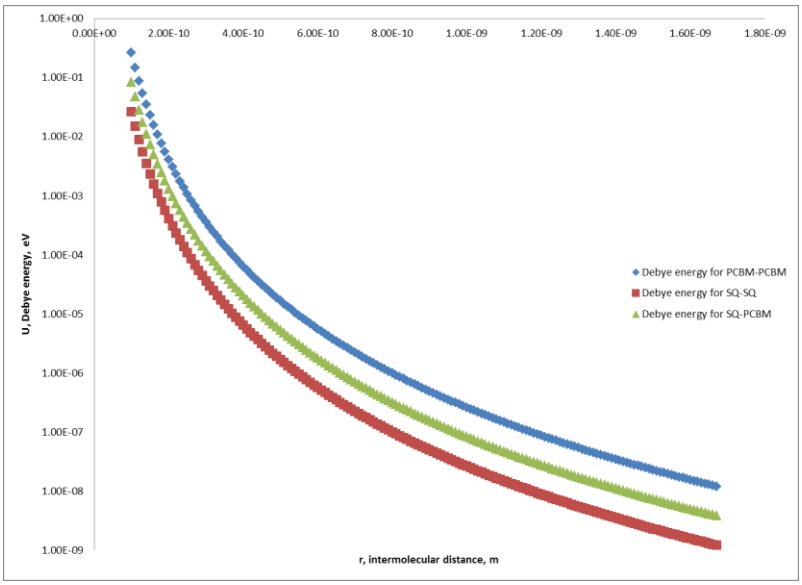

Figure 77 A semi-log plot of Debye energy, made the same way as Figure 5, and with the same purpose.

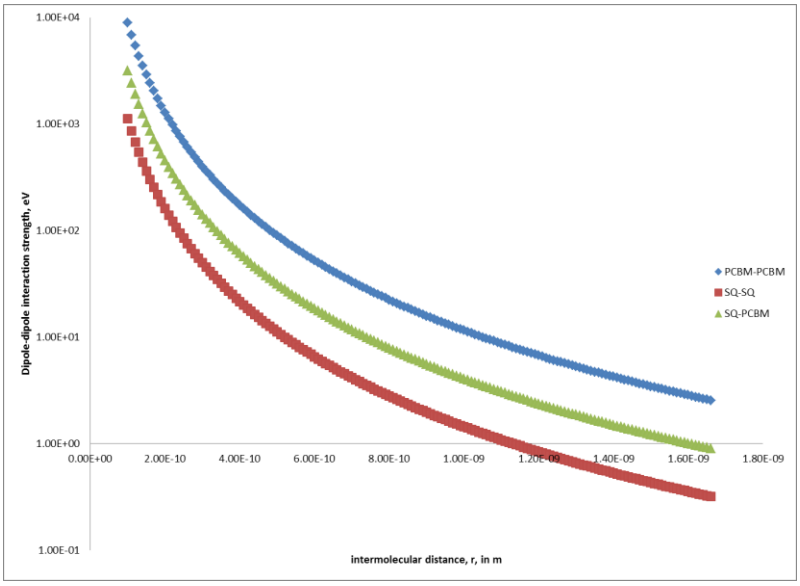

Figure 78 A semi-log plot of the dipole-dipole interaction strength.

It can be seen from the three previous figures that the strength of the various forces is different, and that the dipole-dipole interaction will be the dominant force if permanent dipoles are indeed present. However, too much should not be made of these diagrams, as

they are only meant to offer possibilities for how the systems would behave with parameters that at the very least must be subject to greater scrutiny before formal interpretations could be made.

iv. **Ion-dipole** Typically applicable for molecules in salt solution, with ions present. This interaction will not be discussed further because of the lack of relevance.

v. **Hydrogen bonding** This force requires a hydrogen atom to be covalently bound to an electron withdrawing atom. The structure must have some donatable electrons and the acceptor at a 180 ° angle to the bond of interest for the bond to be strong. This force has the greatest energy contribution of all the molecular forces.

vi. **Charge transfer** This occurs when a two-molecule entity is formed through complete removal of one electron from the orbitals of one molecule to be placed upon the other.

This concludes the summary of the intermolecular forces that govern the formation and existence of a nucleus from which nucleation can occur. We will now consider decomposition, the alternative process for phase transition. Then we will discuss the actual processes of nucleation and decomposition as described by a bimodal diagram showing the relationship between concentration of the two phases (miscible and immiscible) and the Gibbs energy.

7.3.3.3 Decomposition

The process of decomposition is the process that forms a more stable phase from a highly unstable phase through either a liquid-liquid or a liquid-solid transition. It relies upon small amplitude random fluctuations of concentrations that statistically promote continuous and rapid growth. Because it does not require energy (temperature change) in order to occur, it is not an activated process.

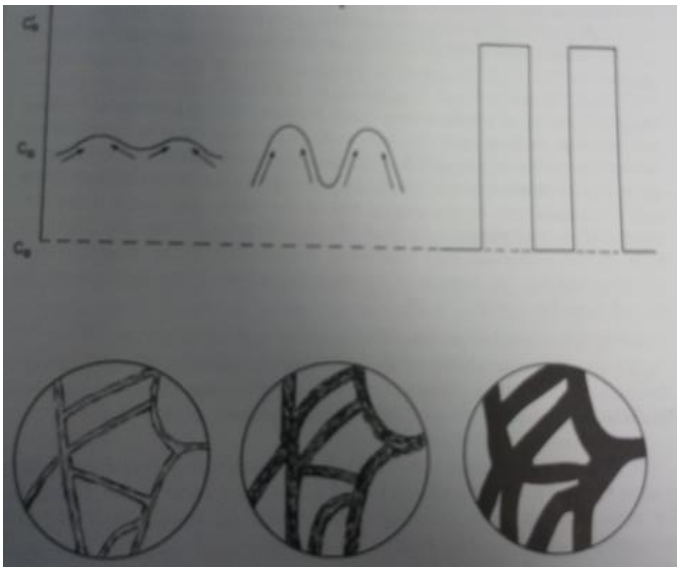

Figure 79 Schematic of the spinodal decomposition process.

The top half of Figure 79 shows concentration on the y-axis and unspecified time evolution on the x-axis. In this multicomponent system, there is an initial concentration of C_0. The left figure in the top half of Figure 79 is showing a random concentration fluctuation of one of the components (component 1), where the individual molecules tend to join energetically favorable permanent clusters. If these molecules continue to diffuse uphill in the direction they were already going in (middle figure), then the system will spontaneously decompose into two phases, with different concentrations of component 1. High

concentrations of component 1 will have a lower energy, thereby creating regions of oscillating concentrations. The kinetics of spinodal composition, and the impact of the oscillating concentration on the resultant morphology, is explained using the Cahn-Hilliard approach.

This approach examines the statistical relationship between the materials system and the existing thermal reservoir for the system, and describes that relationship as a series of fluctuations based on differences in chemical potential.

8. Conclusions

Results from over 2000 squaraine devices are presented within this thesis. The highest efficiency single squaraine device prepared was 5.2%, for a 3:7 blend of the DiPSQ(OH)$_2$:PCBM; the average highest efficiency devices were for the same squaraine, with 4.1 +/- 0.3% achieved in 1:2 blend of DiPSQ(OH)$_2$:PCBM. It was found that the short-circuit current could be manipulated by changing the type of aggregate that was present, which is a direct result of positive impacts upon the rate of exciton dissociation at the BHJ. Direct correlations were established between the presence of aggregates and the formation of crystals, and variations from trends were explained using the kinetics of spin coating and the thermodynamics of annealing. Intense materials characterization was performed for 8 different squaraines, as well as for a variety of cyanine dyes, porphyrins, and oxides that were all considered as viable candidates for inclusion into the device architectures.

Two key results must be highlighted for the P3HT:PCBM devices that were prepared during this thesis work. The first is for gelated P3HT:PCBM devices, which were prepared from a degraded vial of P3HT that was made into a gelated solution through crosslinking of the polymers. Devices prepared immediately without gelation gave efficiencies of 0.63 +/-0.3%. After the gelation process, the efficiencies were 5.2 +/- 0.3%, which is one of the higher efficiencies for that material system when compared to literature[83,155,156]. This is a greater than 8-fold increase in performance. The second key result is for ternary blend devices, prepared with the top performing squaraine to date, DiPSQ(OH)$_2$ and P3HT:PCBM. The ternary blend resulted in efficiencies of 6.6 +/-

0.8%. These results are highlighted here to draw attention to the potential for these two projects (gelation and ternary blends) that were unable to be explored by S. Spencer during the duration of her thesis.

Aggregates are highly useful as electronic and spatial probes of the ultrafast charge photogeneration processes occurring at the bulk heterojunction. Marcus-Hush theory offers a predictive method for understanding which aggregates and materials could offer preferential electron transfer rate constants. If exciton dissociation at the bulk heterojunction is the rate-limiting step as proposed in this work as well as many others, squaraines offer a highly selective energetic and spatial probe of this crucial charge-generating step at the BHJ. Although the efficiency of charge generation should have improved for the devices upon annealing, we have demonstrated that the Marcus-Hush theory can be used to identify why in fact the performance suffered. Additionally, a new approach to understanding the potential exciton dissociation efficiency of a variety of donor species has been proposed. In a complex system with multiple donors, the intermolecular coupling between the donor and acceptor will vary depending on the electronic and spatial properties of the donor species. This variation will impact the exciton dissociation efficiency and could make a species that is energetically less favorable actually be more efficient. Therefore the complete interaction of the donor and acceptor at the bulk heterojunction must be mapped in order to have a full understanding of this rate-limiting step in charge photogeneration.

9.References

(1) Xu, H.; Liu, X. Recent Progress in Metal-Organic Complexes for Optoelectronic Applications. *Chem. Soc. Rev* **2014**, *43*, 3259–3302.

(2) Rosso, K. M.; Morgan, J. J. Outer-Sphere Electron Transfer Kinetics of Metal Ion Oxidation by Molecular Oxygen. *Geochimica et Cosmochimica Acta* **2002**, *66*, 4223–4233.

(3) Clarke, T. M.; Durrant, J. R. Charge Photogeneration in Organic Solar Cells. *Chem. Rev.* **2010**, *110*, 6736–6767.

(4) Reeja-Jayan, B.; Folse, N.; Manthiram, A. Development of Scalable and Low-Cost Polymer Solar Cell Test Platform. *J. Sol. Energy Eng.* **2013**, *135*, 041004–041004.

(5) Lee, W. H.; Cho, J. H.; Cho, K. Control of Mesoscale and Nanoscale Ordering of Organic Semiconductors at the Gate Dielectric/semiconductor Interface for Organic Transistors. *J. Mater. Chem.* **2010**, *20*, 2549–2561.

(6) United States Energy Information Administration. *International Energy Outlook 2011*; DOE/EIA-0484(2011); USEIA, 2011.

(7) International Energy Agency. *World Energy Outlook 2011*; ISBN 978-92-64-12413-4; 2011.

(8) Solomon, S.; Plattner, G.-K.; Knutti, R.; Friedlingstein, P. Irreversible Climate Change due to Carbon Dioxide Emissions. *Proc Natl Acad Sci U S A* **2009**, *106*, 1704–1709.

(9) Martin Parry; O.F. Canziani; J.P. Palutikof; Co-authors. *IPCC Fourth Assessment Report:Climate Change 2007: Working Group II: Impacts, Adaptation and Vulnerability*; Cambridge University Press: Cambridge, UK.

(10) Keith Emory. Best Research-Cell Efficiencies www.nrel.gov/ncpv/images/efficiency_chart.jpg (accessed Jul 19, 2012).

(11) Hoppea, H.; Sariciftci, N. S. Organic Solar Cells: An Overview. *J. Mater. Res* **2004**, *19*, 1925.

(12) Li, G.; Zhu, R.; Yang, Y. Polymer Solar Cells. *Nature Photonics* **2012**, *6*, 153–161.

(13) Gilot, J.; Wienk, M. M.; Janssen, R. A. J. Optimizing Polymer Tandem Solar Cells. *Advanced Materials* **2009**, *22*, E67–E71.

(14) Krebs, F. C.; Tromholt, T.; Jørgensen, M. Upscaling of Polymer Solar Cell Fabrication Using Full Roll-to-Roll Processing. *Nanoscale* **2010**, *2*, 873–886.

(15) Nielsen, T. D.; Cruickshank, C.; Foged, S.; Thorsen, J.; Krebs, F. C. Business, Market and Intellectual Property Analysis of Polymer Solar Cells. *Solar Energy Materials and Solar Cells* **2010**, *94*, 1553–1571.

(16) Krebs, F. C.; Gevorgyan, S. A.; Alstrup, J. A Roll-to-Roll Process to Flexible Polymer Solar Cells: Model Studies, Manufacture and Operational Stability Studies. *J. Mater. Chem.* **2009**, *19*, 5442–5451.

(17) Søndergaard, R.; Hösel, M.; Angmo, D.; Larsen-Olsen, T. T.; Krebs, F. C. Roll-to-Roll Fabrication of Polymer Solar Cells. *Materials Today* **2012**, *15*, 36–49.

(18) Jørgensen, M.; Norrman, K.; Gevorgyan, S. A.; Tromholt, T.; Andreasen, B.; Krebs, F. C. Stability of Polymer Solar Cells. *Advanced Materials* **2011**, *24*, 580–612.

(19) Jørgensen, M.; Norrman, K.; Krebs, F. C. Stability/degradation of Polymer Solar Cells. *Solar Energy Materials and Solar Cells* **2008**, *92*, 686–714.

(20) Olson, D. C.; Shaheen, S. E.; Collins, R. T.; Ginley, D. S. The Effect of Atmosphere and ZnO Morphology on the Performance of Hybrid Poly(3-hexylthiophene)/ZnO Nanofiber Photovoltaic Devices. *J. Phys. Chem. C* **2007**, *111*, 16670–16678.

(21) Søndergaard, R. R.; Makris, T.; Lianos, P.; Manor, A.; Katz, E. A.; Gong, W.; Tuladhar, S. M.; Nelson, J.; Tuomi, R.; Sommeling, P.; Veenstra, S. C.; Rivaton, A.; Dupuis, A.; Teran-Escobar, G.; Lira-Cantu, M.; Sapkota, S. B.; Zimmermann, B.; Würfel, U.; Matzarakis, A.;

Krebs, F. C. The Use of Polyurethane as Encapsulating Method for Polymer Solar cells—An Inter Laboratory Study on Outdoor Stability in 8 Countries. *Solar Energy Materials and Solar Cells* **2012**, *99*, 292–300.

(22) Espinosa, N.; García-Valverde, R.; Urbina, A.; Krebs, F. C. A Life Cycle Analysis of Polymer Solar Cell Modules Prepared Using Roll-to-Roll Methods under Ambient Conditions. *Solar Energy Materials and Solar Cells* **2011**, *95*, 1293–1302.

(23) Anctil, A.; Babbitt, C. W.; Raffaelle, R. P.; Landi, B. J. Cumulative Energy Demand for Small Molecule and Polymer Photovoltaics. *Progress in Photovoltaics: Research and Applications* **2012**, n/a – n/a.

(24) Bronstein, H.; Chen, Z.; Ashraf, R. S.; Zhang, W.; Du, J.; Durrant, J. R.; Shakya Tuladhar, P.; Song, K.; Watkins, S. E.; Geerts, Y.; Wienk, M. M.; Janssen, R. A. J.; Anthopoulos, T.; Sirringhaus, H.; Heeney, M.; McCulloch, I. Thieno[3,2-b]thiophene−Diketopyrrolopyrrole-Containing Polymers for High-Performance Organic Field-Effect Transistors and Organic Photovoltaic Devices. *J. Am. Chem. Soc.* **2011**, *133*, 3272–3275.

(25) Varotto, A.; Nam, C.-Y.; Radivojevic, I.; P. C. Tomé, J.; Cavaleiro, J. A. S.; Black, C. T.; Drain, C. M. Phthalocyanine Blends Improve Bulk Heterojunction Solar Cells. *J. Am. Chem. Soc.* **2010**, *132*, 2552–2554.

(26) Günes, S.; Neugebauer, H.; Sariciftci, N. S. Conjugated Polymer-Based Organic Solar Cells. *Chem. Rev.* **2007**, *107*, 1324–1338.

(27) Ajayaghosh, A. Chemistry of Squaraine-Derived Materials: Near-IR Dyes, Low Band Gap Systems, and Cation Sensors. *Acc. Chem. Res.* **2005**, *38*, 449–459.

(28) Beverina, L.; Salice, P. Squaraine Compounds: Tailored Design and Synthesis towards a Variety of Material Science Applications. *European Journal of Organic Chemistry* **2010**, *2010*, 1207–1225.

(29) Espinosa, N.; Hösel, M.; Angmo, D.; Krebs, F. C. Solar Cells with One-Day Energy Payback for the Factories of the Future. *Energy & Environmental Science* **2012**, *5*, 5117.

(30) Lindholm, F. A.; Fossum, J. G.; Burgess, E. L. Application of the Superposition Principle to Solar-Cell Analysis. *Electron Devices, IEEE Transactions on* **1979**, *26*, 165–171.

(31) Sinton, R. A.; Cuevas, A. Contactless Determination of Current–voltage Characteristics and Minority-carrier Lifetimes in Semiconductors from Quasi-steady-state Photoconductance Data. *Applied Physics Letters* **1996**, *69*, 2510–2512.

(32) Bremner, S. P.; Levy, M. Y.; Honsberg, C. B. Analysis of Tandem Solar Cell Efficiencies under AM1. 5G Spectrum Using a Rapid Flux Calculation Method. *Progress in photovoltaics: Research and Applications* **2008**, *16*, 225–233.

(33) Baruch, P.; De Vos, A.; Landsberg, P. T.; Parrott, J. E. On Some Thermodynamic Aspects of Photovoltaic Solar Energy Conversion. *Solar Energy Materials and Solar Cells* **1995**, *36*, 201–222.

(34) Green. Solar Cell Fill Factors: General Graph and Empirical Expressions. *Solid-State Electronics* **1981**, *24*, 788–789.

(35) Law, K. Y. Squaraine Chemistry: Effects of Structural Changes on the Absorption and Multiple Fluorescence Emission of bis[4-(dimethylamino)phenyl]squaraine and Its Derivatives. *J. Phys. Chem.* **1987**, *91*, 5184–5193.

(36) Vakhshouri, K.; Kozub, D. R.; Wang, C.; Salleo, A.; Gomez, E. D. Effect of Miscibility and Percolation on Electron Transport in Amorphous Poly (3-Hexylthiophene)/Phenyl-C_ ${$61$}$-Butyric Acid Methyl Ester Blends. *Physical Review Letters* **2012**, *108*, 26601.

(37) Patterson, A. L. The Scherrer Formula for X-Ray Particle Size Determination. *Phys. Rev.* **1939**, *56*, 978–982.

(38) Reid, O. G.; Malik, J. A. N.; Latini, G.; Dayal, S.; Kopidakis, N.; Silva, C.; Stingelin, N.; Rumbles, G. The Influence of Solid-state Microstructure on the Origin and Yield of Long-lived Photogenerated Charge in Neat Semiconducting Polymers. *Journal of Polymer Science Part B: Polymer Physics* **2012**, *50*, 27–37.
(39) Dicker, G.; de Haas, M. P.; Siebbeles, L. D. .; Warman, J. M. Electrodeless Time-Resolved Microwave Conductivity Study of Charge-Carrier Photogeneration in Regioregular Poly (3-Hexylthiophene) Thin Films. *Physical Review B* **2004**, *70*, 045203.
(40) Dicker, G. Photogeneration and Dynamics of Charge Carriers in the Conjugated Polymer Poly (3-Hexylthiophene). **2004**.
(41) O'Connor, B. T.; Reid, O. G.; Zhang, X.; Kline, R. J.; Richter, L. J.; Gundlach, D. J.; DeLongchamp, D. M.; Toney, M. F.; Kopidakis, N.; Rumbles, G. Morphological Origin of Charge Transport Anisotropy in Aligned Polythiophene Thin Films. *Adv. Funct. Mater.* **2014**, n/a – n/a.
(42) Scully, S. R.; McGehee, M. D. Effects of Optical Interference and Energy Transfer on Exciton Diffusion Length Measurements in Organic Semiconductors. *Journal of applied physics* **2006**, *100*, 034907.
(43) Tang, C. W.; VanSlyke, S. A.; Chen, C. H. Electroluminescence of Doped Organic Thin Films. *Journal of Applied Physics* **1989**, *65*, 3610–3616.
(44) Terao, Y.; Sasabe, H.; Adachi, C. Correlation of Hole Mobility, Exciton Diffusion Length, and Solar Cell Characteristics in Phthalocyanine/fullerene Organic Solar Cells. *Applied Physics Letters* **2007**, *90*, 103515–103515.
(45) Lunt, R. R.; Benziger, J. B.; Forrest, S. R. Relationship between Crystalline Order and Exciton Diffusion Length in Molecular Organic Semiconductors. *Advanced Materials* **2010**, *22*, 1233–1236.
(46) Niles, E. T.; Roehling, J. D.; Yamagata, H.; Wise, A. J.; Spano, F. C.; Moule, A. J.; Grey, J. K. J-Aggregate Behavior in Poly-3-Hexylthiophene Nanofibers. *The Journal of Physical Chemistry Letters* **2012**.
(47) Shoaee, S.; Clarke, T. M.; Huang, C.; Barlow, S.; Marder, S. R.; Heeney, M.; McCulloch, I.; Durrant, J. R. Acceptor Energy Level Control of Charge Photogeneration in Organic Donor/Acceptor Blends. *J. Am. Chem. Soc.* **2010**, *132*, 12919–12926.
(48) Bakulin, A. A.; Rao, A.; Pavelyev, V. G.; Loosdrecht, P. H. M. van; Pshenichnikov, M. S.; Niedzialek, D.; Cornil, J.; Beljonne, D.; Friend, R. H. The Role of Driving Energy and Delocalized States for Charge Separation in Organic Semiconductors. *Science* **2012**, *335*, 1340–1344.
(49) Suppan, P. The Marcus Inverted Region. In *Photoinduced Electron Transfer IV*; Mattay, J., Ed.; Topics in Current Chemistry; Springer Berlin / Heidelberg, 1992; Vol. 163, pp. 95–130.
(50) Libby, W. F. Theory of Electron Exchange Reactions in Aqueous Solution. *J. Phys. Chem.* **1952**, *56*, 863–868.
(51) Lax, M. The Franck-Condon Principle and Its Application to Crystals. *The Journal of Chemical Physics* **1952**, *20*, 1752–1760.
(52) Onsager, L. Deviations from Ohm's Law in Weak Electrolytes. *The Journal of Chemical Physics* **1934**, *2*, 599–615.
(53) Onsager, L. Initial Recombination of Ions. *Phys. Rev.* **1938**, *54*, 554–557.
(54) Chance, R. R.; Braun, C. L. Intrinsic Photoconduction in Anthracene Single Crystals: Electric Field Dependence of Hole and Electron Quantum Yields. *The Journal of Chemical Physics* **1973**, *59*, 2269–2272.
(55) Chance, R. R.; Braun, C. L. Temperature Dependence of Intrinsic Carrier Generation in Anthracene Single Crystals. *The Journal of Chemical Physics* **1976**, *64*, 3573–3581.

(56) Choi@f@f, H. T.; Sethi@f@f, D. S.; Braun, C. L. Geminate Charge Recombination in the Photoionization of N,N,N′,N′-tetramethyl-p-phenylenediamine (TMPD) in Various Solvents@fa@f). *The Journal of Chemical Physics* **1982**, *77*, 6027–6039.
(57) Pai, D. M.; Enck, R. C. Onsager Mechanism of Photogeneration in Amorphous Selenium. *Phys. Rev. B* **1975**, *11*, 5163–5174.
(58) Braun, C. L. Electric Field Assisted Dissociation of Charge Transfer States as a Mechanism of Photocarrier Production. *The Journal of Chemical Physics* **1984**, *80*, 4157–4161.
(59) Kasha, M. The Exciton Model in Molecular Spectroscopy. *PURE & APPLIED CHEMISTRY* **1965**, *11*, 371.
(60) H. Kautsky; H. Merkel. Phosphoreszenz, Selbstausloschung Und Sensibillisatorwirkung Organischer Stoffe. *Naturwissenschaften* **1939**.
(61) McRae, E. G.; Kasha, M. Enhancement of Phosphorescence Ability upon Aggregation of Dye Molecules. *The Journal of Chemical Physics* **1958**, *28*, 721–722.
(62) Commission, U. S. A. E. *Physical Processes in Radiation Biology: Proceedings of an International Symposium Sponsored by the U.S. Atomic Energy Commission and Held at the Kellogg Center for Continuing Education, Michigan State University, on May 6-8, 1963*; Academic Press, 1964.
(63) Bradley, D. F.; Wolf, M. K. AGGREGATION OF DYES BOUND TO POLYANIONS. *Proc Natl Acad Sci U S A* **1959**, *45*, 944–952.
(64) William W. Brennessel. *Private Communication.*; X-ray Crystallographic Facility of the Department of Chemistry at the University of Rochester.
(65) Turro, N. J.; Scaiano, J. C.; Ramamurthy, V. *Modern Molecular Photochemistry of Organic Molecules*; 1st ed.; University Science Books, 2010.
(66) Kittel, C. *Introduction to Solid State Physics*; 8th ed.; Wiley, 2004.
(67) Madigan, C.; Bulović, V. Modeling of Exciton Diffusion in Amorphous Organic Thin Films. *Phys. Rev. Lett.* **2006**, *96*, 046404.
(68) Menke, S. M.; Holmes, R. J. Exciton Diffusion in Organic Photovoltaic Cells. *Energy Environ. Sci.* **2014**, *7*, 499–512.
(69) Feron, K.; Zhou, X.; Belcher, W. J.; Dastoor, P. C. Exciton Transport in Organic Semiconductors: Förster Resonance Energy Transfer Compared with a Simple Random Walk. *Journal of Applied Physics* **2012**, *111*, 044510.
(70) Sánchez-Carrera, R. S.; Atahan, S.; Schrier, J.; Aspuru-Guzik, A. Theoretical Characterization of the Air-Stable, High-Mobility Dinaphtho[2,3-b:2′3′-f]thieno[3,2-B]-Thiophene Organic Semiconductor. *J. Phys. Chem. C* **2010**, *114*, 2334–2340.
(71) Sokolov, A. N.; Atahan-Evrenk, S.; Mondal, R.; Akkerman, H. B.; Sánchez-Carrera, R. S.; Granados-Focil, S.; Schrier, J.; Mannsfeld, S. C. B.; Zoombelt, A. P.; Bao, Z.; Aspuru-Guzik, A. From Computational Discovery to Experimental Characterization of a High Hole Mobility Organic Crystal. *Nat Commun* **2011**, *2*, 437.
(72) Valleau, S.; Saikin, S. K.; Yung, M.-H.; Guzik, A. A. Exciton Transport in Thin-Film Cyanine Dye J-Aggregates. *The Journal of Chemical Physics* **2012**, *137*, 034109.
(73) Spencer, S.; Cody, J.; Misture, S.; Cona, B.; Heaphy, P.; Rumbles, G.; Andersen, J.; Collison, C. Critical Electron Transfer Rates for Exciton Dissociation Governed by Extent of Crystallinity in Small Molecule Organic Photovoltaics. *J. Phys. Chem. C* **2014**, *118*, 14840–14847.
(74) Chen, W.; Xu, T.; He, F.; Wang, W.; Wang, C.; Strzalka, J.; Liu, Y.; Wen, J.; Miller, D. J.; Chen, J.; Hong, K.; Yu, L.; Darling, S. B. Hierarchical Nanomorphologies Promote Exciton Dissociation in Polymer/Fullerene Bulk Heterojunction Solar Cells. *Nano Lett.* **2011**, *11*, 3707–3713.

(75) Wei, G.; Wang, S.; Sun, K.; Thompson, M. E.; Forrest, S. R. Solvent-Annealed Crystalline Squaraine: PC70BM (1:6) Solar Cells. *Advanced Energy Materials* **2011**, *1*, 184–187.
(76) Paudel, K.; Johnson, B.; Thieme, M.; Haley, M. M.; Payne, M. M.; Anthony, J. E.; Ostroverkhova, O. Enhanced Charge Photogeneration Promoted by Crystallinity in Small-Molecule Donor-Acceptor Bulk Heterojunctions. *Applied Physics Letters* **2014**, *105*, 043301.
(77) Tamura, H.; Burghardt, I. Ultrafast Charge Separation in Organic Photovoltaics Enhanced by Charge Delocalization and Vibronically Hot Exciton Dissociation. *J. Am. Chem. Soc.* **2013**, *135*, 16364–16367.
(78) Shaw, P. E.; Wolfer, P.; Langley, B.; Burn, P. L.; Meredith, P. Impact of Acceptor Crystallinity on the Photophysics of Nonfullerene Blends for Organic Solar Cells. *J. Phys. Chem. C* **2014**, *118*, 13460–13466.
(79) Jung, B.; Kim, K.; Kim, J.; Kim, S.; Kim, E.; Kim, W. Inter-Diffused Ordered Bulk Heterojunction Organic Photovoltaics: Optimized Morphology for Efficient Exciton Dissociation and Charge Transport. *Solar Energy Materials and Solar Cells* **2014**, *120, Part B*, 675–684.
(80) Bansal, N.; Reynolds, L. X.; MacLachlan, A.; Lutz, T.; Ashraf, R. S.; Zhang, W.; Nielsen, C. B.; McCulloch, I.; Rebois, D. G.; Kirchartz, T.; Hill, M. S.; Molloy, K. C.; Nelson, J.; Haque, S. A. Influence of Crystallinity and Energetics on Charge Separation in Polymer–Inorganic Nanocomposite Films for Solar Cells. *Sci. Rep.* **2013**, *3*.
(81) Bernardo, B.; Cheyns, D.; Verreet, B.; Schaller, R. D.; Rand, B. P.; Giebink, N. C. Delocalization and Dielectric Screening of Charge Transfer States in Organic Photovoltaic Cells. *Nat Commun* **2014**, *5*.
(82) Peumans, P.; Forrest, S. R. Separation of Geminate Charge-Pairs at Donor–acceptor Interfaces in Disordered Solids. *Chemical Physics Letters* **2004**, *398*, 27–31.
(83) Kaur, N.; Singh, M.; Pathak, D.; Wagner, T.; Nunzi, J. M. Organic Materials for Photovoltaic Applications: Review and Mechanism. *Synthetic Metals* **2014**, *190*, 20–26.
(84) De Castro, F. .; Heier, J.; Nüesch, F.; Hany, R. Origin of the Kink in Current-Density Versus Voltage Curves and Efficiency Enhancement of Polymer-C Heterojunction Solar Cells. *IEEE Journal of Selected Topics in Quantum Electronics* **2010**, *16*, 1690–1699.
(85) Nüesch, F.; Rotzinger, F.; Si-Ahmed, L.; Zuppiroli, L. Chemical Potential Shifts at Organic Device Electrodes Induced by Grafted Monolayers. *Chemical Physics Letters* **1998**, *288*, 861–867.
(86) Kemerink, M.; Kramer, J. M.; Gommans, H. H. P.; Janssen, R. a. J. Temperature-Dependent Built-in Potential in Organic Semiconductor Devices. *Applied Physics Letters* **2006**, *88*, 192108.
(87) Pope, M.; Swenberg, C. E. *Electronic Processes in Organic Crystals*; 1st ed.; Oxford Univ Pr (Txt), 1982.
(88) Birgerson, J.; Fahlman, M.; Bröms, P.; Salaneck, W. R. Conjugated Polymer Surfaces and Interfaces: A Mini-Review and Some New Results. *Synthetic Metals* **1996**, *80*, 125–130.
(89) Lögdlund, M.; Brédas, J. L. Theoretical Studies of the Interaction between Aluminum and Poly(p-phenylenevinylene) and Derivatives. *The Journal of Chemical Physics* **1994**, *101*, 4357–4364.
(90) Lee, T.-W.; Park, O. O. The Effect of Different Heat Treatments on the Luminescence Efficiency of Polymer Light-Emitting Diodes. *Adv. Mater.* **2000**, *12*, 801–804.
(91) Hallermann, M.; Haneder, S.; Como, E. D. Charge-Transfer States in Conjugated Polymer/fullerene Blends: Below-Gap Weakly Bound Excitons for Polymer Photovoltaics. *Applied Physics Letters* **2008**, *93*, 053307.

(92) Shanbin, Z. Photo and Dark Current Mechanisms in Organic Heterojunction Solar Cells. Doctoral Dissertation, Standford University, 2010.
(93) Mayerhöffer, U.; Würthner, F. Cooperative Self-Assembly of Squaraine Dyes. *Chemical Science* **2012**, *3*, 1215.
(94) Law, K. Y. Organic Photoconductive Materials: Recent Trends and Developments. *Chem. Rev.* **1993**, *93*, 449–486.
(95) Usluer, Ö.; Kästner, C.; Abbas, M.; Ulbricht, C.; Cimrova, V.; Wild, A.; Birckner, E.; Tekin, N.; Sariciftci, N. S.; Hoppe, H.; others. Charge Carrier Mobility, Photovoltaic, and Electroluminescent Properties of Anthracene-Based Conjugated Polymers Bearing Randomly Distributed Side Chains. *Journal of Polymer Science Part A: Polymer Chemistry* **2012**.
(96) Paquin, F.; Latini, G.; Sakowicz, M.; Karsenti, P.-L.; Wang, L.; Beljonne, D.; Stingelin, N.; Silva, C. Charge Separation in Semicrystalline Polymeric Semiconductors by Photoexcitation: Is the Mechanism Intrinsic or Extrinsic? *Phys. Rev. Lett.* **2011**, *106*, 197401.
(97) Takeshima, M.; Matsui, A. H. Frenkel Exciton States in Microcrystallites. *Chemical Physics Letters* **1997**, *266*, 135–138.
(98) Verlaak, S.; Arkhipov, V.; Heremans, P. Modeling of Transport in Polycrystalline Organic Semiconductor Films. *Applied Physics Letters* **2003**, *82*, 745–747.
(99) Ma, W.; Yang, C.; Gong, X.; Lee, K.; Heeger, A. J. Thermally Stable, Efficient Polymer Solar Cells with Nanoscale Control of the Interpenetrating Network Morphology. *Advanced Functional Materials* **2005**, *15*, 1617–1622.
(100) Sun, S. S.; Sariciftci, N. S. *Organic Photovoltaics: Mechanisms, Materials, and Devices*; CRC, 2005; Vol. 99.
(101) Nelson, J.; Kwiatkowski, J. J.; Kirkpatrick, J.; Frost, J. M. Modeling Charge Transport in Organic Photovoltaic Materials. *Acc. Chem. Res.* **2009**, *42*, 1768–1778.
(102) Liang, K.; Law, K. Y.; Whitten, D. G. Estimation of Exciton Sizes in Squaraine Monolayers by Intralayer Photoinduced Electron Transfer. *The Journal of Physical Chemistry* **1995**, *99*, 16704–16708.
(103) Minoshima, K.; Taiji, M.; Misawa, K.; Kobayashi, T. Femtosecond Nonlinear Optical Dynamics of Excitons in J-Aggregates. *Chemical Physics Letters* **1994**, *218*, 67–72.
(104) Hoppe, H.; Glatzel, T.; Niggemann, M.; Hinsch, A.; Lux-Steiner, M. C.; Sariciftci, N. S. Kelvin Probe Force Microscopy Study on Conjugated Polymer/Fullerene Bulk Heterojunction Organic Solar Cells. *Nano Lett.* **2005**, *5*, 269–274.
(105) Cha, H.; Kong, H.; Chung, D. S.; Yun, W. M.; An, T. K.; Hwang, J.; Kim, Y.-H.; Shim, H.-K.; Park, C. E. Thermally Stable Amorphous Polymeric Semiconductors Containing Fluorene and Thiophene for Use in Organic Photovoltaic Cells. *Organic Electronics* **2010**, *11*, 1534–1542.
(106) Spencer, S. D.; Bougher, C.; Heaphy, P. J.; Murcia, V. M.; Gallivan, C. P.; Monfette, A.; Andersen, J. D.; Cody, J. A.; Conrad, B. R.; Collison, C. J. The Effect of Controllable Thin Film Crystal Growth on the Aggregation of a Novel High Panchromaticity Squaraine Viable for Organic Solar Cells. *Solar Energy Materials and Solar Cells* **2013**, *112*, 202–208.
(107) Spencer, S.; Murcia, V.; Reid, O.; Rumbles, G.; Belfield, K.; Cody, J.; Collison, C. Influence of Squaraine Aggregation on Short-Circuit Current and Device Efficiency. In *2012 38th IEEE Photovoltaic Specialists Conference (PVSC)*; 2012; pp. 002775–002779.
(108) Spencer, S.; Hu, H.; Li, Q.; Ahn, H.-Y.; Qaddoura, M.; Yao, S.; Ioannidis, A.; Belfield, K.; Collison, C. J. Controlling J-Aggregate Formation for Increased Short-Circuit Current and

Power Conversion Efficiency with a Squaraine Donor. *Prog. Photovolt: Res. Appl.* **2014**, *22*, 488–493.
(109) Chen, G.; Sasabe, H.; Lu, W.; Wang, X.-F.; Kido, J.; Hong, Z.; Yang, Y. J-Aggregation of a Squaraine Dye and Its Application in Organic Photovoltaic Cells. *J. Mater. Chem. C* **2013**, *1*, 6547–6552.
(110) Würthner, F.; Kaiser, T. E.; Saha-Möller, C. R. J-Aggregates: From Serendipitous Discovery to Supramolecular Engineering of Functional Dye Materials. *Angewandte Chemie International Edition* **2011**, *50*, 3376–3410.
(111) Kaiser, T. E.; Wang, H.; Stepanenko, V.; Würthner, F. Supramolecular Construction of Fluorescent J-Aggregates Based on Hydrogen-Bonded Perylene Dyes. *Angewandte Chemie International Edition* **2007**, *46*, 5541–5544.
(112) Das, A.; Ghosh, S. Contrasting Self-Assembly and Gelation Properties among Bis-Urea-and Bis-Amide-Functionalised Dialkoxynaphthalene (DAN) Π Systems. *Chemistry-A European Journal* **2010**, *16*, 13622–13628.
(113) Molla, M. R.; Ghosh, S. Hydrogen-Bonding-Mediated J-Aggregation and White-Light Emission from a Remarkably Simple, Single-Component, Naphthalenediimide Chromophore. *Chemistry-A European Journal* **2012**, *18*, 1290–1294.
(114) Zhang, C. DFT Study on Methanofullerene Derivative [6,6]-Phenyl-C61 Butyric Acid Methyl Ester. *Acta Physico-Chimica Sinica* **2008**, *24*, 1353–1358.
(115) Song, B.; Rolin, C.; Zimmerman, J. D.; Forrest, S. R. Effect of Mixed Layer Crystallinity on the Performance of Mixed Heterojunction Organic Photovoltaic Cells. *Adv. Mater.* **2014**, *26*, 2914–2918.
(116) Seunguk, N.; Donggu, L.; Jun, Y. K.; Yongju, P.; Changhee, L.; Jason, J. A. Area and Light Intensity Dependence of Buffer Layers on P3HT:PCBM Solar Cells. *Journal of the Korean Physical Society* **2011**, *59*, 207.
(117) Ideality Factor http://pveducation.org/pvcdrom/solar-cell-operation/ideality-factor (accessed Sep 5, 2013).
(118) Garcia-Belmonte, G.; Munar, A.; Barea, E. M.; Bisquert, J.; Ugarte, I.; Pacios, R. Charge Carrier Mobility and Lifetime of Organic Bulk Heterojunctions Analyzed by Impedance Spectroscopy. *Organic Electronics* **2008**, *9*, 847–851.
(119) Bisquert, J. Theory of the Impedance of Electron Diffusion and Recombination in a Thin Layer. *J. Phys. Chem. B* **2002**, *106*, 325–333.
(120) Shah, J. M.; Li, Y.-L.; Gessmann, T.; Schubert, E. F. Experimental Analysis and Theoretical Model for Anomalously High Ideality Factors (n>2.0) in AlGaN/GaN P-N Junction Diodes. *Journal of Applied Physics* **2003**, *94*, 2627–2630.
(121) Forrest, S. R. The Limits to Organic Photovoltaic Cell Efficiency. *MRS bulletin* **2005**, *30*, 28–32.
(122) Zeng, L.; Tang, C. W.; Chen, S. H. Effects of Active Layer Thickness and Thermal Annealing on Polythiophene: Fullerene Bulk Heterojunction Photovoltaic Devices. *Applied Physics Letters* **2010**, *97*, 053305–053305.
(123) Weickert, J.; Dunbar, R. B.; Hesse, H. C.; Wiedemann, W.; Schmidt-Mende, L. Nanostructured Organic and Hybrid Solar Cells. *Advanced Materials* **2011**, *23*, 1810–1828.
(124) Chen, H. Y.; Hou, J.; Zhang, S.; Liang, Y.; Yang, G.; Yang, Y.; Yu, L.; Wu, Y.; Li, G. Polymer Solar Cells with Enhanced Open-Circuit Voltage and Efficiency. *Nature Photonics* **2009**, *3*, 649–653.

(125) Grancini, G.; Maiuri, M.; Fazzi, D.; Petrozza, A.; Egelhaaf, H.-J.; Brida, D.; Cerullo, G.; Lanzani, G. Hot Exciton Dissociation in Polymer Solar Cells. *Nature Materials* **2013**, *12*, 29–33.
(126) Godovsky, D. Modeling the Ultimate Efficiency of Polymer Solar Cell Using Marcus Theory of Electron Transfer. *Organic Electronics* **2011**, *12*, 190–194.
(127) Schwenn, P. E.; Gui, K.; Zhang, Y.; Burn, P. L.; Meredith, P.; Powell, B. J. Kinetics of Charge Transfer Processes in Organic Solar Cells: Implications for the Design of Acceptor Molecules. *Organic Electronics* **2012**, *13*, 2538–2545.
(128) Chen, G.; Sasabe, H.; Sasaki, Y.; Katagiri, H.; Wang, X.-F.; Sano, T.; Hong, Z.; Yang, Y.; Kido, J. A Series of Squaraine Dyes: Effects of Side Chain and the Number of Hydroxyl Groups on Material Properties and Photovoltaic Performance. *Chem. Mater.* **2014**, *26*, 1356–1364.
(129) Kaake, L. G.; Barbara, P. F.; Zhu, X.-Y. Intrinsic Charge Trapping in Organic and Polymeric Semiconductors: A Physical Chemistry Perspective. *J. Phys. Chem. Lett.* **2010**, *1*, 628–635.
(130) Gaynor, W.; Burkhard, G. F.; McGehee, M. D.; Peumans, P. Smooth Nanowire/polymer Composite Transparent Electrodes. *Advanced Materials* **2011**, *23*, 2905–2910.
(131) Michael Mehan. *X-Ray Photoelectron Spectroscopy Report, Private Communication.*
(132) Gust, D.; Moore, T. A.; Moore, A. L. Molecular Mimicry of Photosynthetic Energy and Electron Transfer. *Acc. Chem. Res.* **1993**, *26*, 198–205.
(133) Gould, I. R.; Young, R. H.; Mueller, L. J.; Farid, S. Mechanisms of Exciplex Formation. Roles of Superexchange, Solvent Polarity, and Driving Force for Electron Transfer. *J. Am. Chem. Soc.* **1994**, *116*, 8176–8187.
(134) Lees, E.; Kelly, K.; Bougher, C.; Spencer, S.; Heaphy, P.; Cody, J.; Collison, C.; Coffey, T.; Conrad, B. Characterization of Organic Solar Cell Morphology. In *Bulletin of the American Physical Society*; American Physical Society, 2013; Vol. Volume 58, Number 1.
(135) Coffey, D. C.; Larson, B. W.; Hains, A. W.; Whitaker, J. B.; Kopidakis, N.; Boltalina, O. V.; Strauss, S. H.; Rumbles, G. An Optimal Driving Force for Converting Excitons into Free Carriers in Excitonic Solar Cells. *J. Phys. Chem. C* **2012**, *116*, 8916–8923.
(136) Mulliken, R. S. Molecular Compounds and Their Spectra. II. *J. Am. Chem. Soc.* **1952**, *74*, 811–824.
(137) B.J.McC. Molecular Complexes : R.S. Mulliken and W.B. Person, Wiley-Interscience, New York and London, 1969, Pp. xv+498, Price £9.25. *Journal of Molecular Structure* **1971**, *10*, 155.
(138) Cotton, F. A. *Progress in Inorganic Chemistry*; John Wiley & Sons, 2009.
(139) Hush, N. S. Homogeneous and Heterogeneous Optical and Thermal Electron Transfer. *Electrochimica Acta* **1968**, *13*, 1005–1023.
(140) Reimers, J. R.; Hush, N. S. Electronic Properties of Transition-Metal Complexes Determined from Electroabsorption (Stark) Spectroscopy. 2. Mononuclear Complexes of ruthenium(II). *J. Phys. Chem.* **1991**, *95*, 9773–9781.
(141) Creutz, C.; Newton, M. D.; Sutin, N. Metal—lingad and Metal—metal Coupling Elements. *Journal of Photochemistry and Photobiology A: Chemistry* **1994**, *82*, 47–59.
(142) Hilborn, R. C. Einstein Coefficients, Cross Sections, F Values, Dipole Moments, and All That. *arXiv:physics/0202029* **2002**.
(143) Barbara, P. F.; Meyer, T. J.; Ratner, M. A. Contemporary Issues in Electron Transfer Research. *The Journal of Physical Chemistry* **1996**, *100*, 13148–13168.
(144) Cave, R. J.; Newton, M. D. Calculation of Electronic Coupling Matrix Elements for Ground and Excited State Electron Transfer Reactions: Comparison of the Generalized Mulliken–

Hush and Block Diagonalization Methods. *The Journal of Chemical Physics* **1997**, *106*, 9213–9226.
(145) Spano, F. C.; Yamagata, H. Vibronic Coupling in J-Aggregates and Beyond: A Direct Means of Determining the Exciton Coherence Length from the Photoluminescence Spectrum†. *The Journal of Physical Chemistry B* **2011**.
(146) Spano, F. C. The Spectral Signatures of Frenkel Polarons in H-and J-Aggregates. *Accounts of chemical research* **2009**, *43*, 429–439.
(147) Mayerhöffer, U.; Deing, K.; Gru\ss, K.; Braunschweig, H.; Meerholz, K.; Würthner, F. Outstanding Short-Circuit Currents in BHJ Solar Cells Based on NIR-Absorbing Acceptor-Substituted Squaraines. *Angewandte Chemie International Edition* **2009**, *48*, 8776–8779.
(148) Wei, G.; Shiu, K. T.; Giebink, N. C.; Forrest, S. R. Thermodynamic Limits of Quantum Photovoltaic Cell Efficiency. *Applied Physics Letters* **2007**, *91*, 223507–223507.
(149) Jelley, E. E. Spectral Absorption and Fluorescence of Dyes in the Molecular State. *Nature* **1936**, *138*, 1009–1010.
(150) Chen, H.; Farahat, M. S.; Law, K. Y.; Whitten, D. G. Aggregation of Surfactant Squaraine Dyes in Aqueous Solution and Microheterogeneous Media: Correlation of Aggregation Behavior with Molecular Structure. *Journal of the American Chemical Society* **1996**, *118*, 2584–2594.
(151) Law, K. Y.; Bailey, F. C. Squaraine Chemistry. Synthesis, Characterization, and Optical Properties of a Class of Novel Unsymmetrical Squaraines: [4-(dimethylamino)phenyl](4'-Methoxyphenyl)squaraine and Its Derivatives. *J. Org. Chem.* **1992**, *57*, 3278–3286.
(152) Kim, Y. S.; Liang, K.; Law, K. Y.; Whitten, D. G. An Investigation of Photocurrent Generation by Squaraine Aggregates in Monolayer-Modified Tin Oxide (SnO2) Electrodes. *The Journal of Physical Chemistry* **1994**, *98*, 984–988.
(153) Germack, D. S.; Chan, C. K.; Kline, R. J.; Fischer, D. A.; Gundlach, D. J.; Toney, M. F.; Richter, L. J.; DeLongchamp, D. M. Interfacial Segregation in Polymer/fullerene Blend Films for Photovoltaic Devices. *Macromolecules* **2010**, *43*, 3828–3836.
(154) Zhang, X.; Bronstein, H.; Kronemeijer, A. J.; Smith, J.; Kim, Y.; Kline, R. J.; Richter, L. J.; Anthopoulos, T. D.; Sirringhaus, H.; Song, K.; Heeney, M.; Zhang, W.; McCulloch, I.; DeLongchamp, D. M. Molecular Origin of High Field-Effect Mobility in an Indacenodithiophene–benzothiadiazole Copolymer. *Nat Commun* **2013**, *4*.
(155) Piris, J.; Dykstra, T. E.; Bakulin, A. A.; Loosdrecht, P. H. M. van; Knulst, W.; Trinh, M. T.; Schins, J. M.; Siebbeles, L. D. A. Photogeneration and Ultrafast Dynamics of Excitons and Charges in P3HT/PCBM Blends. *J. Phys. Chem. C* **2009**, *113*, 14500–14506.
(156) Zhao, J.; Swinnen, A.; Van Assche, G.; Manca, J.; Vanderzande, D.; Mele, B. V. Phase Diagram of P3HT/PCBM Blends and Its Implication for the Stability of Morphology. *J. Phys. Chem. B* **2009**, *113*, 1587–1591.
(157) Lipnik, A. A. BINDING AND DECAY OF THE MOTT EXCITON BY PHONONS AND IMPURITY CENTERS. *SOVIET PHYSICS-SOLID STATE* **1962**, *3*, 1683–1689.
(158) LIPNIK, A. CHARGE CARRIER DRAG ON MOTT EXCITONS AND THE EFFECT OF ZERO AND NEGATIVE MOBILITY. *SOVIET PHYSICS-SOLID STATE* **1964**, *6*, 828–829.
(159) LIPNIK, A. CERTAIN CHARACTERISTICS OF THE PROCESS OF PAIR COUPLING TO FORM AN EXCITON AND EXCITON DISSOCIATION BY PHONONS-EFFECT OF THESE PROCESSES ON THE BEHAVIOR OF NONEQUILIBRIUM CARRIERS. *SOVIET PHYSICS-SOLID STATE* **1964**, *6*, 823–827.
(160) Langevin, P. L'ionization Des Gaz. *Ann. Chim. Phys* **1903**, *28*, 443.
(161) Langevin, P. Recombinaison et Mobilites Des Ions Dans Les Gaz. *Ann. Chim. Phys* **1903**, *28*, 122.

(162) Alivisatos, P.; Barbara, P. F.; Castleman, A. W.; Chang, J.; Dixon, D. A.; Klein, M. L.; McLendon, G. L.; Miller, J. S.; Ratner, M. A.; Rossky, P. J.; Stupp, S. I.; Thompson, M. E. From Molecules to Materials: Current Trends and Future Directions. *Advanced Materials* **1998**, *10*, 1297–1336.

(163) Pensack, R. D.; Guo, C.; Vakhshouri, K.; Gomez, E. D.; Asbury, J. B. Influence of Acceptor Structure on Barriers to Charge Separation in Organic Photovoltaic Materials. *The Journal of Physical Chemistry C* **2012**, *116*, 4824–4831.

10. Appendices

10.1. Appendix A: Additional Figures

Modeling Absorbance Spectra

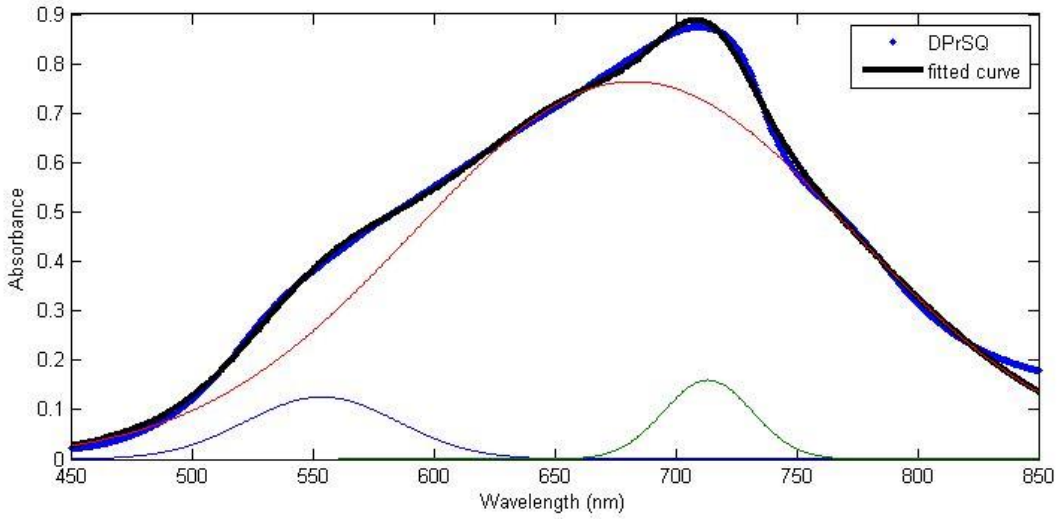

A tri-gaussian fit of DPrSQ with 95% confidence intervals.

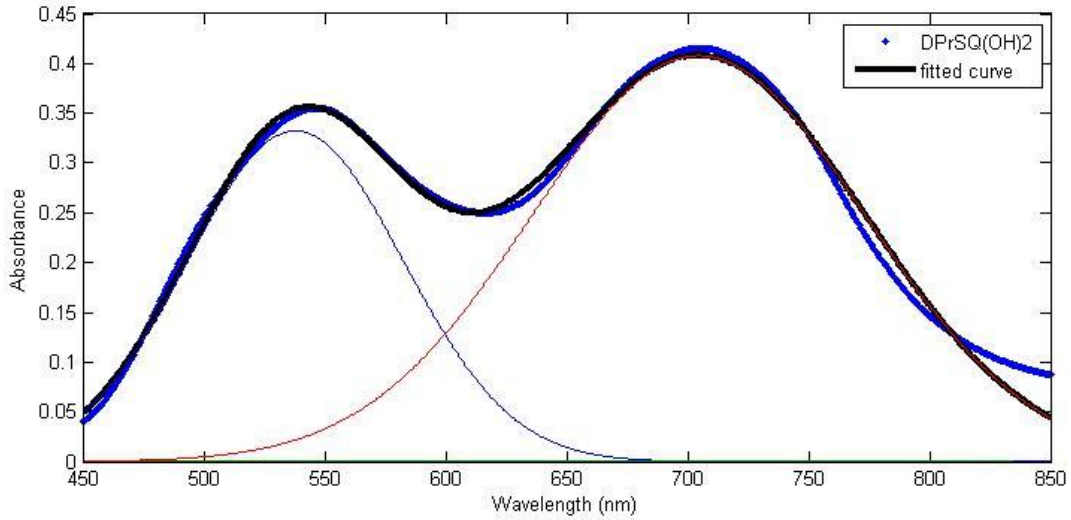

A tri-gaussian fit of DPrSQ[OH]$_2$ with 95% confidence level.

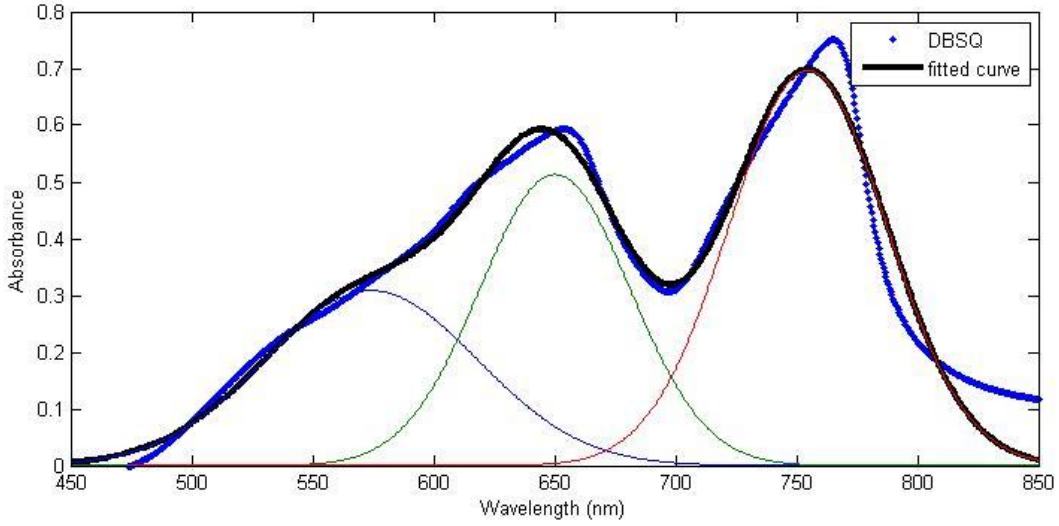

A tri-gaussian fit of DBSQ with 95% confidence level.

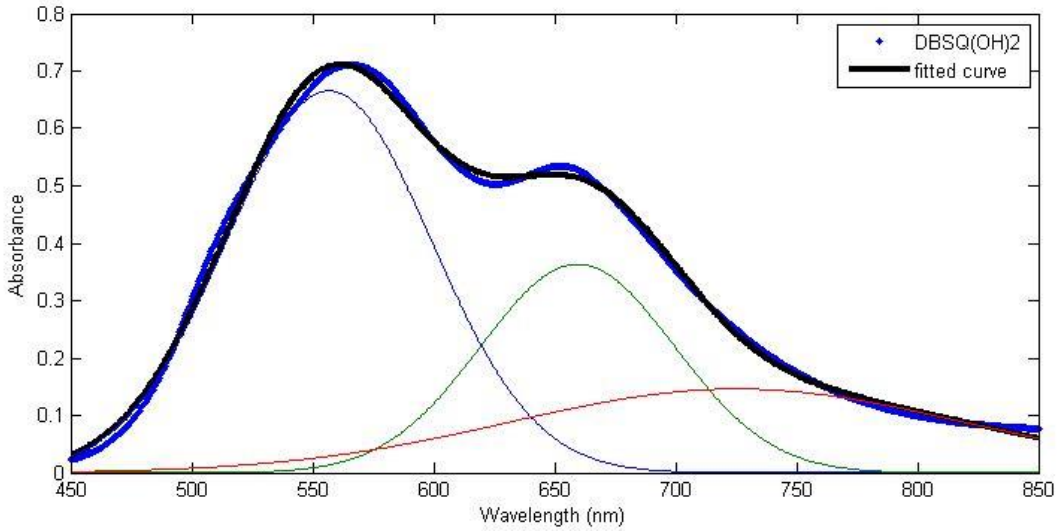

A tri-gaussian fit of DBSQ[OH]$_2$ with 95% confidence level.

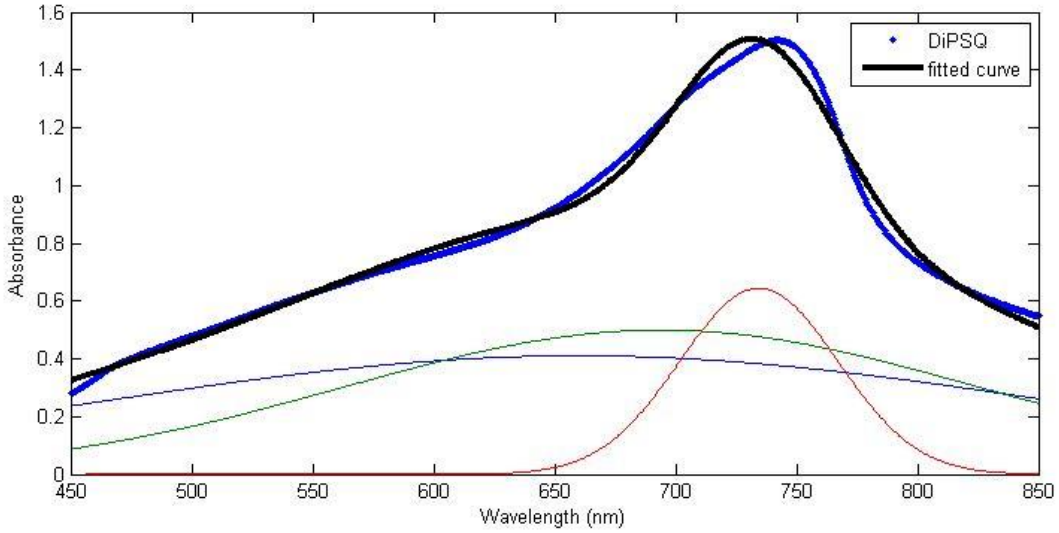

A tri-gaussian fit of DiPSQ with 95% confidence level.

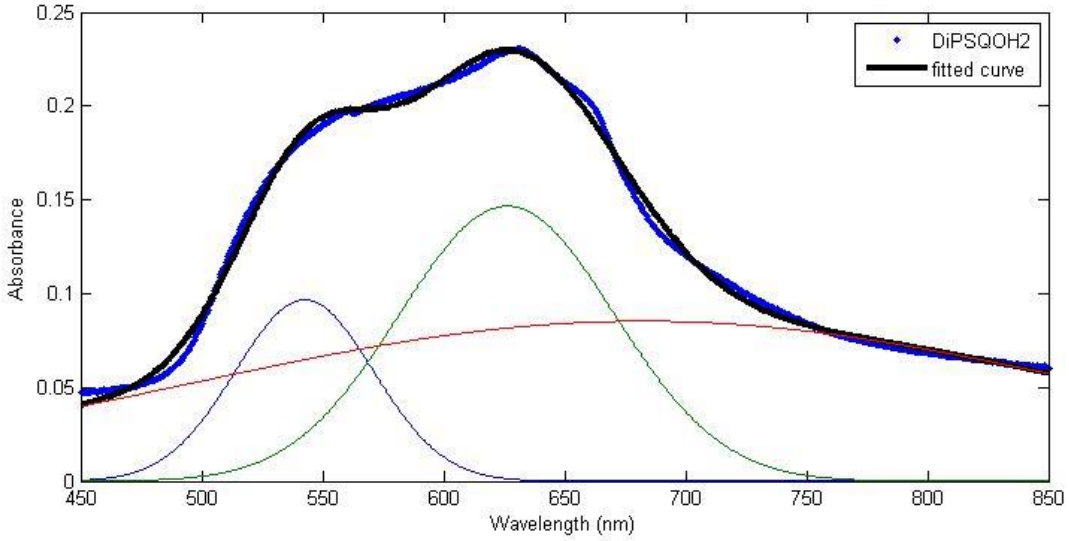

A tri-gaussian fit of DiPSQ[OH]$_2$ with 95% confidence level.

Values from NIST used to extrapolate the instrument response function width for accurate calculation of the τ value from the Scherrer equation.

Profile Fitting Report

[SRM675_Mica_Apr-07-2014.raw] Commander Sample ID

R = (Un-refined), Total Area = 288411 (5043), Crystallinity = ?

@ 2-Theta	d(Å)	Height	Area(a1)	Area%	FWHM	XS(Å)
8.862 (0.002)	9.9708 (0.0036)	21622 (583)	116925 (2920)	100.0	0.068 (0.002)	>1000 (?)
17.760 (0.001)	4.9900 (0.0008)	1108 (36)	5502 (186)	4.7	0.061 (0.002)	>1000 (?)
26.776 (0.001)	3.3268 (0.0004)	22940 (903)	107877 (4012)	92.3	0.058 (0.002)	>1000 (?)
28.501 (0.001)	3.1292 (0.0002)	2123 (49)	12332 (296)	10.5	0.072 (0.002)	>1000 (?)
45.389 (0.001)	1.9965 (0.0001)	4323 (107)	26466 (599)	22.6	0.074 (0.002)	>1000 (?)
55.140 (0.002)	1.6643 (0.0001)	1339 (38)	14788 (419)	12.6	0.136 (0.004)	>1000 (?)
69.289 (0.009)	1.3550 (0.0003)	417 (27)	4522 (382)	3.9	0.159 (0.014)	>1000 (?)

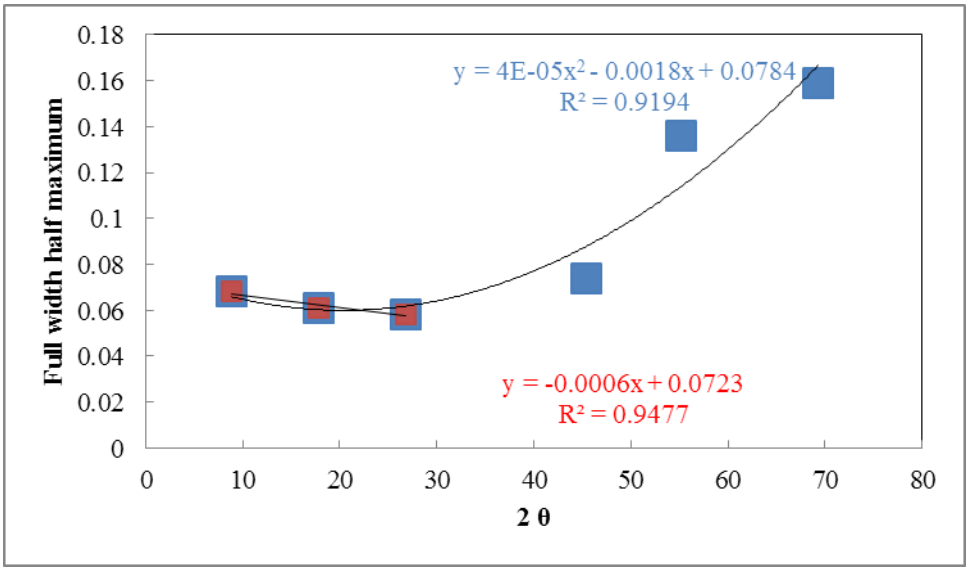

ccx

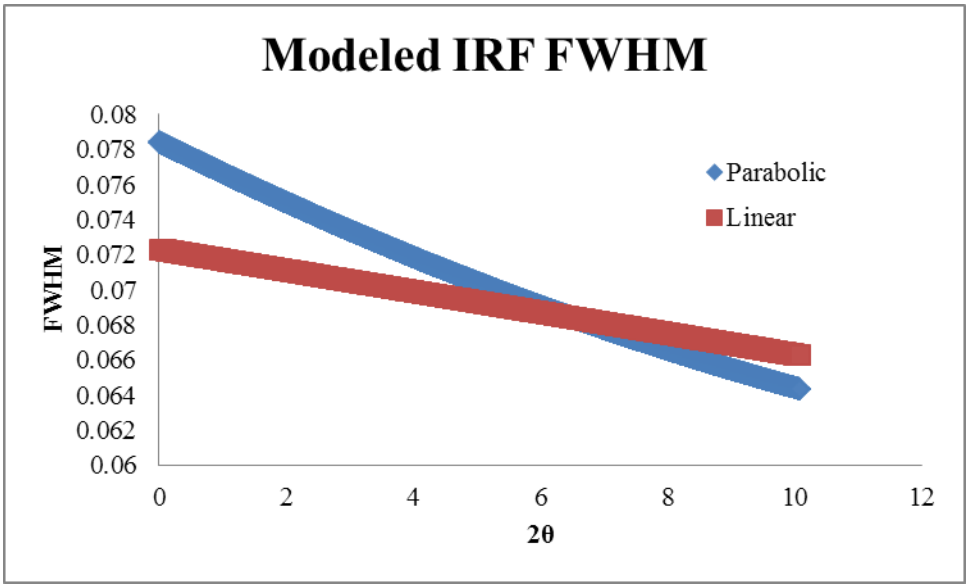

Co-solvent Work

Purpose of Experiment.

In order to realize the goal of fully solution-processable bulk heterojunction device layers made from squaraines and PCBM, the effect of 10 different co-solvents on the intensity and position of the NIR absorbance peak was examined. By understanding which solvent systems are able to cause J-aggregation (as demonstrated by a red shift in the peak) and H-aggregation (blue shift) for both the squaraine alone and with acceptor (PCBM) present, I hope to predict the ideal solvent system for maximum NIR absorption. As shown by Marks et al, subtle variations in π-π stacking properties that have minor effects on solution phase molecular observables can result in significant differences in OPV performance.[1]Follow-up to this work will be the optimization of the device solution processing for maximum red spectral shift and blue spectral shift. These optimized

devices will then be characterized with absorbance, fluorescence, spectral response, AFM, and I-V measurements in order to correlate device performance with aggregation type.

Methodology in Brief.

The 10 co-solvents were selected based on prior work performed by Hyo-Yang Ahn and Jason Staub. They were selected to span a variety of dielectric constants, molecular weights, and boiling points; this allows for the maximum amount of different solvent-solvent and solvent-solute interactions to be characterized. The devices were all made with the same concentration of either squaraine:cosolvent or squaraine:PCBM:cosolvent. The devices were all prepared identically in terms of solution preparation, spin-coating conditions, and drying time. The devices were all measured under identical conditions using the UV-VIS Shimadzu in the Main Lab of the NPRL at RIT.

Detailed Experimental Techniques.

Table One. List of Co-solvents used and important physical properties.

Solvent	MW (g/mol)	Boiling Point (°C)	Viscocity (mPa*s)	Dielectric Constant
Chloroform	119.38	61.2	0.54	4.81
Water	18.0153	99.98	1	80.1
DMSO	78.13	189	2.14	47.2
o-xylene	106.16	144.4	0.8102	2.568
Toluene	92.14	110.6	0.5867	2.4
o-DCB	147.01	180.5	1.32	7.5
acetone	58.08	56.3	0.304	20.7
hexanes	86.18	68.7	0.2923	1.89
THF	72.11	66	0.461	7.52
Naptha	162.62	112	0.413	5

DMA	87.12	166	2.14	38.85

The desired concentration of SQ55 stock was approximately 3 mg/mL in chloroform, and the actual concentration was 3.0022 mg/mL. An initial stock concentration of PCBM in chloroform of 40.0 mg/mL was prepared. The target concentration ratio was 3:7 of SQ55:PCBM. The co-solvent concentration was 8.1 %. In order to achieve identical concentrations throughout the different samples, when only SQ55:chloroform was used, 185 microliters of the SQ55 stock was pipetted into a chloroform-rinsed vial, and then 15 microliters of the co-solvent was added. For the control, 15 microliters of chloroform was added as co-solvent. When SQ55:PCBM:Co-solvent was the desired blend, 150 microliters of SQ55 was pipetted into a chloroform rinsed vial, 34.7 microliters of PCBM was added, and 15 microliters of co-solvent was added. This is detailed in step-wise fashion below. It is incredibly important that the solutions be exposed to air as little as possible because of the low boiling point of both chloroform and some of the co-solvents.

Results.

The results presented here are but a brief description of the data that was collected and analyzed. Each of the significant absorbance peaks was quantified by change in intensity and shift in position relative to a control containing only the solute(s) and chloroform, the principal solvent. These two changes were then plotted as a function of the respective co-solvent's molecular weight, dielectric constant, viscosity, and boiling point. (Graphs 1-8) In addition, the results are presented in table format so that each change can be numerically identified. (Tables 1 and 2). In Graph 9, the absorbance data for the controls

SQ55:Chloroform and SQ55:PCBM:Chloroform are displayed with each absorbance peak identified by reference name and wavelength. Graph 10 displays the absorbance spectrum with incorporation of tetrohydrofuran as co-solvent and Graph 11 displays the absorbance spectrum with incorporation of dimethylacetamide as co-solvent.

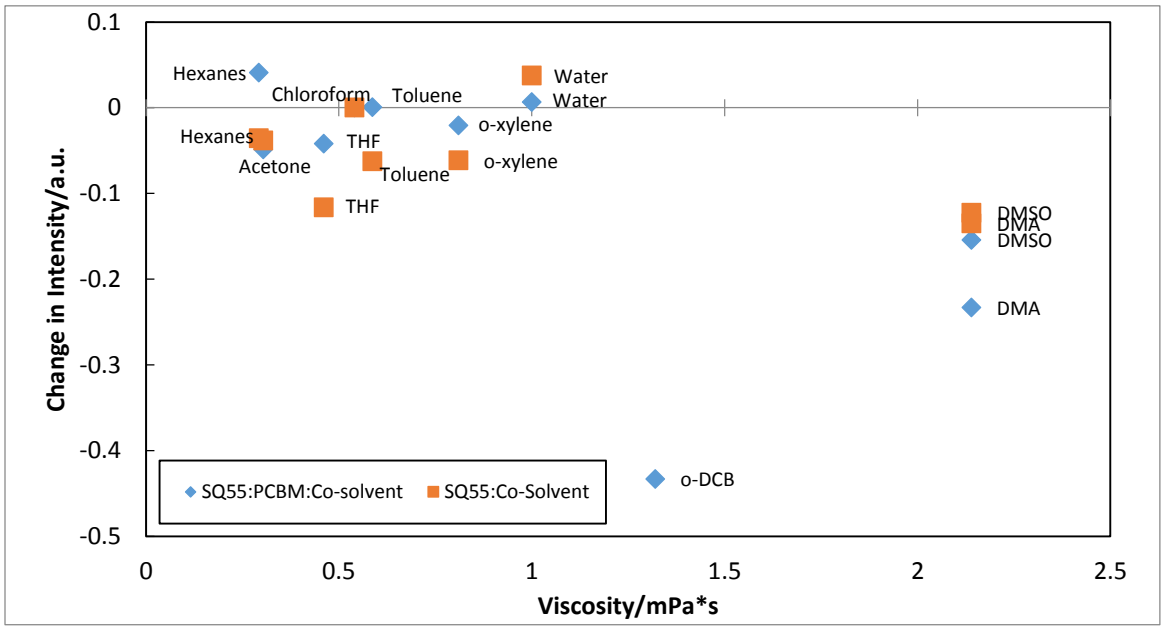

Graph One. Changes in Intensity of J-aggregate Peak (NIR peak) with respect to viscosity.

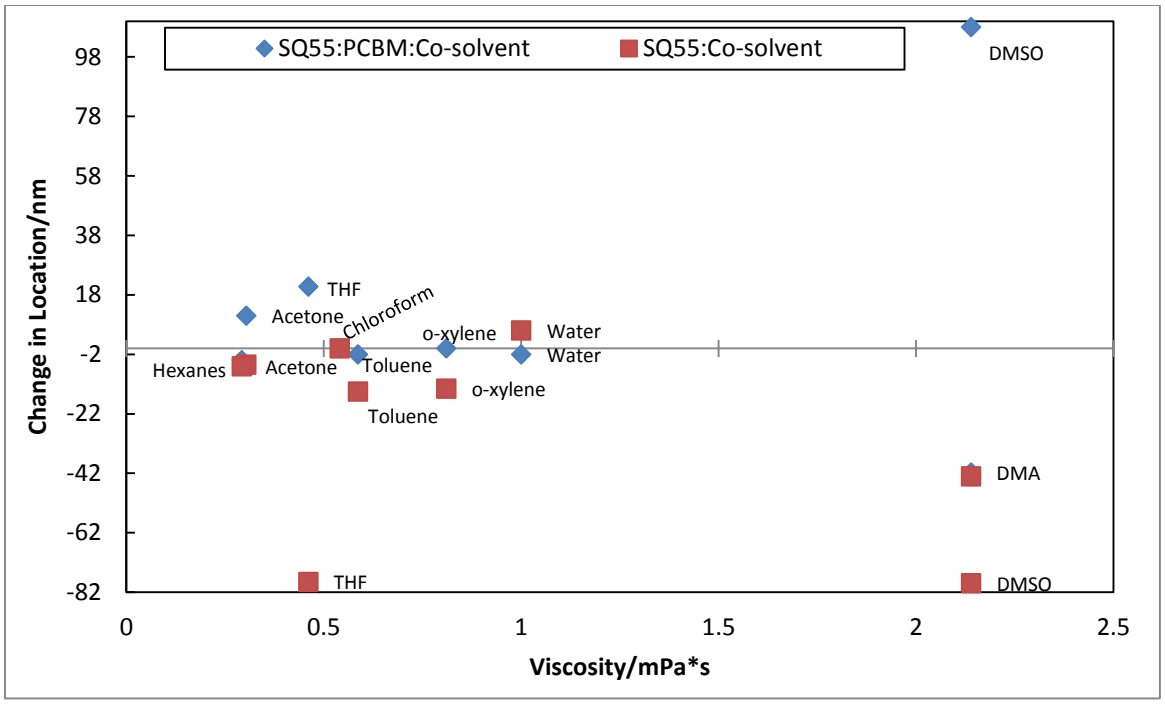

Graph Two. Shift of J-aggregate Peak with respect to viscosity.

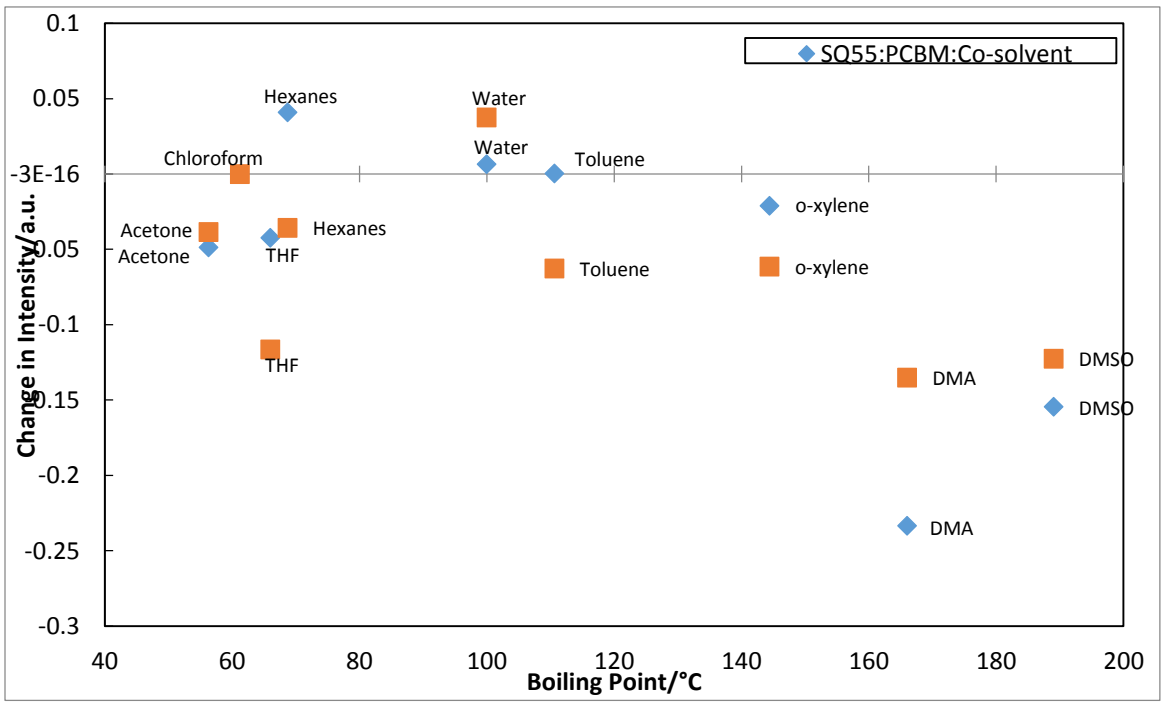

Graph Three. Changes in Intensity of J-aggregate Peak (NIR peak) with respect to boiling point.

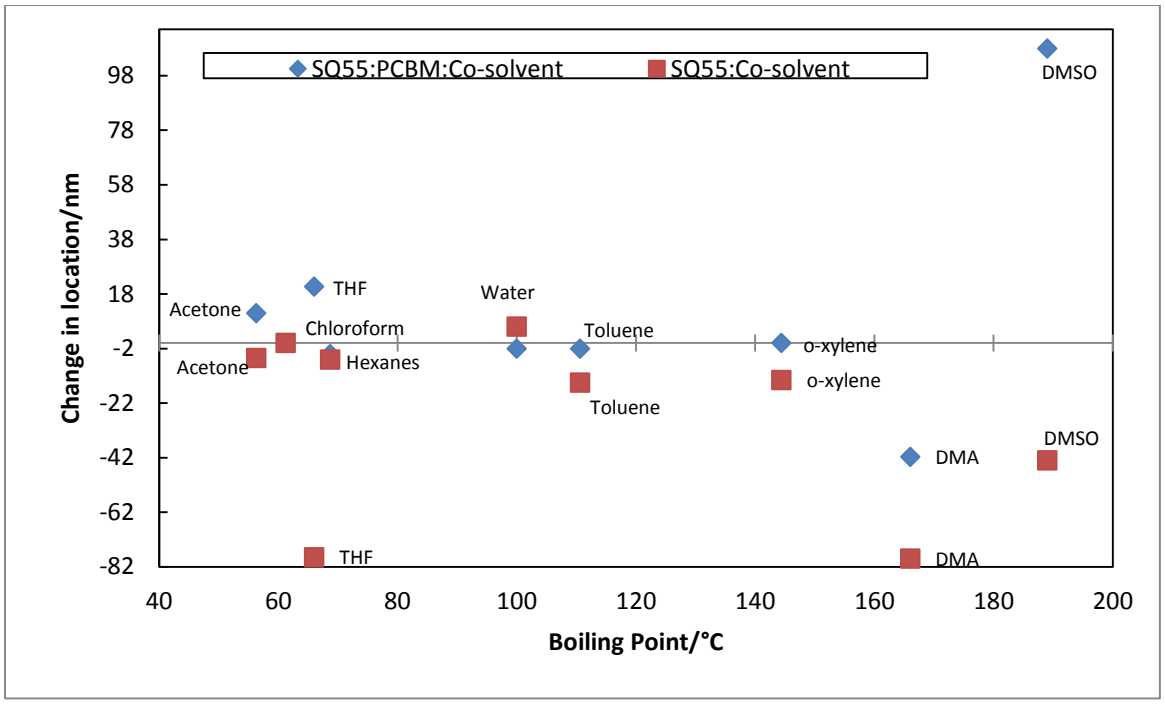

Graph Four. Shift of J-aggregate Peak with respect to boiling point.

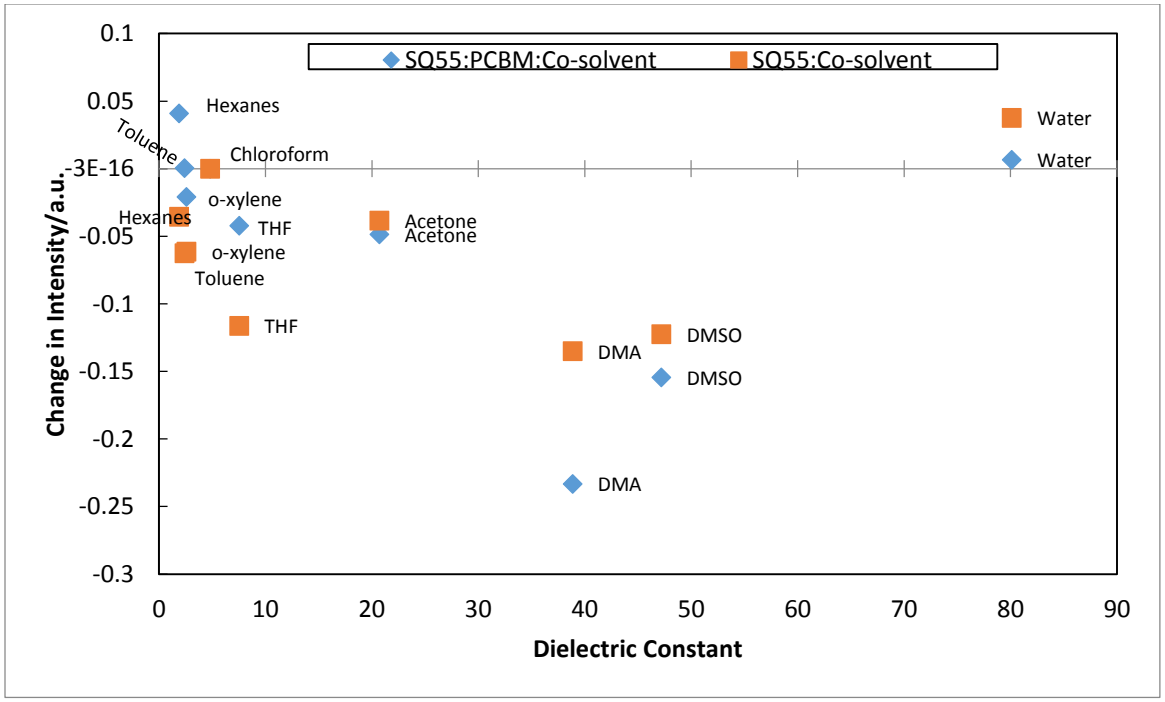

Graph Five. Changes in Intensity of J-aggregate Peak (NIR peak) with respect to dielectric constant.

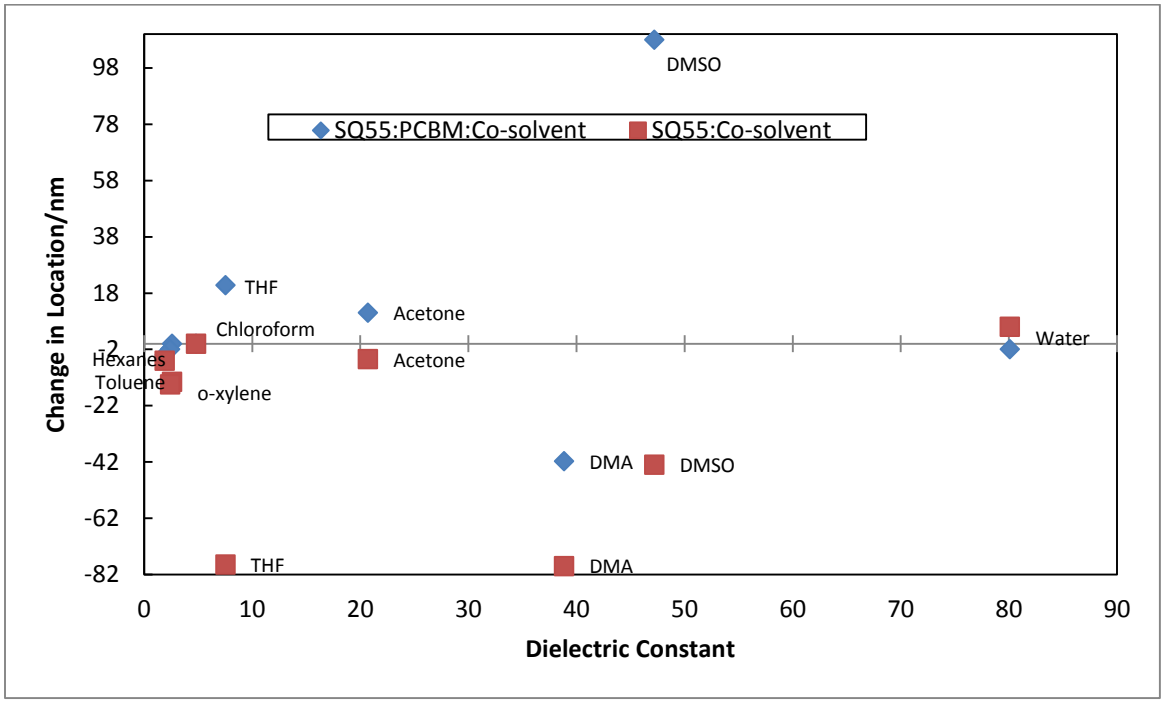

Graph Six. Shift of J-aggregate Peak with respect to dielectric constant.

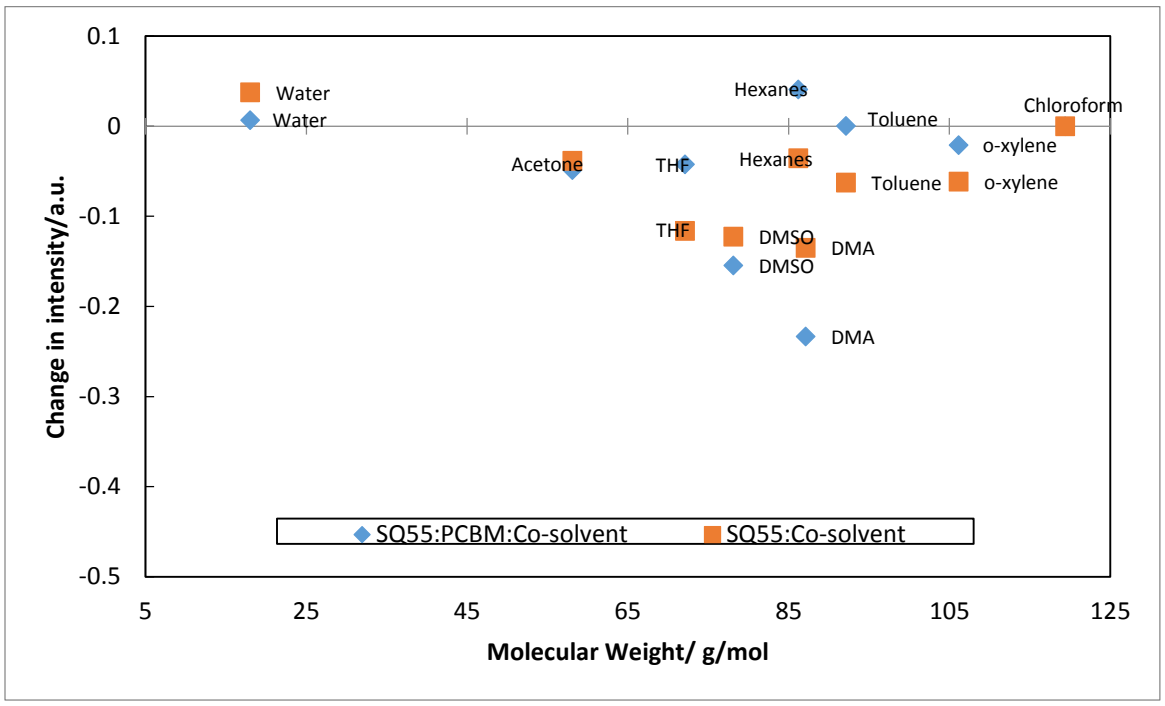

Graph Seven. Changes in Intensity of J-aggregate Peak (NIR peak) with respect to molecular weight.

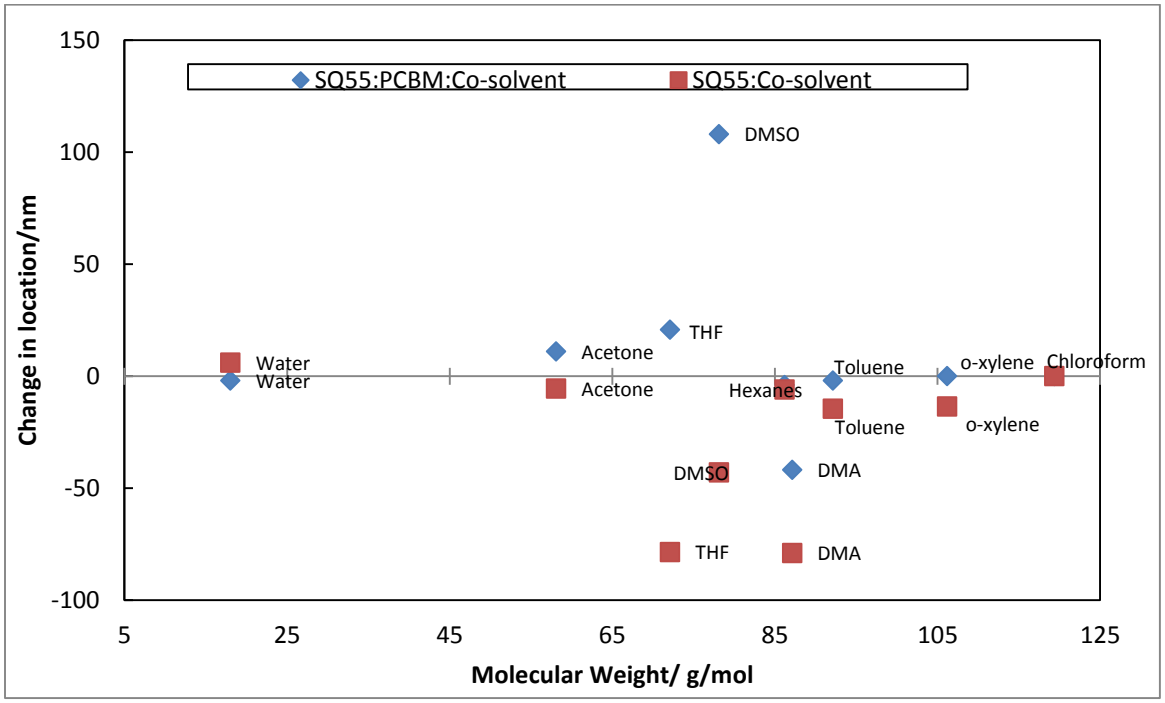

Graph Eight. Shift of J-aggregate Peak with respect to molecular weight.

Table One. Summary of Shifts and Intensity changes for SQ55:Co-solvent.

	Near IR Peak (1)		UV-VIS Peak (2)		UV peak (3)	
Solvent	Δ intensity (a.u.)	Δ location (nm)	Δ intensity (a.u.)	Δ location (nm)	Δ intensity (a.u.)	Δ location (nm)
Chloroform	0	0	0	0	0	0
Water	0.037518	6	-0.049286	14.5	-0.011526	-0.5
DMSO	-0.122492	-43	0.109653	-6	-0.008663	0
o-xylene	-0.06145	-13.5	-0.03566	0	-0.013933	-3.5
Toluene	-0.062652	-14.5	-0.028875	0	-0.012802	0

o-DCB						
acetone	-0.03843	-5.5	-0.051354	3.5	-0.014581	-0.5
hexanes	-0.035628	-6	-0.035927	0.5		
THF	-0.116271	-78.5	0.074506	-4		
Naptha						
DMA	-0.135022	-79	0.041973	-7		

Table Two. Summary of Shifts and Intensity Changes for SQ55:PCBM:Co-solvent.

	Near IR Peak (1)		UV-VIS Peak (2)		UV peak (3)	
Solvent	Δ intensity (a.u.)	Δ location (nm)	Δ intensity (a.u.)	Δ location (nm)	Δ intensity (a.u.)	Δ location (nm)
Chloroform	0	0			0	0
Water	0.006566	-2			0.052346	0
DMSO	-0.154419	108	0.0820565	-3.75		
o-xylene	-0.020919	0			0.008216	0
Toluene	0.000354	-2			0.06895	1
o-DCB						
acetone	-0.0485715	11	0.0178335	-14.25	0.11215875	74.5
hexanes	0.040923	-4			0.095708	-0.5
THF	-0.0421925	20.75	0.003318	-14.75	0.1286095	40
Naptha						
DMA	-0.2333	-41.75	0.0800535	-6		

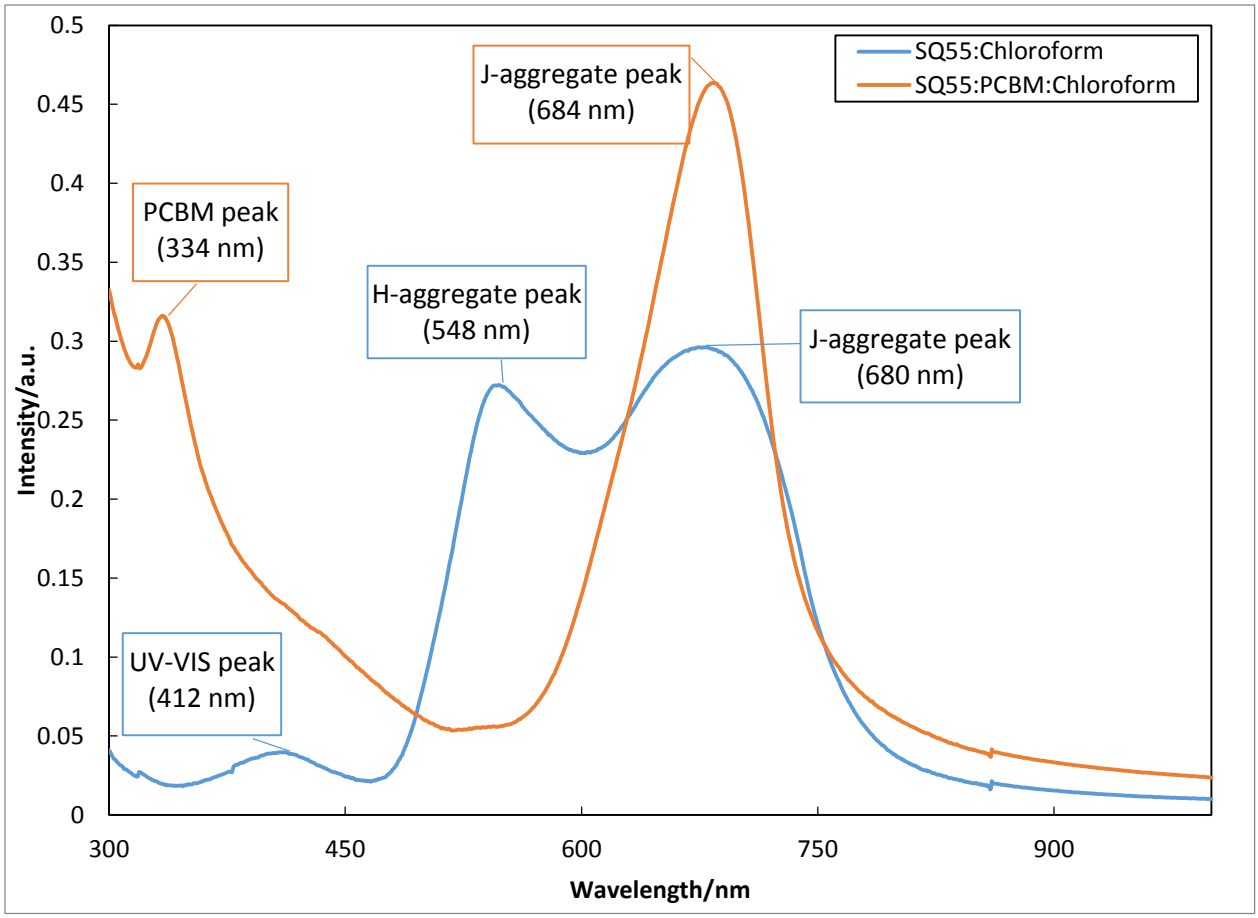

Graph 9. Absorbance Spectra of SQ55 in Chloroform and SQ55:PCBM in Chloroform.

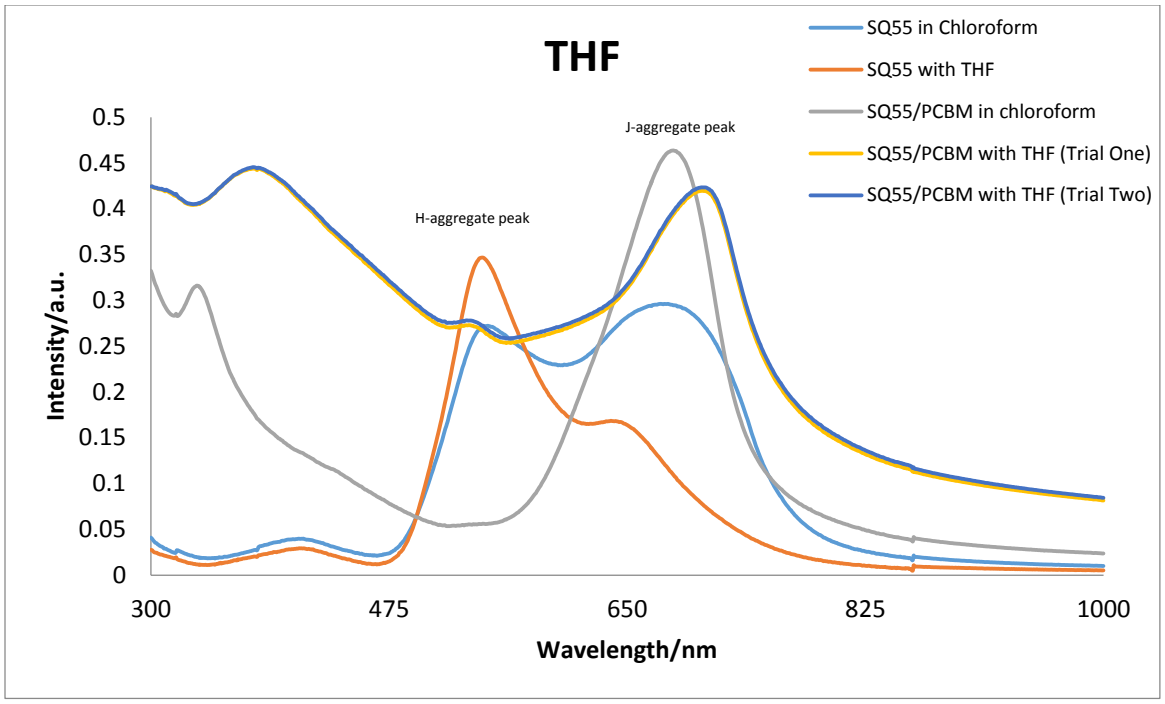

Graph 10. Effect of THF on Absorbance Spectra.

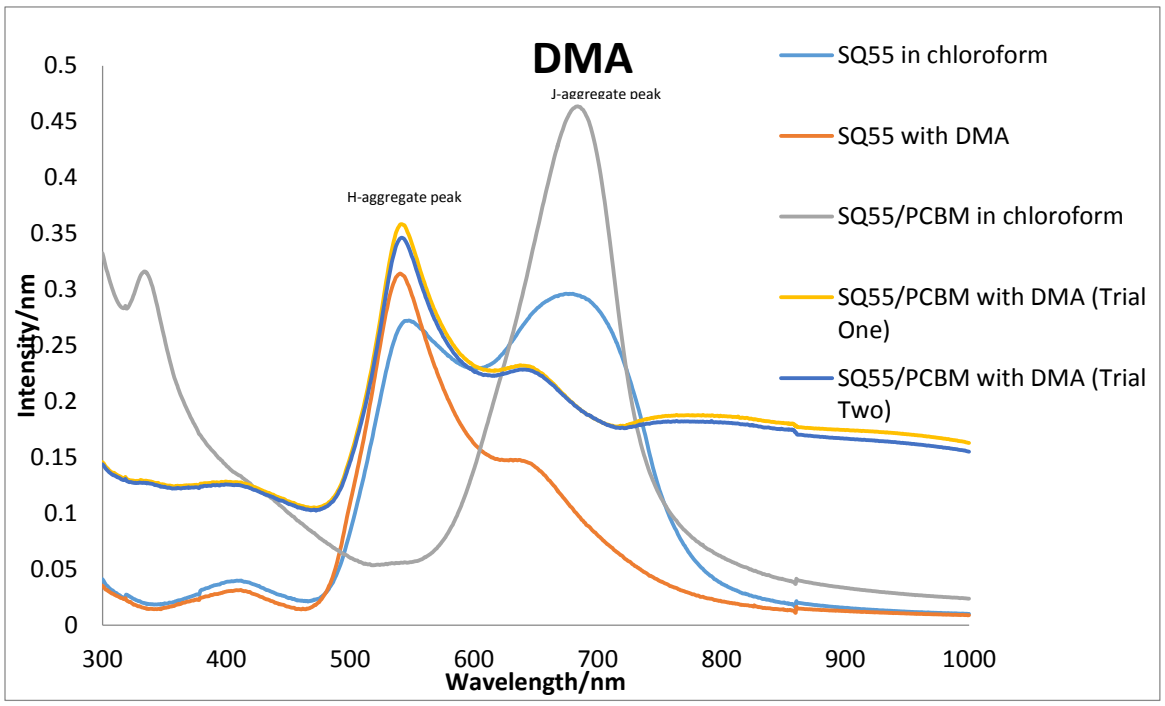

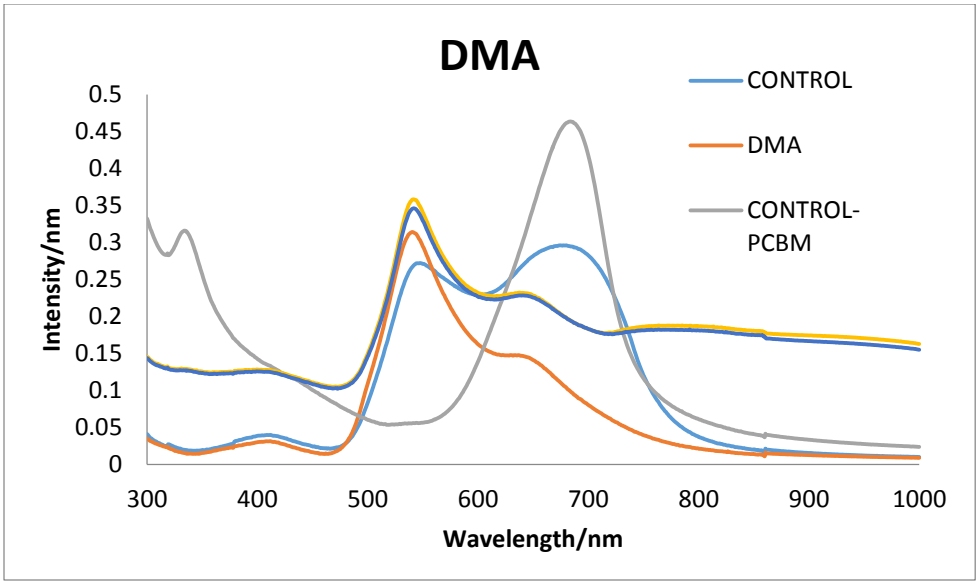

Graph 11. Effect of DMA on Absorbance Spectra.

Table Three. Characterization Values of the Two Co-Solvents.

Solvent	MW (g/mol)	Boiling Point (°C)	Viscocity (mPa*s)	Dielectric Constant
THF	72.11	66	0.461	7.52
DMA	87.12	166	2.14	38.85

Discussion.

It can be seen from the absorbance spectra that both co-solvents alone caused H-aggregation in the film blends. When PCBM is added, J-aggregation becomes preferential in the THF blend. Because of THF's relatively low boiling point, it evaporates very quickly allowing the interaction of the PCBM and the squaraine to dominate during the spin coating process causing the resultant absorbance to closely parallel that of the control with minor shifting to the red. In comparison, DMA is a high boiling point solvent with high viscosity and much greater polarity then THF. It interacts

with the SQ05 to a much greater degree then the PCBM as shown by little change from the SQ05:DMA absorbance to the SQ05:PCBM:DMA absorbance.

The differing optical properties of the squaraine based on the co-solvent and/or PCBM that is present in the system is based on the differences in structural packing. The differences in structural packing between the two aggregates can be more accurately defined as the difference in slip angles of the stacked molecules.

Figure One. The blue lines are dye molecules arranged in aggregate form to show the slip angle.

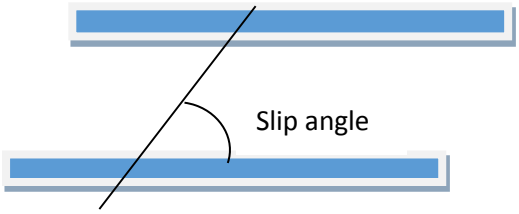

When the squaraines are aligned in parallel, simple exciton theory predicts the formation of the two excitonic bands; one higher and one lower than the monomer energy level. SQ05 can aggregate either in sandwich (H-aggregate) arrangement or head-to-tail (J-aggregate arrangement. It appears as if the incorporation of PCBM AND THF helps to stabilize the J-dimer formation. On the other hand, the incorporation of PCBM and DMA may help to stabilize the H-dimer formation. The underlying causes of this apparent stabilization are still being investigated and will be more thoroughly described once the fluorescence and AFM work has been completed.

Summary

I believe that the two solvent systems will cause the optimized devices to have different electronic properties. I believe that the THF system will have much higher spectral response in the NIR region than the DMA system. I believe that the IPCE for the THF system will be greater because of increased photon collection as compared to the DMA system. In addition, I predict increased hole mobility and therefore a higher fill factor for the THF system because the head-to-tail arrangement creates greater driving force for hole transfer through the squaraine aggregates. In addition, I expect that the AFM scans will reveal different intercalation of the donor and acceptor moieties due to the change in aggregate type.

Thermodynamic Analysis

Because of the equality

$$\delta = \left(\frac{\Delta E^v}{V}\right)^{\frac{1}{2}}$$

the enthalpy portion of the Gibbs Energy of Mixing equation can therefore be rewritten as

$$\frac{\Delta H}{V} = (\delta_1 - \delta_2)^2 \phi_1 \phi_2$$

giving the final full equation as

$$\Delta G^M = kT\left(N_1 + \frac{N_2 V_2}{V_1}\right)\left[\phi_1 ln\phi_1 + \phi_2(\frac{V_1}{V_2})ln\phi_2 + (\delta_1 - \delta_2)^2 \phi_1 \phi_2\right]$$

This can then be manipulated to include size ratios for calculation of spinodal and binodal behavior of a system in order to generate phase diagrams.

a. Phase Diagrams

In order to generate phase diagrams, the Hildebrand solubility equation must be solved for

specific cases. Phase diagrams offer a way to examine the behavior of a two component system upon temperature and compositional changes. The Hildebrand solubility equation allows for input of empirically determined parameters like the volume of the molecules and the solubility parameters. For this work, the volume of the squaraine was calculated by estimating their length on the long axis using C-C single and double bond lengths (see Table I) and then calculating the volume of the squaraine as an ellipsoid. The volume of the PCBM was calculated by estimating its diameter using C-C double bond lengths and then calculating the volume of the PCBM as a sphere.

Table I. Bond lengths and values for volumes of molecules.

Squaraine			
#C-C single bonds	5	C-C single bond length (A)	1.54
#C-C dbl bonds	8	C-C dbl bond length (A)	1.34
#C-N bonds	2	C-N bond length (A)	1.355
#C-O dbl bonds	2	C-O dbl bond length (A)	1.23
Total length (A)	21.13	Total height (A)	5.14
Total area (A^2)	341.029748		
Total volume(A^3)	2337.19054		
Total Volume(m^3)	2.33719E-27		
PCBM			
#C-C dbl bonds	16	C-C dbl bond length (A)	1.34
		total radius	10.72
Total area (A^2)	33.6608		

Total volume(A^3)	5157.660372	
Total Volume(m^3)	5.15766E-27	

The Hildebrand solubility equations are quite large.

$$\ln[1-(\phi_2)_A]+\left(1-\frac{1}{r}\right)(\phi_2)_A+V_1\frac{(\delta_1-\delta_2)^2}{kT}(\phi_2)_A{}^2$$
$$=\ln[1-(\phi_2)_B]+\left(1-\frac{1}{r}\right)(\phi_2)_B+V_1\frac{(\delta_1-\delta_2)^2}{kT}(\phi_2)_B{}^2$$
$$\ln[(\phi_2)_A]+(1-r)[1-(\phi_2)_A]+V_2\frac{(\delta_1-\delta_2)^2}{kT}[1-(\phi_2)_A]^2 \quad (2.62)$$
$$=\ln[(\phi_2)_B]+(1-r)[1-(\phi_2)_B]+V_2\frac{(\delta_1-\delta_2)^2}{kT}[1-(\phi_2)_B]^2$$

The two equations can be solved for various size ratios differences ($r = V_1/V_2$), temperatures (T), and solubility parameter differences. The first solution of the equations generates the binodal curve by setting the size ratio to 1 to generate the following equation.

$$ln\left[\frac{1}{\phi_{2A}}-1\right]=\frac{V_1(\delta_1-\delta_2)^2}{RT}[1-2\phi_{2A}]$$

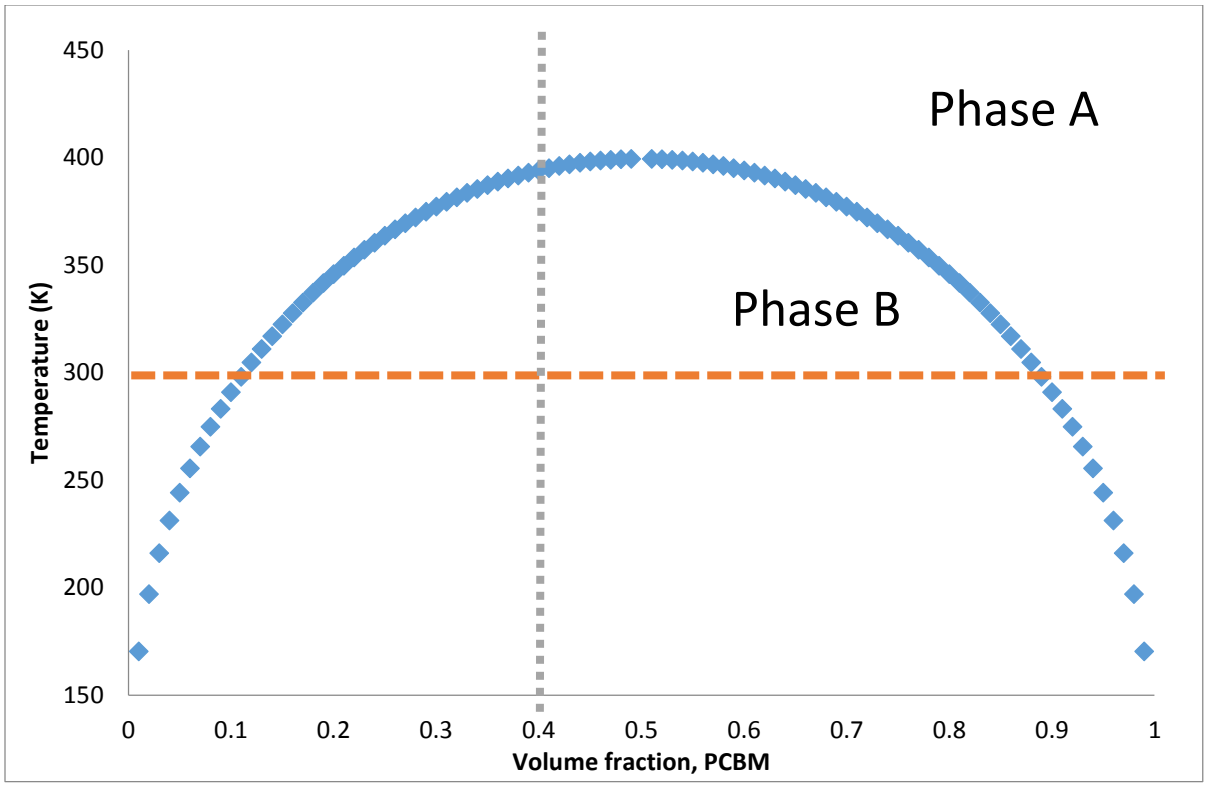

Figure 7. Theoretical binodal curve for SQ:PCBM mixture, size ratio=1, solubility parameter difference = 5.29 cal/cm^3.

It can be seen in Figure 7 that at any given temperature, a line can be drawn to find the points of equilibrium for specific concentrations. The red dashed line at 300 K illustrates this point; when the volume fraction of PCBM is less than 0.1 (10%) or greater than 0.9 (90%) it will all be in Phase A. When the volume fraction of PCBM is between 0.1 and 0.9 it will be in Phase B. If a vertical line is drawn at a specific PCBM volume fraction, the impact of changing temperature can be examined. The green dotted line at 0.4 (40%) volume fraction PCBM illustrates this second technique. If the mixture is initially at 400 K it will be in Phase A, and then as it is cooled it will move into Phase B. However if the mixture is initially at 0.05 (5%) volume fraction PCBM and cooled from 400 K to room

temperature, it will remain in Phase A. These two tie lines demonstrate the large amount of information that can be gleaned from these phase diagrams.

Another approach for solution of the equations is to determine the spinodal curves at a variety of size ratios. This is done by starting fresh from the Gibbs equation

$$\Delta G^M = kT\left(N_1 + \frac{N_2 V_2}{V_1}\right)\left[\phi_1 ln\phi_1 + \phi_2(\frac{V_1}{V_2})ln\phi_2 + (\delta_1 - \delta_2)^2\phi_1\phi_2\right]$$

and calculate the partial molar free energy by taking the partial derivative of the Gibbs equation with respect to the number of molecules.

$$\Delta\mu_i = \frac{\partial \Delta G}{\partial N_i}\Big| P, T, N_j$$

The volume fractions are rewritten in terms of numbers of molecules and size ratio, r.

$$\phi_1 = \frac{N_1}{N_1 + rN_2}; \phi_2 = \frac{rN_2}{N_1 + rN_2}$$

Substituting this into the Gibbs equation and dividing both sides by kT gives

$$\frac{\Delta G^M}{kT} = \left[N_1 ln\frac{N_1}{N_1 + rN_2} + N_2 ln\frac{rN_2}{N_1 + rN_2} \quad + \frac{V_1}{kT}(\delta_1 - \delta_2)^2\frac{rN_1N_2}{N_1 + rN_2}\right]$$

Taking the differential in order to calculate the partial molar free energy, the following equation is obtained after converting back to volume fractions.

$$\Delta\mu_1 = kT\left[ln\phi_1 + \left(1 - \frac{1}{r}\right)\phi_2 + V_2\frac{(\delta_1 - \delta_2)^2}{kT}\phi_2^2\right]$$

Finally, a spinodal equation can be obtained by applying the criterion $\frac{\partial \Delta\mu_1}{\partial \phi_2}\Big| T, P = 0$, which states that the chemical potential of one component will not change with respect to the volume fraction of the other component at constant temperature and pressure.

$$0 = \left(1 - \frac{1}{r}\right)(1 - \phi_2) + 2\phi_2(1 - \phi_2)\frac{V_1}{kT}(\delta_1 - \delta_2)^2 - 1$$

This was solved analytically and supplied with the estimated volume as shown in Table I, as well as the same solubility parameter difference used to generate the binodal plot shown in Figure 7. A variety of volume ratios were chosen as shown in Figure 8.

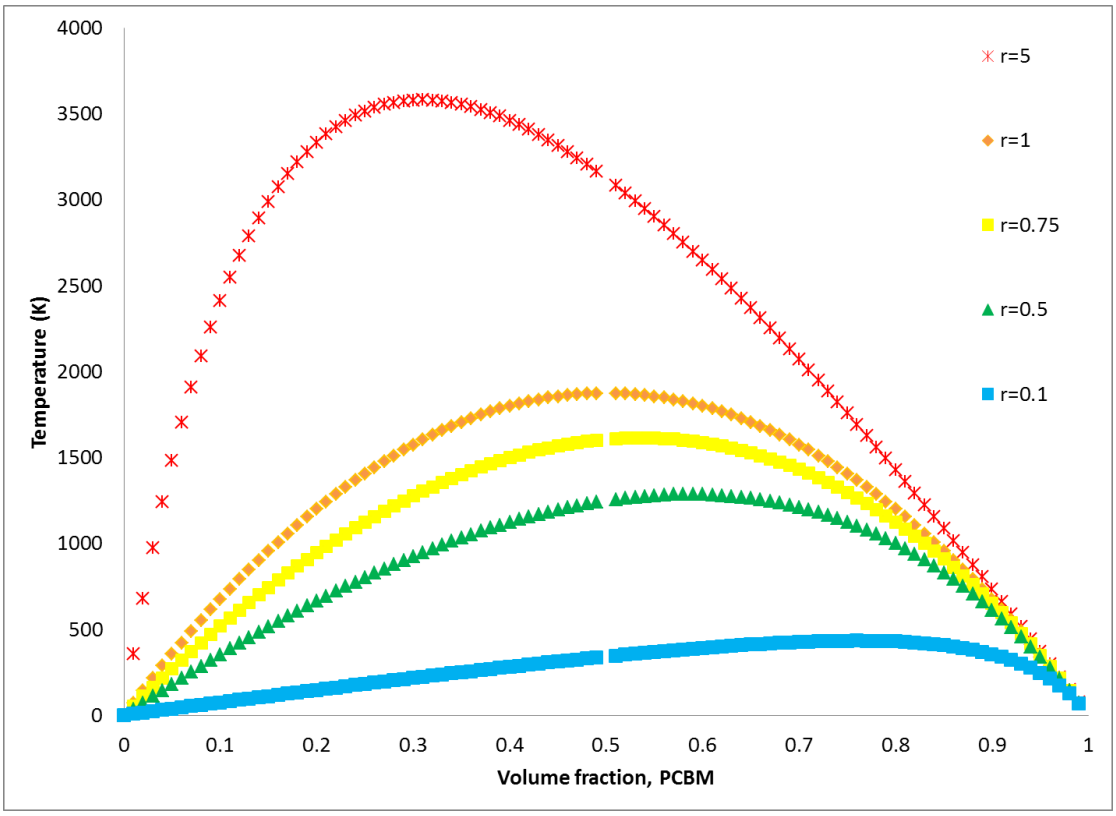

Figure 8. Theoretically generated spinodal curves for SQ:PCBM mixture.

I. Discussion

a. Interpretation of Results

Some of the results are fundamental and qualitative. For example, we were able to decide that the SQ:PCBM solution during spin coating is likely to form domains that are describable using spinodal decomposition, while the SQ:PCBM film during annealing is

likely to undergo phase transitions through nucleation and growth. The film mixture can be described as a "solution" in that it is a mixture composed of two unique components. Each of these components has at least two phases, amorphous and crystalline, and these will coexist in the film depending upon the temperature and volume fraction of each of the components. The Flory-Huggins approach to modeling our system is not going to be the best approach because we have a lack of experimental data to fit to the model, like Enrique Gomez's group was able to[36,163]. The Hildebrand solubility parameter approach was able to actually generate graphs for us, and the solubility parameter could conceivably be determined experimentally for our materials. The volume could also be determined using computational chemistry. I believe that this approach will be the most beneficial in terms of generating usable theory.

I have been unable to determine the impact of r by simultaneously solving equation 2.62. That remains an unanswered question. Additionally, there are several problems with the temperature ranges that have been generated thus far. I do not feel that I have a completely solid grasp on how the equation needs to be manipulated to fit our systems, and what the potential weaknesses of the Hildebrand model could be. Investigating the Flory Huggins treatment in depth allowed me to see that it would cause problems for our system because there was no way to incorporate partial miscibility, which we think we have in our system due to the intercalation of the SQ and PCBM domains. I don't know if the Hildebrand approach will actually allow for this treatment. I think the Hildebrand approach does have the significant advantage of allowing for inclusion of experimentally determined results, whereas Flory-Huggins only fits to data. Additionally, the Hildebrand approach allows for a "backdoor" empirical look at the total amount of molecular forces

of attraction that are generating the domains in our films. Further data collection would be required in order for us to be able to actually get an idea of which forces were predominate in our films, as we would only be able to really look at the total interaction strength, w. Even then, we would only be able to calculate that strength if the Stachard mean approximation held for our system, and I have not convinced myself that it does.

b. Presentation of the Course

The course started with a Gomez paper that I reviewed in journal club that used the Flory-Huggins model to explain their data. I was tasked with explaining both the paper and the Flory-Huggins approach. Upon attempting this, I realized that I needed a much more extensive treatment of polymer thermodynamics and turned to the library. I generated a series of 90 minute lectures/discussion presentations on the topic of Thermodynamics of Polymer-Polymer Miscibility and presented them. I also made a spreadsheet to do a complete theoretical model of the Hildebrand approach, and presented that. I then ended with the paper being read right now.

c. Possible Changes to the Course

I think this was a very difficult course to give because it was so broad and not really guided by anything besides my own interests. I tried my best to give thorough treatments of the things that I found interesting, but I often under or overestimated what the other participants knowledge base and interest level was. I tried to consistently articulate that my goal was to understand the annealing process, and explain how each thing/presentation/spreadsheet I prepared related to that, but I feel that I failed at making the connection for others more often than not.

For this to be a better course, I would want to choose a specific path ahead of time and stay focused on it by picking **one** method to evaluate, or one specific problem to solve. I would give tangible requirements for what knowledge needed to be imparted to the group. I would do a survey ahead of time to see what people knew and what they didn't. I would want the other members of the class to be doing as much work as I was so that we would all progress together and I could be questioned and challenged in ways that broadened my understanding and caused me to have deeper and more critical insights regarding the information that I was learning and teaching. I would definitely make sure that I went through and derived the entire math before a presentation so that I was more confident with the interpretations of the results. Finally I think this should have been a 4-hr a week course instead of two. There is so much value in better understanding thermodynamics, and especially the thermodynamics of our systems.

II. Conclusions and Future Work

This quarter course gave a broad overview of the field of polymer thermodynamics with focus on two possible approaches to understand and describe phase equilibrium and phase transitions of multi-component systems. Phase diagrams were generated for one system the Collison Group is studying. Future work includes measuring solubility parameters for materials experimentally, calculating spatial values of molecules computationally, and figuring out how to simultaneously solve two equations chock full of natural logarithms and variables. Additionally, I believe it would behoove all the participants to write a very brief summary of how thermodynamics can guide understanding of devices and films, and how we can benefit from being able to use them as a predictive/explanatory tool.

10.2. Appendix B: Raw Data

$DiPSQ(OH)_2$ Full Matrix Study Data

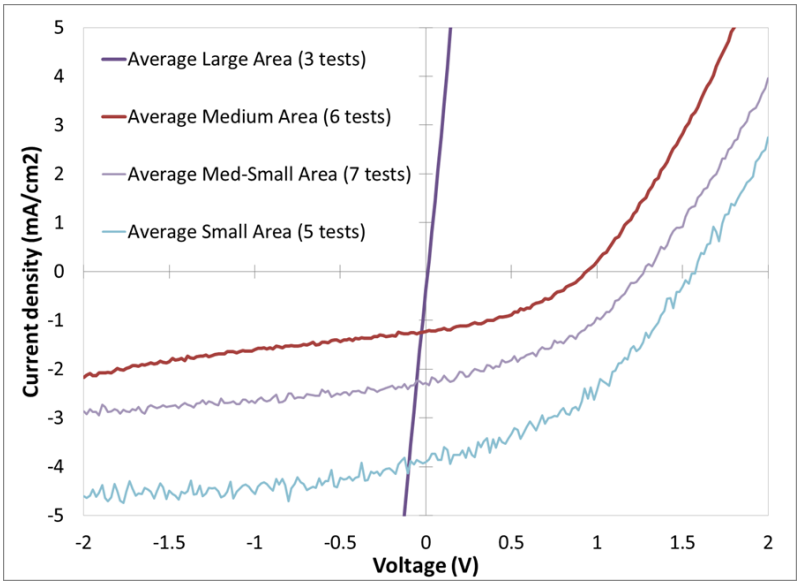

Unannealed SQ:PCBM devices.

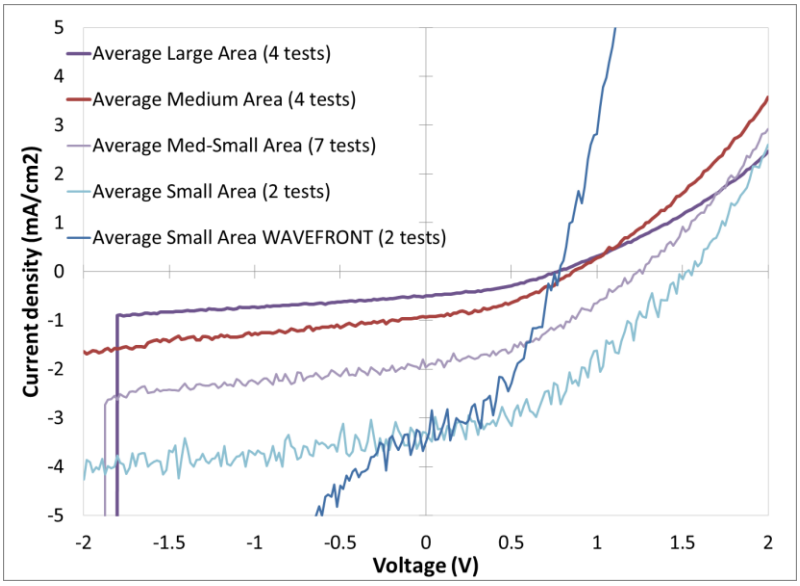

Current-voltage curves for SQ:PCBM devices annealed at 150°C for 60 s.

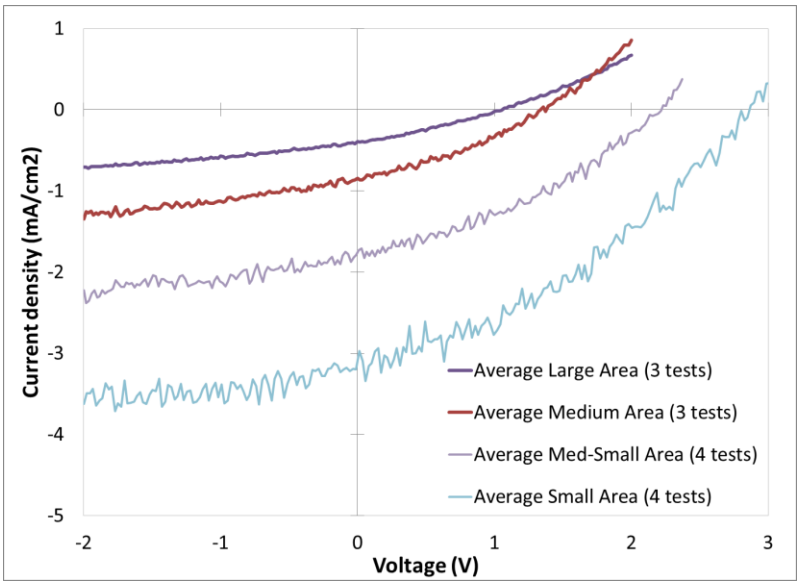

SQ:PCBM devices annealed at 165°C for 60 s.

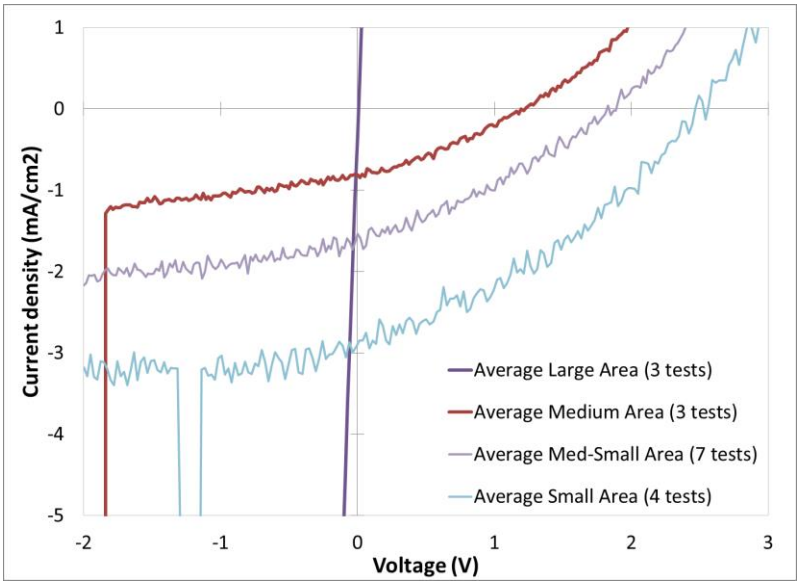

SQ:PCBM devices annealed at 180°C for 60 s.

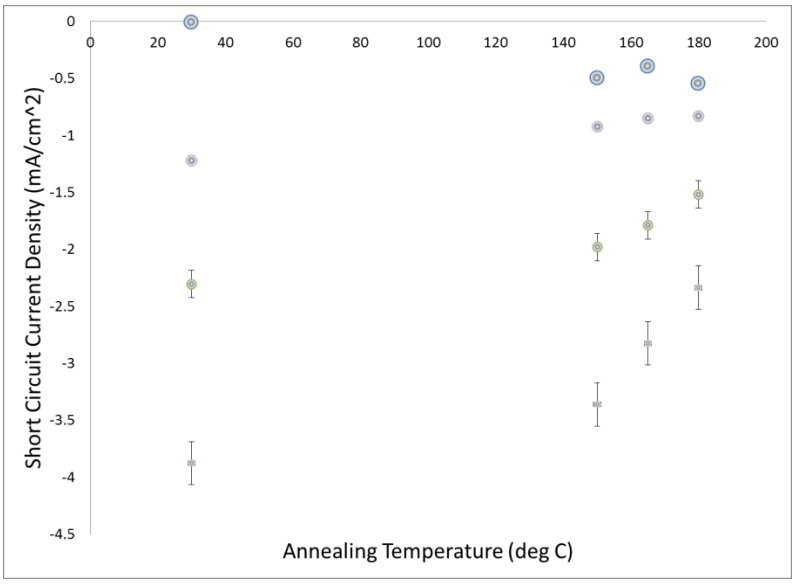

Another way of looking at the change in current density. The circles are meant to reflect actual device sizes of the solar cells.

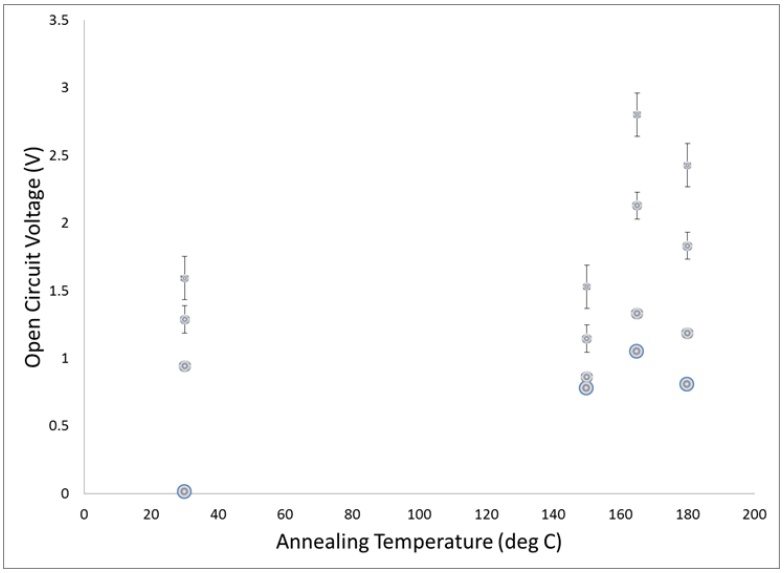

Another perspective on open circuit voltage and area/temperature changes.

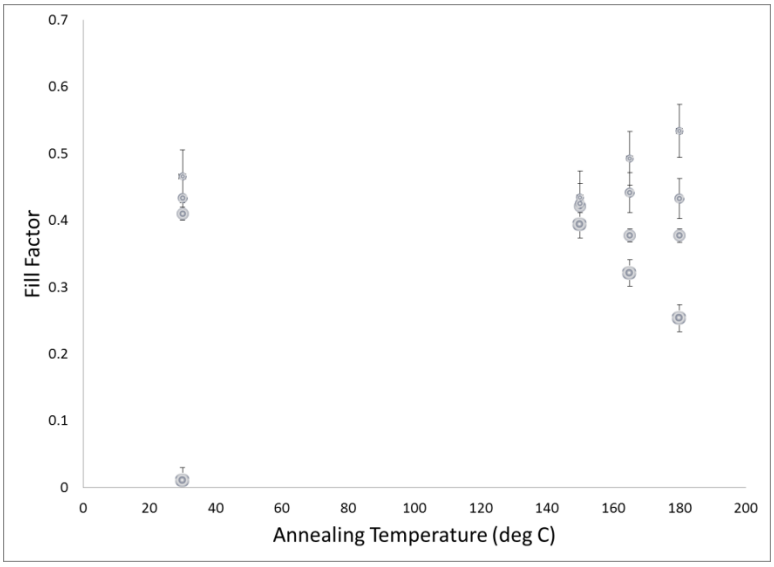

Changes in fill factor with annealing temperature.

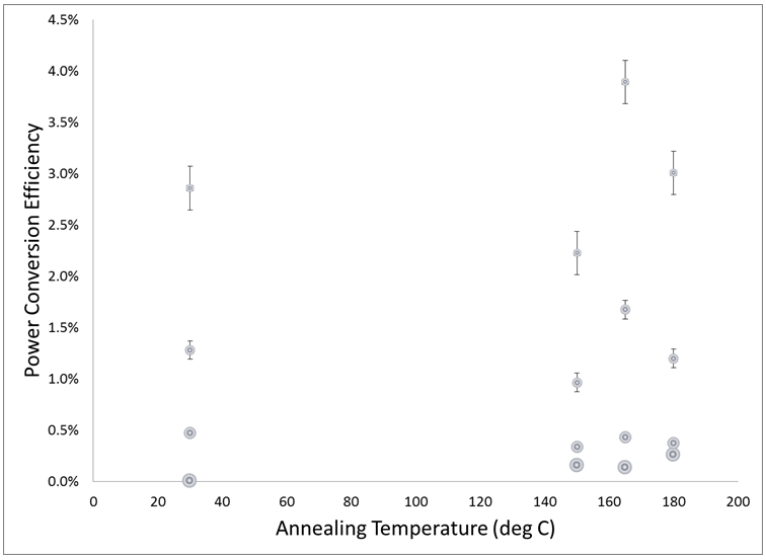

Efficiency as a function of temperature.

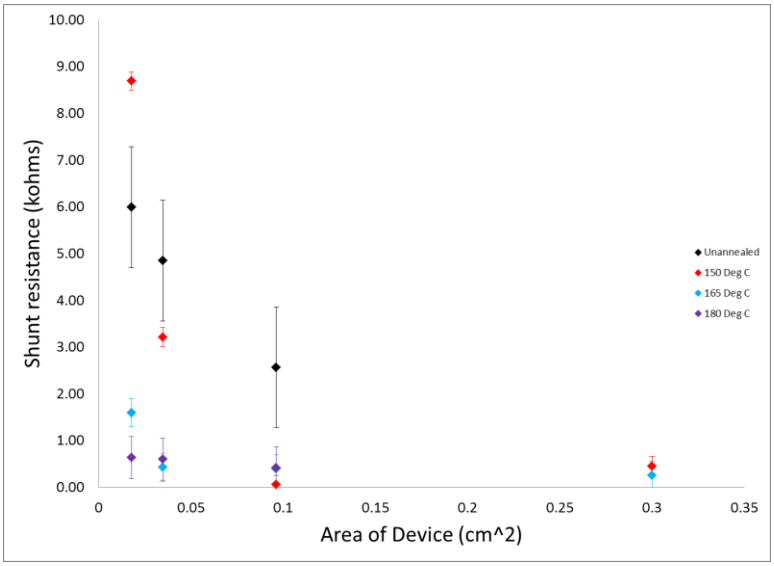

Shunt resistance and area.

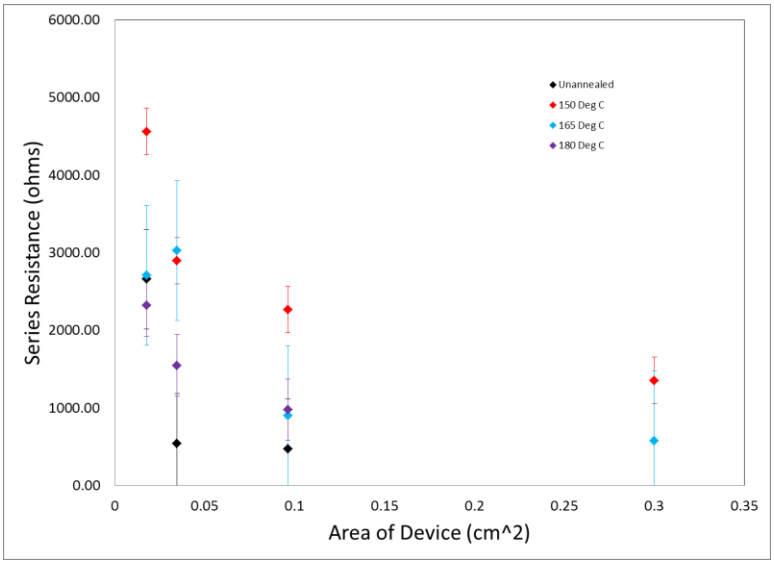

Series resistance and area.